DATE DUE	DATE DUE	DATE DUE
SEP 05 1998		
MAY 27 2000		

STRUCTURAL PROPERTIES OF HIGH PERFORMANCE POLYMER FIBERS AND THEIR EFFECTS ON FIBER-MATRIX ADHESION

by

Javad Kalantar

A DISSERTATION

Submitted to
Michigan State University
in partial fulfillment of the requirements
for the degree of

DOCTOR OF PHILOSOPHY

Department of Chemical Engineering

1991

ABSTRACT

STRUCTURAL PROPERTIES OF HIGH PERFORMANCE POLYMER FIBERS AND THEIR EFFECTS ON FIBER-MATRIX ADHESION

by

Javad Kalantar

During the past three decades, many important types of high-strength and high-modulus polymer reinforcing fibers have been developed. These fibers possess combinations of stiffness, high strength, high toughness, and low density that rival the properties of inorganic reinforcing fibers such as glass and carbon fibers. However, these polymer fibers generally exhibit weak adhesive and interfacial properties. This study sought to develop a fundamental understanding of structural and chemical properties of polymer fibers that influence their adhesive and interfacial behavior. This knowledge is critical for developing approaches to improve the engineering performance of these fibers.

Several physical and chemical treatments of polymer fibers that produce different extents of structural and chemical alterations were examined in this study. Polymer treatments with coupling agents (titanium and zirconium organometallic complexes), polymer coatings (butadiyne, Parylene-N, Parylene-C), chemical treatments (fluorination, sulfonation), plasma treatments (O_2, CF_4, He, CO_2, NH_3, N_2O, Ar, H_2O), ion implantations (Ti^+,Ar^+,N^+,He^+), and structural modifications (sol-gel infusion, Friedel-Crafts chain crosslinking) were examined. The study concentrated on polyaramid fibers (Kevlar® 29, 49, 149, and Technora®), aromatic heterocyclics (p-Phenylene Benzobisoxazole), and ultra-high-modulus polyethylene fibers (Spectra® 1000) as well as

model polycarbonate and polyethylene in sheet and bulk forms. The knowledge developed, however, should be applicable to other high performance polymer fibers.

Examinations of plasma treatments and coupling agents provided insights to the interfacial limitations of fiber-matrix adhesion. Ion implantation, sol-gel, Friedel-Crafts, and sulfonation treatments were examined because of their ability to affect the inter-fiber cohesive interactions. Results show that the skin-core morphology and/or wetting properties of high performance polymer fibers can limit their adhesive and interfacial load transfer properties. However, once these limitations are overcome, fiber lateral cohesive properties become the limiting factor. Therefore, the key to improving the fiber-matrix interfacial load transfer of high performance polymer fibers is both to improve the wettability, and to increase the fiber lateral cohesive strength.

The study also developed a new sample preparation and spectroscopic analysis method to quantify the composition of the polymer interphase at high resolution. This method significantly facilitates atomic and chemical analysis of the polymer interphase. The application of the method to determine sulfur distribution in sulfonated polycarbonate samples provided experimental data for mass-transfer modeling of the sulfonation surface treatment.

To my parents and family,

for all the love and support

you've given me.

Acknowledgements

I like to acknowledge and thank those individuals who have greatly influenced my intellectual as well as personal development leading to this milestone. My parents, Hassan and Parvin, who stressed the importance of education and through many sacrifices provided me with unconditional emotional and financial support. Professor Lawrence T. Drzal who gave me his full support during my Master and Ph.D. education. Professor Drzal gave me the freedom to grow, mature and achieve under his capable guidance. He taught me excellence by his example.

My personal associations at the Composite Materials and Structures Center (CMSC) will remain very special to me. My colleagues, Shri Iyer, Tesh Rao, Brent Larson, Craig Chmielewski, Richard Schalek, Hassan Almossawi, Pedro Franco-Herrara, Sanjay Padaki, Himanshu Asthana, Murty Vyakarnam, Matt Kendziorski, Greg Fisher, Ed Drown, and many others made CMSC the exceptional place it is. My association with Richard Schalek was particularly productive both in research and in friendship. Thanks to you all for your support and, more importantly, for your friendship.

As with most undertakings of this size, this dissertation was shaped by the ideas of many people. My Ph.D. committee members, Prof. D. S. Grummon, Dr. R.J. Morgan, Prof. M.C. Hawley, and Prof. K. Berglund gave me direction and support. I particularly thank Prof. D.S. Grummon for his professional guidance as well as his personal friendship. I was always fascinated by Dr. Morgan's stimulating ideas and excellent insight into my area of dissertation. It was always a pleasure to discuss my work with Prof. Hawley who generously gave me his time. Prof. Berglund taught me about sol-gels and gave me excellent suggestions. Special thanks to Dr. E. Grulke and W. Walles for their insights into sulfonation treatments and taking the time to share them.

My appreciation to the staff of CMSC, Mike Rich and Dr. Kevin Hook for teaching me a variety of instrumentations. Arlene Klingbiel always assisted me in the many ways that only a good secretary can with a added bonus of a friendly personality. Thanks to Brian Rook for his helpful hints and suggestions.

My time at Michigan State University was also highlighted by many people who will remain my life-long friends. Farshid and Shabnam shared and comforted me during my highs and lows. Farzad and Setareh amazed me with their hospitality and generosity. Farshid and Kathy always made me feel welcomed.

My sincere gratitude to the E.I. du Pont de Nemours & Co. and Dow Chemical Co. for providing financial support for this research.

Finally, I would like to express my appreciation to the staff of Center for Electron Optics for their help and informative discussions.

Table of Contents

List of Tables

List of Figures

Nomenclature

A = Interface area (mm^2)
A_f = Fiber cross-sectional area
A_m = Matrix cross-sectional area
c_i = Molar concentration of component i
C_1 = Concentration of species 1
C_{1i} = Initial concentration of species 1
d = Fiber diameter (μm)
D = Diffusion coefficient
f = Helmholtz free energy per unit area
F = Wetting force (mg)
E_f = Fiber compressive modulus (GPa)
E_m = Matrix compressive modulus (GPa)
E_{1f} = Axial fiber elastic modulus (GPa)
E_K = binding energies of the K shell atomic orbital
E_L = binding energies of the L shell atomic orbital
E_M = binding energies of the M shell atomic orbital
E_{KLM} = Kinetic energy of an electron emitted by a KLM Auger transition
E_{KE} = Kinetic energy of photoelectron orbital
E_{BE} = Binding energy of the atomic orbital
G = Gibbs free energy
G_m = Matrix shear modulus (GPa)
j_1 = mass-transfer flux of species 1
K = Reaction equilibrium constant
l_c = Fiber critical length (mm)
$l_{c,theo}$ = Theoretical fiber critical length (mm)
n_i = Number of moles of component i
p = Presure of the phase (atm)
r_1 = Rate of production per volume of species 1
R = Gas constant
S = Entropy of the system (J)
T = Temperature (°C)
V = Volume of the phase (l)

Greek

Γ_i = Surface excess of component i = n_i/A
γ = Surface tension (dyne/cm)
γ_L^d = Dispersive component of surface energy of liquid (dyne/cm)
γ_L^p = Polar component of surface energy of liquid (dyne/cm)
γ_L^t = Total surface energy of liquid (dyne/cm)
γ_s^d = Dispersive component of surface energy of solid (dyne/cm)
γ_s^p = Polar component of surface energy of solid (dyne/cm)
γ_s^t = Total surface energy of solid (dyne/cm)
γ_f = Fiber surface energy (dyne/cm)
γ_m = Matrix surface energy (dyne/cm)
ϵ = Fiber and Matrix strain
ϵ_i = Cross-chemical potential of component i = df/c_i
Θ = Liquid contact angle (degree)
σ_{cf} = Fiber compressive strength (MPa)
σ_m = Matrix stress (MPa)
σ_{uf} = Fiber tensile strength (GPa)
τ = Interfacial shear strength (MPa)
μ_i = Chemical potential of component i (J/mol)
ν_{1f} = Fiber Poisson's ratio
ϕ_s = Spectrometer work function.

CHAPTER 1

Introduction

1.1 HIGH PERFORMANCE POLYMER FIBERS

The term "high performance polymer fibers" refers to organic fibers that posses high axial tensile properties comparable to those of the inorganic reinforcing fibers (Deteresa 1985). These fibers have tensile properties that are at least an order of magnitude greater than more common textile fibers. High performance fibers possess a unique combination of stiffness, high strength, high toughness, and low density that makes them an attractive alternative to inorganic reinforcing fibers such as glass and carbon fibers. Zahr *et al.* (1989) have presented an overview discussion of the unique properties of aramid fiber polymer composites. In general, on a per weight bases, high performance polymer fibers have a significant advantage over other inorganic reinforcing materials. **Figure 1.1** shows a plot of specific tensile strength and modulus of some reinforcing fibers as well as some conventional materials (Agrawal *et al.* 1980, Kumar 1989). Tensile properties of the high performance polymers fibers approach their theoretical maximums, which is achieved by a high degree of polymer chain alignment and reduction of defects in the

fiber structure. However, the high performance polymer fibers, generally exhibit weak adhesive properties. The level of fiber-matrix adhesion controls many properties of fiber-reinforced composites such as transverse strength, shear strength, and flexure. The weak adhesive properties of high performance polymer fibers significantly limits their structural applications.

Significant amounts of research have been devoted to the study of the interfacial properties of glass and carbon fibers and many surface treatment techniques and coupling agents have been developed. For glass and carbon fibers these surface treatment techniques can double or triple the interfacial bond strength (Riggs *et al.* 1982, Wu 1982, Bjorksten *et al.* 1952). For the liquid crystalline polymer fibers, many workers have attempted to obtain similar adhesion improvements with interfacial treatment methods but they have been generally unsuccessful.

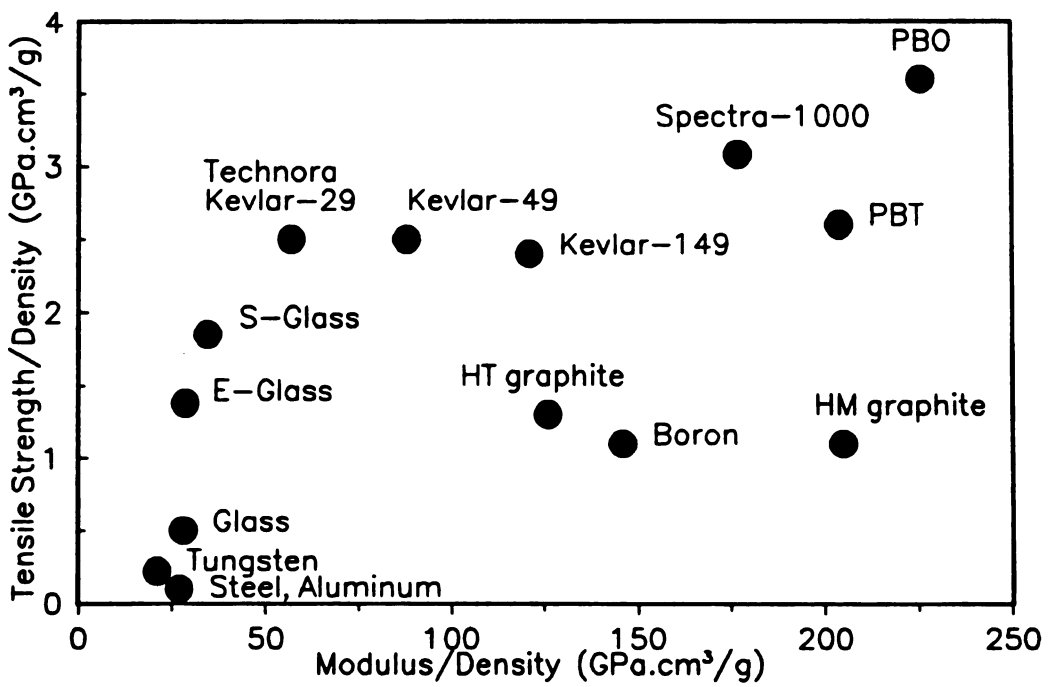

Figure 1.1 - Specific tensile properties of reinforcing fibers and conventional bulk materials.

Cooke (1987) and Allred (1983) have documented various attempts on the development of surface treatment techniques for the Kevlar aramid fibers. These works assume that the low adhesive properties of the aramid fibers are mainly the result of a chemically inert fiber surface (Penn *et al.* 1985) and to a lesser degree mechanical properties of the fibers (Drzal 1983). Despite many efforts, promising coupling agents have not been developed (Penn *et al.* 1983) and surface treatments such as surface oxidation techniques and plasma treatments improve adhesion but are usually accompanied by significant loses in fiber tensile strength (Wertheimer *et al.* 1981). There have been approaches that suggest forming chemically active groups on the aramid fiber surface can double the interfacial bond strength (Allred *et al.* 1985, Wu *et al.* 1986) without tensile strength losses but these results have not been substantiated. A previous study of aramid-epoxy adhesion by the Kalantar and Drzal (1990[b]) has shown that the morphology of the aramid fibers and not the surface chemistry of the fiber is limiting their adhesive properties.

This study examines five approaches to chemical and morphological modification of surface and bulk properties of the high performance polymer fibers. **Table 1.1** lists the examined approaches and their expected effects on the fiber morphological and chemical properties. These approaches systematically explore structure-property relations of the high performance polymer fibers. Each treatment technique produces different extent of fiber chemical and morphological alterations that allow a particular aspect of fiber adhesive behavior to be examined. Effects of these techniques on structure-property relations of high performance polymer fibers are detailed in their respective chapters.

Table 1.1 - Effects of different approaches on the morphology and chemistry of high performance polymer fibers.

Treatment	Chemistry		Morphology	
	Surface	Bulk	Surface	Bulk
Coupling Agents, Fiber Coatings	+			
Plasma and Corona Treatments	+		+	
Chemical Treatments	+		+	
Ion Implantation	+	+	+	+
Structural Modifications	+	+	+	+

1.2 Dissertation Overview

The goals of this study are: to investigate structural properties of high performance polymer fibers that affect their adhesive behavior; to develop a fundamental understanding of the fiber structural limitations; to evaluate several novel techniques that can enhance the fiber adhesive performance properties; and to suggest ways to improve adhesive properties of the high performance polymer fibers.

An experimental overview of the dissertation is shown in **Figure 1.2.** Although, the main theme of this dissertation is the relations between the adhesive and structural properties of the high performance polymer fibers, the study also investigates several important polymer treatments that merit their own particular discussion. Hence, the dissertation is organized into several chapters, each containing a discussion of a specific

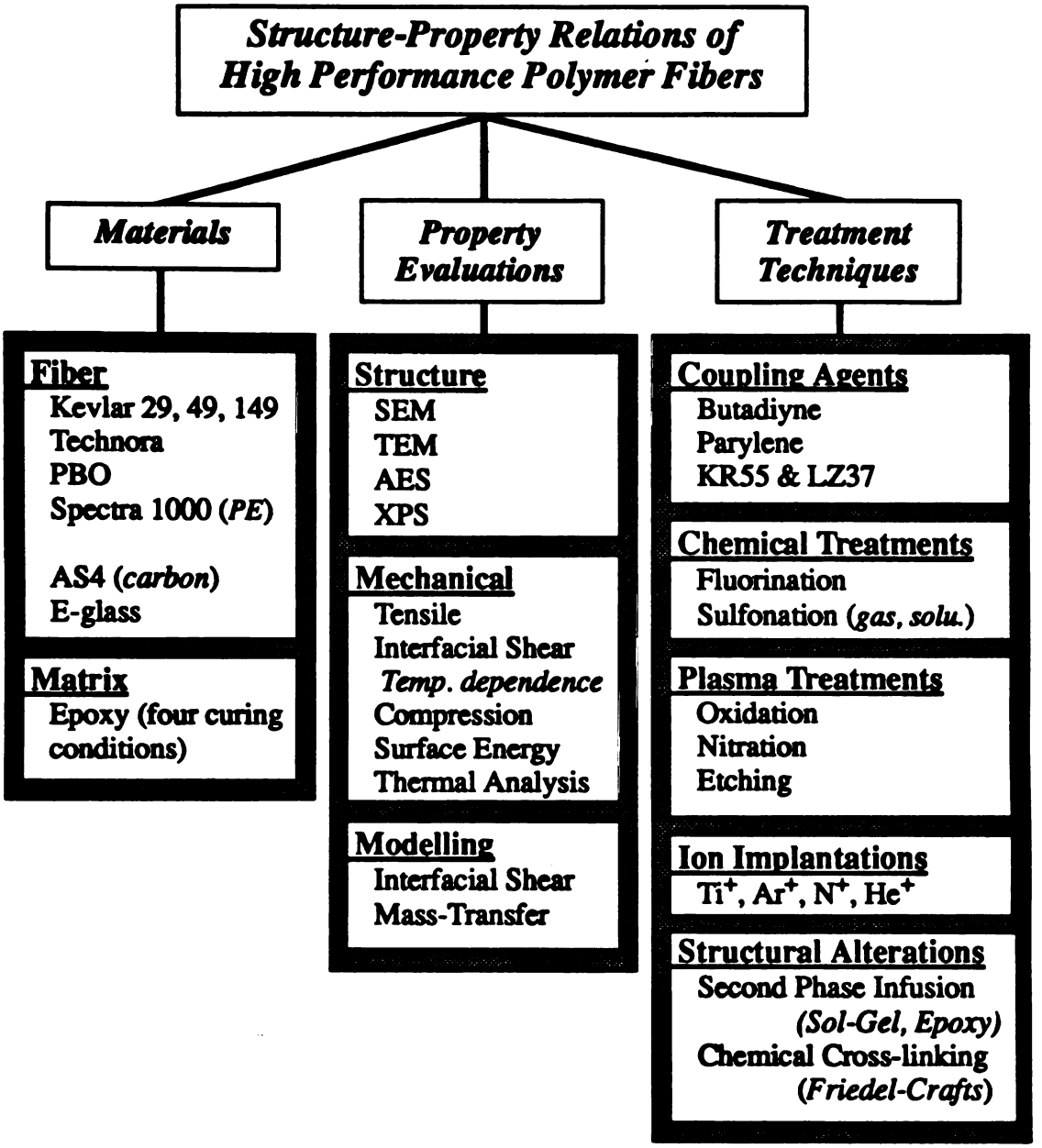

Figure 1.2 - Overview of the experimental plan.

type of polymer treatment. Conclusions at the end of each chapter mainly address the examined treatment, but the relevancy of the conclusions to the main theme of the dissertation is also discussed. The main conclusions of the dissertation are finally coalesced in the last chapter to provide a comprehensive overview of the structure-property relations of the high performance polymer fibers.

Chapter 2 details the experimental techniques used in this dissertation. Some discussions on background literature for the examined techniques are also presented. Chapter 3 provides general discussion and observation on the adhesive properties of high performance polymer fibers. Data presented in this chapter are used as the baseline data throughout the dissertation. Chapter 4 examines effects of coupling agents and fiber coatings on adhesive properties of the high performance polymer fibers. Chapter 5 concentrates on the plasma and corona surface treatments of PBO and Spectra-1000 fibers. Chapter 6 presents a discussion of sulfonation surface treatment and a brief examination of the fluorinated Kevlar-49 fibers. Sulfonation of polymers both in fiber and sheet forms are also investigated to develop an understanding of mass-transfer phenomena that may limit the extent of polymer treatment penetrations. In Chapter 7, effects of ion implantation on mechanical and chemical properties of the aramid and polyethylene fibers are investigated. Chapter 8 examines approaches to infiltrate the high performance polymer fibers and reinforce transverse cohesive properties of the fiber. Chapter 9 presents the conclusions of this dissertation and proposes some recommendation for further developments.

CHAPTER 2

Experimental

2.1 MATERIALS

Aramid fibers examined in this study were Kevlar-29®, Kevlar-49®, Kevlar-149® fibers (E.I. du Pont, Wilmington, DE) and Technora® fibers (Teijin Limited, Japan). Polyethylene fibers were the ultra-high-modulus Spectra®-1000 (Allied Signal, Morristown, NJ). To eliminate possible interference by fiber sizing, the fibers were soxhlet extracted in absolute ethanol for 24 hours and then dried overnight at 125°C. PBO (p-Phenylene BenzobisOxazole) fibers were provided by Dow Chemical (ref. # XV-0383-C8700975-008). These PBO fibers contained no sizing and were used "as received". Other examined fibers were AS-4® carbon fibers (Hercules, Magna, UT), and E-glass fibers (Pittsburgh Paint Glass, Pittsburgh, PA).

The epoxy resin was D.E.R. 331 which is a Diglycidyl Ether of Bisphenol A (DGEBA) epoxy (Dow Chemical, Midland, MI). Four different curing conditions, ambient, 75-100°C, 75-125°C and 175°C curing were selected for this study.

For the ambient curing condition, the curing agent was DiEthyleneTriAmine (DETA) (Aldrich, Milwaukee, WI). The D.E.R.331/DETA system contained a 11.0/100 mass ratio of curing agent to epoxy. The mixture was degassed in a vacuum oven for 15 minutes at -29 in.Hg (gauge pressure). DETA is highly reactive and its epoxy mixture was degassed only at room temperature to avoid gelling. At low curing temperatures this epoxy system was still too brittle for the critical length testing. Subsequent post-curing of the DETA systems was required to increase its fracture strain. The post-curing time and temperatures were determined by the glass transition temperature (T_g) of the matrix. During the post-cure, the oven temperature was maintained below the T_g of the matrix. This was to avoid building up thermal stresses. At each post-curing temperature, initially the T_g was only a few degrees above the oven temperature. After a certain time the glass transition temperature was increased allowing the oven temperature to be raised in steps of 10°C. For the DETA systems, the curing schedule was: 25°C for 48 hours, followed by 4 hours post-curing at 40°C, 50°C, 60°C, 70°C, and 80°C. Subsequent TMA examinations showed only ~0.1% post-curing shrinkage for this epoxy system (Kalantar *et al.* 1990[b]).

For the 75-100°C and 75-125°C curing, the curing agent was m-PhenyleneDiAmine (mPDA) (Aldrich, Milwaukee, WI). For the D.E.R.331/MPDA system, a 14.5/100 mass ratio of MPDA and epoxy were combined. The 75-100°C curing was used for the droplet test and involved curing for 24 hour at ambient temperature followed by 2 hours at 75°C and 3 hours at 100°C. The 75-125°C curing was used for fragmentation and single fiber compression tests, and consisted of curing at 75°C for 2 hours and post-

curing post-curing at 125°C for 2 hours.

For the 175°C curing condition a mixture of two curing agents MPDA and DiEthylTolueneDiAmine (DETDA) (Ethyl Corp., Baton Rouge, LA) were combined. For D.E.R.331/MPDA/DETDA system, a 7.25/100 mass ratio of MPDA and a 11.75/100 mass ratio of DETDA were mixed. The mixture was degassed in a vacuum oven at 75°C for 5 minutes at -29 in.Hg to reduce the viscosity of the solution as well as removing entrapped bubbles. The 175°C system was used for the fragmentation test, and involved a 3 hour cure at 175°C.

2.2 INTERFACIAL SHEAR STRENGTH CHARACTERIZATION

Characterization of the interfacial adhesion was done by fragmentation and droplet techniques. Drzal *et al.* (1991) have presented a comprehensive review of these adhesion tests. **Figure 2.1** shows a schematic of a single fiber fragmentation process. Axial stress is transferred to the fiber through shear at the interface (A). The fiber axial stress rises until the fiber fracture strength is reached (B). Continued application of stress to the specimen results in the repetition of the fragmentation process until all the fragment length become shorter than the length need to transfer the fracture stress (C). This maximum fragmentation length is called the critical length (l_c).

For the fragmentation test, a single fiber was embedded in a dogbone shaped polymer matrix. The dogbone sample was subjected to a tensile load using a tensile testing jig (**Figure 2.2**) and the fiber fragmentation process was monitored under an optical microscope until the critical length was reached. For the polymer fibers that exhibit a

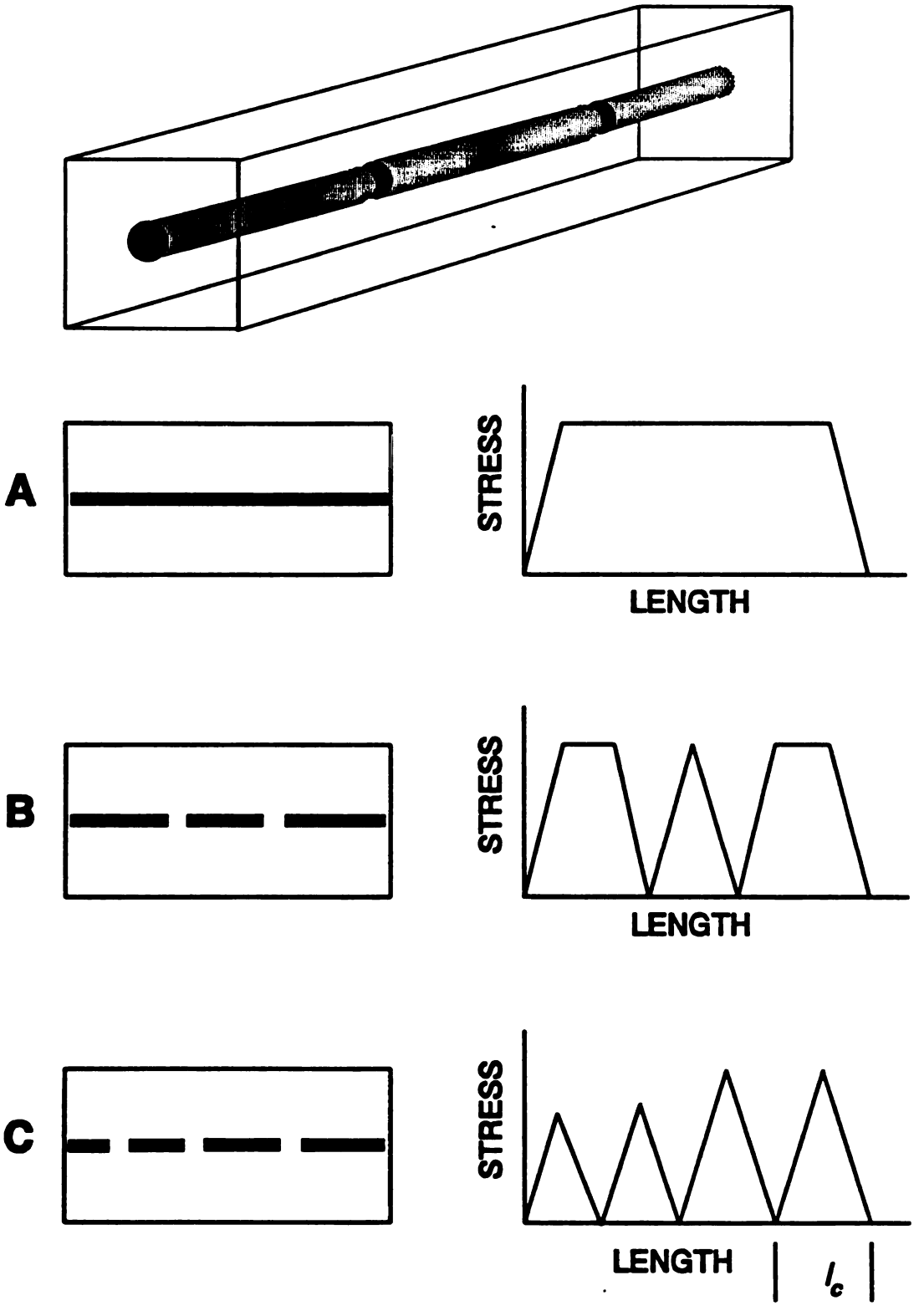

Figure 2.1 - Schematic of single fiber fragmentation process.

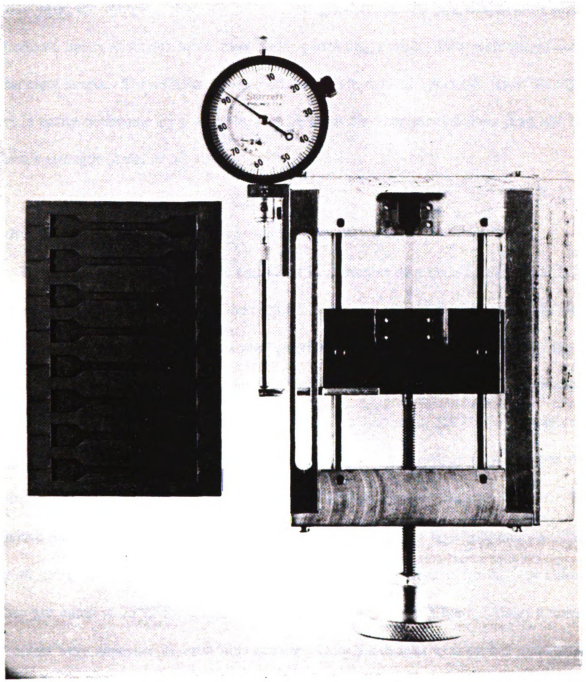

Figure 2.2 - A sample mold and tensile jig used for the single fiber fragmentation test.

fibrillar fragmentation, the average critical lengths were obtained by counting the number of failed regions within a 22 mm fiber length. This 22 length was marked by a glass slide over the sample. For the carbon and glass fibers the fragmentation process produces easily distinguishable fiber ends, permitting a direct measurement of each fragment length. The relation between critical length (l_c) and interfacial shear strength (τ) is easily obtainable by a force balance between the fiber surface shear load and its tensile strength (Kelly *et al.* 1965):

$$\tau = \frac{\sigma_{uf}}{2}\left(\frac{d}{l_c}\right) \qquad (2.1)$$

where σ_{uf} is the fiber tensile strength and d is the fiber diameter.

For the droplet test, a fiber is embedded in a droplet of a matrix and tensile load needed to pull the fiber free from the droplet is measured. Plots of each debonding load verses the fiber-droplet interfacial area provides a measure of their interfacial shear strength. **Figure 5.3** shows the apparatus used for the droplet test. The experimental procedure for the droplet test has been described by Rao *et al.* (1991[b]). Droplets of liquid epoxy are deposited on the fiber by lightly passing a syringe of resin over the fiber. The surface tension of the epoxy pulls the liquid into concentric droplets. To reduce loss of curing agent form small droplets by diffusion at high temperatures (Rao *et al.* 1991[b]), the droplets are allowed to gel at ambient conditions for 24 hour before they are cured at 75°C for 2 hour and post-cure at 100°C for 3 hour. About a dozen droplets were deposited on each fiber sample. Only the droplet with perfect cylindrical symmetry were used for the measurements. Further discussion of the droplet test have been presented by Miller *et al.* (1987), Gilbert *et al.* (1990) and Mcalea *et al.* (1988).

1 LOAD CELL
2 BLADE MICROMETER
3 X-Y TRANSLATION STAGE
4 ACTUATOR
5 BASE

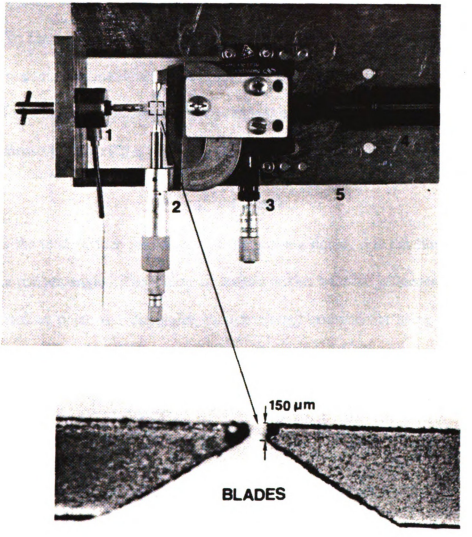

Figure 2.3 - Droplet test apparatus.

2.3 SURFACE ENERGY CHARACTERIZATION

Contact angles of fibers with three liquids, water, ethylene glycol, and methylene iodide were measured using a Wilhelmy technique. The instrument is similar to the setup used by Hammer *et al.* (1980). A single fiber is carefully mounted on an aluminum hook with a cyanoacrylate adhesive. Fiber and hook are then suspended on the arm of a Cahn microbalance. A small beaker of the liquid is slowly raised to the fiber tip. The force before and after contact with the liquid is recorded by a digital data acquisition system. The instrument (Waterbury 1991) automatically lowers the fiber five times at 0.5 mm steps and records the force changes after a few seconds of equilibration time. The measured force (F) is related to the contact angle through use of the equation:

$$F = \gamma_L^t \pi d \cos\theta \qquad (2.2)$$

where γ_L^t is the total surface free energy of the probing liquid, d is the fiber diameter, and Θ is the contact angle. The measured contact angles with the reference liquids are then converted to polar and dispersive surface energy components using the method proposed by Kaelble *et al.* (1974):

$$\frac{\gamma_L^t(1 + \cos\theta)}{2\sqrt{\gamma_L^d}} = \sqrt{\gamma_S^d} + \sqrt{\gamma_S^p}\sqrt{\frac{\gamma_L^p}{\gamma_L^d}} \qquad (2.3)$$

where γ^p, γ^d, and γ^t refer to polar, dispersive, and total surface energies, and subscript L and S refer to liquid and solid material. The measured contact angles of equation (2.2) were converted into the polar and dispersive components using Program WILHEMY (Appendix G). This program performs a regression fit to equation (2.3) using the surface

Table 2.1 - Surface energy components (dyne/cm) of reference liquids used for Wilhelmy contact angle measurements (Hammer *et al.* 1980).

Liquid	Polar	Dispersive	Total
Water	51.0	21.8	72.8
Ethylene Glycol	19.0	29.3	48.3
Formamide	26.0	32.3	58.3
Methylene iodide	2.4	48.4	50.8

energy components of the probing liquids. Surface energy components of some reference liquids are listed in the **Table 2.1.**

2.4 SURFACE CHEMISTRY CHARACTERIZATION

Baun (1980) has listed more than eighty different surface analysis techniques to study adhesion. For polymer-polymer interfaces, the number of these techniques is limited because of the fragile nature of polymer surfaces. Gillberg (1987) has presented an overview of some of these techniques such as AES, ESCA, and electron microscopy for polymer surface analysis. Occhiello *et al.* (1989) also reviewed spectroscopic techniques for characterization of polymer composite interfaces. A brief description of several relevant analytical techniques is presented here.

2.4.1 X-ray Photoelectron Spectroscopy

Surface analysis by X-ray Photoelectron Spectroscopy (XPS), also known as Electron Spectroscopy for Chemical Analysis (ESCA), is accomplished by irradiating a sample with a monoenergetic x-ray beam and analyzing the electrons emitted. Mg Kα x-rays (1253.6 eV) or Al Kα x-rays (1486.6 eV) are commonly used. These irradiated photons cause photoionization of the atoms in the surface region of the sample that results in emission of two types of electrons, photoelectrons and Auger electrons. Probabilities of the interactions of these emitted electrons with matter far exceeds those of the irradiated photons, so while the photons can penetrate the solid sample in orders of 1-10 μm, emitted electrons can escape only tens of Angstroms of solid. Therefore, the electrons used in XPS analysis of the solids originate within tens of Angstroms of the top surface region. The emitted electrons have kinetic energies (E_{KE}) given by:

$$E_{KE} = h\nu - E_{BE} - \phi_s \qquad (2.4)$$

where $h\nu$ is energy of the x-ray photons, E_{BE} is the binding energy of the atomic orbital from which the electron originates, and ϕ_s is spectrometer work function (energy needed for the electron to leave the spectrometer).

The electrons leaving the sample are detected by an electron spectrometer according to their kinetic energy. The analyzer is operated to accept electrons that have energies within a fixed narrow range, this fixed window is called the "pass energy", hence, the narrower the pass energy the higher the resolution of the energy scan. Scanning for different energies is accomplished by electrostatically retarding the electrons before they reach the detectors. This retardation voltage may be varied from zero up to the photon

energy (energies of the electrons emitted cannot exceed the energy of the ionizing photons). The probe for XPS is X-ray photons, which are less disruptive to the surface than the electron beam of AES. XPS is inherently more sensitive than AES to the chemical environment of the elements but examines a larger area of the sample surface.

For a typical XPS investigation where the surface composition is unknown, a wide scan survey spectrum of the surface is obtained first to identify the elements that are present. Once the elemental composition is determined, narrower detailed scans of the selected peaks are used for a more comprehensive analysis of the chemical composition.

XPS analyses were conducted on a Perkin-Elmer PHI 5400 ESCA system using an Al Kα toroidal monochromatic source (PHI 10-410). Spectra were collected at a base pressure of approximately 10^{-9} torr and electron take-off angle of 65° using a position sensitive detector (PSD) on a 180° hemispherical analyzer set at 44.75 eV pass energy for the survey scans (0-1000 eV) and 35.75 eV for the narrow scans of the elemental regions used for composition analyses. Size of the analysis area was 1×3 mm.

2.4.2 Auger Electron Spectroscopy

The Auger Electron Spectroscopy (AES) technique for the chemical analysis is based on the similar process as the XPS technique, except in AES the analysis surface is irradiated with a beam of electrons. The incident electrons ionize atoms of the surface creating vacancies in their inner electron shell. The ionized atoms relax to a lower energy state by filling the inner shell vacancies by the electrons from the lower energy shells. This relaxation process release characteristic "Auger electrons" as well as x-ray

photons that can be used to identify the excited atoms. Auger transitions are typically denoted by three capital letters such as KLL, KLM, LMM, *etc.* The letter on the left refers to the electron shell in which the initial vacancy occurred; the middle letter refers to the shell from which an electron comes to fill the initial vacancy; and the letter on the right refers to the shell from which the Auger electron is emitted. Therefore, kinetic energy of an emitted KLM Auger electron (E_{KE}) is given by:

$$E_{KLM} = E_K - E_L - E_M - \phi_S \qquad (2.5)$$

where E_K, E_L, and E_M are the binding energies of the atomic orbital from which the electrons originate, and ϕ_s is the spectrometer work function.

Similar to the XPS, the AES technique only examines the electrons that originate within the tens of Angstroms of the top surface region. The principle advantage of the AES over XPS technique is the ability to focus and scan the probing electron beam, and obtain information on the spatial distribution of surface elements at high magnifications. However, to analyze the surface composition in practical time scales requires AES to utilize a fast electron spectrometer. Therefore, AES technique is less sensitive to the chemical environment of the elements than the XPS technique.

All AES analysis were carried out using a Perkin-Elmer PHI 660 Scanning Auger Microprobe. Samples were analyzed at 1000 to 30000× magnifications. AES beam conditions for analyses were 1.5 to 10 nA beam current and 3 to 10 kV beam energy. For the surfaces of unknown composition, initially a survey spectrum was obtained to determine the surface composition. The spatial distribution of the interested element was then monitored by its AES signal peak height. Signal intensities were plotted in line-scan

or map fashions.

For some samples, a short (>50 nm) ion beam sputtering of the analysis surface was conducted to remove the surface contaminates. However, longer sputtering times were avoided because a high dose sputtering of polymers would preferentially remove the non-carbon surface elements and produces a carbonized surface composition (see Chapter 7).

2.5 Microscopic Characterizations

Microscopic techniques such as light microscopy, scanning electron microscopy (SEM), and transmission electron microscopy (TEM), are useful in the study of interfacial microstructure. Light microscopy requires little sample preparation and is non-destructive, but its magnifications are low. SEM microscopy can deliver higher magnification and resolution than light microscopy but provides only topographical information. TEM is the most useful microscopic method for interfacial investigations. Samples as thin as 50-60 nm can be shaved from the interface by ultra-microtoming. TEM can show the details of the interface up to 500,000× magnifications. A procedure for ultra thin microtomy of composite material is presented in Appendix F.

Observation of fiber-matrix interfacial morphology was obtained by transmission electron microscopy (TEM) using a JEOL CX100 TEM. In the TEM micrographs presented in this dissertation, direction of the sectioning is shown by an arrow and designated magnifications are shown by scale bars. Topography of sample surface were characterized by scanning electron microscopy (SEM) using a JEOL JSM-T330 SEM.

CHAPTER 3

Adhesive Properties of High Performance Polymer Fibers

This chapter presents some discussions on the adhesive and structural properties of high performance polymer fibers. Tensile and adhesive behavior of the untreated fibers are examined and compared to their predicted values. These discussions provide valuable insights to mechanisms that control the adhesive properties of high performance polymer fibers. The data presented in this chapter also serve as the reference properties for other results of this dissertation.

3.1 INTRODUCTION

To produce high performance polymer fibers a highly ordered extended chain morphology is required. Flaws and cracks that are detrimental to the fiber strength must also be minimized. The most successful high performance polymer fibers have been prepared from rigid-rod liquid crystalline polymers. The liquid crystalline polymers with their highly ordered liquid morphologies are good candidates to initiate the high order required for the high performance polymer fibers. Indeed, the commercial synthesis of high-modulus fibers came about with the advent of rigid-chain polymers and fiber spinning from their liquid crystalline solutions. Today, the primary commercial high performance polymer fibers are made from liquid crystalline polymers. An ultra-high-modulus polyethylene fiber that is spun from a gel solution has also been commercialized.

A "liquid crystal" is a substance with optical anisotropy like a crystal but with a low viscosity like a liquid. The liquid crystalline state with one-dimensional order is called nematic. In nematic solutions, the long axis of molecules are generally parallel, but their positions may be random. The nematic solutions of polymers usually involve rigid-chain polymers. The rigid-chain polymers are elongated molecules with flat segments such as benzene rings and posses high rigidity along their long axis. Monomer structures of some liquid crystalline polymer fibers are shown in **Figure 3.1.** These rigid-rod polymers exhibit extremely high viscosities when melted or tend to decompose before melting at high temperatures (>250°C). Therefore, to prepare these fibers, organic solvents or inorganic acids are employed to dissolve them into liquid crystalline solutions

before spinning. High performance polymer fibers are generally produced from nematic liquid crystalline polymer precursors.

There are three main types of liquid crystalline polymers which exhibit the rigid-rod liquid morphology: aramids (aromatic polyamides) such as p-phenylene terephthalamide (PPTA); aromatic heterocylic polymers such as p-phenylene benzobisoxazole (PBO) and p-phenylene benzobisthiazole (PBT); and the family of thermotropic aromatic copolyesters (Sawyer *et al.* 1986) such as naphthyl-phenyl copolyesters (NTP). White (1985) has presented a historical survey of development of liquid crystalline polymers. It is interesting to note that some of the strongest natural fibers such as silk and cellulose

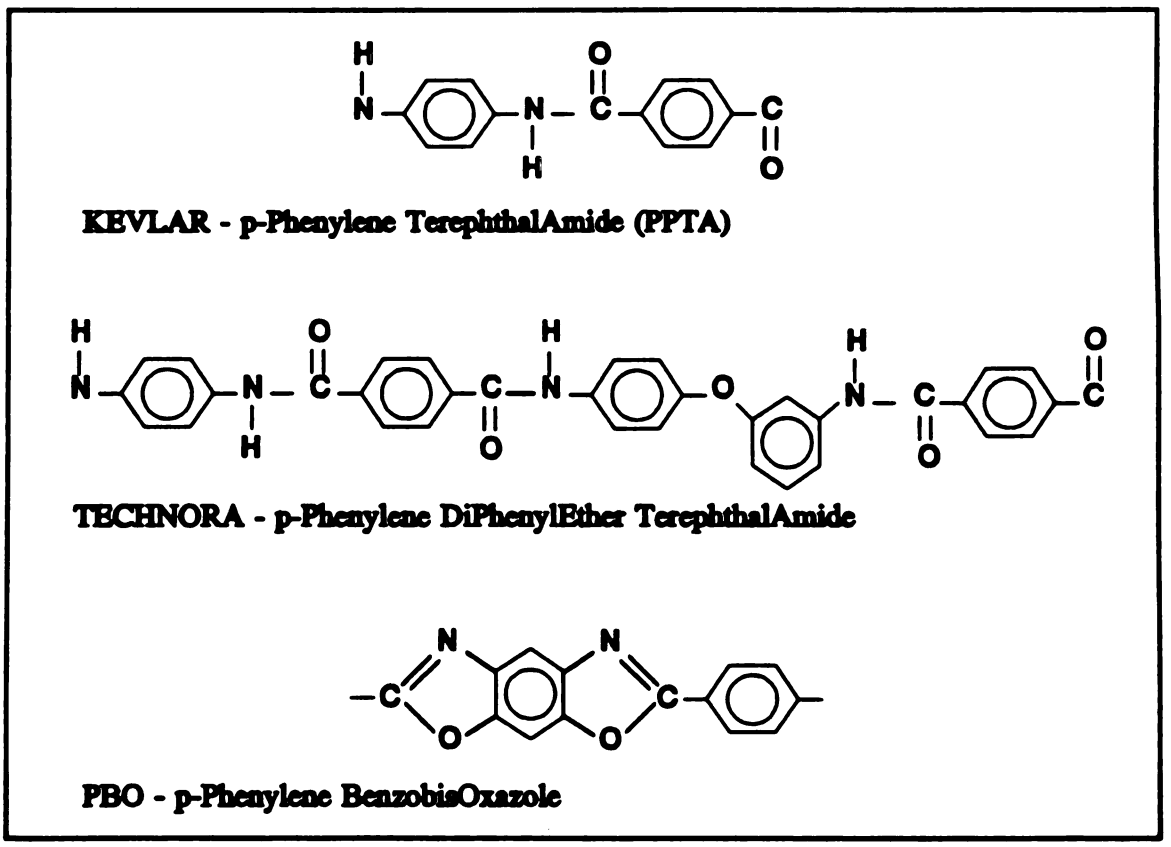

Figure 3.1 - Monomer structure of some liquid crystalline polymers used in high performance polymer fibers.

also form liquid crystalline states when dissolved in solvents. There are also many natural fibers such as those present in coconut husk, pineapple, banana, and bamboo, which exhibit morphologies similar to the synthetic liquid crystalline polymers (Chand *et al.* 1988).

A process for the formation of aramid (PPTA) fibers has been reported by Morgan *et al.* (1989[a]). Aramid fibers are produced by the condensation polymerization of terephthaloyl chloride and p-phenylene diamine. The PPTA is polymerized using a stoichiometric ratio of the reactants. The HCl formed during polymerization is neutralized with a NaOH wash. The PPTA polymers are then dissolved in a concentrated H_2SO_4 solvent to produce low viscosity PPTA liquid crystalline solution for the fiber fabrication. The solution (~20 wt% PPTA) is extruded at 80°C from spinneret orifices into fiber form by a "dry-jet wet spinning" process (Blades 1973). The resulting yarns are neutralized with NaOH and water "washed" to remove the resulting Na_2SO_4 salt. Further drying and drawing treatments increase the fiber stiffness and strength.

Reviews of aramid fiber morphology have been presented by Kalantar *et al.* (1990[a]) and Panar *et al.* (1983). Aramid fibers consist of cylindrical crystallites about 60 nm in diameter and about 200 nm in length. These rods are aligned in the fiber direction, longitudinally connected by macromolecules passing through the rods and radially connected by hydrogen bonding. The fibers have a different morphology between their interior and exterior regions because of the extrusion and coagulation processes of their fabrication. This morphology of the fiber is called the "skin-core" morphology and has been postulated to be the main mechanism responsible for the weak adhesive properties

of the fibers (Kalantar *et al.* 1990[b], Greszczuk 1969). Similar skin-core morphologies for other liquid crystalline polymers such as PBO fibers have been reported (Krause *et al.* 1988, Woodward 1988) which are also attributed to the extrusion and coagulation steps in their production. There are also other solvent fiber processing techniques such as those used for the fabrication of Technora aramid fibers (p-phenylene/0,4-diphenylether terephthalamide) that are expected to result in a lower degree of skin-core morphological difference than the fibers spun by a dry-jet wet spinning process. (Technora fibers are spun from a N-methyl pyrrolidone solution and then into a water bath, Morgan 1989[b]).

Commercial high performance ultra-high-molecular-weight (UHMW) polyethylene fibers are manufactured by a gel-spinning process (O'Sullivan 1991). The starting polyethylene has a molecular weight in the range of 2 to 6 million which is as much as 100 times more than the commercial grade high-density polyethylene. A solution of ~5 wt% of the UHMW polyethylene in decahydronaphthalene solvent is extruded through spinnerets to form gel-like fibers. These fibers are then stretched to about 300× their length at a temperature close to the polymer's melting point of ~145°C to form the final high performance polymer fibers. The final fibers posses greater than 95% chain orientation and up to 85% degree of crystallinity. For a given polymer molecular weight, the ultimate mechanical properties of gel-spun fibers are controlled by choice of solvent, polymer concentration, and spinning temperature (Kalb *et al.* 1980). Other fibers such as ethylene-vinyl alcohol (EVOH) fibers have also been produced by gel-spinning procedures (Schellekens *et al.* 1990).

For high-modulus polyethylene fibers, different fiber morphologies may result from the gel-spinning process depending on the drawing conditions of the fiber (Hofmann *et al.* 1989). Under low drawing, a "shish-kebab" morphology which consists of a central rod or ribbon with overgrowths of folded chains are formed (Billmeyer 1984). Under high degrees of drawing, the initial shish-kebab morphology transforms into extended polymer chains (Brady *et al.* 1989) and a fibrillar microstructure results. Commercial high performance ultra-high-molecular-weight (UHMW) polyethylene fibers are hot-drawn under high stress conditions and exhibit the extended chain fibrillar morphology.

The almost perfect chain alignment of high performance polymer fibers results in their high tensile properties. Tensile properties of the high performance polymer fibers are relatively close to predicted values of their perfect crystal properties (Smith 1990) which is evidence for their highly ordered morphologies. However, composites made with high performance polymer fibers generally exhibit low transverse properties, independent of matrix (Mittleman *et al.* 1985, Smith *et al.* 1985, Brady *et al.* 1990). The level of fiber-matrix interactions controls many properties of fiber-reinforced composites such as transverse strength, shear strength, and flexure. The low transverse properties of high performance polymer fibers significantly limits their structural applications.

Composite materials combine two or more dissimilar materials to yield a composite with properties superior to those of its constituents. For example, reinforcing glass fibers embedded in a polymer matrix can form strong fiber-glass panels. Since composites, by definition, are heterophase materials, interphase regions are inherent features of their structure. The composite interphase may be defined as a transition

region between constituent materials, across which a gradation of mechanical and chemical properties occurs. The "interphase" contains the "interface", formed by the contact of two surfaces plus the region on both sides where the material is different from the bulk. The structure and composition of the composite interphase controls the extent of interaction between its constituents and significantly affects the behavior of the composite (Grezczuk 1969, Chamis 1974, Tsai *et al.* 1974). In general the optimum condition of the composite interphase depends on the particular application and its expected loads. For example, for continuous fiber reinforced composites a strong interphase improves off-axis properties of the composite such as transverse strength and flexure. For some applications such as fracture toughness, however, a weak interphase is desirable.

There are two approaches to the investigation of the composite interphase. One approach deals with the interfacial aspects of bond forming and concentrates on the physical-chemistry of the interphase. The other approach deals with macrostructural aspects and mechanical analysis of the interphase region. The two approaches must be combined for a complete explanation of the composite interphase. An extended review of the current literature on the aramid-epoxy interphase and the adhesion related properties of the aramid fibers has been presented by Kalantar *et al.* (1990[a]).

3.2 EXPERIMENTAL

Aramid fibers examined in this study were Kevlar-29, Kevlar-49, Kevlar-149 (E.I. du Pont, Wilmington, DE) and Technora fibers (Teijin Limited, Japan). The polyethylene fibers were the ultra-high-modulus Spectra-1000 (Allied Signal, Morristown, NJ). PBO fibers were provided by Dow Chemical (ref. # XV-0383-C8700975-008). To eliminate possible interference by fiber sizing, the fibers were soxhlet extracted in absolute ethanol for 24 hours and then dried overnight at ambient conditions.

Four epoxy systems were used: DER331/MPDA/DETDA 175°C/3hr, DER331/DETA and ambient cure with the fragmentation test, and DER331/MPDA RT/24hr/75°C-2hr/100°C/3hr with the droplet test (described in Chapter 2). Single fiber tensile strengths were measured by ASTM D3379 tensile test. Surface compositions of the fibers were characterized by XPS. Fiber-matrix interfacial morphology was examined by transmission electron microscopy (TEM) of ultrathin microtomed sections cut normal to the fiber axis. Fiber surface energies were characterized by Wilhelmy measurements using water, ethylene glycol and methylene iodide as probing liquids. These experimental conditions are detailed in Chapter 2.

3.3 RESULTS AND DISCUSSIONS

Measured tensile properties of the examined high performance polymer fibers are listed in **Table 3.1.** These data are used throughout this dissertation as the baseline properties. **Figure 3.2** compares the tensile modulus of the high performance polymer fibers with their tensile fracture strain. The higher modulus fibers tend to show lower fracture strains and vise versa. Generally, tensile fractures are defect controlled, while tensile moduli are controlled by the bulk properties of the fibers. However, **Figure 3.2** shows a correlation could exist between the two properties. The high moduli of these fibers have been achieved by ordering the polymer chains in the axial fiber direction. As the extent of fiber orientation increases the overall fiber tensile modulus increases, but the movements of the chains become more restricted and the fiber fracture strain is

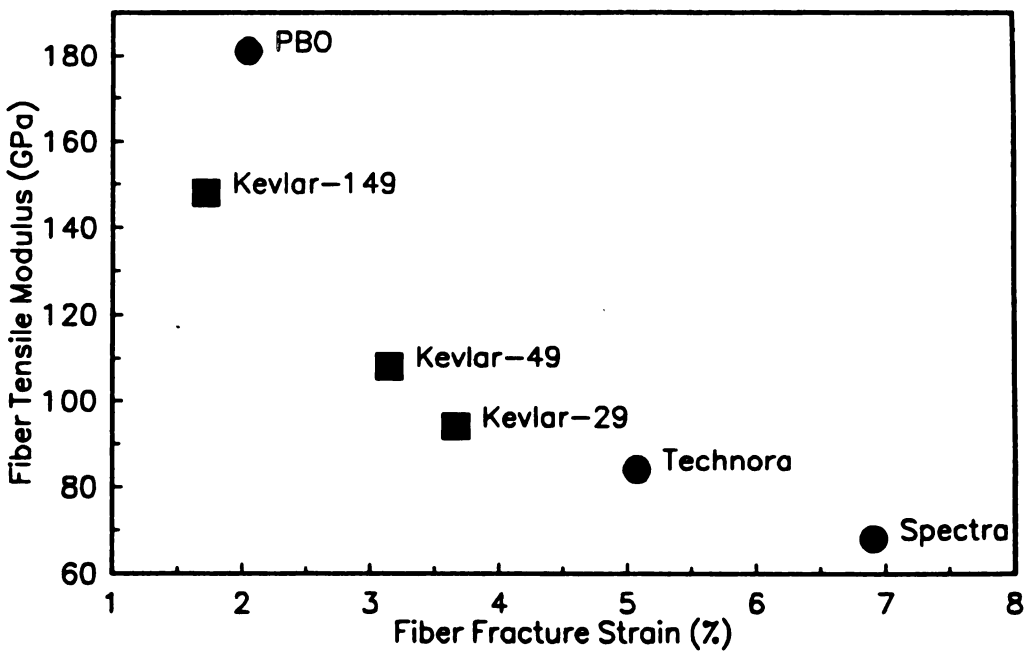

Figure 3.2 - Tensile fracture strain of high performance polymer fibers verses their tensile modulus.

Table 3.1 - Tensile properties of high performance polymer fibers.

Property	Kevlar-29	Kevlar-49	Kevlar-149
No. of Tests	25	21	20
Diameter (μm)	12.2 ± 0.9	12.1 ± 0.5	13.0 ± 0.5
Tensile Modulus (GPa)	94 ± 9	108 ± 7	148 ± 6
Tensile Strength (GPa)	3.09 ± 0.46	3.49 ± 0.24	2.38 ± 0.25
Fracture Strain (%)	3.67 ± 0.40	3.15 ± 0.24	1.72 ± 0.23

Property	Technora (*aramid*)	PBO (*p-phenylene-benzobisoxazole*)	Spectra-1000 (*polyethylene*)
No. of Tests	14	22	12
Diameter (μm)	12.0 ± 0.9	18.8 ± 2.1	28.7 ± 2.7
Tensile Modulus (GPa)	84 ± 4	181 ± 17	68 ± 9
Tensile Strength (GPa)	3.72 ± 0.27	3.42 ± 0.55	2.65 ± 0.29
Fracture Strain (%)	5.08 ± 0.32	2.05 ± 0.45	6.91 ± 1.30

reduced. This trend is evident in the Kevlar fibers that have the same polymer chemistry. Kevlar 29 and 49 reportedly have a pleated sheet morphology (Dobb *et al.* 1977). Conversely, Kevlar 149, which exhibits 80-90% of its theoretically predicted tensile modulus, does not show the pleated morphology which suggests "straightening" of the pleated sheet structure and increased orientation (Krause *et al.* 1989). The implication of previous observations is that reducing relative mobility of adjacent polymer chains (*e.g.*, by cross-linking), should result in increased tensile modulus but reduced fracture strain of the fibers (also see section 7.3.2).

Table 3.2 compares the interfacial shear strength (ISS) of the examined high performance polymer fibers. The "as received" Kevlar-49 and Technora fibers possess proprietary sizings that were removed by an ethanol washing process. Both "washed" and "as received" fibers were examined to evaluate the effects of fiber sizing on the fiber interfacial properties. For other unsized fibers, "washed" fibers were also examined to ascertain the washing process does not alter the fiber adhesive properties. For the liquid crystalline polymer fibers, three curing conditions were examined to assess the effect of thermal stresses on the fiber interfacial shear strength.

To examine some of trends in the ISS data, a three dimensional stress model (Whitney *et al.* 1980) has been examined. Previously, it was demonstrated that the model could not reasonably predict the actual ISS values of aramid fibers because of the failure of its linear elastic fiber fragmentation assumption (Kalantar *et al.* 1990[b]). However, the model provides valuable insights to the expected trends for various fibers. A combination of experimental and theoretical data are used to predict the ISS trends. The

Table 3.2 - Interfacial shear strength (ISS) of high performance fibers.

Fiber		ISS Fragmentation test (MPa)		
		Ambient Cure	75/125°C cure	175°C cure
Kevlar-149	*Washed*	-	16.7 ± 1.3 (12)	-
	As Rec.	-	16.3 ± 1.4 (12)	17.3 ± 1.4 (10)
Kevlar-49	*Washed*	17.5 ± 1.3 (27)	17.9 ± 1.2 (12)	18.0 ± 1.0 (25)
	As Rec.	-	18.2 ± 1.3 (12)	17.6 ± 1.3 (17)
Kevlar-29	*Washed*	-	19.5 ± 2.7 (20)	20.9 ± 3.2 (7)
	As Rec.	-	19.9 ± 1.8 (10)	20.6 ± 2.8 (8)
Technora	*Washed*	-	22.4 ± 2.0 (23)	28.7 ± 1.9 (7)
	As Rec.	-	33.2 ± 2.2 (10)	36.6 ± 2.7 (5)
PBO	*Washed*	11.5 ± 1.5 (27)	16.1 ± 1.4 (14)	17.8 ± 1.4 (14)
E-Glass	*As Rec.*	-	-	28.9 ± 11.4 (219)
AS4 (carbon)	*As Rec.*	29.6 ± 9.3 (614)	-	41 ± 12 (572)
ISS Droplet test 75/100°C cure (MPa)				
Spectra-1000	*As Rec.*	2.95 ± 0.17 (18)		

Washed: washed with Ethanol
As Rec.: tested as received
(the numbers in parentheses represent the number of samples tested)

Table 3.3 - Material property data.

Material	Diameter (μm)	Tensile Modulus (GPa)	Tensile Strength (GPa)	Fracture Strain (%)
E-Glass	17.1 ± 1.2	72[2]	1.08 ± 0.22	3.15 ± 0.24
AS4 (Carbon)	8.1 ± 0.3	231[2]	5.86[2]	1.72 ± 0.23
Epoxy Ambient Cure		3.14 ± 0.11		
75/125°C cure[1]		3.32 ± 0.06	0.0947 ± 0.0012	5.3 ± 0.2
175°C cure		2.84 ± 0.15		

[1] Rao *et al.* 1991 [a]
[2] nominal literature value

theoretical critical length ($l_{c,theo}$) is given by:

$$l_{c,theo} = 2.375\sqrt{\frac{E_{1f} - 4\nu_{12f}G_m}{G_m}} \qquad (3.1)$$

where E_{1f} is the axial fiber elastic modulus, ν_{1f} is axial fiber Poisson's ratio, and G_m is the matrix elastic modulus. To predict a theoretical ISS value, $l_{c,theo}$ is inserted into equation 2.1 using the experimental tensile strength data of Table 3.1.

Figure 3.3 compares the experimental and theoretical ISS values of the "as received" fibers for the 175°C/3hr curing condition. Material property data for E-glass fibers, AS-4 carbon fibers, and various epoxy systems are listed in Table 3.3. Figure 3.3 shows that interfacial shear strength (ISS) of the inorganic fibers agree with the theoretical values, whereas the organic fibers exhibit ISS strengths about half their predicted values. The discrepancy between theoretical and experimental results can be attributed to the

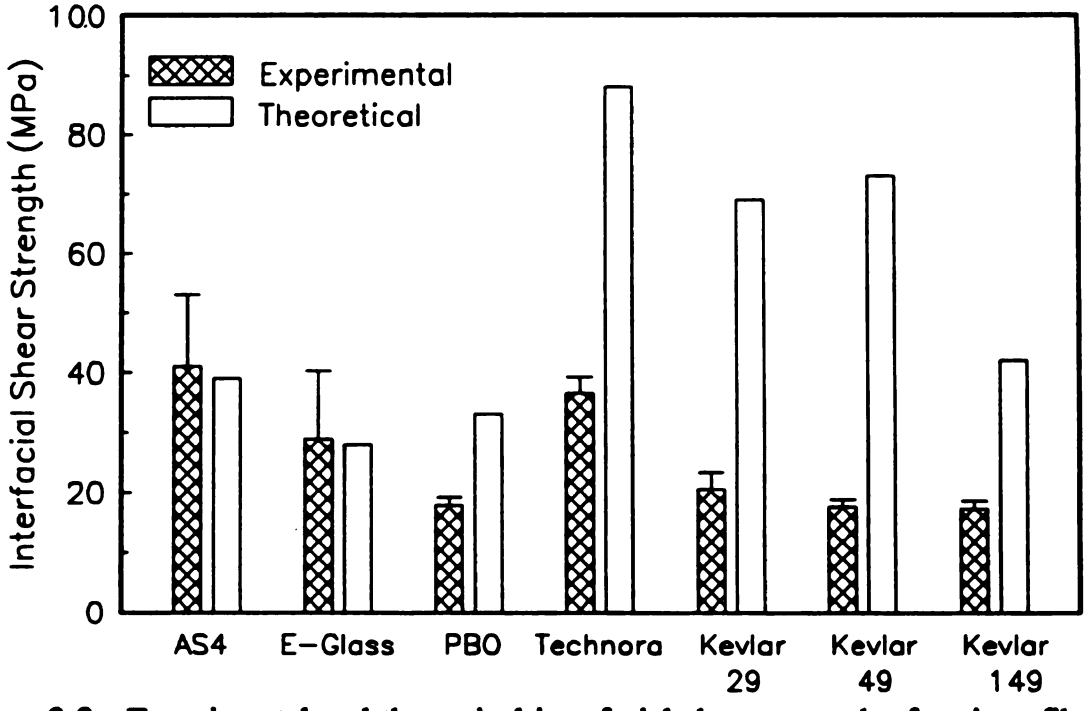

Figure 3.3 - Experimental and theoretical interfacial shear strength of various fibers.

model's assumptions that the fibers are transversely isotropic and undergo linear elastic deformations. **Figure 3.4** shows the optical micrographs of Kevlar-49 and AS-4 carbon fiber fragments under bright-field and cross-polarized lighting. For the carbon fiber, the fiber fragments into whole segments, whereas the Kevlar-49 fibers fragment by axial cracks that result in fibrillated segments. Therefore, for the high performance polymer fibers, the predicted results of this model could only provide a qualitative measure of various trends. For example, the model suggests that Technora fibers, with their lower tensile modulus than Kevlar-49 fibers, are expected to exhibit higher ISS values than Kevlar-49 for the same epoxy matrix.

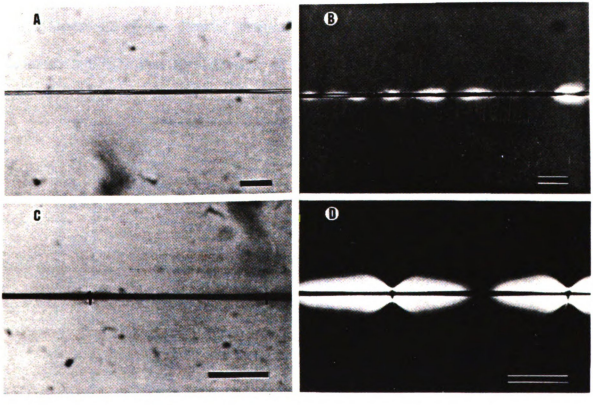

Figure 3.4 - Optical micrographs of fiber fragments. (A) Kevlar-49 bright-field, (B) Kevlar-49 cross-polarized, (C) AS-4 bright-field, (D) AS-4 cross-polarized. bar = 100 μm

Figure 3.5 examines the effect of curing thermal stresses on the interfacial shear strength properties of "washed" PBO, Kevlar-49 and Technora fibers. Of the three curing conditions, the 175°C curing exerts the highest thermal stresses and the Ambient curing the lowest thermal stresses (Kalantar *et al.* 1990[b]). For the Technora fiber the ambient cure data was not obtainable because this epoxy system is more brittle when cured at ambient conditions compared to the other curing conditions. The ambient cured Technora sample broke before the fiber critical length could be measured. **Figure 3.5** shows that interfacial shear strength of the Kevlar-49 samples were not affected by the curing conditions, whereas Technora and PBO samples show increased ISS values for the higher thermal stresses. These results suggest that the failure mode of the Kevlar fibers are independent of the thermal stresses of their surrounding matrix. It will be demonstrated later that the adhesion of the Technora and PBO fibers have some

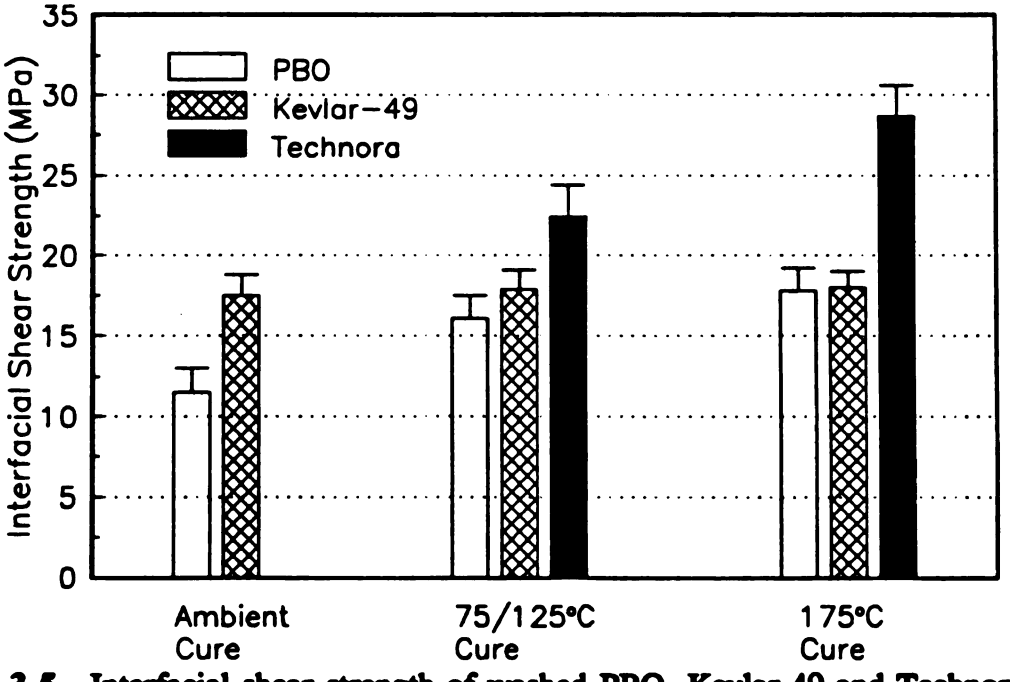

Figure 3.5 - Interfacial shear strength of washed PBO, Kevlar-49 and Technora fibers for three different curing conditions.

additional limitations that may be affected by the stress environment of the matrix.

Technora and Kevlar-49 fibers were the only fibers that were sized by their manufactures to improve their handling and/or adhesive properties. **Figure 3.6** shows the interfacial shear strength (ISS) changes between the "as received" (sized) and "washed" (unsized) fibers for two curing conditions. The Kevlar-49 fiber shows similar ISS values for the "washed" and "as received" fibers, whereas, the Technora fibers show over 30% higher ISS values for the "as received" fibers than the "washed" fibers. These observations suggests that fiber sizing is enhancing Technora-epoxy adhesion but is not affecting Kevlar-epoxy adhesion.

Figure 3.7 compares the surface energy of several high performance polymer fibers with the liquid epoxy. The "as received" Technora fiber shows surface energy components that closely match the epoxy surface energy components. Kaelble (1971) has

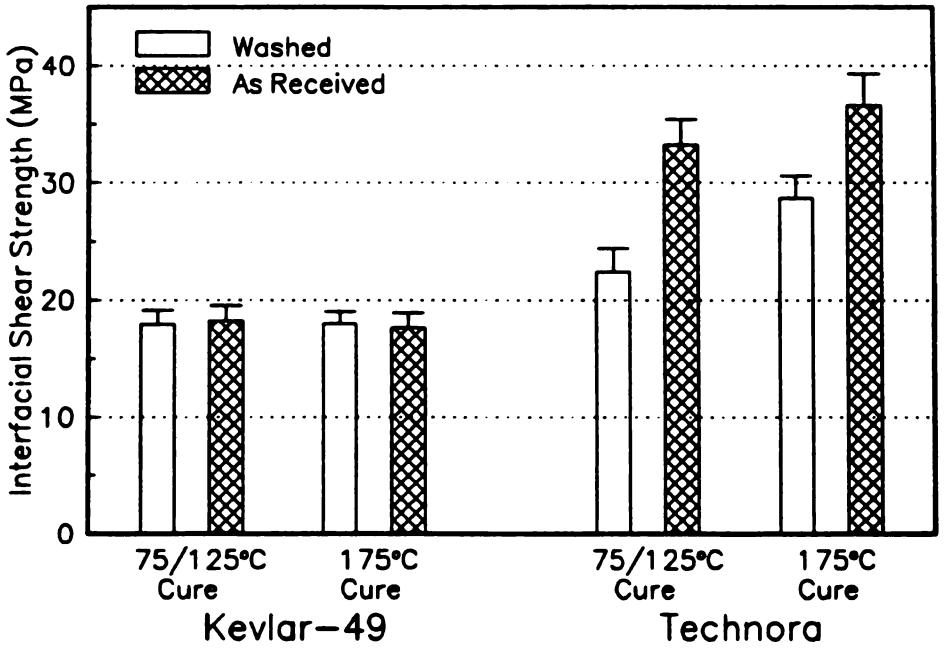

Figure 3.6 - Interfacial shear strength (ISS) of "as received" (sized) and "washed" (unsized) Kevlar-49 and Technora fibers for two curing conditions.

suggested that a close match between polar and dispersive components of surface free energy of the adherents can result in their optimum wetting properties. The "washed" Technora fiber shows over twice the polar component of surface energy of the epoxy which my result in less than optimum wetting properties. The surface energy similarities of the fiber sizing and epoxy may also result in sizing-epoxy mutual diffusion and increased fiber-matrix coupling. The sizing may also increase the modulus of the surrounding matrix enhancing the load carrying capacity of the interphase. Conversely, "washed" and "as received" Kevlar fibers have similar surface energy components. Note that the unsized Kevlar-29 fibers show similar surface energy components for their "washed" and "as received" fibers which suggest that the washing process does not affect the fiber surface wetting properties.

Work by Gutowski (1990) has shown that in the absence of chemical bonding,

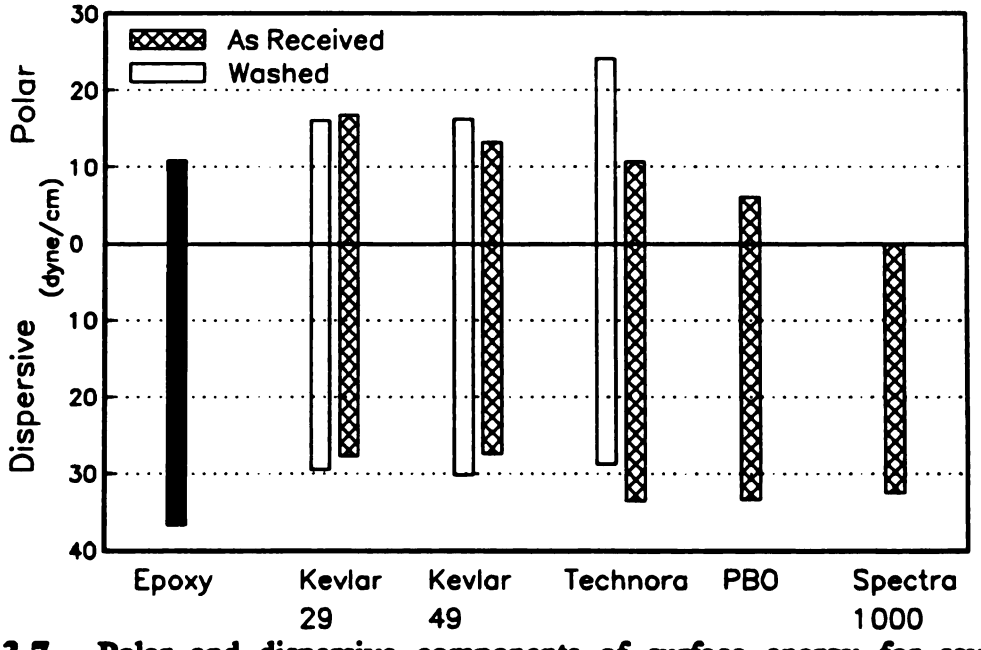

Figure 3.7 - Polar and dispersive components of surface energy for several high performance polymer fibers and liquid epoxy. Only Kevlar-49 and Technora fibers were sized.

maximum adhesion between the matrix and fiber occurs when the surface energy of the fiber (γ_f) and matrix (γ_m) are equal and when (γ_f/γ_m) < 1 only incomplete wetting could occur. PBO and Spectra-1000 fibers show lower total surface free energy than the liquid epoxy which suggests incomplete wetting with the epoxy. Incorporation of polar functional groups could potentially enhance their wetting compatibility with the liquid epoxy (discussed in Chapters 5 and 6).

The weak lateral interactions of the high performance polymer fibers is demonstrated by their skin separation. **Figure 3.8** shows SEM micrographs of a Kevlar-49 aramid fiber that shows fiber skin separation in the form of a helical ribbon. **Figure 3.9** shows a similar skin separation for an untreated PBO fiber. Technora fibers also exhibit skin separation (Takata 1987), although they are expected to have less of the skin-core morphological differences than other examined liquid crystalline polymer fibers.

TEM micrographs of the liquid crystalline polymer fibers also demonstrate their weak lateral cohesive properties. **Figure 3.10** shows a typical section of an "as received" Kevlar-49 fiber. Interfacial separation is parallel to the cutting direction and there are cohesive fiber fibrillation near the fiber-matrix parting areas. Similar fiber surface fibrillation are also observed for other aramid fibers. **Figure 3.11** shows TEM micrographs of "as received" and "washed" Technora fibers. The "as received" fiber (**Figure 3.11A**) shows more fiber surface fibrillation than the "washed" fiber (**Figure 3.11B**), suggesting stronger adhesive interactions of the latter. **Figure 3.6** also showed that the "as received" Technora fibers exhibit over 30% higher interfacial shear strength values than the "washed" fibers.

Figure 3.12 illustrates TEM micrographs of an "as received" PBO fiber that shows a thin layer of the fiber skin is adhering to the epoxy side of the interphase separation. This observation suggests that PBO fibers have a thin surface layer that fails during the application of shear stress. There is additional evidence for the presence of the PBO skin layer. **Figure 3.13** shows an optical micrograph of "as received" PBO fibers that exhibit the presence of kink bands in some fibers. The kink bands are probably the result of compressive stresses induced during the fiber manufacturing process. **Figure 3.14** shows SEM micrographs of the same PBO fibers, which do not show any kinks on the fiber surfaces suggesting that the kink bands are internal. In the Chapter 6, it is shown that etching removal of the PBO surface layer exposes its sub-surface kinked line structure. These observations confirm the presence of a thin surface layer on the PBO fibers.

Spectra-1000 polyethylene fibers also exhibit a combination of interfacial and cohesive fiber-matrix separation similar to the liquid crystalline polymers. **Figure 3.15** shows TEM micrographs of a radially sectioned Spectra-1000 fiber. The micrographs show extensive interfacial adhesive failure which suggest weak fiber-matrix bonding. A higher magnification view (**Figure 3.15B**) shows fiber fibrillation near some interfacial parting areas. Therefore, for the untreated Spectra fibers interfacial shear failure is dominated by interfacial adhesive failure along with some fiber cohesive failure.

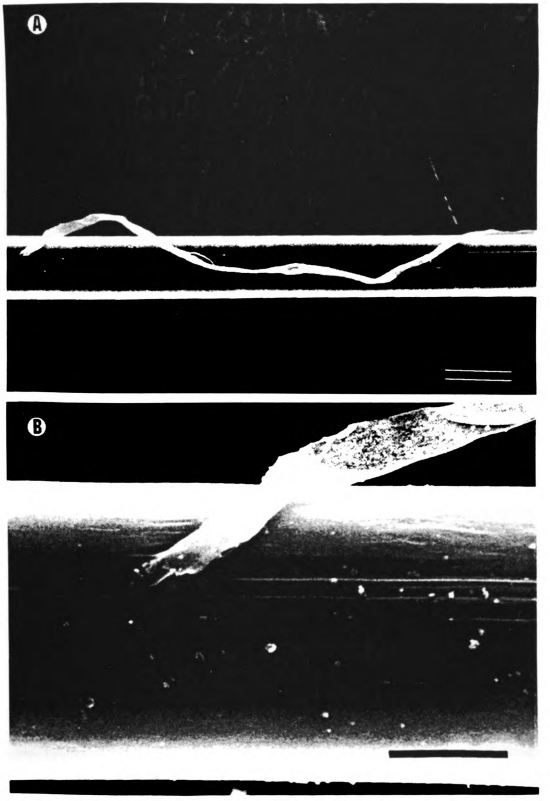

Figure 3.8 - SEM micrographs of untreated Kevlar-49 showing torn fiber skin in a form of a helical ribbon. (A) bar = 10 μm (B) bar = 5 μm

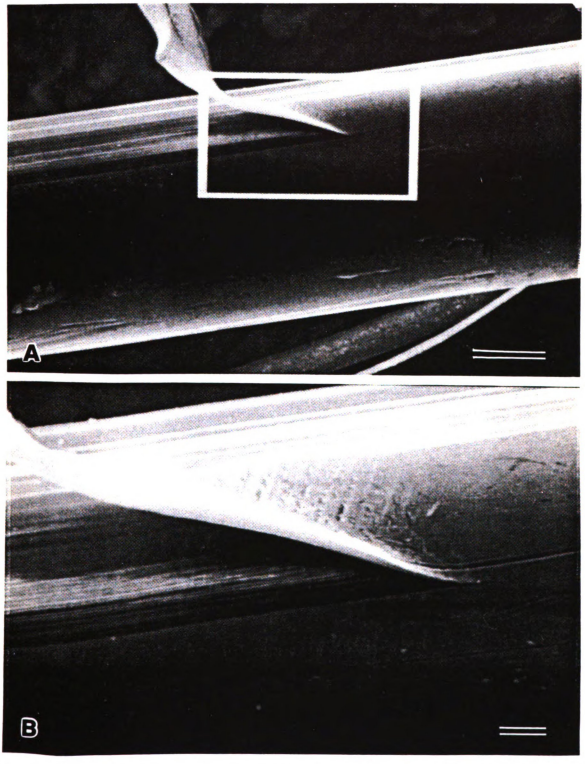

Figure 3.9 - SEM micrographs of a PBO fiber skin separation.
(A) bar = 5 μm (B) bar = 1 μm

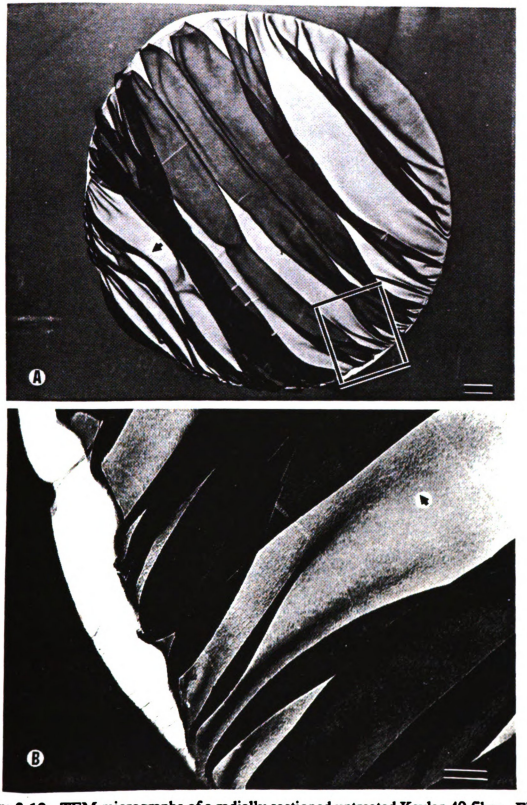

Figure 3.10 - TEM micrographs of a radially sectioned untreated Kevlar-49 fiber. Fiber-matrix interphase shows both interfacial separation and fiber cohesive fibrillation. (A) bar = 1 μm (B) bar = 250 nm

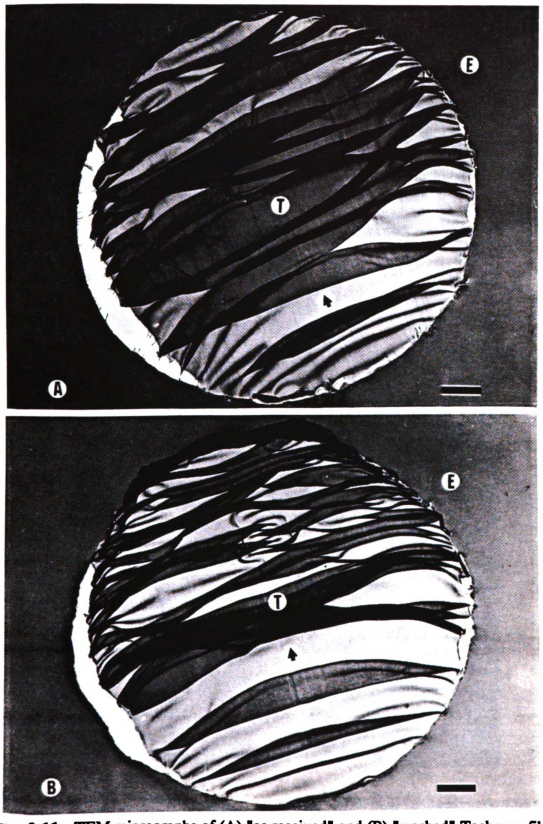

Figure 3.11 - TEM micrographs of (A) "as received" and (B) "washed" Technora fibers. The "as received" fiber is more fibrillated than the "washed" fiber. bar = 1 μm

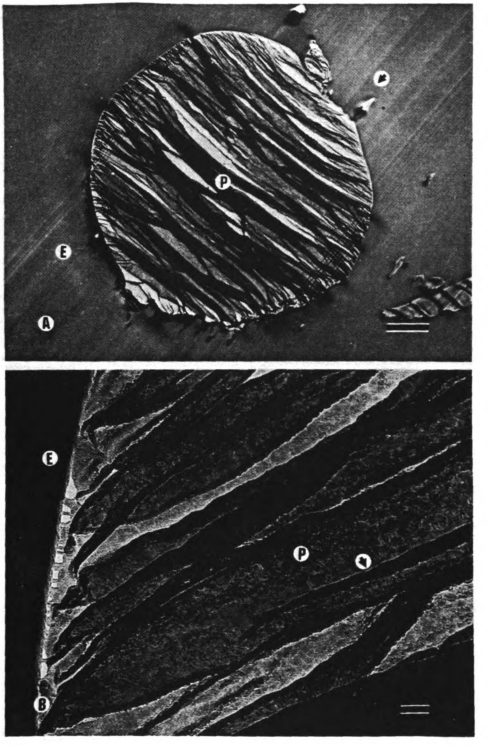

Figure 3.12 - TEM micrographs of an "as received" PBO fiber, showing a thin layer of the fiber skin is adhering to the epoxy side of the interphase separations.
(A) bar = 2 μm (B) bar = 100 nm

Figure 3.13 - Optical micrograph of "as received" PBO fibers, showing presence of compressive kink bands.

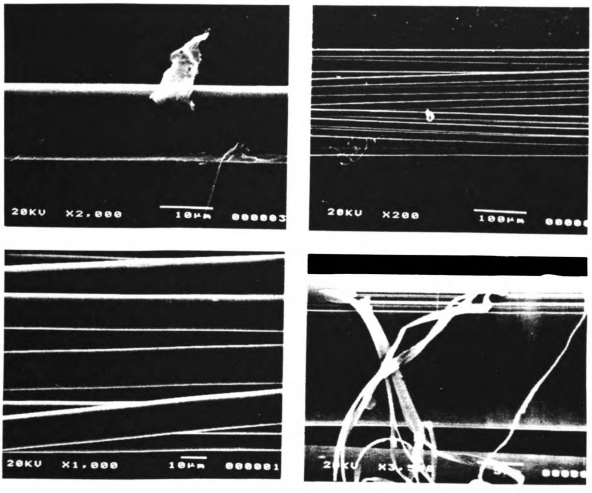

Figure 3.14 - SEM micrograph of "as received" PBO fibers. Kink bands are not apparent on the fiber surface.

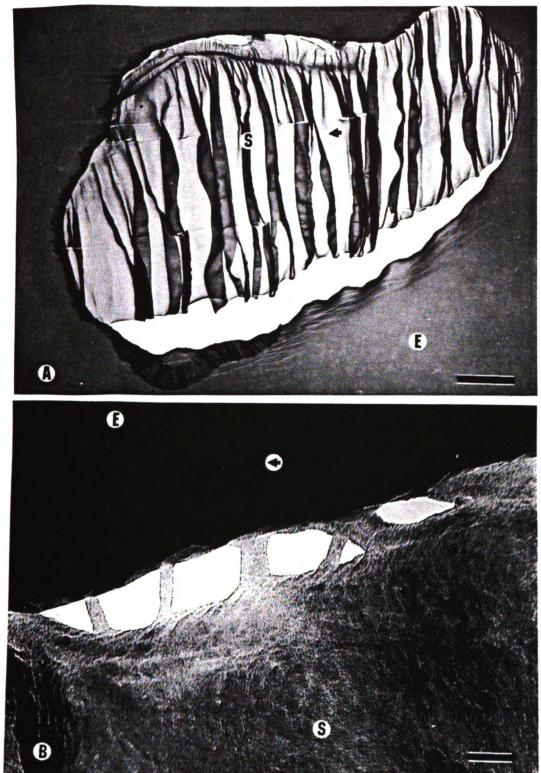

Figure 3.15 - TEM micrographs of an "as received" Spectra-1000 polyethylene fiber, showing extensive interfacial adhesive failures and a few fiber cohesive failures.
(A) bar = 5 μm (B) bar = 100 nm

3.4 CONCLUSIONS

- For the examined curing conditions, the higher thermal stresses at higher curing temperatures increased interfacial shear strength (ISS) of the Technora and PBO fibers, whereas, ISS values of the Kevlar-49 fibers were unaffected by the increased thermal stresses.
- PBO and Spectra-1000 fibers exhibit low polar components of fiber surface energy, whereas Technora fibers exhibit excessive polar component. Both cases result in less than optimum wetting compatibility with liquid epoxies.
- PBO fibers exhibit a cohesively weak skin layer that fails within the fiber during PBO-epoxy interfacial separation.
- Comparison of experimental and predicted interfacial shear strength (ISS) of the polymer fibers suggests that increasing lateral interactions of the aligned polymer chains could significantly increase their interfacial load carrying capacity.
- Enhancement of lateral chain interactions is expected to reduce their relative mobility, thus reducing the fiber fracture strain but increasing its tensile modulus.

Results of this chapter suggest that wetting properties and/or skin-core morphology of the high performance polymer fibers can significantly affect their adhesive behavior. The examined high performance polymer fibers exhibit internal fiber fibrillation which suggest weak lateral interactions between adjacent polymer chains. This observation suggests that the cohesive fibrillation of the fibers is ultimately responsible for their shear failure mechanism.

CHAPTER 4

Fiber Coating and Coupling Agent Treatments of High Performance Polymer Fibers

In this chapter, effects of several types of fiber coatings and coupling agents on adhesive properties of Kevlar-49 aramid fibers are examined. These treatments only affect the fiber-matrix interphase properties, therefore, allowing the effects of the interphase on fiber-matrix adhesion to be examined without perturbation form changes in fiber-matrix properties. This approach should provide valuable insights to the significance of fiber-matrix interphase on the adhesive properties of high performance polymer fibers.

4.1 INTRODUCTION

Coupling agents are materials that are able to strongly interact by physical or chemical means between two substrates. Coupling agents can be either directly applied to the fiber or be dissolved in the liquid resin and diffuse to the fiber-matrix interface. Coupling agents are typically applied in minute quantities since their excessive presence could introduce a weak boundary layer at the fiber-matrix interface.

Liquid coupling agents based on organometallic complexes have recently claimed improved bonding between polymer fibers and polymer resins. Gabayson *et al.* (1988) have reported increased interfacial bonding and enhanced processing for a variety of polymer systems with the application of organometallic coupling agents. Sugerman *et al.* (1989) have reported up to 20% increase in flexural and compressive strength, and 80% increase in impact strengths of Kevlar-49/Novalak-MNA short fiber composites with the application of various titanium and zirconium based coupling agents. **Figure 4.1** illustrates the principle of the organometallic coupling agents. The titanium or zirconium derived coupling agent reacts with the free proton at the substrate interface resulting in formation of an organic monomolecular layer on the surface of the substrate. The new organic layer can then interact with the polymer matrix and enhance the fiber-matrix interactions. These coupling agents, however, should be applied only in low concentration (parts per thousand) to avoid producing weak boundary layers on the substrate surfaces. In this study, two types of titanium or zirconium based coupling agents have been examined.

Fiber coatings are applied to fiber-matrix interface in much larger quantities than the

coupling agents and form macroscopic layers at the fiber matrix interface with composition independent of the substrate; therefore, the mechanical properties of the coating material is expected to significantly affect the fiber-matrix interactions. Fiber coating can enhance fiber-matrix interactions by enhancing interfacial adhesion mechanisms. For example, in chapter 3 it was shown that the interfacial shear strength reductions of the sized Technora fiber is more than 30% higher than the unsized fiber. This ISS increase was attributed the improved epoxy compatible surface energy components of the sized fiber. Therefore, application of the fiber coatings to the Technora fiber can enhance their thermodynamic wetting properties.

Vapor deposited fiber coatings are particularly good candidates for enhancing the adhesive properties of high performance polymer fibers. The mobile vapor molecules can produce good fiber surface wetting and may even penetrate the fiber interior to form mechanical anchors within the fiber structure. Reagents such as butadiyne, ethylene, and

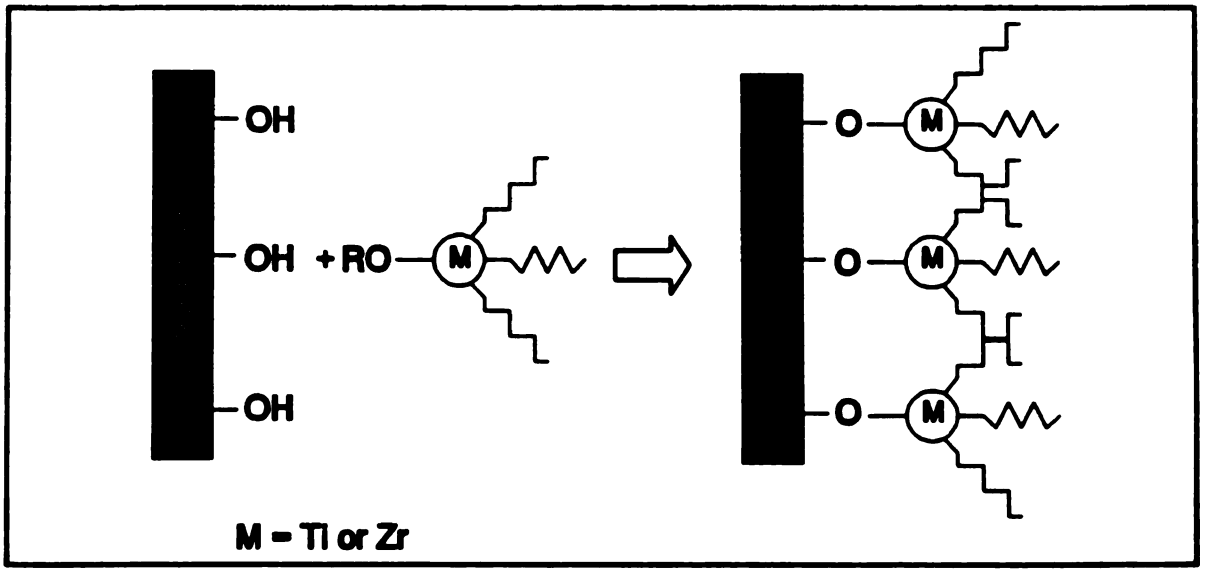

Figure 4.1 - General reaction scheme of a titanium or zirconium based coupling agent with the hydroxyl groups of a polymer substrate.

p-xylene can form strong and reactive films of coatings on the fiber exterior that can then be bonded with the matrix. In this study, butadiyne and p-xylene gas deposited fiber coatings have been investigated.

Butadiyne (C_4H_2) is a diacetylene monomer that can undergo a thermal polymerization to form a polymer film from its vapor phase (Snow 1985). Butadiyne polymerization produces a highly reactive coating on the surface of the fiber that can then interact with the matrix. The reaction scheme of butadiyne polymerization is shown in **Figure 4.2.** The deposited polymer structure has been characterized as a complex combination of polyene and polyacene structures (Snow 1985). Armistead *et al.* (1987) have examined interfacial shear strength (ISS) of butadiyne coated AS-4 and HMS-4 carbon fibers using the ISS fragmentation test. They reported up to 50% ISS increases for the AS-4 fibers but no measurable ISS enhancement for the HMS-4 fibers was detected.

Parylenes are the other gas phase fiber coatings examined in this study. Parylene is

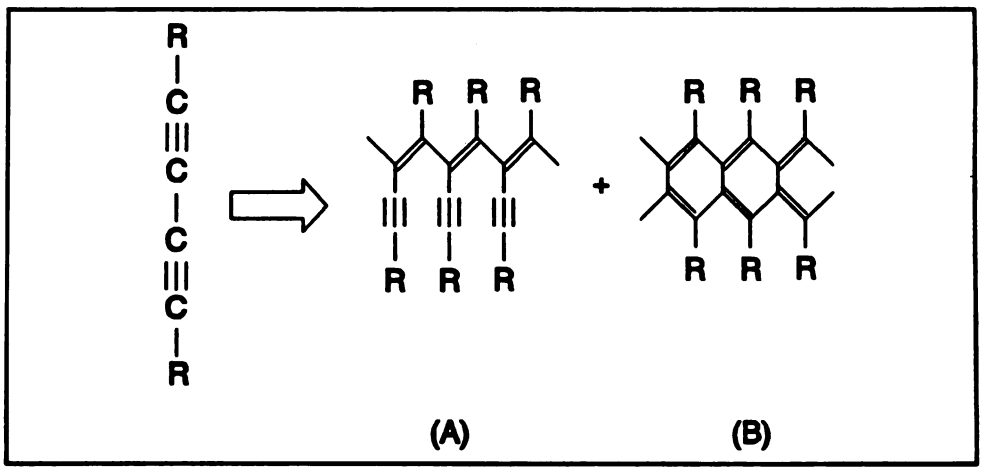

Figure 4.2 - Polymerization of diacetylene monomers produce a combination of substituted (A) polyene and (B) polyacene structures.

the generic name for members of a p-xylylene thermoplastic polymer series developed by Union Carbide. There are three type of Parylene available commercially which are shown in **Figure 4.3.** Parylene-N is a primary dielectric and is used in electronics devices. Parylene-C has several useful electrical properties along with very low permeability to moisture and is used for the coating of electronic circuitry. Parylene-D has similar electrical properties as other parylenes but has the best chemical resistance of all other parylene grades. The parylene polymers are deposited from the vapor phase at pressures around 0.1 torr and ambient temperatures. The initial vapor monomer is highly reactive which results in its simultaneous adsorption and polymerization on the substrate (Beach 1987). Parylene polymerization produces poly-para-xylylene chains that are greater than 5000 units long. Application of parylene for adhesion promotion has not been reported in the literature. In this study, parylenes were considered as coatings for aramid fibers because of their chemical compatibility with the fibers.

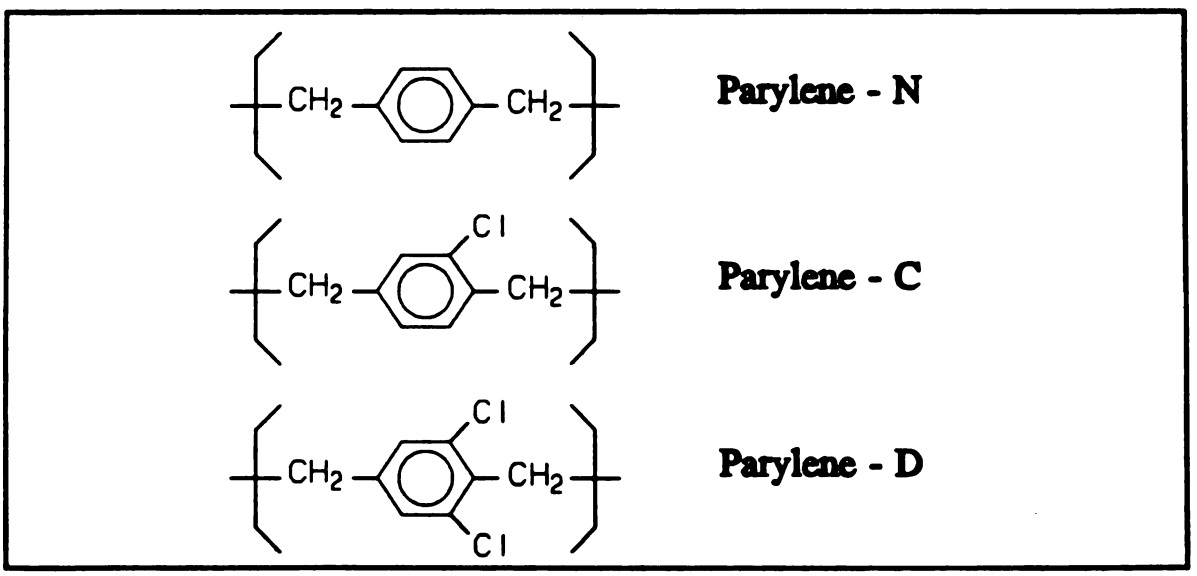

Figure 4.3 - Various types of parylene polymer available.

4.2 EXPERIMENTAL

Four types of fibers were examined, Kevlar-49 aramid, PBO aromatic heterocyclic AS-4 carbon, and E-glass fibers. Three curing conditions, ambient, 75°C/2hr-125°C/2hr, and 175°C/3hr were selected for this study. Interfacial shear strengths were characterized by the fragmentation tests. Single fiber tensile strengths were measured using a modified ASTM D3379 test with 25 mm test gage length and a nominal elongation rate of 0.135 mm/min. Thermal expansion of the parylene coated fibers were evaluated by a du Pont thermal mechanical analyzer (TMA model 943) using a 10 mm fiber gauge length. Material and experimental conditions are detailed Chapter 2.

The liquid coupling agents were designated as **KR55** (titanium IV tetrakis bis 2-propenolato methyl -1-butanolato adduct 2 moles di-tridecyl hydrogen) and **LZ37** (zirconium IV 2,2-bis propenolato methyl butanolato, tris 4-amino-bezoato-O) (Kenrich Petrochemicals, Inc., Bayonne, NJ). The recommended amount of coupling agent was 0.2-0.3 weight percent. Both the recommended amounts and a ~1.5% concentration of each coupling agents were examined in this study.

For the butadiyne treatments, three tows of treated and one untreated Kevlar-49 fibers were supplied by Dr. A.W. Snow at the Naval Research Lab. The butadiyne treatments of the Kevlar-49 fibers were conducted as follow: A tow of fiber was wrapped around a rectangular winder and inserted into a soxhlet extractor. Fibers were washed with chloroform for 3 hour, followed by 1 hour of vacuum drying at room temperature. The fibers were then transferred to a tubular reactor which was heated to 150°C, evacuated and backfield to 650 torr with butadiyne. The butadiyne deposition was measured by

percent weight gain. Three deposition quantities 0.50 wt% (2 hour reaction time), 0.84 wt% (4.25 hr), and 1.39 wt% (8 hr) were conducted, which displayed a progressive development of brown coloration. The treated fiber tows showed some fiber clustering especially for the 1.39% treated and to a lesser extend for the 0.84% treated fibers. The agglomeration made separation of the individual fibers difficult. The interior fibers sometimes had a lighter color than the exterior fibers, which indicated the non-uniformity of the coatings.

Parylene coatings of Kevlar-49, PBO, AS-4 and E-Glass fibers were conducted at Novatran Corporation (Clear Lake, WI). The parylene deposition process has been described by the Novatran Publications. The process consists of three distinct steps. The first step is vaporization of the solid dimer ($\sim$250°C and $\sim$1 torr). The second step is the division (pyrolysis) of the dimer ($\sim$680°C and $\sim$0.5 torr) to produce the monomeric diradical, p-xylylene. Finally, the monomer enters the deposition chamber ($\sim$25°C and $\sim$0.1 torr) where it simultaneously adsorbs and polymerizes on the substrates. Both thick and thin coatings of different parylenes have been investigate. Table 4.1 lists the experimental protocol for parylene treatments of various fibers. The proprietary adhesion promoter A-174 was also examined to enhance the coupling between the parylene and its substrates. The treatment G was immersed in liquid epoxy immediately after the fiber coatings to evaluate effect of aging on the coating. On arrival, sample G was rinsed with acetone to remove excess epoxy and after a brief vacuum drying the fibers were cast and cured.

Table 4.1 - Parylene experimental protocol and curing conditions examined for each fiber treatment.

Label	Condition	Kevlar-49	PBO	AS-4	E-Glass
A	3 μm Parylene-C	175 Ambient	175 Ambient	175 Ambient	175
B	7 μm Parylene-C	175 Ambient	175 Ambient	175 Ambient	175
C	10 nm Parylene-N	175 75/125	-	-	-
D	100 nm Parylene-N	175 75/125	-	-	-
E	A-174 on fiber + 10 nm Parylene-N	175 75/125	-	-	-
F	A-174 on fiber + 10 nm Parylene-N + A-174 on parylene	175 75/125	-	-	-
G	Same as F but stored and shipped in epoxy	175 75/125	-	-	-

4.3 RESULTS AND DISCUSSION

Effects of various fiber coating and coupling agent treatments on adhesive properties of high performance polymer fibers are presented separately.

4.3.1 Coupling Agents

Both low and high concentration of KR55 and LZ37 liquid coupling agents were examined. Figure 4.4 shows the interfacial shear strength (ISS) of the treated and untreated Kevlar-49 aramid and AS-4 carbon fibers for the 175°C curing condition. For the Kevlar-49 fibers their ISS values are unaffected by the coupling agents but for the

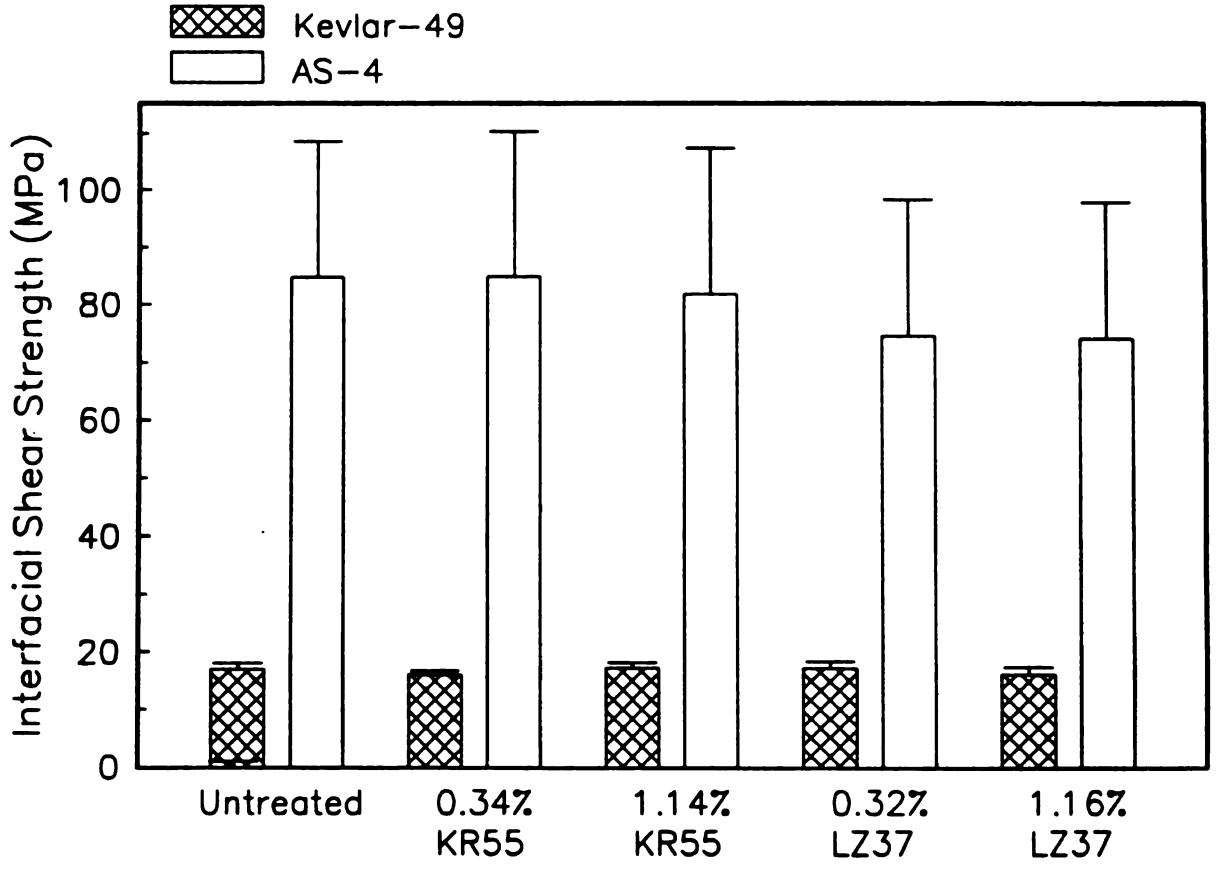

Figure 4.4 - Interfacial shear strength of Kevlar-49 aramid and AS-4 carbon fibers with liquid coupling agent mixed 175°C cured epoxy.

AS-4 fibers there are about 12% reduction in their ISS values for the LZ37 coupling agents. The reductions for the AS-4 carbon fiber occurs despite the abundant presence of hydroxyl groups on these fibers (Hook *et al.* 1990).

The enhanced mechanical properties of polymer composites reported by Gabayson *et al.* (1988) and Sugerman *et al.* (1989) may be due to improved processing introduced by the organometallic coupling agents. The single fiber test represent an ideal case of fiber-matrix wetting, whereas, in the multifilament composites, tow impregnation of the fiber bundles are important consideration. A liquid coupling agent could improve the fiber tow impregnation by enhancing fiber wetting or the resin flow properties, thus helping to produce defect-free composites. Improvements of interfacially controlled composite properties by producing defect-free parts, however, is only a processing enhancement which is different from an intrinsic improvement of the fiber-matrix interfacial shear strength.

4.3.2 Butadiyne Coatings

Figure 4.5 shows the interfacial shear strength (ISS) of the butadiyne treated Kevlar-49 aramid fibers for the 175°C curing condition. No significant changes in the ISS results is observed. Fiber tensile strengths were also unaffected by the treatments. **Figure 4.6** illustrates a TEM micrograph of a 0.84% butadiyne treated fiber that exhibits increased interfacial fibrillation. Therefore, the butadiyne coating has increased the aramid-matrix adhesion as evidenced by extensive interfacial fibrillation, however, the improved adhesion has not overcome the fiber surface structural limitations and the

Kevlar-epoxy interfacial shear strength is unaffected. Nonetheless, the butadiyne treated aramid surface is at least as strong as the untreated surface, suggesting that butadiyne is not producing a new weak surface layer. The vapor deposition and fast reaction of butadiyne should enhance wetting properties of non-wetting surfaces. Snow (1981[a], 1981[b], 1984) has demonstrated that butadiyne may be deposited onto polyethylene or Teflon substrates. Therefore, butadiyne treatment may be a useful coating for surfaces that exhibit poor wetting compatibilities with epoxy resins.

Figure 4.5 - Interfacial shear strength of butadiyne treated Kevlar-49 aramid fibers with 175°C cured epoxy.

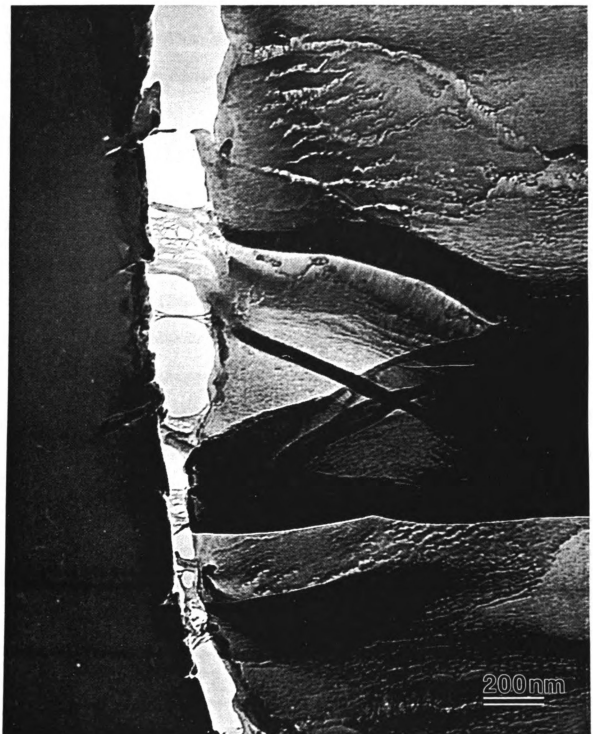

Figure 4.6 - TEM micrograph of a 0.84 wt% butadiyne treated Kevlar-49 fiber.

4.3.3 Parylene Coating

Effects of thick parylene coatings (treatments A and B) on tensile properties of Kevlar-49 and E-Glass fibers were examined. Because thickness of these coatings are comparable to the fiber diameters, the contribution of the coatings was evaluated using:

$$\sigma_{cor} = \frac{P}{A_f + \frac{E_c}{E_f} A_c} \qquad (4.1)$$

where σ_{cor} is the fiber tensile strength corrected for the coating contribution, P is the load applied to the sample, A_f is the fiber cross-sectional area, A_c is the coating cross-sectional area, E_c is the coating tensile modulus (2.76 GPa for Parylene-C), and E_f is the fiber tensile modulus (Tables 3.1 and 3.2). Equation 4.1 is derived in Appendix A. Table 4.2 lists the tensile strength and diameter of 3 and 7 μm Parylene-C treat fibers. The coated Kevlar-49 the coated fibers do not show significant changes in their tensile strength, however, for the E-Glass fibers there are measurable increases in the tensile strength of the coated fibers. Tensile strength increases of the E-Glass fibers can be

Table 4.2 - Tensile strength and diameter of 3 and 7 μm Parylene-C treated Kevlar-49 and E-Glass fibers.

Fiber	Diameter (μm)	Tensile Strength (GPa)
Kevlar 49	12.7 ± 0.5	2.81 ± 0.46
3 μm Parylene-C	19.2 ± 0.7	1.23 ± 0.16
7 μm Parylene-C	27.9 ± 1.0	0.609 ± 0.088
3 μm Parylene-C σ_{cor}		2.73 ± 0.36
7 μm Parylene-C σ_{cor}		2.70 ± 0.39
E-Glass	17.1 ± 1.2	1.08 ± 0.22
7 μm Parylene-C	33.7 ± 2.2	0.382 ± 0.084
7 μm Parylene-C σ_{cor}		1.33 ± 0.35

attributed to the deposition process and hydrophobic nature of the parylene coating. Michalske *et al.* (1987) has shown that water can weaken a glass by chemically attacking the glass molecules at a crack tip. A surface coating that can block the opening of the cracks and restrict the passage of water molecules, should increase the strength of the glass. Parylene vacuum deposition allows for water removal and its small monomers permit crack penetration. Parylene has also a low moisture and gas permeability that should block moisture from reaching the crack tips. The fiber tensile tests have been performed at 25 mm gage lengths, greater tensile strength increases are expected for the shorter gage length samples because of statistical reduction of the number of large defects in the shorter gage length samples.

To evaluate effects of thermal stresses on the fiber-matrix interfacial shear strength, both the ambient and 175°C cured epoxies were examined. **Figure 4.7** shows the interfacial shear strengths of the Kevlar 49, PBO, AS-4 and E-Glass fibers for the treatments A and B. For all the fibers the parylene coatings reduce the interfacial shear strength. The ISS reductions can be attributed to the effects of the parylene's low modulus. Equation **2.1** does not explicitly include effects of thermal stresses and the matrix modulus, but more complex models such as those proposed by Whitney *et al.* (1980) (see equation **3.1**) or Cox *et al.* (1952) demonstrate that lowering the modulus of fiber-matrix interphase modulus would reduce efficiency of interfacial load transfer. The ISS reductions of the parylene coated fibers are much more pronounced for the inorganic E-glass and AS-4 carbon fibers than the organic Kevlar-49 and PBO polymer fibers. These observations suggest that the interfacial properties of the organic fibers are not

much superior to the mechanical properties of the parylene layers.

Figure 4.7 also shows that for the parylene coated fibers there are ISS increases at the higher temperature curing condition. Untreated Kevlar-49 fibers do not exhibit temperature trends (see **Figure 3.4**), but the parylene coated fibers show ISS increases for the higher curing temperature. This temperature trend of the coated Kevlar-49 fibers may be attributed to the thermal expansion effects of the thick parylene layer. **Figure 4.8** illustrates the longitudinal thermal expansion of untreated and Parylene-C coated Kevlar-49 fibers. The effects of the coating is to introduce additional longitudinal compressive stress on the embedded fiber during the cool down from oven temperatures to ambient conditions. This longitudinal compression in turn results in increased interfacial radial compressive stress due to Poisson's ratio effects (Kalantar *et al.* 1990 [b]). The shear load carrying capacity the parylene interphase may be increased by the

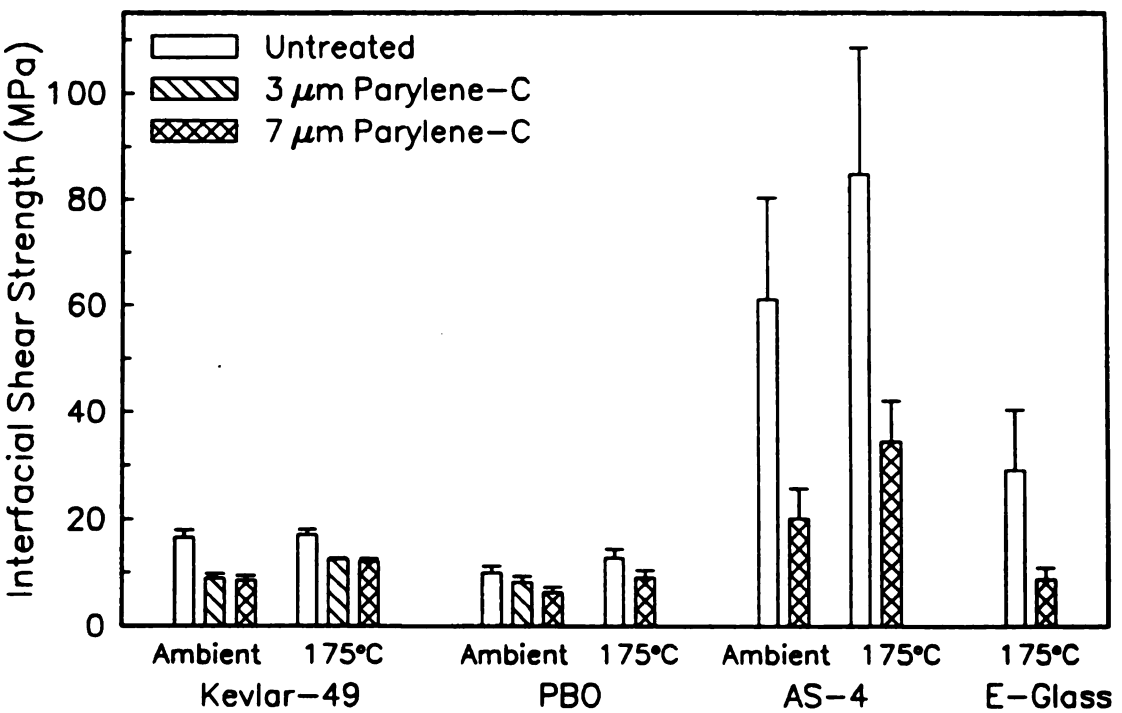

Figure 4.7 - Interfacial shear strength of treatments 3 and 7 μm Parylene-C coatings for Kevlar-49, PBO, AS-4 and E-Glass fibers at two curing conditions.

increased excess radial stress, resulting in the increased ISS values.

Figure 4.9 illustrates the fracture process of 7 μm Parylene-C coated Kevlar-49 aramid and AS-4 carbon fibers. The fibers have been embedded in the 175°C cured epoxy matrices. On load application, for the Kevlar-49 sample, the parylene coating fractures before the fiber (A), whereas, for the AS-4 fibers, fiber fracture occurs before the parylene fracture (D). This observation suggest that the parylene coating is more brittle than the Kevlar-49 fiber but more ductile than the AS-4 fiber. For both fibers, their fractures results in displacements and conical fractures of the parylene coating (B), (C), (E), and (F).

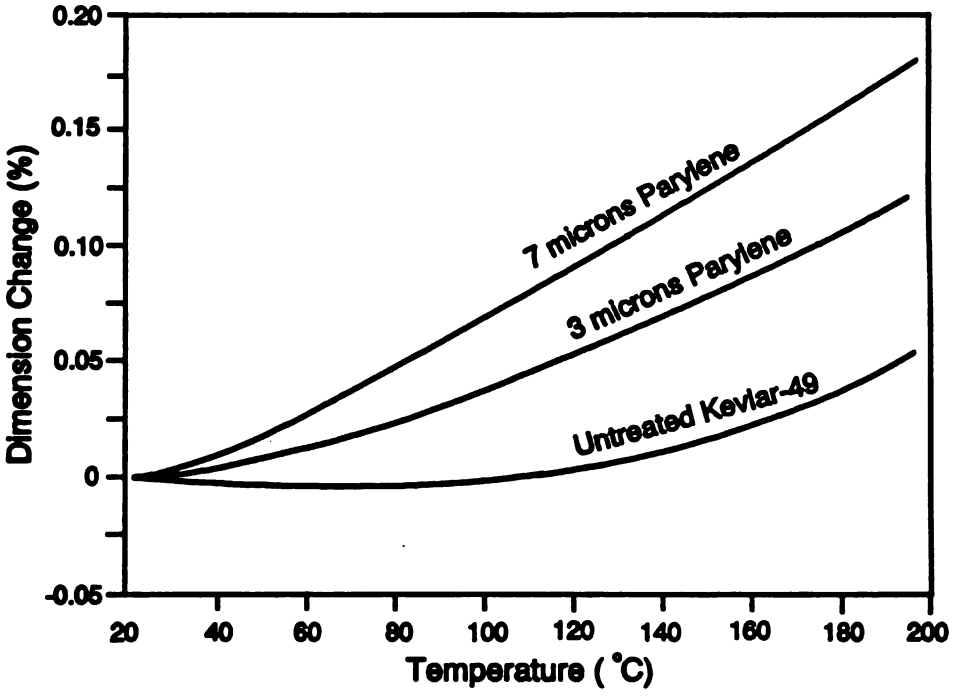

Figure 4.8 - Longitudinal thermal expansion of the untreated and Parylene-C treated Kevlar-49 fibers. The parylene coatings tend to longitudinally compress the fiber during the cool down.

Figure 4.10 shows the TEM micrographs of a 3 μm parylene-C coated Kevlar-49 fiber sectioned radially. The micrographs show extensive fibrillation of the coating both on the fiber and epoxy sides. The parylene fibrillation suggest that parylene itself has an ordered morphology with even weaker lateral cohesive properties than those of the Kevlar-49 fibers. Therefore, cohesive failures of the parylene layer is limiting the load transfer between fiber and matrix.

Thin Parylene-N coatings of Kevlar-49 fibers resulted in similar observations as the thick coating. Treatments C, D, E, F, and G resulted in an average ISS value of 9.7 MPa (compared to 18 MPa for untreated fibers), which is lower than the average values obtained for the thick parylene-C coatings (12.4 MPa). This observation correlates with the lower modulus of parylene-N (2.41 GPa) than parylene-C (2.76 GPa).

Figure 4.11 shows TEM micrographs of a Kevlar-49 fiber with coating F. This coating has the A-174 adhesion promoter and shows only limited interfacial separation. The adhesion promoter has altered the epoxy morphology to form what appear to be two concentric bands around the fiber perimeter. Each band is about 50 to 80 nm thick. The similarities in interfacial shear strength of thin Parylene-N coatings with and without the adhesion promoter suggest that the parylene layer is itself the weak boundary layer. Therefore, interfacial shear strength of Parylene-N treated aramid fibers are still limited by the fibrillation of the parylene layer.

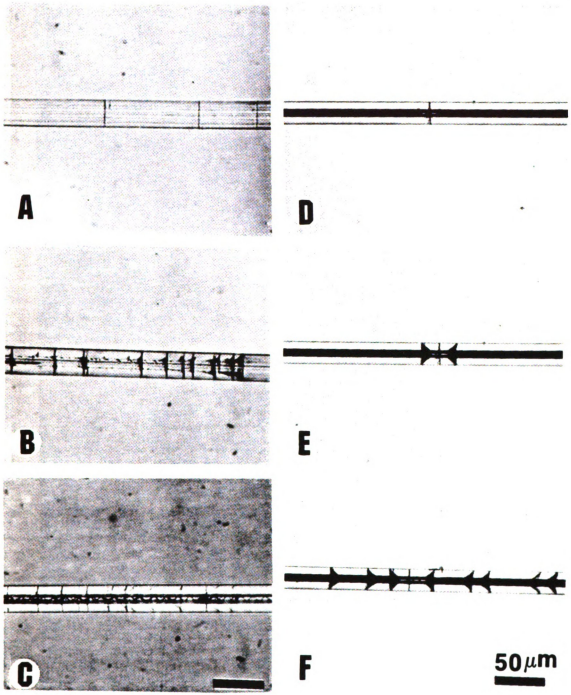

Figure 4.9 - Fracturing process of 7 μm Parylene-C coated Kevlar-49 aramid and AS-4 carbon fibers.

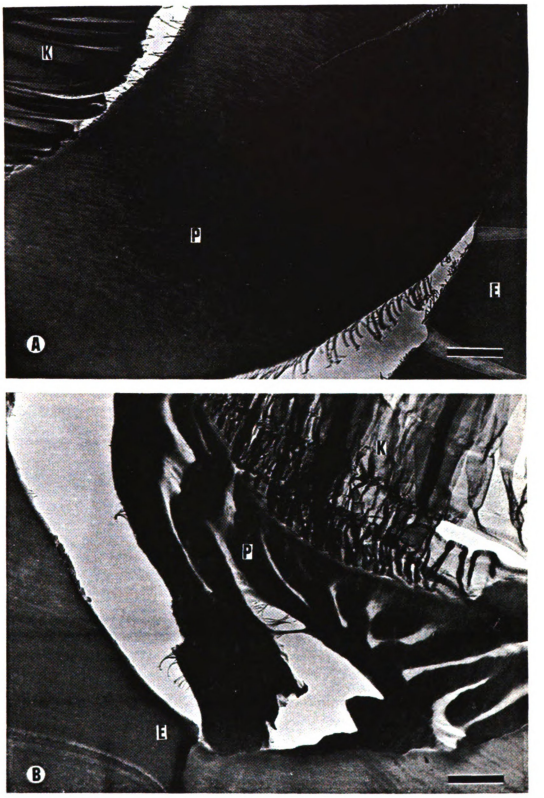

Figure 4.10 - TEM micrographs of radial sections of a 3 μm Parylene-C coated Kevlar-49 fiber in the 175°C cured epoxy system. (A) bar = 1 μm (B) bar = 1μm

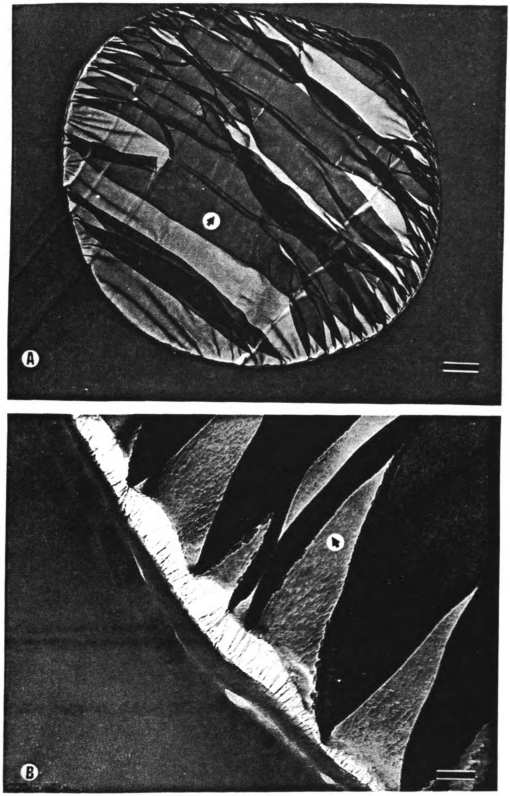

Figure 4.11 - TEM micrographs of radial sections of a thin Parylene-N coated Kevlar-49 fiber (treatment F). (A) bar = 1 μm (B) bar = 100 nm

4.4 CONCLUSIONS

- Examined organometallic coupling agents marginally reduced the interfacial shear strength (ISS) of AS4 carbon fibers but did not affect Kevlar-49 ISS values.
- Butadiyne treated Kevlar-49 fibers exhibit improved fiber-matrix bonding, however, the ISS of Kevlar-49 fibers are unaffected suggesting that fiber cohesive failure is still limiting their fiber-matrix adhesion.
- Parylene coatings could enhance tensile properties of E-glass fibers by providing a moisture barrier but did not affect tensile properties of the polymer fibers.
- Interfacial shear strength of the parylene coated fibers were drastically reduced due to the low modulus and tensile strength of the parylene polymer. The parylene coating also demonstrated that the interfacial shear strength of the organic fibers are not much stronger than to the mechanical properties of the parylene layers.
- The shear load carrying capacity the parylene interphase can be increased by compressive stresses that are induced by the sample curing process.

The similarity of the ISS values of untreated and parylene coated polymer fibers suggest that the high performance polymer fibers possess mechanically weak adhesive properties. Since, surface chemistry modification can not enhance the bulk mechanical properties of a polymer fiber, therefore, coupling agents and/or fiber coatings can only be effective if the wetting or chemistry of the fiber-matrix interface is limiting their adhesive interactions.

Parylene results also suggest that the thermal stresses of the curing process can affect shear load carrying capacity of the fiber-matrix interphase. This observation may explain the ISS temperature trends that were observe for the untreated Technora and PBO fibers but were absent for the Kevlar-49 fibers (see Chapter 3). Interfacial bonding of the Kevlar-49 fibers are merely limited by the internal fiber fibrillation, whereas, Technora and PBO fibers exhibit additional wetting and weak surface layer limitations. The surface property limitations of the Technora and PBO fibers may be affected by the stress environment of the matrix resulting in their observed ISS temperature trends.

CHAPTER 5

Plasma and Corona Treatments of High Performance Polymer Fibers

In this chapter, the effects of corona and plasma treatments on mechanical and chemical properties of the PBO and polyethylene fibers have been investigated. These treatments can alter chemistry and morphology of polymer surfaces without modifying their bulk properties; allowing examination of surface limited adhesion mechanisms and how these limitations influence adhesive properties of high performance polymer fibers.

5.1 INTRODUCTION

A plasma is an excited gas region where positive and negative space charges are created. To generate a plasma the gas must be excited by some power input such as AC, DC, electromagnetic radiation, or nuclear reactions. There are three categories of plasma: hot, mixed, and cold plasma. A hot plasma such as solar corona has high equilibrium temperatures and must be maintained by nuclear reactions or laser excitations. A cold plasma such as that in a neon lamp has its bulk gas in ambient temperatures but its free electrons may have high kinetic energies that result in their highly reactive chemical environments. A mixed plasma is between the hot and cold plasma. In this report plasma treatments refer to cold plasma phenomena exclusively.

A plasma may contain atoms, molecules, ions, free radicals, free electrons, and metastable species. The excited species present in a plasma can interact with the treating substrate to produce a variety of effects such as surface layer removal (etching and cleaning), chemical modification, cross-linking, and polymerization (Kinloch 1987). In polymer materials the low molecular weight polymers and contaminants tend to accumulate on the surface to minimize the surface free energy (see Appendix B). These low molecular weight species create interfacial weak boundary layers that are detrimental to adhesion. The excited species of the plasma can remove these surface species from the substrate. The surface degradation caused by plasma treatment can reduce the molecular weight of the surface polymer or contaminants which then vaporize into the reaction chamber. The surface degradation can also etch the surface and increase its contact surface area. Plasma may contain chemically reactive excited species such as

free radicals and ions that chemically interact with the substrate to produce reactive surface sites and increase surface free energy. Without active oxygen and nitrogen species the surface groups may interact to cross-link the surface molecules (Cross-linking by Activated Species of INert Gas, "CASING"). If the plasma contains polymerizable gas monomers, then the deposition of the polymer phase onto the substrate surface is possible.

A corona discharge is the flow of electricity from a high voltage conductor through ionized air between the conductor and an insulator, and is usually exhibited as a faint glow adjacent to the surface of the conductor. Normally air is a nonconductor, however, it contains small number of ions produced, for example, by the cosmic rays. A charged conductor draws the oppositely charged ions to neutralize itself. When the drawn ions receive a high acceleration, their collision with other air molecules produces more ions and the surrounding air becomes conductive. Corona discharge is the result of an electrical breakdown in the surrounding gas. Corona discharge can introduce oxygen-containing groups onto the substrate surface through reactions with ozone, water, oxygen, nitrogen, and different free radicals (Briggs *et al.* 1983). The extent of each reaction depends on the composition of the reaction gas. The corona discharge reactions can degrade and clean the substrate surface (Kim *et al.* 1971, Carley *et al.* 1978), form sites for hydrogen bonding (Owens 1975, Blythe *et al.* 1978, Lanauze *et al.* 1990), increase the surface free energy (Carley *et al.* 1978, Baszkin *et al.* 1978), and cause surface cross-linking (Kim *et al.* 1971).

A glow discharge plasma is similar to corona discharge but it is produced at a less

than atmospheric pressure. Glow discharge can be established by AC, DC, or electromagnetic power inputs, but radio-frequency (RF) plasma are the most common method because of their efficiency in sustaining the plasma. Plasma generated by RF excitement can be contained in the RF field (primary plasma) or carried outside by gas flow and diffusion (secondary plasma). Depending on the reactor configuration primary or secondary plasma may cover the working volume (Rose *et al.* 1986). In general, controlling parameters for a glow discharge plasma are: process gas, power dissipation, excitation frequency, gas flow rate, and plasma chamber geometry. A schematic diagram of a glow discharge reaction chamber is shown in Figure 5.1.

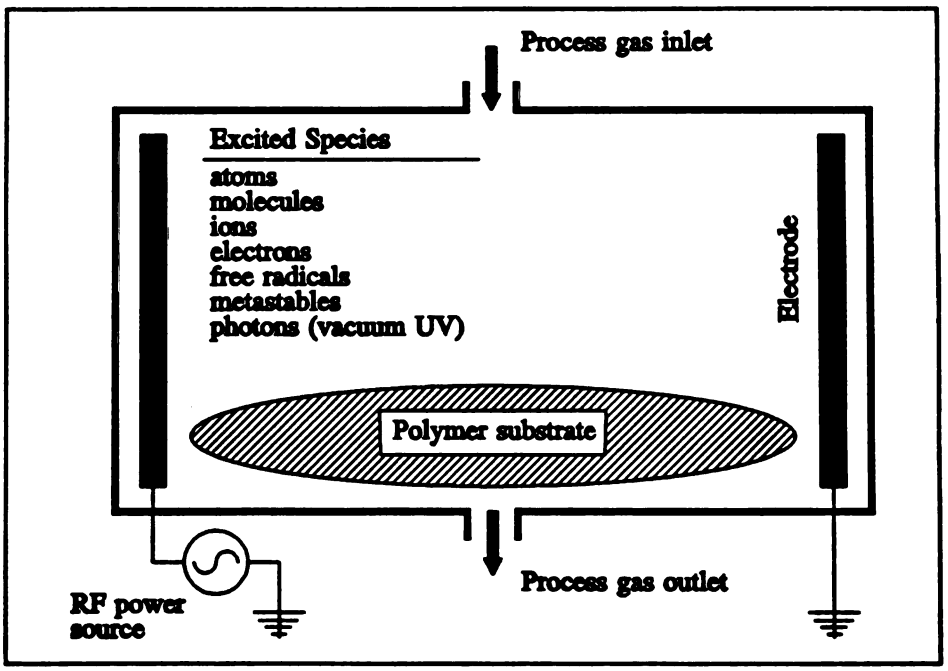

Figure 5.1 - Schematic diagram of the surface modification of polymers in a glow discharge reactor.

The most commonly used gases in a glow discharge are oxygen, nitrogen, air, argon, helium, nitrous oxide, ammonia, water, and tetrafluoromethane (CF_4). Each gas or mixture has a distinct plasma characteristic. The efficiency of the chemical processes also depend on the gas pressure and energy input. Decreasing the gas pressure and/or increasing the RF power increases the mean free path, degree of excitation, and concentration of the active species that are important in aggressive processes such as cleaning and degradation. In general, low pressure and high RF power provides fast but more surface sensitive reactions.

Rose *et al.* (1986) and Liston (1989) have reported on the effects of plasma treatments on polymers. In general, plasma treatments of polymers produces four major effects: cleaning (removal of unbounded contaminations), surface activation (wetting or non-wetting), chain cross-linking and etching (removal of the polymer substrate). For any set of process condition and gas chemistry, all effects are present to different extent. Typically, an oxygen and/or nitrogen containing plasma can produce surface cleaning, higher surface energies and reactive polar groups. The efficiency of chain scission is vastly enhanced by mixing CF_4 into a process gas. A gas plasma of CF_4 and O_2 is a particularly aggressive plasma for most polymers and is used for the etching treatments of polymers. Inert gas plasmas can be used to cross-link the polymer surfaces. In an inert gas plasma, the polymer chains that are broken by the activated species of the plasma are without chemically active radicals in the gas phase to react with, so the polymer sites react with each other and cross-link the polymer chains. Inert gases can also enhance the surface wetting because they create sites for polar functional groups to

attach to when exposed to oxygen or nitrogen in the air (Nakayama *et al.* 1991). Polar groups could be introduced to the polymer substrates when the plasma gas contains nitrogen, ammonia, nitrous oxide, oxygen, or water (Hansen *et al.* 1965, Holmes *et al.* 1990). A pure CF_4 gas plasma, however, lowers the surface energy of the polymer substrate and makes the polymer non-wettable because the polymer chains become similar to fluorocarbon chains.

Plasma reactors can also be used to form polymer materials from a monomer plasma gas. Plasma polymerization has several advantages over the conventional polymerization techniques including thin film formation, perfect conformance to the substrate contours, one-step monomer synthesis and polymerization, and cleaning and/or conditioning of the substrate surface before deposition. Plasma polymerization processes have good substrate surface penetration and coverage that promotes grafting the deposited polymer film to the substrate. The polymer grafting resulting from plasma polymerization is not notably affected by the nature of the substrate and provides little alteration of the bulk properties of the substrate (Yasuda 1985). Polymer films produced by plasma polymerization can be considered as coupling agents for fiber-matrix adhesion because of their ability to graft with the substrate fiber and then covalently react with the resin matrix. Plasma polymerization has the ability of depositing a film of virtually any monomer that has a vapor phase (Bell 1983). In a study by Inagaki *et al.* (1982) several polymer substrates were first exposed to argon plasma to clean the substrate and then a monomer gas (trimethylsilydimethlamine or hexamethyldisiloxane) was injected to form the polymer films. They have reported improved adhesion between hexamethyldisilazane treated

fibers with epoxy resins.

Occhiello *et al.* (1991) have examined the adhesive properties of oxygen plasma treated polypropylene (PP) sheets. The locus of failure for PP-epoxy joints was found to be adhesive for the untreated samples and cohesive for the plasma treated samples. For the plasma treated PP, the PP-epoxy joints failed within the PP bulk, but close to the modified PP interphase which suggests the cohesive strength of the PP had become the limiting factor in the PP-epoxy adhesion. The PP-epoxy joints also showed increases in the shear strength which was attributed to the introduction of polar functional groups to the plasma treated PP surfaces. Similarly, for plasma treated polyethylene fibers Ladzesky *et al.* (1983) have reported a shift from an adhesive failure for the untreated sample to a cohesive failure for the treated samples.

There are reports on the improvement of aramid adhesive properties by glow discharge treatments, however, these reports show that fiber-matrix adhesion improvements are accompanied by fiber strength deteriorations. Wertheimer *et al.* (1981) have reported 10% to 85% increases in the peel strength of the aramid-epoxy composites after exposure to a microwave plasma, but along with a 35% reduction in fiber tensile strength. Allred *et al.* (1985) have reported a glow discharge treatment for aramid fibers that improves their adhesive properties without fiber strength deterioration. Using a RF plasma in the presence of ammonia gas Allred has reported a two-fold increase in the interlaminar peel strength of treated Kevlar-49/epoxy composites and failure mode changes from interface failure to mixtures of fiber and matrix failure. Gaur *et al.* (1990) have also report doubling of interfacial shear strength between various

plasma treated Kevlar-49 aramid fibers and an epoxy matrix as determined by a droplet test. Conversely, using a droplet test method, Kupper *et al.* (1991) have reported 10-20% increase in the ISS values of various plasma treated Kevlar-49 fiber, but 10-20% ISS reduction for the plasma treated Technora fibers (note that the droplet test technique typically show about 20% error). In general, the large increase in the interfacial shear strength of the plasma treated aramid fibers reported by Allred *et al.* (1985) and Gaur *et al.* (1990) have not been widely validated by other researchers and plasma treatments of aramid fibers merit closer examination.

5.2 EXPERIMENTAL

The polymer fibers examined in this study were p-Phenylene BenzobisOxazole (PBO) aromatic heterocyclic supplied by Dow Chemical (Midland, MI) (ref. # XV-0383-C8700975-008) and ultra-high-modulus Spectra-1000 polyethylene fibers supplied by Allied Signal (Morristown, NJ). Both fibers were unsized and were used "as received".

Plasma treatments of the PBO fibers were conducted by Plasma Science, Inc. (Belmont, CA). Plasma treated PBO fibers were sealed in nitrogen-purged bags and were shipped overnight. Plasma and corona treated Spectra-1000 fibers were provide by the Allied Signal, treated with their proprietary treatment condition.

The epoxy systems used were the DER331/MPDA/DETA 175°C/3hr (fragmentation test), and DER331/MPDA RT/24hr/75°C/2hr/100°C/3hr (droplet test). Single fiber tensile strengths were measured by ASTM D3379 tensile test. These experimental conditions are detailed in Chapter 2.

5.3 RESULTS AND DISCUSSION

Results of PBO and polyethylene plasma treatments are discussed separately but conclusions for both fibers are combined to develop a comprehensive understanding of the effects of plasma and corona treatments on the surface properties of high performance polymer fibers.

5.3.1 PBO Plasma Treatments

In Chapter 3, it was demonstrated that adhesive properties of the PBO fibers are limited by a cohesively weak surface layer that fails within the fiber during interfacial separation. Plasma treatment could improve the fiber adhesive properties by variety of mechanisms such as etching the fiber skin and/or cross-linking the surface polymers to strengthen the fiber surface properties. PBO fibers also exhibited lower polar surface energy than liquid epoxy which suggest incomplete wetting with liquid epoxy. Plasma treatments could introduce polar functional groups to enhance the PBO-epoxy wetting compatibility.

In this study, plasma treatments of PBO fibers with variety of plasma gases have been examined to determine which treatment is the most effective for enhancing the adhesive properties of the PBO fiber. **Table 5.1** lists the treatment protocol for the first set of plasma treatments. A variety of different plasma gases and conditions were examined. **Table 5.1** also lists the possible polymer surface alteration mechanisms that are expected to dominate for each treatment condition. **Figure 5.2** shows percent changes in tensile and interfacial shear strengths of the plasma treated fibers with respect to the untreated

Table 5.1 - Plasma treatment condition for the first set of PBO plasma treatments. The expected major surface changes are also listed.

Label	Gas (Flow %)	Power (watts)	Time (min.)	Major Effect
A	O_2 50%	300	3.00	Cleaning
B	O_2 25% CF_4 25%	300	3.00	Etching
C	He 50%	300	3.00	Cross-linking
D	CO_2 50%	299	3.00	Polar-sites
E	NH_3 50%	299	3.00	Polar-sites
F	NH_3 50%	445	3.00	Polar-sites
G	N_2O 50%	299	3.00	Polar-sites
H	N_2O 50%	455	3.00	Polar-sites
I	Ar 50%	300	3.00	Cross-linking
J	H_2/N_2 50%	299	3.00	Cleaning
K	Ar 50% + 100% CO_2	299 0	3.00 3.00	Cross-linking + Polar-sites
L	Ar 50% + 100% O_2	299 0	3.00 3.00	Cross-linking + Polar-sites
M	H_2O 100%	299	3.00	Cleaning

fiber. In general, tensile strengths are not affected by the plasma treatments except for the O_2/CF_4 (treatment B) which show about 28% tensile strength reduction. The O_2/CF_4 plasma is a highly corrosive treatment that results in etching removal of the polymer substrates. **Figure 5.2** also shows that some treatments have increased the interfacial shear strength (ISS) of the PBO fibers. For example, treatment D (CO_2) exhibits over 40% ISS increase. The O_2/CF_4 and CO_2 plasma treatments showed the greatest influence on the PBO properties and were chosen for further examination.

For the second set of PBO plasma treatments, O_2/CF_4 and CO_2 treatments were examined with various input energy and exposure times. **Table 5.2** lists the experimental protocol for the second set of PBO plasma treatments. **Figure 5.3** shows percent

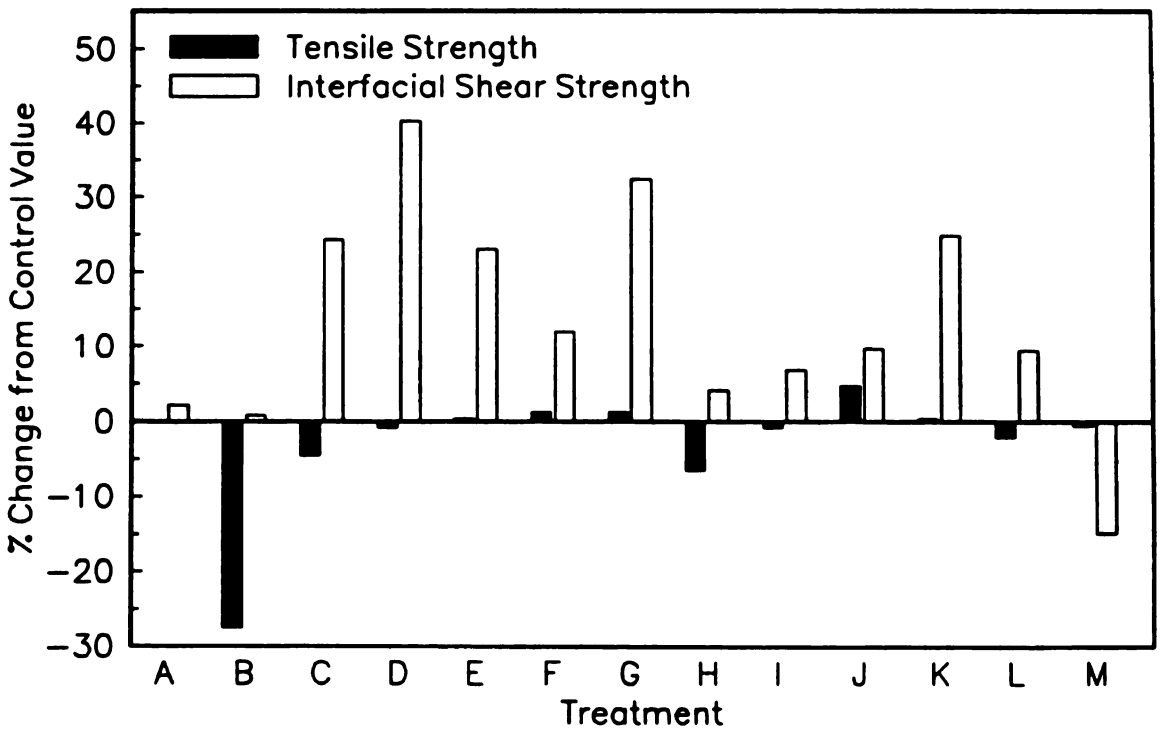

Figure 5.2 - Percent changes in tensile and interfacial shear strengths of the first set of plasma treated PBO fibers.

Table 5.2 - Plasma treatment condition for the second set of PBO plasma treatments.

Label	Gas (Flow %)	Power (watts)	Time (min.)
N	CO_2 50%	301	0.50
O	CO_2 50%	301	0.75
P	CO_2 50%	301	1.00
Q	CO_2 50%	479	0.50
R	CO_2 50%	479	0.75
S	CO_2 50%	479	1.00
T	O_2 25% CF_4 25%	301	0.50
U	O_2 25% CF_4 25%	301	0.75
V	O_2 25% CF_4 25%	301	1.00
W	O_2 25% CF_4 25%	395	0.50
X	O_2 25% CF_4 25%	397	0.75
Y	O_2 25% CF_4 25%	395	1.00

changes in tensile and interfacial shear strengths of the plasma treated fibers with respect to the untreated fiber. All plasma treatments show interfacial shear strength increases, but the O_2/CF_4 treatments generally show greater increases than CO_2 treatments. In particular treatment W (O_2/CF_4, 395 watts, 0.5 min) shows about 56% ISS increase. **Figure 5.3** also shows that except for treatment Y (O_2/CF_4, 395 watts, 1.0 min), the examined plasma conditions do not significantly affect the PBO tensile strength. These results illustrate the viability of plasma treatments for improving interfacial shear strength of the PBO fibers. The mechanisms of adhesion improvements for the plasma treated PBO fibers are examined next.

As discussed previously in Chapter 3, virgin PBO exhibit internal kink bands that are

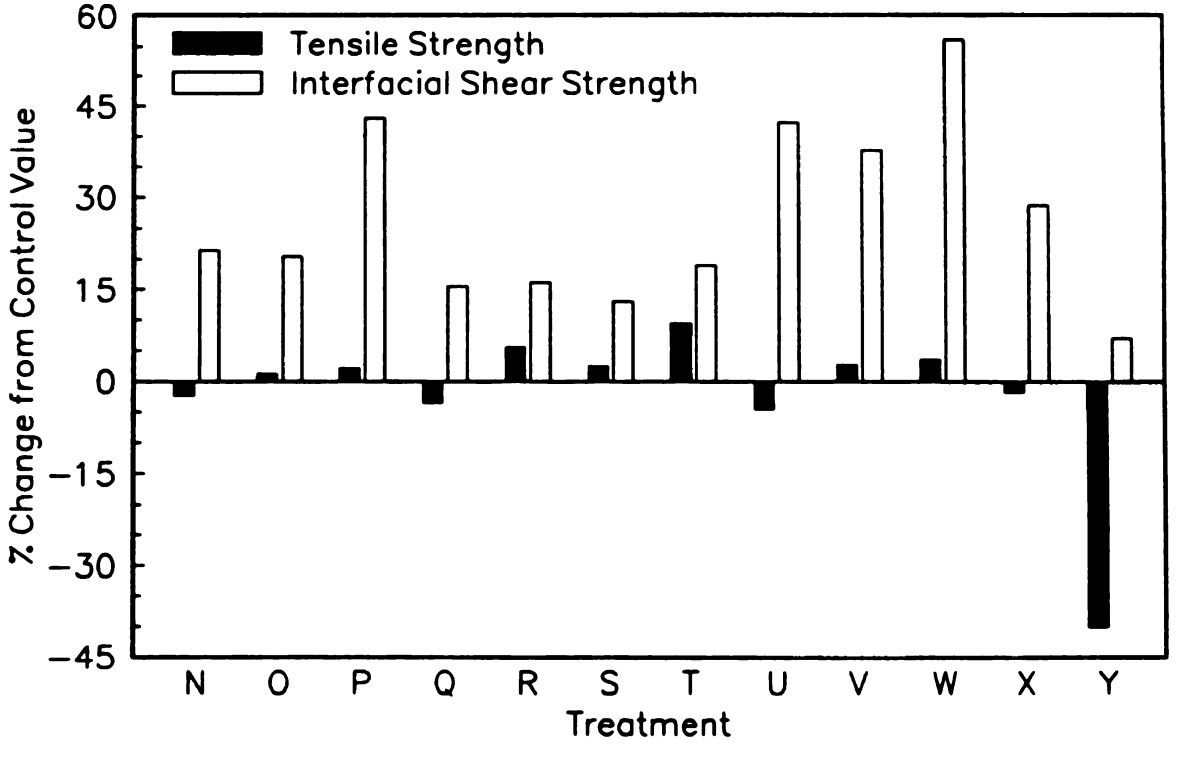

Figure 5.3 - Percent changes in tensile and interfacial shear strengths of the second set of plasma treated PBO fibers.

not apparent on the fiber surface. **Figure 5.4** illustrates the SEM micrographs of 0.5, 0.75 and 1.0 minutes O_2/CF_4, 397 watts PBO plasma treatments (W, X, Y). These micrographs show the development of PBO surface etching by the plasma treatment, as evidenced by the gradual appearance of the fiber internal kinks. Initially, the O_2/CF_4 plasma treatments increase the PBO-epoxy interfacial shear strength, but as the surface etching proceeds, eventually the fiber tensile properties begin to deteriorate. Treatment Y exhibit about 40% tensile strength reduction.

TEM micrographs of treatment W are shown in **Figure 5.5**. The micrographs still show internal fibrillation of the PBO fiber but the external fiber surface layer that was observed for the untreated fibers (**Figure 3.12**) is now absent. Plasma treatment results suggest that the etching removal of the weak surface layer of the PBO fibers can significantly (~50%) enhance their interfacial shear strengths with an epoxy resin; however, once the fiber skin weak boundary layer is removed, the cohesive fibrillation of the fiber limits the interfacial load transfer of the PBO fibers. Therefore, for the PBO fibers plasma etching must be optimized to remove the weak fiber surface layer without exceeding and deteriorating the fiber tensile properties.

SEM examination of the CO_2 plasma treated fibers did not exhibit discernable surface morphological changes like those observed with the O_2/CF_4 plasma treatments. Therefore, the ISS increases of the CO_2 plasma treated fibers (treatments N-S) should be mainly the result of some chemical modification of the PBO fiber surfaces. **Figure 5.6** compares the surface energy of several plasma treated fibers with the liquid epoxy. Note that the treatment P (CO_2) exhibits a much improved epoxy compatible surface energy

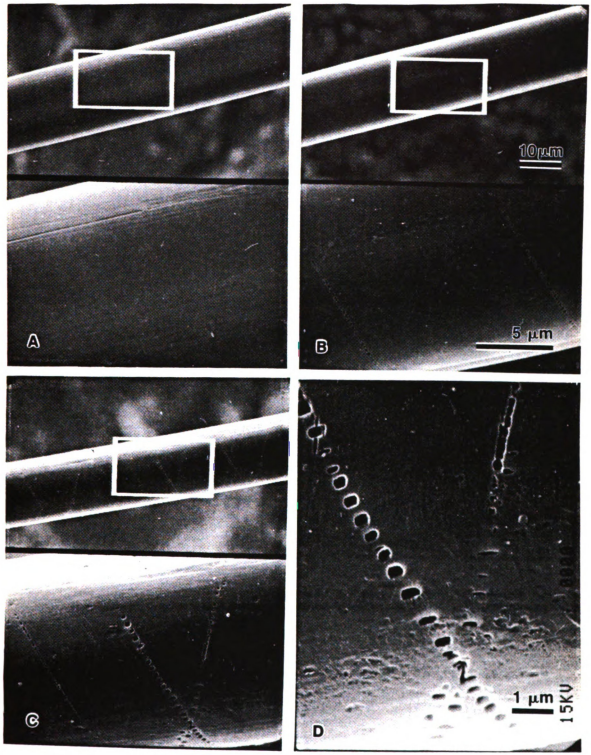

Figure 5.4 - SEM micrographs of (A) 0.5, (B) 0.75 and (C,D) 1.0 min. O_2/CF_4, 397 watts PBO plasma treatments.

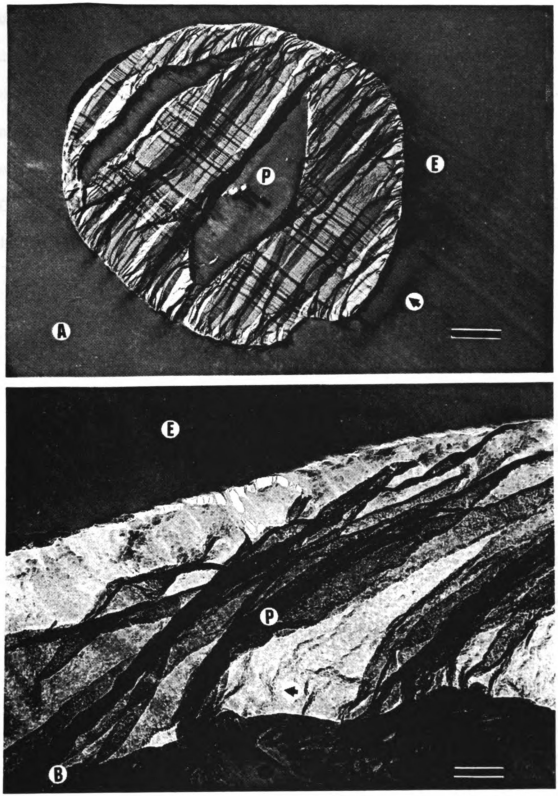

Figure 5.5 - TEM micrographs of a 1.0 min. O_2/CF_4, 397 watts PBO plasma treated fiber (treatment Y). (A) bar = 2 μm (B) bar = 250 nm

components compared to the untreated PBO fibers. The O_2/CF_4 plasma treated fiber (treatments U, V, and W) also exhibit increased polar component of surface energy which enhances their wetting properties with the liquid epoxy. However, the surface energy components of the O_2/CF_4 are less than optimum, and better wetting properties are expected if the surface energy components could better match the epoxy components (Gutowski 1990). Introduction of fiber-matrix covalent chemical bonding for the CO_2 plasma treated fibers is another possible mechanism of adhesion improvement.

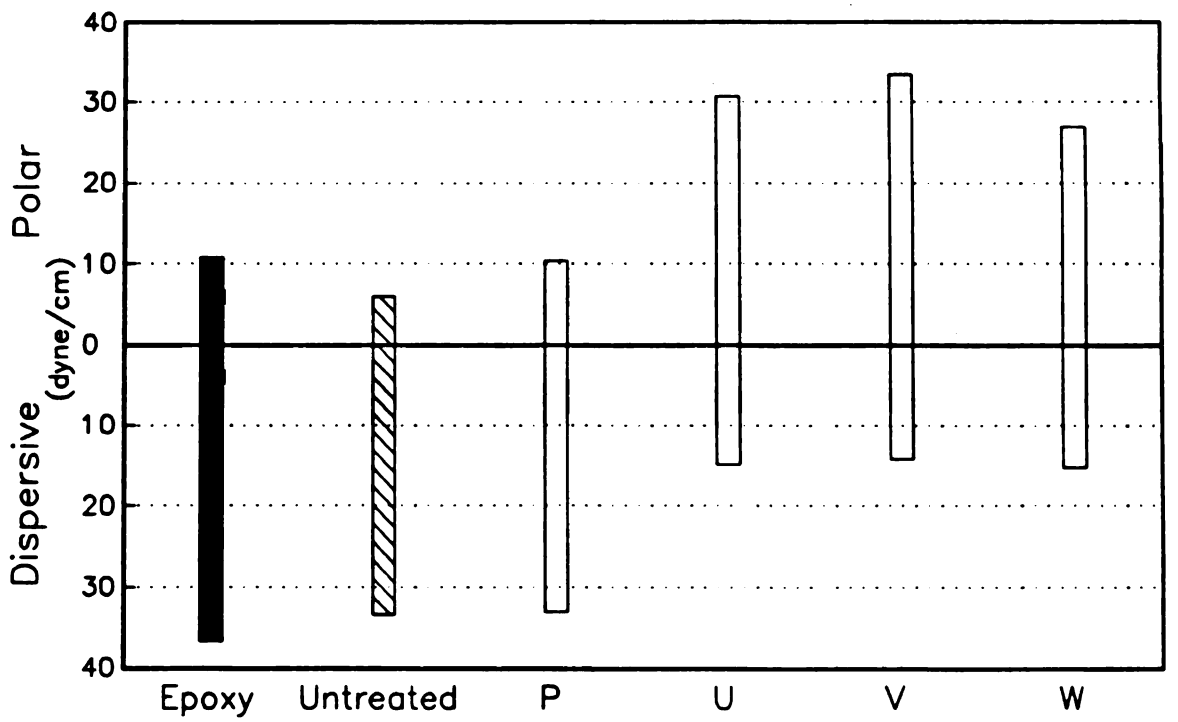

Figure 5.6 - Polar and dispersive components of surface energy for second set of plasma treated PBO fibers.

5.3.2 Polyethylene Corona and Plasma Treatments

In Chapter 3, the low adhesive properties of the Spectra-1000 polyethylene fibers were attributed to their poor surface energy compatibility with the liquid epoxy. In this section, effects of plasma and corona treatments on adhesive properties of Spectra-1000 fibers are examined.

Figure 5.7 compares the interfacial shear strength (ISS) of the plasma and corona treated Spectra-1000 fibers as determined by the droplet test. Both treatments produce about 300% increases in the ISS values compared to the untreated fibers. **Figure 5.8** compares the surface energy components of the fibers with a liquid epoxy. There is now a polar component of surface energy for the plasma treated fibers which is quite significant when compared with the untreated fibers. However, the surface energy of the corona treated fibers only exhibit an increase in the dispersive component of their surface

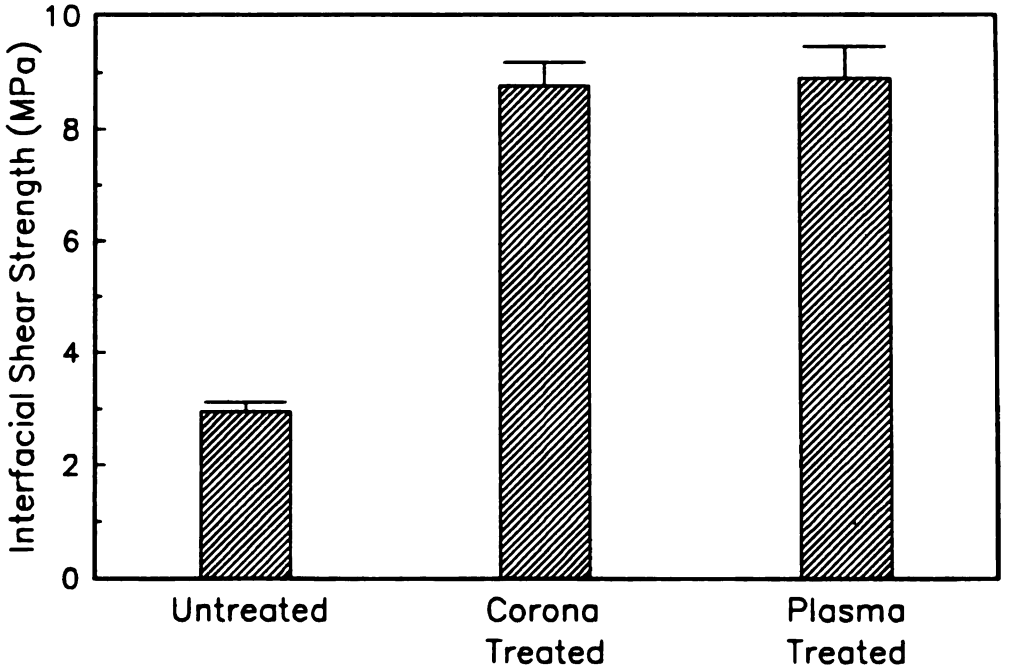

Figure 5.7 - Interfacial shear strength of untreated, corona treated and plasma treated Spectra-1000 polyethylene fibers as determined by the droplet test.

energy. **Figure 5.9** shows the atomic concentration of the examined fibers as determine by XPS. The oxygen contents of the corona and plasma treated fibers are about 4 to 5 times higher than the untreated fibers which suggests presence of new chemical functionalities on the treated fibers. These new chemical functionalities may provide sites for covalent chemical bonding between fiber and matrix molecules.

Figure 5.10 shows superimposed XPS narrow scans of oxygen signal for the plasma and corona treated fibers. Note that the plasma treated fibers show additional presence of oxygen signal in the 532-534 eV region. For the plasma treated fibers, their increased polar component of surface energy may be due to this additional type of oxygen. Other researchers have also reported the addition of new polar functional groups to the surface of plasma treated Spectra-1000 fibers (Morra *et al.* 1990, Nguyen *et al.* 1988). The increased number of polar functional groups on the plasma treated fibers increases their

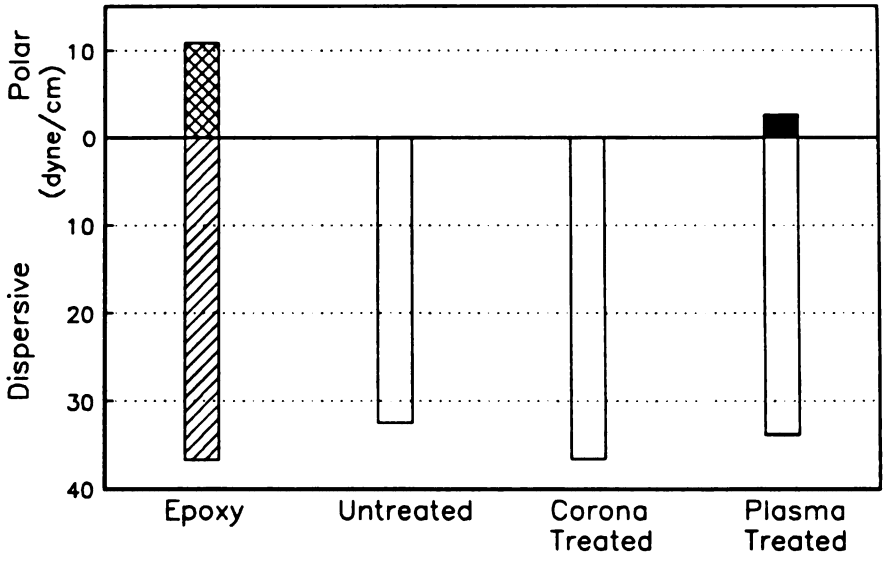

Figure 5.8 - Polar and dispersive components of surface energy for untreated, corona treated and plasma treated Spectra-1000 polyethylene fibers.

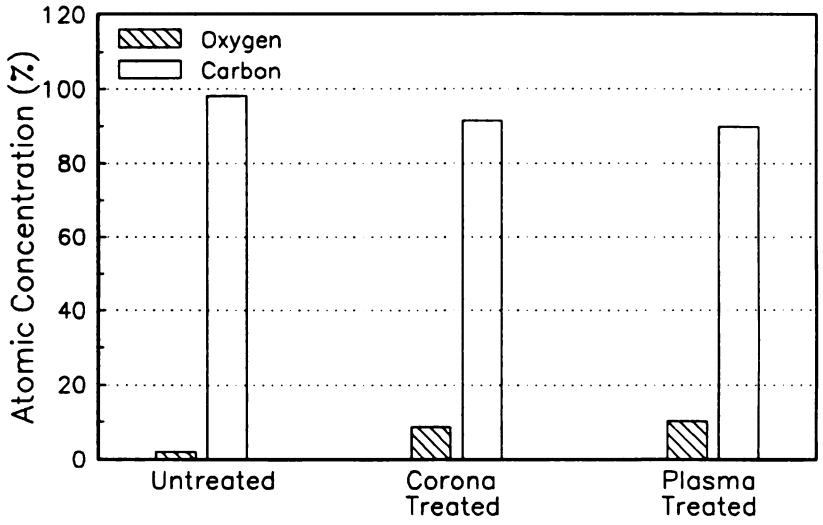

Figure 5.9 - XPS atomic concentrations of untreated, corona treated and plasma treated Spectra-1000 polyethylene fibers.

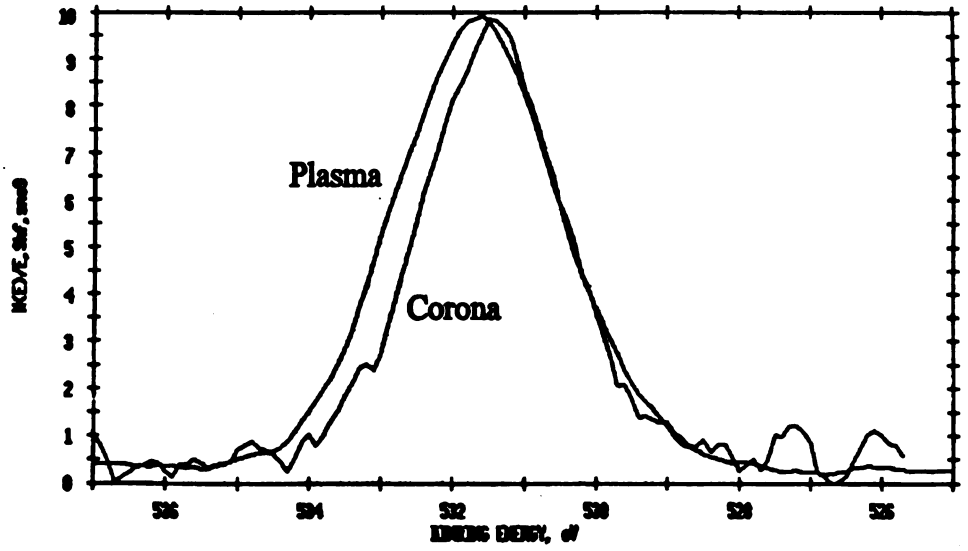

Figure 5.10 - Superimposed XPS signals of oxygen region for corona and plasma treated Spectra-1000 polyethylene fibers.

polar component of surface energy, thus, enhancing the fiber thermodynamic wetting with a liquid epoxy.

The previous observations indicate that despite the chemical and surface energy differences between the corona and plasma treated polyethylene fibers, their ISS increases are similar, suggesting an adhesion improvement mechanism that is only moderately dependent on the chemical modification of the fiber surfaces.

Etching of the polyethylene surfaces by oxygen plasma and corona treatments that could introduce mechanical interlocking adhesion mechanisms that can significantly enhance fiber-matrix mechanical interactions (Nguyen *et al.* 1988, Choe *et al.* 1990). **Figure 5.11** compares SEM micrographs of an untreated Spectra-1000 fiber with plasma and corona treated fibers. The untreated fiber has a relatively smooth surface with some surface crazing that is attributed to their manufacturing process (Postema *et al.* 1987). Conversely, both corona and plasma treated fibers exhibit rough and pitted surface topography. The plasma treated fibers show more surface etching than the corona treated fibers. Ladizesky *et al.* (1982) have reported that plasma treatments of ultra-high-modulus polyethylene fibers produces an etched surface, into which resin can penetrate to produce mechanical interlocking between fiber and resin. Untreated polyethylene fibers exhibited smooth surfaces and the locus of fiber-matrix failure is interfacial, whereas, the plasma treated fibers showed ruptures within the filaments during fiber-matrix separation. Therefore, the ISS increases of the corona and plasma treated Spectra-1000 fibers can be mainly attributed to the mechanical interlocking mechanism introduced by these treatments.

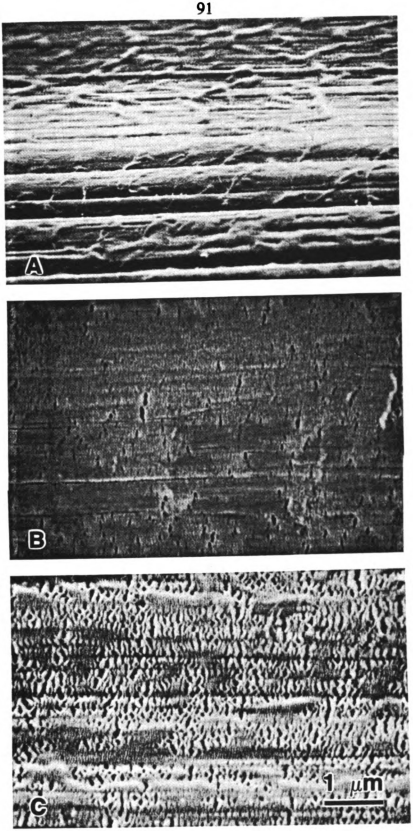

Figure 5.11 - SEM micrographs of (A) untreated, (B) corona treated, and (C) plasma treated Spectra-1000 polyethylene fibers.

5.4 CONCLUSIONS

- Plasma treatments of PBO fibers suggest that the etching removal of the weak surface layer of the fibers can significantly (~50%) enhance their interfacial shear strengths with an epoxy resin; however, once the fiber skin weak boundary layer is removed, the cohesive fibrillation of the fiber limits the interfacial load transfer of the PBO fibers. Plasma treatments can also significantly enhance the fiber wetting compatibility with liquid epoxy resins.
- Plasma and corona treatments of polyethylene fibers can increase their interfacial shear strengths by about 300%. The polyethylene-epoxy adhesion improvements are mainly due to mechanical interlocking mechanisms introduced by micropitting of the fiber surfaces. Wetting and chemical bonding properties the fiber-matrix interphase may also be enhanced by the plasma and corona treatments.

Results of this study demonstrate that plasma and corona surface treatment techniques can enhance wetting properties of polymer fiber, produce surface roughness, remove weak surface layers and introduce functional groups for covalent chemical bonding. Therefore, for high performance polymer fibers such as PBO, Spectra-1000, and Technora which exhibit adhesive surface limitations, plasma and corona surface treatments are viable approaches to overcome their respective surface limitations. However, once these surface limitations are overcome, the fiber lateral cohesive properties become the limiting factor.

CHAPTER 6

Sulfonation and Fluorination Treatments of Polymers

This chapter presents a discussion of fluorination and sulfonation polymer surface treatments. Through these chemical treatments, effects of fiber-matrix interphase chemistry on adhesive properties of high performance polymer fibers are examined. Examination of polymer sulfonation also helped to develop valuable insights on mass-transfer phenomena that may limit the extent of fiber structural modification (discussed in Chapter 8). The sulfonation portion of this study has been conducted in collaboration with Dr. Y. Muraoka (Muraoka *et al.* 1991[a,b,c], Kalantar *et al.* 1991[a]).

6.1 INTRODUCTION

Chemical modification of polymer surfaces by fluorination and/or sulfonation treatments have reported to enhance adhesive properties of the polymer substrate. Dixon *et al.* (1976[a],1977[a]) have reported improved adhesion and water transport properties for the fluorinated synthetic fibers such as polyesters, polyolefins, and polyacrylonitriles. Walles (1989) has also reported improved adhesion, wettability, abrasion resistance, vapor barrier properties of polymers through sulfonation surface treatments.

Figure 6.1 shows the general reaction schemes for the fluorination and sulfonation of hydrocarbons. Generally, fluorination of the organic polymers proceed to form a fluorinated carboxylated (acid fluorides, -FC=O) on the polymer substrate; these

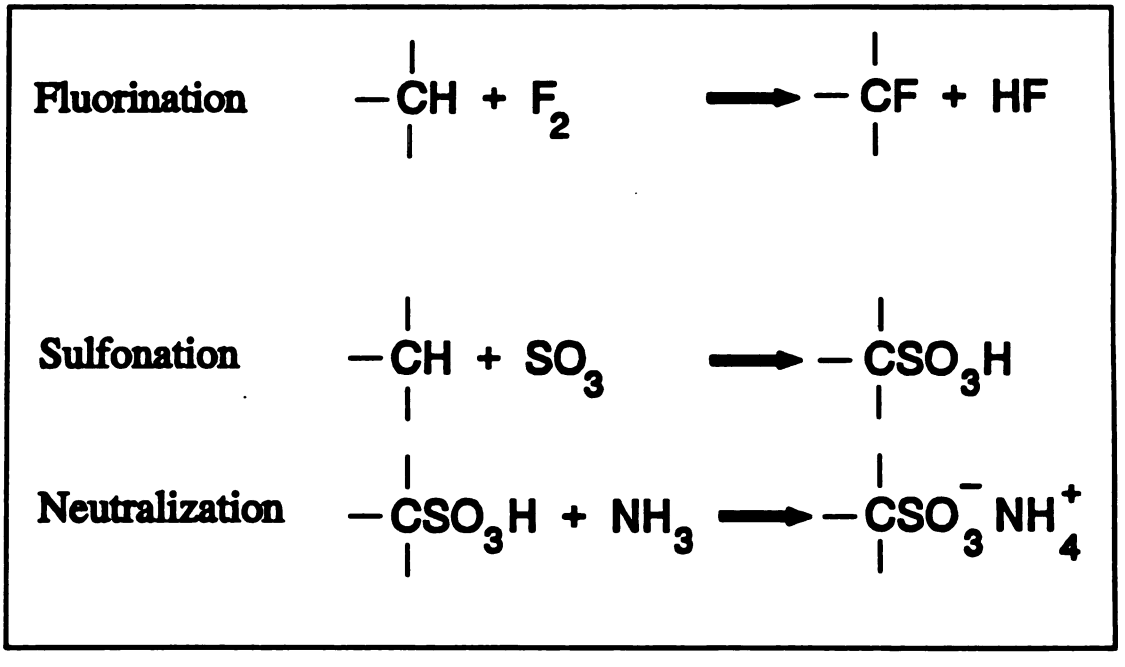

Figure 6.1 - General reaction schemes for fluorination and sulfonation of hydrocarbons.

carboxylate groups are only the ultimate reaction products, and are formed mainly after the polymer is exposed to oxygen (Dixon *et al.* 1976[b], 1977[b]). The fluorination reactions also produce the highly corrosive HF species as a byproduct of the fluorination reaction. Conversely, Sulfonation of polymers do not produce corrosive byproducts like the fluorination treatments. Furthermore, sulfonated polymers can be neutralized with any number of cations to produce a variety of barrier properties (Walles 1989). Muraoka *et al.* (1991[a]) have presented a discussion on the reaction schemes of polycarbonate sulfonation.

Fluorination of polymers is carried out by exposing the polymer surface to a fluorinating mixture comprising from 0.1 to 20 vol% elemental fluorine gas and the remainder a carrier gas such as argon or nitrogen. The level of oxygen in the fluorinating mixture is kept to a minimum since high levels of oxygen could be detrimental to the treatment (Dixon *et al.* 1977[b]).

Sulfonation of polymers can be carried out with sulfonating agents such as sulfur trioxide or its adduct with various organic compounds, sulfuric acid, pyrosulfuric acid (oleum), chlorosulfonic acid. Gas phase sulfonation of automobile gas tanks is a common industrial application of polymer sulfonation treatment and is conducted by exposing the polyethylene tank to ~10 vol% SO_3 in N_2 carrier gas for about 10 minutes, and then neutralizing with NH_3 gas.

Other types of chemical treatments to improve adhesive properties of high performance polymer fibers have also been reported. Mercx *et al.* (1990) have reported up to 70% fiber pull-out strength increases for the oxalylchloride surface treatment of

Twaron aramid fibers. Wu *et al.* (1986) have reported on incorporation of amine functional groups on the Kevlar-49 aramid fibers by bromination reactions followed by ammonolysis, nitration, and reduction. They report doubling of the T-peel strength and up to 50% interlaminar shear strength increases for the treated Kevlar-49 composite specimen. The improved fiber-matrix of these fiber treatments were accompanied by a shift of locus of failure from adhesive fiber failures to cohesive fiber fibrillation.

In this study, fluorination of Kevlar-49 fibers and sulfonation of Kevlar-49, Technora, and PBO fibers are investigated to assess the effects of fiber-matrix interphase chemistry on adhesive properties of high performance polymer. Sulfonation of polyethylene and polycarbonate sheets have also been examined to develop an understanding of mass-transfer phenomena that may be limiting the extent of polymer treatment penetrations.

6.2 EXPERIMENTAL

Polymer fibers examined in this study were Kevlar-49 (E.I. du Pont, Wilmington, DE) and Technora (Teijin Limited, Japan) aramid fibers, Spectra-1000 ultra-high-modulus polyethylene fibers (Allied Signal, Morristown, NJ), PBO (p-Phenylene Benzobis Oxazole) aromatic heterocyclic fibers (Dow Chemical, Midland, MI). The polycarbonate material was LEXAN 8050 sheets (thickness 20 mils, non-UV stabilized) supplied by General Electric Co. (Pittsfield, MA).

Three epoxy systems were used in this study,: DER331/MPDA/DETDA 175°C/3hr, DER331/MPDA 75°C/2h/125°C/2hr (fragmentation test) and DER331/MPDA RT/24hr/75°C/2hr/100°C/3hr (droplet test). Single fiber tensile strengths were measured

by ASTM D3379 tensile test. These and other experimental procedures are detailed in Chapter 2.

The fluorination treatments of Kevlar-49 fibers were done by Air Products and Chemicals Inc. (Emmaus, PA). Four proprietary gaseous surface treatments designated as 9629-80-A, 9629-80-B, 9629-80-C, and 9629-80-D (called treatments A, B, C, and D respectively) were provided. These treatments showed a progressive development of a green coloration. Fibers were shipped via express mail in nitrogen purged, heat sealed bags, and were cast in epoxy immediately after their arrival.

The sulfur trioxide used for the sulfonation treatments was supplied in the stable solid form (Aldrich Chemical, WI). The Freon solvent used for solution treatments was 1,1,2-trichloro-1,2,2-trifluoro ethane (Eastman Kodak, NY). A solution of SO_3 in the Freon solvent was used for the sulfonation medium. The SO_3/Freon solution was prepared by pouring Freon solvent into a one liter glass vessel precharged with solid SO_3 solid polymers. The solution was left for a week at ambient temperature to equilibrate SO_3 and Freon solubility. Glass-wool was inserted into the bottle to prevent the polymer sample from coming into contact with solid SO_3 material at the bottom of the flask. The sulfonation was carried out by placing materials into the SO_3/Freon flask. The flask was shaken by hand occasionally.

Three treatment temperatures nominally called warm, ambient, and chilled were examined. For the chilled sulfonation, the flask was placed in a freezer maintained at $-17 \pm 2°C$. Ambient temperatures were maintained at $22 \pm 3°C$. For the warm sulfonation, the flask was place in a convection oven maintained at $37 \pm 3°C$.

Determination of the SO_3 concentration in the solution was carried out by extracting SO_3 from the Freon solvent into water and then titrating with a NaOH solution. The equilibrium SO_3 solution was determined to be 0.012 N for the chilled solution, 0.037 N for the ambient temperature solution, and 0.052 N for the warm solution. For the polycarbonate sulfonation all three treatment temperatures were examined, but for the polyethylene sulfonation only the ambient treatment temperature was examined.

For the polyethylene samples, color changes from an initial bright white to brown were observed as the sulfonation reaction proceeded. For polycarbonate and aramid samples no color changes were observed during the sulfonation.

To assess the effects of neutralization process on the polycarbonate sulfonation, samples were neutralized either with 1 N aqueous NH_4OH solution for 30 minutes, or 1 N $AgNO_3$ for 1 hour, or left unneutralized by rinsing only with Freon or water. For the unneutralized polycarbonate samples, a thin brown film was observed to form when samples were exposed to ambient air. This brown liquid film is probably due to environmental moisture that reacts with the excess SO_3 on the treated surfaces. The liquid film was less present on the chilled sulfonated samples and more on the warm sulfonated samples.

For the sulfonation treatment of the fibers, fiber were first dried at 125°C for 4 hours to remove their absorbed water. The fibers were then inserted in 0.0003N solution of SO_3 in Freon for 30 hours. Fibers were dried at ambient conditions for 1 hour and then cast in the 75°C/2hr/125°C/2hr epoxy system.

Sulfonation penetration of treated sample were determined by an AES technique.

Details of the sample preparation technique for the AES analysis are presented in Appendix C (Kalantar *et al.* 1990[c]). In summary, the sample is initially coated with a thick gold layer (~50 nm) and then the analysis surface is shaved with a diamond knife to prepare a smooth and clean surface surrounded by gold boundaries. The analysis surface is recoated with a thin gold layer (~2 nm) which helps to avoid sample charging but is thin enough to allow the emitted Auger electrons from the material below the gold layer to be detected.

All AES analyses were carried out using a Perkin-Elmer PHI 660 Scanning Auger Microprobe. Samples were analyzed at 10000 to 30000× magnifications. AES beam conditions for analysis were 1.5 to 3 nA beam current and 3 to 10 kV beam energy. The sulfur AES signal intensity was monitored at each point on the sample from the signal peak height and was plotted in line-scan fashion. A short (>50 nm) ion beam sputtering of the treated surfaces was conducted to remove the surface contaminants, but longer sputtering times were avoided because high dose sputtering of polymers would preferentially remove the non-carbon (sulfur and oxygen here) surface elements and would produce a carbonized surface composition (see Chapter 7).

The surface compositions of the samples were examined by XPS. Sample surface texture before and after treatments were examined by SEM, operating at 15.0 kV beam energy and 5000× magnification.

6.3 RESULTS AND DISCUSSION

The results of the fluorination and sulfonation treatments are discussed separately to provide an exclusive discussion for each type of chemical treatment.

6.3.1 Aramid Fluorination

Table 6.1 shows XPS atomic composition of the fluorinated Kevlar-49 fibers. Note that the untreated Kevlar-49 fibers exhibit an oxidized surface composition as evidenced by their large oxygen content compared to their monomer stoichiometry. Treatments **A**, **C**, and **D** have resulted in similar levels of fluorination (~ 22 atomic%), while, treatment **B** has resulted in higher fluorine content (~32%) and lower oxygen content (~12%) than the other treatments. The atomic% ratios of oxygen/carbon, nitrogen/carbon, and fluorine/carbon are plotted in the **Figure 6.2**. Treatments **A**, **C**, and **D** have resulted in O/C ratios higher than the untreated fibers which suggests

Table 6.1 - XPS atomic composition of fluorinated Kevlar-49 aramid fibers.

Sample	C%	O%	N%	F%
Theoretical	78	11	11	-
Untreated	73	20	7.4	-
Treatment A	52	20	5.0	23
Treatment B	51	12	4.7	32
Treatment C	53	20	5.2	22
Treatment D	51	19	4.5	25

~4% relative error bar for each experimental datum.

formation of acid fluorides on the treated fibers. Treatment B, however, shows O/C ratio lower than untreated fibers which may be attributed to removal of the original oxidized layer of the aramid substrate by the fluorination treatment.

Tensile strengths of the fluorinated fibers also suggest that etching alteration of the aramid surfaces by the treatment B. **Figure 6.3** compares tensile strength and interfacial shear strength (fragmentation test) of the fluorinated Kevlar-49 fibers with the untreated fiber. Tensile strength of treatment B fibers is about 10% lower than other fibers which confirms substantial fiber chain scission has occurred by this treatment. The interfacial shear strengths of the fluorinated fibers, however, is unaffected by the treatments.

Figure 6.4 shows TEM micrographs of fiber-matrix interface for the treatment D. The micrograph shows improved fiber-matrix adhesion but the interfacial fibrillation have been shifted toward the fiber interior. Other fluorination treatments show similar

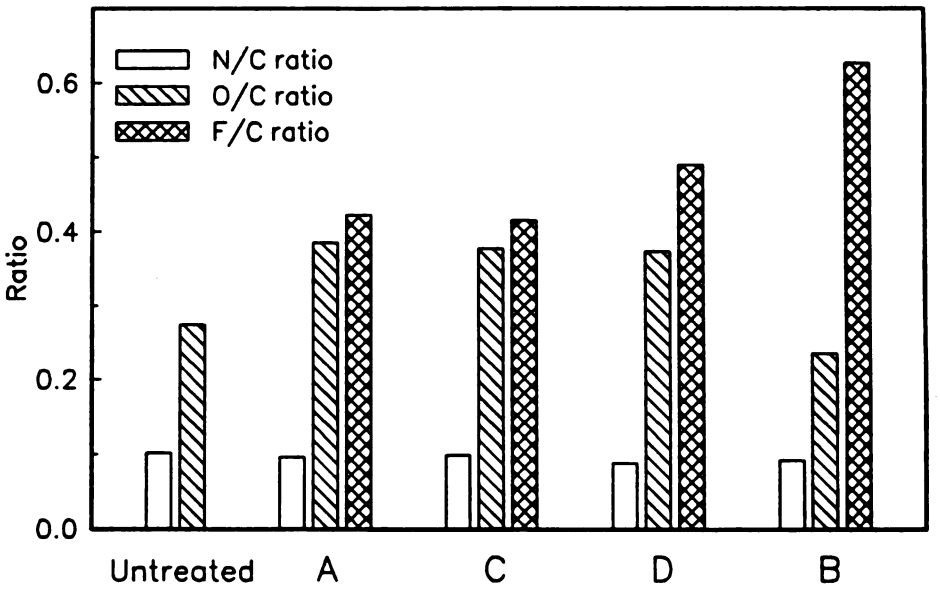

Figure 6.2 - Ratios of atomic% of nitrogen, oxygen, and fluorine over carbon, for the fluorinated Kevlar-49 aramid fibers.

improved adhesion to the treated aramid fiber surfaces. The lack of increase in the aramid-epoxy interfacial shear strength despite the improved fiber-matrix adhesion suggests that the adhesive properties of the aramid fibers are still limited by the cohesive failures of the fiber rather than the extent of fiber-matrix interfacial bonding.

SEM micrographs of untreated and treatment B fiber are shown in **Figure 6.5**. The treated fiber shows smoother surface texture (**Figure 6.5B**) than the untreated fibers suggesting morphological modification of the fiber surface by the treatment. The other fluorinated fibers do not show any discernable surface topography difference form the untreated fibers.

Therefore, fluorination of Kevlar-49 aramid fibers can increase the level of fiber-matrix adhesion, but the aramid-epoxy interfacial shear strength is not affected by this enhanced fiber-matrix adhesion.

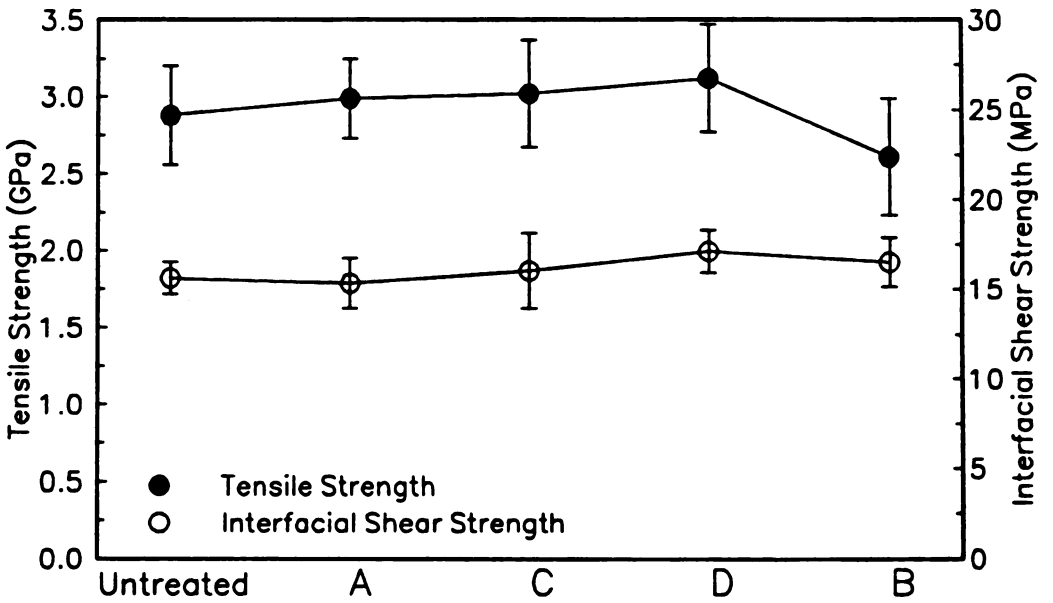

Figure 6.3 - Tensile strength and interfacial shear strength (fragmentation test) of the fluorinated and untreated Kevlar-49 aramid fibers.

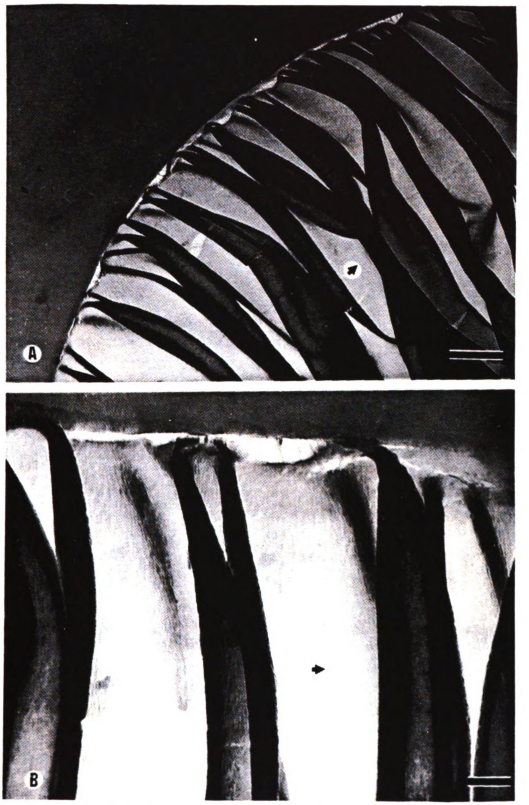

Figure 6.4 - TEM micrographs of a radially sectioned fluorinated Kevlar-49 aramid fiber (treatment D). (A) bar = 500 nm (B) bar = 100 nm

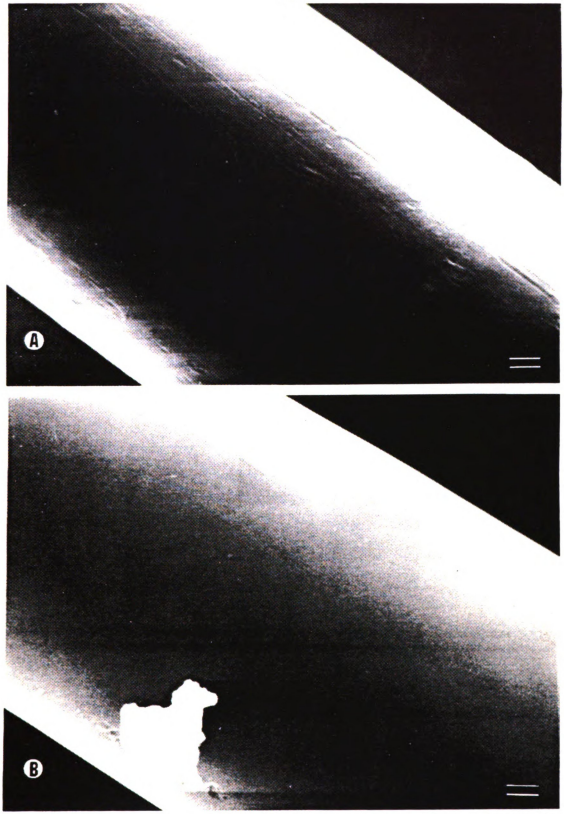

Figure 6.5 - SEM micrographs of (A) untreated and (B) treatment B fluorinated Kevlar-49 fibers. bar = 1 μm

6.3.2 Sulfonation of High Performance Polymer Fibers

Figure 6.6 show the relative ratios of tensile strength and interfacial shear strength (fragmentation test) of Kevlar-49, Technora, and PBO fibers. All of the sulfonated fibers show some tensile strength reduction. Sulfonated Technora and PBO fibers show slight interfacial shear strength increases, whereas, Kevlar-49 fibers ISS are unchanged. **Figure 6.7** shows TEM micrographs of radially sectioned, sulfonated Kevlar-49 fiber. The micrographs show that a surface layer of the fiber is adhering to the epoxy and cohesive separation is taking place within the fiber. Similarly, other sulfonated high performance polymer fibers show that the sulfonated fiber exterior adhering to the matrix and the locus of failure shifting toward the fiber interior. In Chapter 3 and 5, it was

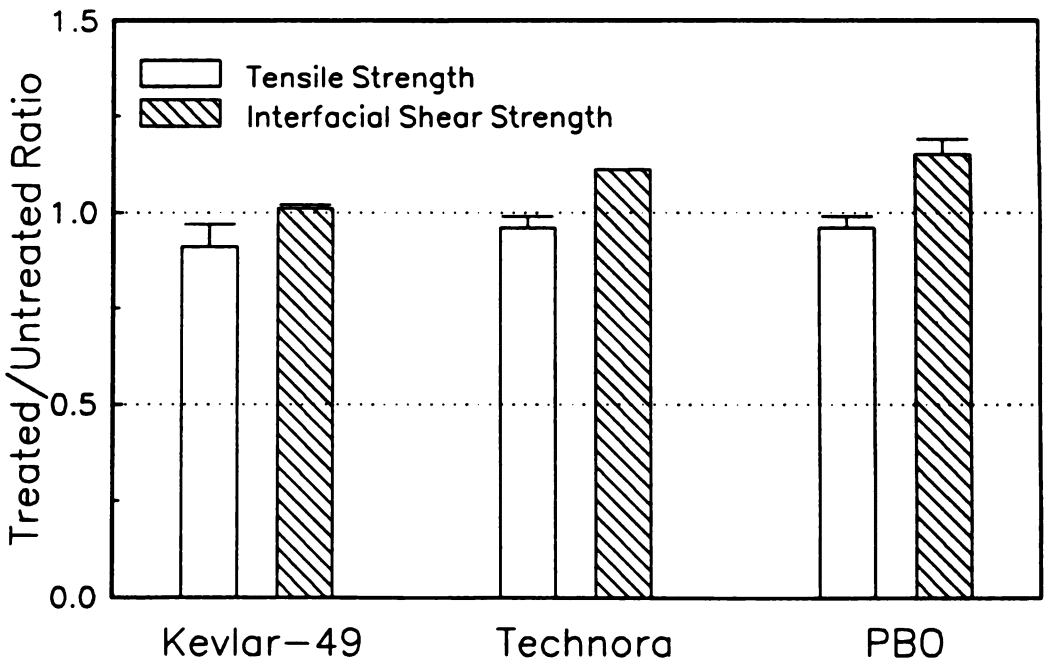

Figure 6.6 - Relative ratios of tensile strength and interfacial shear strength of sulfonated fibers compared to their untreated values.

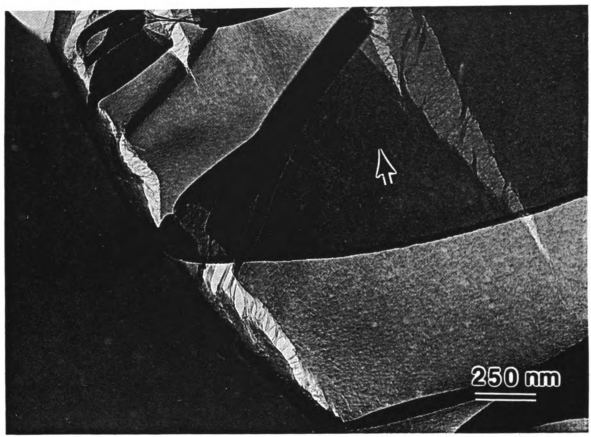

Figure 6.7 - TEM micrographs of a radially sectioned, sulfonated Kevlar-49 aramid fiber showing extensive fiber cohesive failure.

demonstrated that the adhesive properties of high performance polymer fibers are ultimately limited by the fiber cohesive fibrillation, however, epoxy adhesion of Technora and PBO fibers are further limited by other surface limitations. Both Technora and PBO fibers have less that optimum surface energy compatibility with liquid epoxy. Furthermore, PBO fibers have a weak surface boundary layer that separates within the fiber during interfacial shear failure. The ISS increases of sulfonated Technora and PBO fibers are probably due to reduction of their respective surface limitations which enhance the fiber-matrix load transfer efficiency.

TEM analyses of sulfonated high performance fibers also suggested that sulfur penetration is limited to only a few thousand angstroms into the fiber structure. Sulfonation of polycarbonate sheets is examined next to help to develop an understanding of these diffusion-limited polymer treatments.

6.3.3 Polycarbonate Sulfonation

Table 6.2 shows the XPS atomic composition of the sulfonated polycarbonate samples. Some samples exhibit trace amounts of iron which are probably deposited during the manufacturing of the sheets. The amount of sulfur on the polycarbonate samples decreases after water rinse, $AgNO_3$, or NH_4OH neutralization steps. In particular, the NH_4OH neutralization reduces the sulfur content to trace amounts. The sulfur content reduction during the NH_4OH neutralization may be due to dissolution of the sulfonated species (NH_4OH is a solvent for the polycarbonate), or the basic attack of the sulfonated functionalities.

AES analysis of polycarbonate samples for both solution and gas phase sulfonation treatments were conducted. **Figure 6.8A** shows a low magnification view of an analysis surface. The surface is cut through the thickness of the treated sheet and the sulfonated regions are at the left and right edges of the analysis surface. **Figure 6.8B** shows the line-scan spectrum for a 1-hour gas phase treated and NH_4OH neutralized polycarbonate sample. The line-scan is superimposed on the SEM image of the sample. The thickness of the sulfonated region appears to be about 1.5 microns which is similar to the values obtained for the 1-hour solution phase sulfonation. The SEM image shows a bright structurally modified region about 1 micron thick which is thinner than the sulfonated

Table 6.2 - XPS atomic composition of polycarbonate surfaces.

Sample	C%	O%	S%	N%	Other
Theoretical	84	16			
Untreated					Fe%
As Received	78 ± 1	20 ± 1		0.8 ± 0.2	0.9 ± 0.4
Freon washed	83 ± 1	17 ± 1		none	none
Freon rinsed					
Solution rxn[1]	63 ± 2	31 ± 2	5.8 ± 0.6		
Water rinsed					
Solution rxn[1]	74 ± 1	24 ± 1	2.6 ± 0.1		
$AgNO_3$ rinsed					Ag%
Solution rxn[2]	63	28	4.6	0.6	3.2
NH_4OH rinsed					Fe%
Solution rxn[3]	72 ± 2	23 ± 1	1.3 ± 0.3	2.9 ± 0.5	0.6 ± 0.3
Gaseous rxn[4]	77 ± 1	20 ± 1	0.6 ± 0.2	2.0 ± 0.4	0.8 ± 0.4

[1] combination of 20, 45 hours, and 3, 7 days data.
[2] 20 hours solution sulfonation followed by 2 hours in 1N $AgNO_3$ solution, and 1 hour water rinse.
[3] combination of three 30 minutes and three 2 hours data.
[4] combination of three 10 minutes and three 1 hour data.

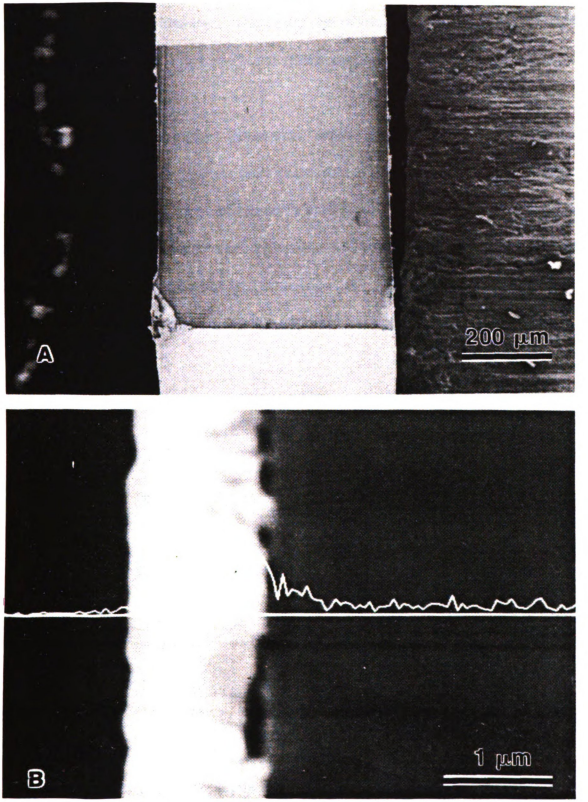

Figure 6.8 - AES analysis of sulfonated polycarbonate. (A) a low magnification view of an analysis surface. (B) line-scan for a 1-hour gas phase sulfonated sample.

region indicated by the line-scan. This bright region was observed for all other NH_4OH neutralized samples; the Freon and water rinsed samples did not show such structurally modified regions.

Figure 6.9 shows sulfur penetration depths for solution phase sulfonated polycarbonate. The figure covers time spans from 10 minutes to a week of treatment times for the three sulfonation temperatures examined. Penetration depths are plotted versus square root of reaction time to assess concentration dependency of sulfonation penetration diffusion coefficient (see Appendix D). The chilled (-17°C) sulfonated samples show a constant slope for the examined sulfonation times which suggests a

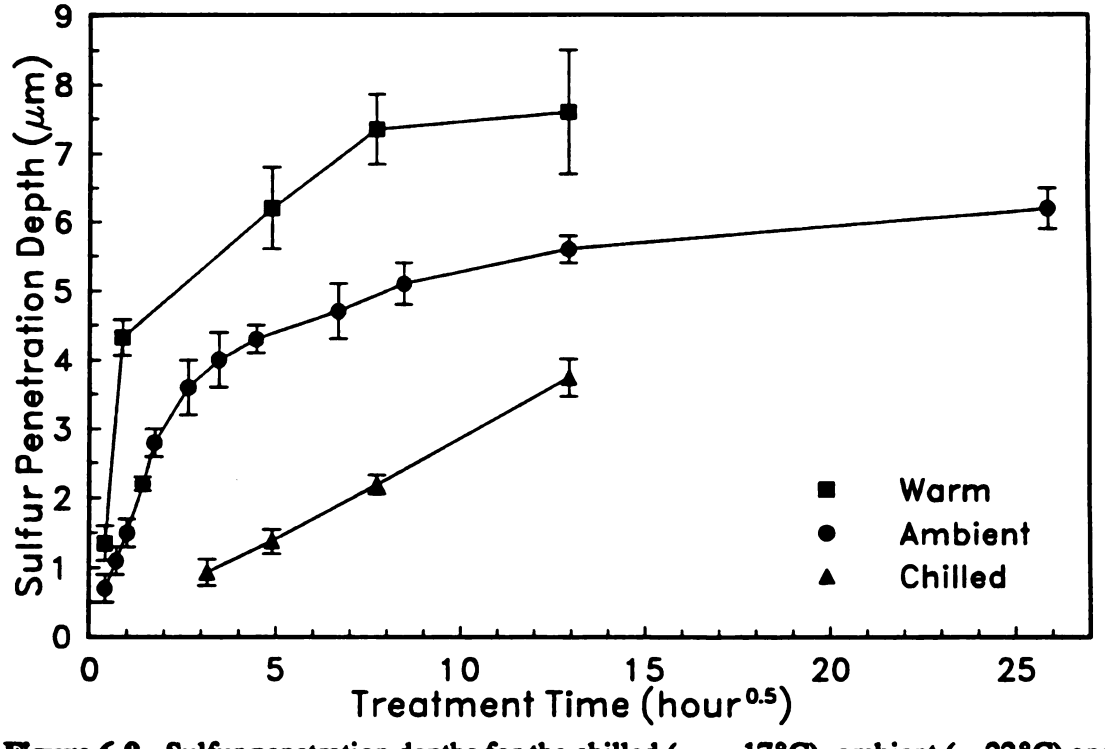

Figure 6.9 - Sulfur penetration depths for the chilled (~ −17°C), ambient (~22°C) and warm (~37°C) solution phase sulfonated polycarbonate, plotted verses square root of time (determined by AES line-scans).

diffusion coefficient that is independent of the extent of concentration variation (see equation D.8). For the ambient (22°C) and warm (37°C) sulfonation, however, the profiles show that after about 3.5 μm of sulfonation penetration the diffusion coefficient becomes highly concentration dependent. These observations suggest that for the ambient and warm sulfonation of polycarbonate, the sulfur penetration into a polycarbonate film is limited by the formation of a barrier layer of sulfonated material that reduce the diffusion coefficient and thus penetration depth of the sulfonation treatment.

Figure 6.10 shows SEM micrographs of untreated and sulfonated polycarbonate surfaces. The untreated polycarbonate sample is essentially flat and featureless (**Figure 6.10A**). The 1-hour gas phase treated and NH_4OH neutralized sample exhibits an etched surface with many pitted and flaked regions (**Figure 6.10B**). The 2-hour solution treated and NH_4OH neutralized polycarbonate appears to have pock marked features and many specks of 200 nm particles (**Figure 6.10C**). These SEM micrographs suggests the solution treatments can flush materials from the surface producing a more smooth topography than the gas phase sulfonation treatments.

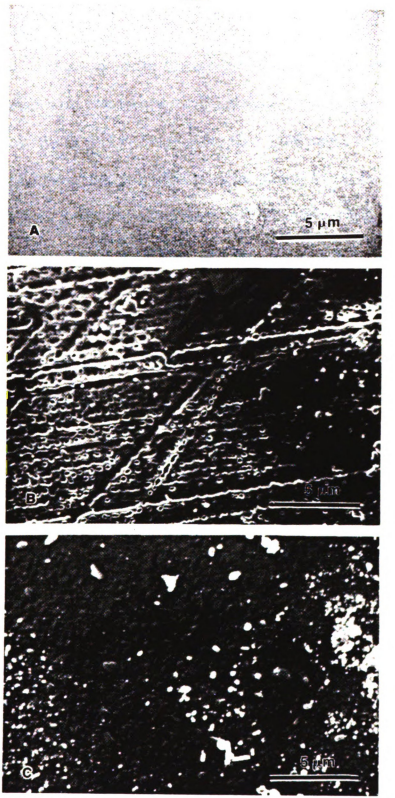

Figure 6.10 - SEM micrographs of sulfonated and untreated polycarbonate surfaces. (A) Untreated sample, (B) 1-hour gas phase sulfonated sample. (C) 2-hour solution phase treated samples.

6.3.4 Polyethylene Sulfonation

In Chapter 5, plasma and corona treatments of Spectra-1000 ultra-high-molecular-weight polyethylene fibers showed about 350% increase in the interfacial shear strength (ISS) of the treated fibers. ISS increases of the plasma and corona treated Spectra-1000 fibers were mainly attributed to a combination of the surface etching that could introduce mechanical interlocking adhesion mechanisms and improved wetting properties of the fibers with the epoxy resin. In this section, ambient sulfonation treatments of untreated, corona, and plasma treated Spectra-1000 polyethylene fibers are examined to assess the effects further chemical alterations of these fibers.

Figures 6.11, 6.12, and 6.13 show XPS atomic compositions of the sulfonated Spectra-1000 polyethylene fibers. The sulfur and oxygen contents increases are due to SO_3 addition and nitrogen is the result of the NH_4OH neutralization step. Note that atomic composition of plasma pretreated fibers reaches its plateau sooner than the corona pretreated fibers which in turn plateaus sooner than the unpretreated fibers. This trend is noticed more clearly in the plot of sulfur atomic% shown in **Figure 6.14**. The initial (5 min. sulfonation) increase in sulfur contents of plasma-pretreated, corona-pretreated, and unpretreated sulfonated fibers are 5.10, 2.81, and 1.15% respectively. All sulfonated fibers reach a ~8% sulfur content after about 1 hour of sulfonation.

The sulfonation rate dependency of the polyethylene fibers on the surface pretreatments suggests that the etching or conditioning of the polyethylene surface makes them more accessible for the sulfonation reactions to occur. Spectra-1000 fibers are made from ultra-high-molecular-weight polyethylene and are highly crystalline. It is

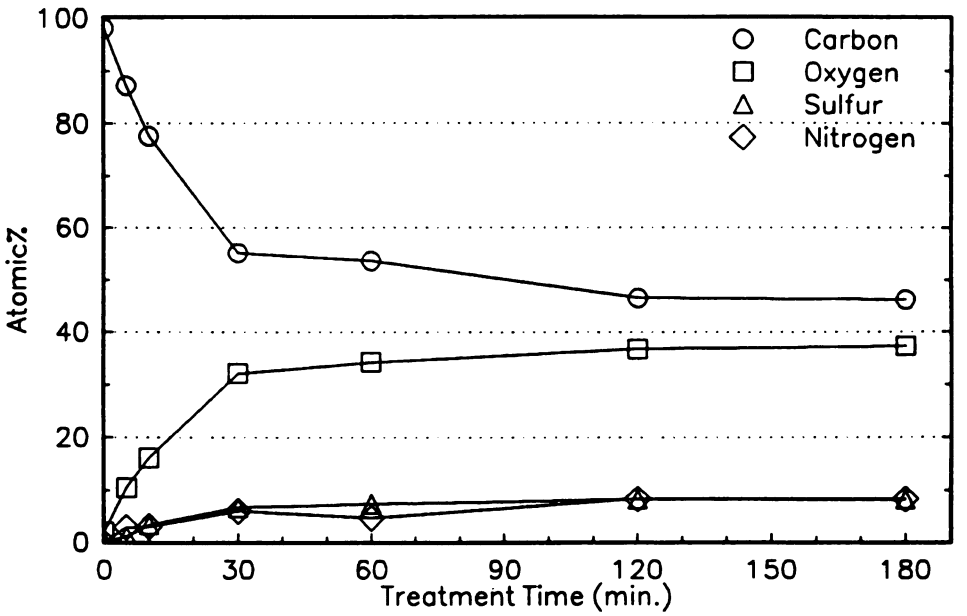

Figure 6.11 - XPS atomic composition of sulfonated Spectra-1000 (without pretreatment) polyethylene fibers.

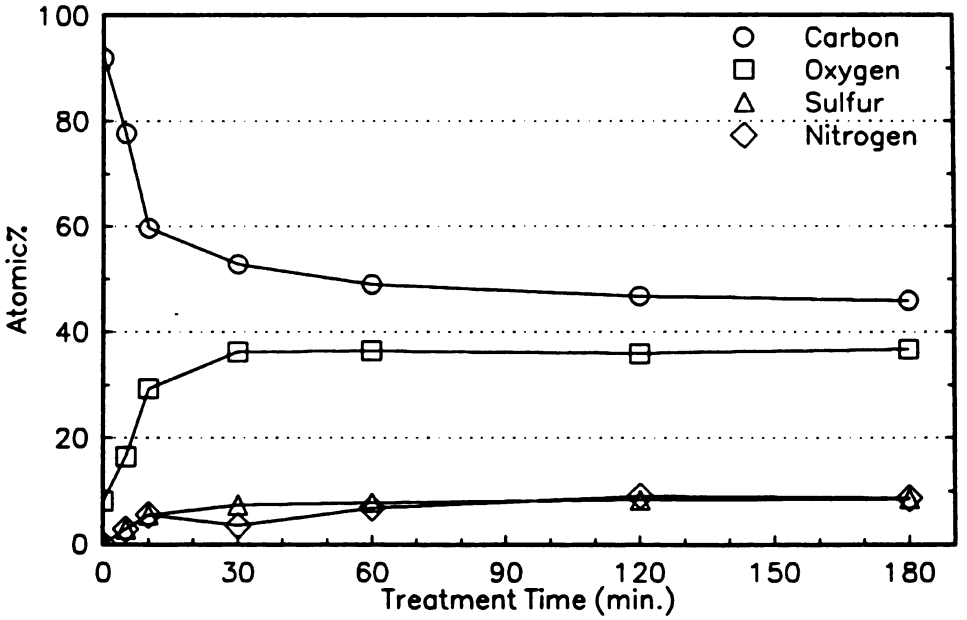

Figure 6.12 - XPS atomic composition of sulfonated Spectra-1000 (Corona pretreated) spectra fibers.

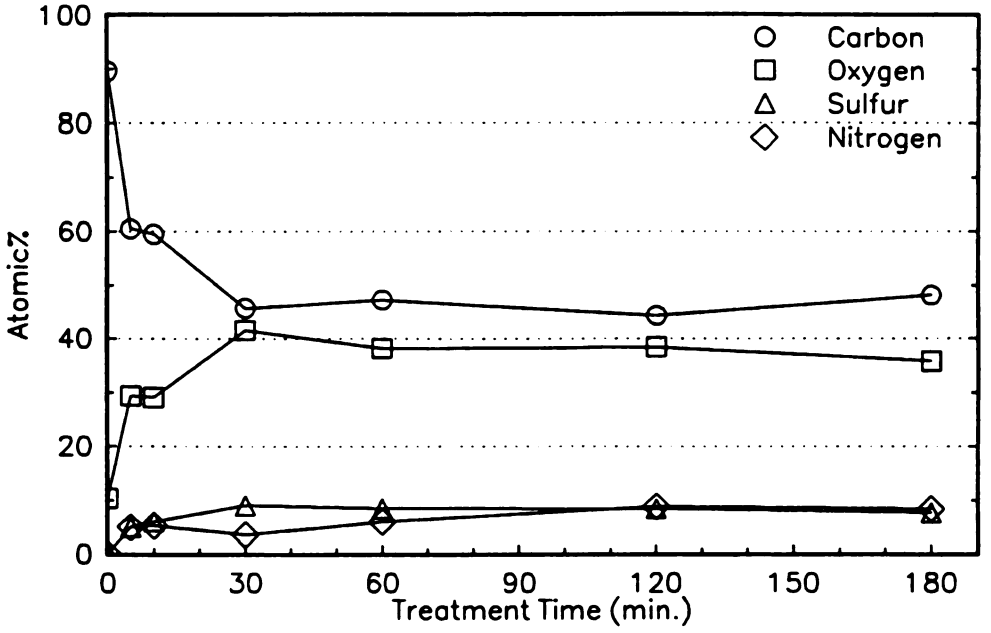

Figure 6.13 - XPS atomic composition of sulfonated Spectra-1000 (Plasma pretreated) polyethylene fibers.

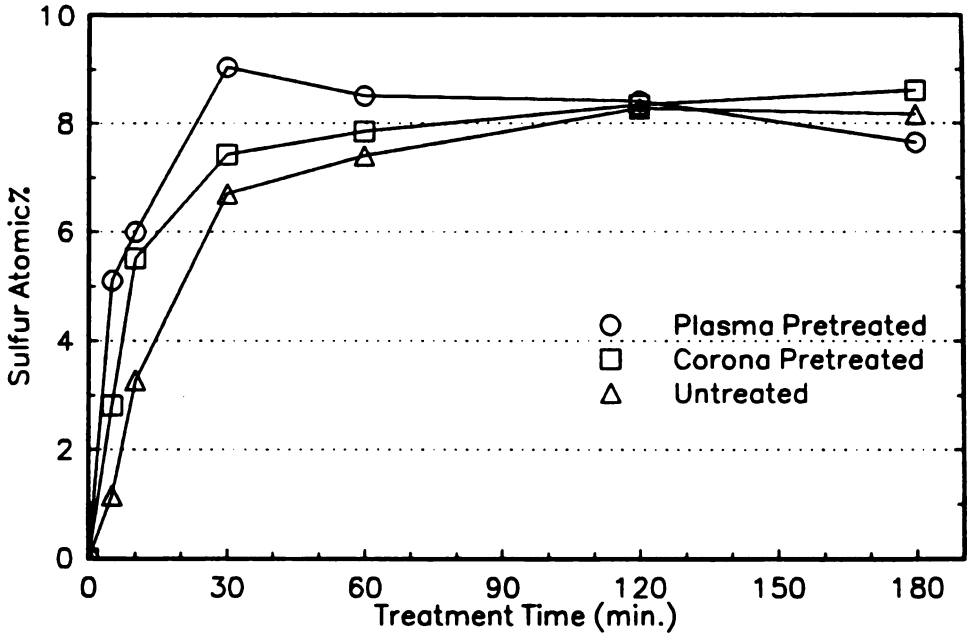

Figure 6.14 - Sulfur atomic% of sulfonated un-pretreated, corona pretreated, and plasma pretreated Spectra-1000 polyethylene fibers.

demonstrated (next) that lower molecular weight polyethylene exhibits much higher sulfonation penetration rate than the higher molecular weight polymer. Therefore, any mechanism such as plasma etching that can reduce the molecular weight or crystallinity of the polyethylene polymer should increase their sulfonation rate.

AES examinations of sulfonated polyethylene fibers suggest that the molecular weight or crystallinity of the polyethylene polymer affects their sulfonation rate. AES line-scan of sulfonation penetration depth for the unpretreated Spectra-1000 fibers measures only 0.9 ± 0.2 after 1-hour, and 1.2 ± 0.2 μm after 3-hour sulfonation. However, sulfonation of high density polyethylene produced over 15 μm of sulfur penetration after only 10 to 15 minutes of SO_3 exposure (see Appendix E). Similar observations have been reported by Holden *et al.* (1985). Their study of gas barrier properties of highly oriented polyethylene films has shown that the solubility of gases are proportional to the amorphous volume fraction of the films. They showed that increasing the crystallinity of the films significantly reduces the diffusion coefficient of the gases. This effect is particularly marked for the larger gas molecules.

The previous observations on molecular-weight effects on polyethylene sulfonation penetration also tend to negate the possibility of presence of a low molecular weight layer on the fiber surfaces. If a low molecular-weight layer is present on the unpretreated fibers then they should exhibit faster surface sulfonation than the "cleaned" plasma and corona pretreated samples; this is not observed experimentally. In addition, the polyethylene fiber had undergone soxhlet extractions in ethanol for 24 hours and fibers were sulfonated in a Freon solvent. Both ethanol and Freon could remove such weakly

bonded low molecular weight surface polymers.

Figure 6.15 shows tensile property changes of sulfonated Spectra-1000 polyethylene fibers compared to their initial pretreated values. The sulfonated fibers show much greater tensile strength reductions than modulus reductions. Introduction of new surface defects by the sulfonation treatments can significantly affect tensile strength of the fibers since tensile strengths are defect controlled. Whereas, tensile modulus is determined by bulk properties, and its reduction can be accounted by the reduced effective cross-sectional area of the fiber as the result of the sulfonation ($\sim 1\ \mu m$ sulfur penetration).

Figure 6.16 compares the surface energy of the sulfonated Spectra-1000 fibers with epoxy resin. For all fibers, the polar components of surface energy increases as the sulfonation treatment times are increased. Again the plasma pretreated fiber shows a faster rate of polar component increases than the corona pretreated and unpretreated

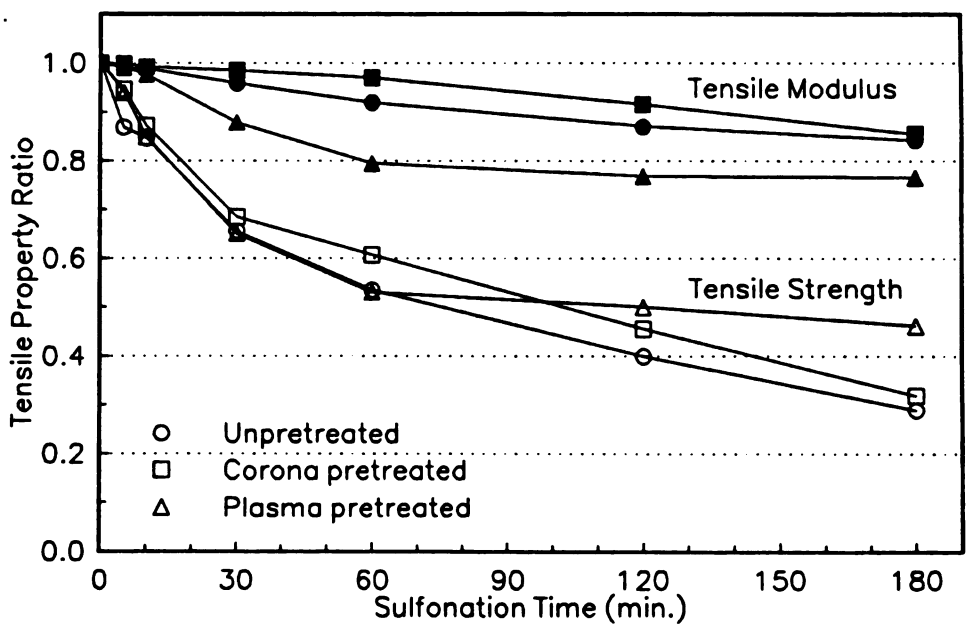

Figure 6.15 - Tensile strength and modulus changes of sulfonated fibers relative to their untreated values.

fibers.

Figure 6.17 plots fiber surface sulfur concentration versus the polar component of surface energy, showing increasing polar surface energy as SO_3 functional groups become incorporated into the treated surfaces. Note that the plasma pretreated fibers exhibit higher polar surface energy component at any given sulfur concentration than the un-pretreated or the corona pretreated fibers. In Chapter 5 it was demonstrated that the plasma treated polyethylene fibers have a polar component of surface energy that is absent in the untreated and corona treated fiber (**Figure 5.8**). Evidently, the initial polar functionalities of the plasma treated fibers are retained after the sulfonation treatment resulting in their increased polar component of surface energy.

Figure 6.18 shows SEM micrographs of epoxy droplets on untreated, plasma pretreated/5 minutes sulfonated, and plasma pretreated/3 hours sulfonated, polyethylene fibers. The meniscus of the epoxy on these fibers show a reducing contact angle as sulfonation time increases indicating in improved fiber-matrix wetting.

Figure 6.19 shows the percent increase in the interfacial shear strength (ISS) of the sulfonate Spectra-1000 polyethylene fibers relative to their pretreated and unpretreated samples. Sulfonated fibers exhibit up to 450% ISS increases which are much higher than those obtained by corona or plasma treatments alone (~300%). In Chapter 7, it is demonstrated that ion implantation of Spectra-1000 polyethylene fibers can cross-link the fiber surface structure and increase its ISS values by about 350% before the locus of shear failure shifts completely into the fiber interior. Therefore, the ISS increases beyond 350% are likely due to mechanisms other than fiber property modification. For

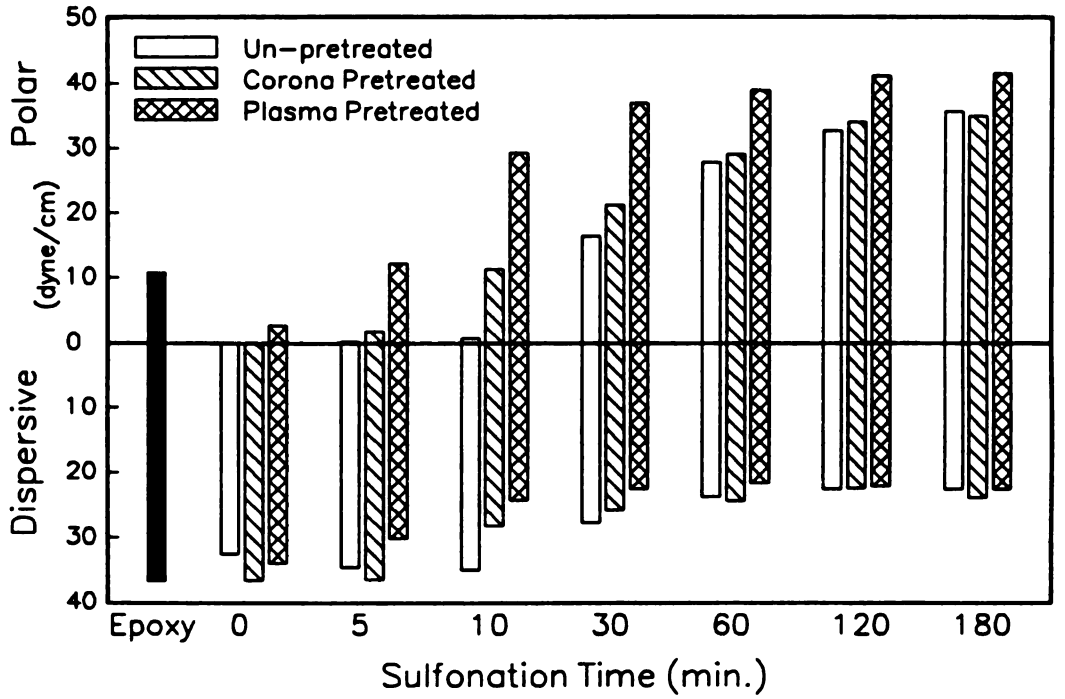

Figure 6.16 - Polar and dispersive components of surface energy for un-pretreated, corona pretreated, and plasma pretreated sulfonated Spectra-1000 polyethylene fibers.

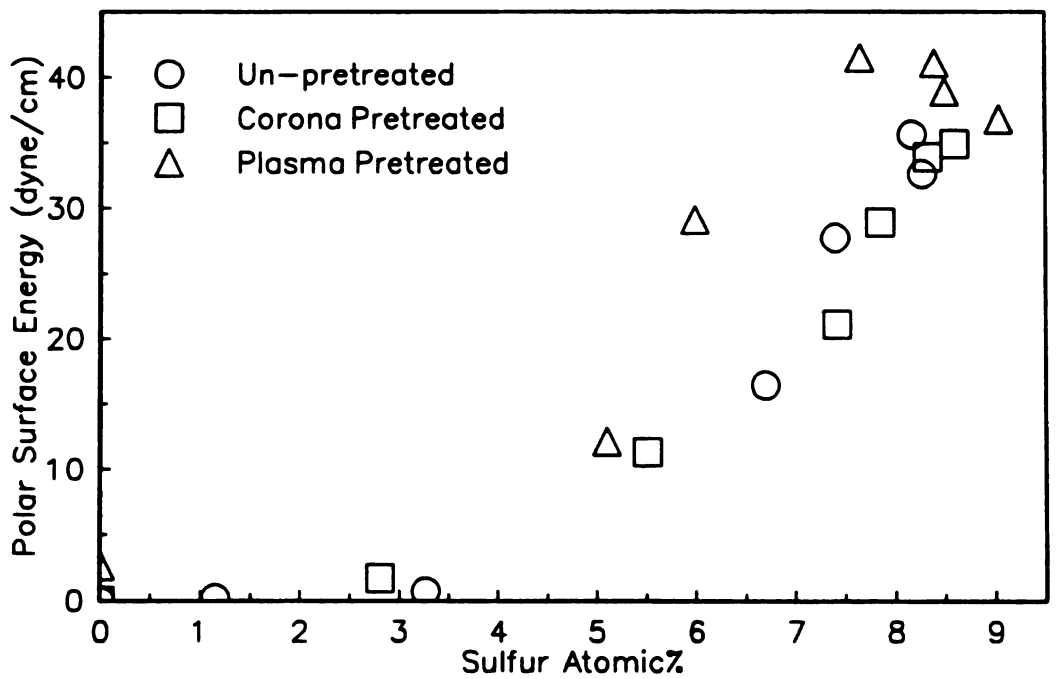

Figure 6.17 - Plot of sulfur atomic% for un-pretreated, corona pretreated, and plasma pretreated sulfonated Spectra-1000 polyethylene fibers versus their polar components of surface energy.

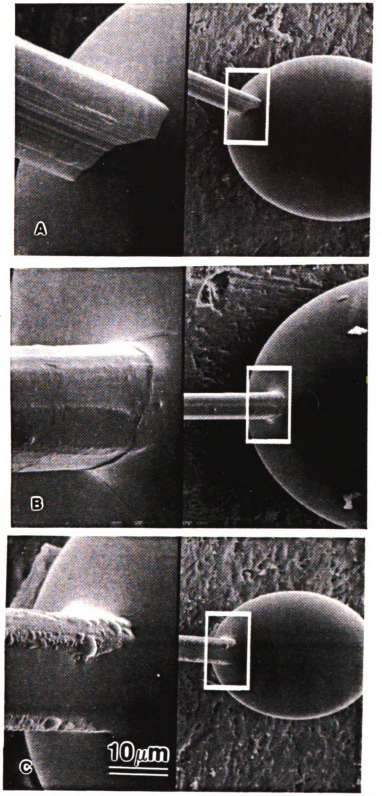

Figure 6.18 - SEM micrographs of epoxy droplets on (A) untreated, (B) plasma pretreated/5 minutes sulfonated, and (C) plasma pretreated/3 hours sulfonated, Spectra-1000 polyethylene fibers.

the >30 minutes sulfonated fibers the sulfur composition is about 8 atomic%. These highly sulfonated surfaces could alter the chemistry of the fiber-matrix interphase resulting in a brittle and increased modulus fiber-matrix interphase. Rao *et al.* (1991[a]) have shown that increasing modulus of a fiber-matrix interphase increases the efficiency of their interfacial load transfer, hence increases fiber-matrix ISS value. The introduction of a brittle (increased modulus) interphase by the sulfonation treatment is evident in the fracturing process of the sulfonated fibers. **Figure 6.20** shows a shear failed sulfonated PBO fiber. The sample exhibits radial matrix cracks around the treated fibers which were absent in the untreated fiber samples. Other sulfonated high performance polymer fibers exhibit similar matrix cracks. These observations suggest that the sulfonation treatments of the Spectra-1000 fibers can enhance their ISS by producing an increased modulus fiber-matrix interphase, thus, increasing the interfacial load transfer efficiency.

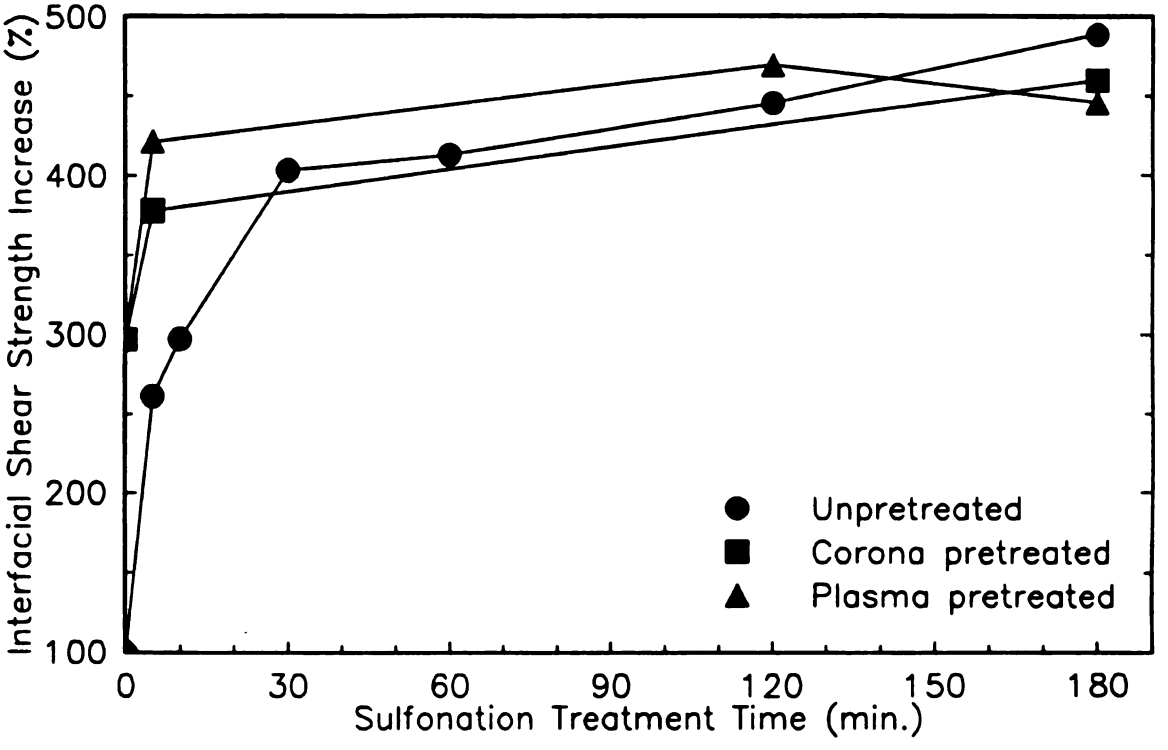

Figure 6.19 - Interfacial shear strength increase of sulfonated Spectra-1000 polyethylene fibers compared to untreated value (measured by the droplet test).

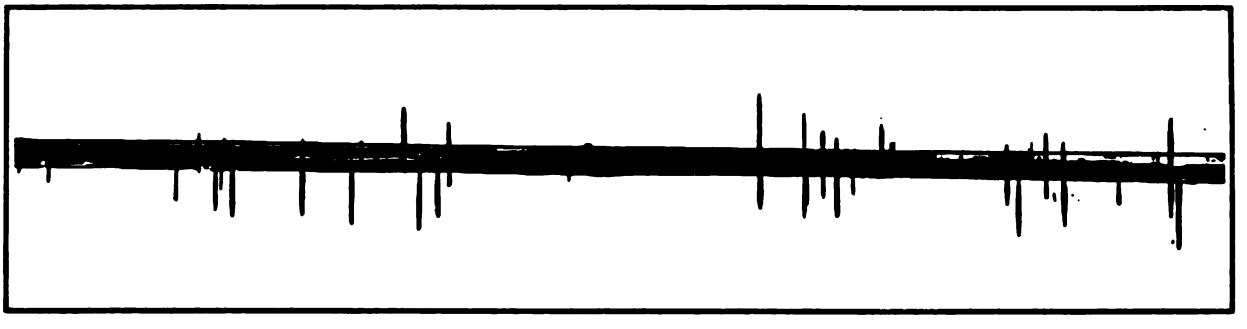

Figure 6.20 - Digitized optical micrograph of a sulfonated PBO fiber under shear stress.

6.4 CONCLUSIONS

- Both fluorination and sulfonation treatments of Kevlar-49 aramid fibers could increase the fiber-matrix adhesion as evidenced by the shift in the locus of fiber-matrix separations from the interface into the fiber interior, however, aramid-epoxy interfacial shear strength (ISS) is not affected by these treatments. Conversely, sulfonated Technora and PBO fibers exhibit increased ISS values.

- Sulfonation treatments of polycarbonate films demonstrated that the diffusion of sulfur species into the polycarbonate film is limited by a formation of a barrier layer of sulfonated materials that reduce the penetration depth of sulfonation treatments.

- Sulfonation treatments of Spectra-1000 polyethylene fibers show that the pretreatment of fibers with a plasma or corona treatment could notably increase their sulfonation rate. Surface polarity of Spectra-1000 fibers was also increased as the result of SO_3 surface incorporation. Sulfonated Spectra-1000 fibers showed ISS increases higher than those obtained by corona and plasma treatments alone. The ISS increases of the sulfonated fibers are attributed to enhancement of polyethylene-epoxy wetting compatibility and introduction of an increased modulus fiber-matrix interphase.

Results of this study show that chemical surface treatments of high performance polymer fibers can introduce functional groups which can improve chemical and mechanical properties of the fiber surfaces. Therefore, interfacial shear strength of fibers such as Technora, PBO and Spectra-1000 that exhibit surface limited adhesive properties can be enhanced by these chemical treatments. Chemical treatments can also alter chemical and mechanical properties of the fiber-matrix interphase to increase its load carrying capacity, thus increasing the interfacial shear strength of the high performance polymer fibers.

CHAPTER 7

Ion Implantation of High Performance Polymer Fibers

In this chapter, effects of ion implantation on mechanical and chemical properties of the aramid and polyethylene fibers are investigated. Unlike the treatments discussed in the previous chapters, ion implantation is a nonequilibrium technique that permits modification of polymer chemistry and morphology without dependency on conditions such as diffusivity or reaction rate. Therefore, by simply controlling the ion beam parameters, the extent and depth of polymer modification can be preselected. Through the ion implantation approach, effects of both the fiber-matrix interphase and fiber bulk properties on adhesive properties of high performance polymer fibers are examined.

This study of ion implantation of polymers has been a collaborative research among several investigators and portions of these results have been published elsewhere: Ozzello *et al.* 1989, Kalantar *et al.* 1989, Kalantar *et al.* 1990[4], and Grummon *et al.* 1991.

7.1 INTRODUCTION

Ion implantation is a process by which a beam of high-velocity ions are injected into the near surface region of a solid. Typically, the ion beam is generated by an arc chamber that is placed inside a high voltage electric field. The arc chamber generates a positive ion plasma which is then extracted by the electric field into a positive ion beam. The beam of positive ions thus formed are directed to a mass-separating magnet that selects only one ion specie. The resulting isotopically pure ion beam is then focused and accelerated using other arrays of magnets and electrodes and acquires tens-to-hundreds of kilovolts in kinetic energy before striking the target. The whole ion implantation process is conducted inside a vacuum chamber.

Ion beam implantation technology has been employed by electronic industries extensively, particularly for the doping of the semiconductors. Other applications of ion beam implantation include enhancing fatigue and corrosion resistance, producing novel materials, and precision machining. Implantation to enhance polymer-polymer adhesion, however, has not been extensively reported in the literature.

An incident ion loses its initial kinetic energy through interactions with nuclei and electrons of the target materials. The energy loss occurs through elastic scattering by the target atomic nuclei or by excitation of its electrons. The excited and recoiled target atoms and electrons transfer and dissipate their energy by interactions with other target materials. The incident ion eventually distributes its initial kinetic energy in a cascade of atomic recoils and electron excitations that slow and stop the incident ion within the target or recoil it off the target.

There are two types of ion-target interactions, atomic processes and electronic processes. The atomic processes of the ion beam are responsible for most of the structural changes of the target material, while, the electronic processes mainly affect the chemical state of the target materials. The energy expended in both types of ion-target interactions can lead to significant physical and chemical changes in target material and the spatial distribution of each interaction determines the extent of the property modification. For most materials, the combinations of mass-energy interrelations makes the effects of different atomic and electronic interactions hard to distinguish.

During the ion-target interactions the ions can become deflected from their original direction of motion resulting in different depths of implantation. Some of the target structural properties that can complicate the modeling of the ion implantation distribution are the crystallinity of the target atoms and the target physical surface. In crystalline targets the properties of the target are strongly directional, which can result in a complex phenomenon of correlated collisions called "channeling". The target physical surface also complicates the ion-target interactions because of the possibility of ion deflection. Generally, the case of amorphous targets where most of the ions penetrate the target are the simplest cases for analytical solutions of ion implantation distribution (Brice 1975, Ziegler 1985). Other factors affecting the ion implantation distribution are the ion species, ion energy, ion flux (dose), and temperature. The spatial distribution of ion-target interactions is generally called "range distribution". There are several reviews on the evaluation of range distributions of ion implantation (Kumakhov *et al.* 1981, Mayer *et al.* 1970, Wilson *et al.* 1973, Carter *et al.* 1968).

Ion beam implantation can alter the chemistry, surface energy, and morphology of a polymer surface which could potentially improve its adhesive properties. Ion-target electronic interactions can produce sites for covalent chemical bonding between the fiber and matrix molecules or cross-link the fiber surface polymers and hinder the development of a cohesive weak boundary layer. Electronic interactions can also increase the surface free energy of fiber and enhance its wetting properties. Ion-target atomic interactions can improve the fiber adhesive properties by etching the fiber surface to either increase its surface area or remove the fiber surface weak boundary layer; however, excessive atomic interactions may weaken the fiber surface. Work by Dresselhaus *et al.* has shown that the ion implantation tends to cross-link the polymers with unbranched chains, while, polymers with complex side chains tend to degrade. Their work also shows that ion implantation tends to more selectively remove non-carbon atoms from the polymers similar to a pyrolysis processes. In general, to improve polymer adhesion the main thrust of ion implantation should be to maximize the electronic interactions that can improve the wetting and chemical bonding within the fiber surface and to minimize the atomic interactions that may degrade the polymer in the implanted region.

Puglisi (1989) has reviewed some of the effects of the ion beam on the polymer substrate. For polymer materials, ion doses equal or greater than 10^{14} ions/cm^2 produce amorphous carbonized materials with only partial memory of the original polymer composition. At these moderate to high doses the nuclear interactions produce random atomic displacements, while, electronic interactions drive to maintain chemical stability. At doses lower than 10^{13} ions/cm^2 both nuclear and electronic interactions can produce

scission (bond-breaking) and aggregation (bond-forming) reactions. The scission reactions give products such as H_2, C_2H_2, etc., and aggregation reactions produce products with higher molecular weight than the target polymer. The extent of scission and aggregation reactions depends on the chemistry of the target. For example, for polymethylmethacrylate the scission reactions dominate, but for polystyrene the aggregation reactions prevail (Puglisi 1989).

Previous work on polymer surface modification by ion implantation has been shown to increase the adhesion of polyethylene (PE) to metallic titanium films (Bodo *et al.* 1986) and to increase UHMW-PE/epoxy interfacial shear strength (Ozzello *et al. 1989).* Licciardello *et al.* (1987) have reported that ion implantation of polystyrene produces cross-linked structures that are chemically different from that obtained by electron bombardments. Adem *et al.* (1988) have shown that oxygen implantation into polyvinyledene fluoride results in hydrogen and fluorine rearrangement on the polymeric chain. Ishitani *et al.* (1989) have reported on the applications of SIMS, FTIR, Raman and ESR to study oxygen implanted polyethylene. They conclude that ion implantation of the polymer introduces complicated chemical reactions which ultimately result in the generation of amorphous carbon. Yoshida *et al.* (1987) have examined the structure and morphology of ion-implanted polyimide films and reports that carbonization of the implanted polymer layer as a result of the polymer scission and loss of oxygen and nitrogen atoms. Bertrand *et al.* (1987) have examined helium implantation of polyethylene terephalate polymers which show bond breaking and surface damage as the result of implantation. Suzuki *et al.* (1988) have reported that ion implantation brakes

up the silicone rubber polymer to form new radicals which can significantly enhance the polymer wettability. Similarly, Torrisi *et al.* (1988) have demonstrated the degradation of the polytetrafluoroethylene polymer as the result of helium ion implantation. Ion implantation of polymer substrates is a new area of research which is actively under investigation, however, applications of ion implantation to enhance adhesive properties of polymers has not been investigated extensively. In this study, the effects of ion implantation on adhesive properties of Kevlar-49 aramid and Spectra-1000 polyethylene fibers are examined.

7.2 EXPERIMENTAL

Two epoxy systems were used in this study, the DER331/MPDA/DETDA 175°C/3hr (fragmentation test) and the DER331/MPDA RT/24hr/75°C/2hr/100°C/3hr (droplet test) systems. Single fiber tensile measurements were done by ASTM D3379 tensile test. Fiber surface elemental compositions were characterized by XPS. Fiber-matrix interfacial morphologies were examined by TEM. These experimental procedures are detailed in Chapter 2.

Both Kevlar-49 aramid and Spectra-1000 were soxhlet extracted with ethanol before they were sent for the implantation treatments. The ion implantation were done by *Spire Corporation* (Bedford, MA) according to the protocol shown in **Table 7.1.** Ion beam currents were between 0.2 to 5 μA. Fibers were implanted by laying individual fibers on a 75 mm square aluminum frame which held them in contact with a chilled aluminum heat sink. Later XPS studies showed no evidence of re-sputtered aluminum on any of the irradiated samples. For each implantation condition, several hundred lengths of fibers and several strips of fabric (10×75 mm^2) were irradiated. After irradiation, the fibers were left on their frames and sealed in nitrogen-purged bags to prevent absorption of atmospheric moisture. Most of the implanted fibers were embedded in epoxy within four days after irradiation.

Table 7.1. Ion implantation protocols for polyaramid and polyethylene fibers.

ION	Energy (keV)	Dose (ions/cm^2)	Implant Depth (nm ± 10% var.)
Kevlar-49 Polyaramid			
Ar^+	75	1×10^{15}	100
N^+	30	1×10^{14}	102
N^+	30	5×10^{14}	102
N^+	30	1×10^{15}	102
Ti^+	100	1×10^{15}	111
N^+	100	2×10^{13}	320
N^+	100	1×10^{14}	320
N^+	390	2×10^{12}	937
N^+	400	5×10^{12}	954
N^+	400	2×10^{13}	954
N^+	400	1×10^{14}	954
N^+	390	2×10^{14}	937
He^+	390	1×10^{13}	1550
Spectra-1000 Polyethylene			
Ar^+	75	1×10^{14}	130
Ti^+	100	1×10^{15}	135
He^+	400	1×10^{13}	1637

7.3 RESULTS AND DISCUSSION

Results of aramid and polyethylene ion implantation are discussed separately to provide an exclusive discussion for each fiber type. Conclusions for both fibers are then combined to develop a comprehensive understanding of the effects of ion implantation on adhesive properties of high performance polymer fibers.

7.3.1 Aramid Ion implantation

Figure 7.1 shows the XPS elemental composition of 400 keV N^+ implanted fibers (in fabric form) for various doses. For these implantation, 10^{14} N^+/cm^2 dose exhibit about 6% increase in carbon, 15% reduction in nitrogen, and 22% reduction in oxygen. Lower dose implantation, however, show only marginal composition changes. In **Figure**

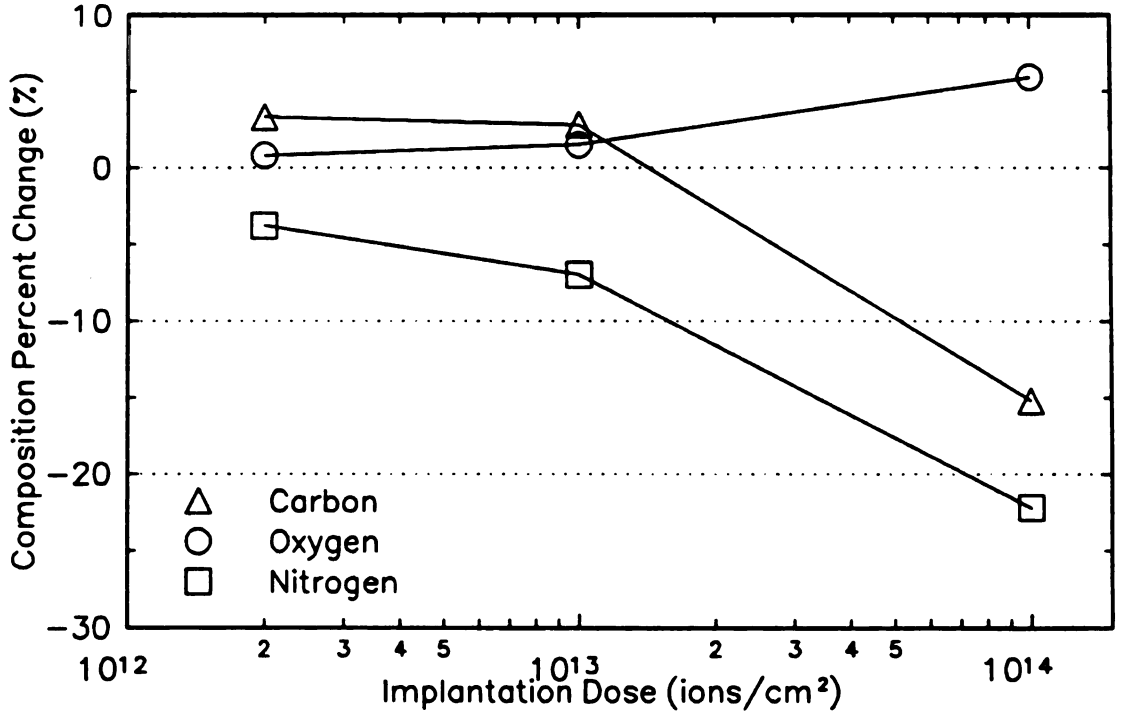

Figure 7.1 - XPS elemental composition changes of 400 keV N^+ implanted Kevlar-49 aramid fibers relative to untreated fiber.

7.1, carbonization of the aramid surface appears to take place at doses higher than 10^{13} ions/cm^2, however, the aramid carbonization dose can increase for lighter and lower energy ions (Venkatesan *et al.* 1987). The initial slight increases in nitrogen and carbon, and reduction in oxygen relative to untreated fibers may be attributed to sputtering of the Kevlar-49 oxidized surface layer (see **Table 6.1**).

Effects of fiber surface carbonization are also apparent in the fiber morphology as observed by TEM. Generally, fibers implanted with doses at or above 10^{14} ions/cm^2 show contrast effects in TEM micrographs which appear as a darkening in the fiber external region, corresponding roughly to the ion projected range. **Figure 7.2** shows this darkened region for a 10^{14} N^+/cm^2 400 keV fiber embedded in an epoxy matrix. The darkened zone on this fiber appears only on the left side due to line-of-sight shielding by an adjacent fiber. Note that the thickness of the carbonized region is about 1 μm as predicted by the TRIM-90 program (Guimaraes *et al.* 1989, Biersack *et al.* 1980) shown in **Table 7.1**. The implanted region shows good adhesion around the fiber-matrix interface except over the region where the fiber was not implanted (upper fiber perimeter in **Figure 7.2A**). This observation is evidence for the improvement of aramid-epoxy adhesion by the ion implantation treatment. The XPS results for the 10^{14} N^+/cm^2 400 keV treatment (**Figure 7.1**) confirm that the dark region around the fiber perimeter is due to the fiber carbonization.

Conversely, at doses at or below 10^{13} ions/cm^2 this near surface darkening is absent for the 400 keV N^+ implanted aramid fibers. **Figure 7.3** shows TEM micrographs of a 10^{13} N^+/cm^2 400 keV implanted fiber. The section show excellent fiber-matrix

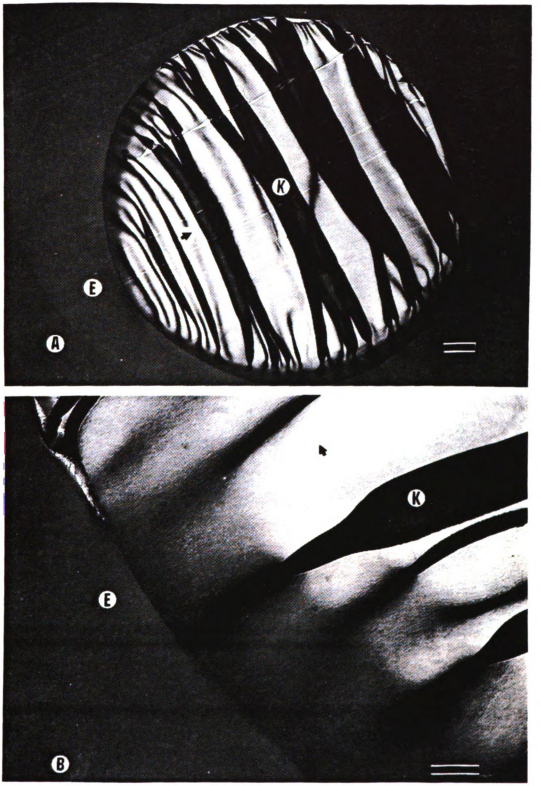

Figure 7.2 - TEM micrographs of 400 keV 10^{14} N^+/cm^2 irradiated Kevlar-49 fiber. (A) whole fiber K in matrix E, (B) detailed view of the interphase. (A) bar = 1 μm (B) bar = 200 nm

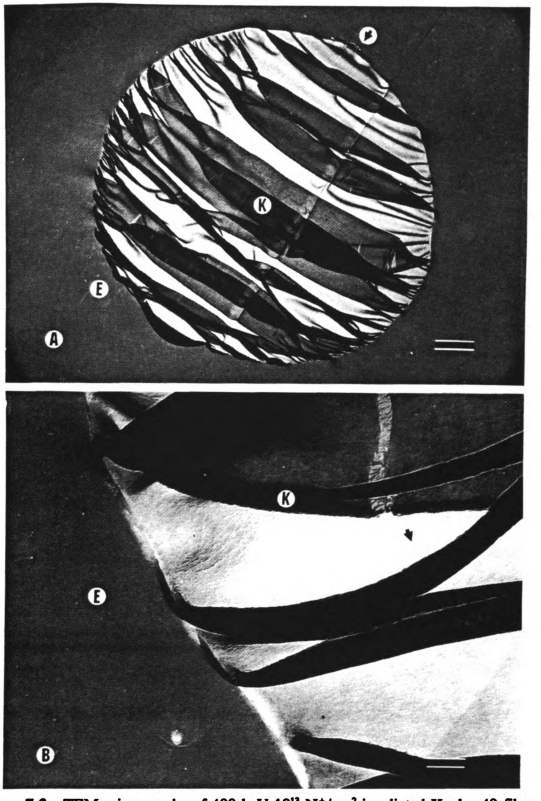

Figure 7.3 - TEM micrographs of 400 keV 10^{13} N^+/cm^2 irradiated Kevlar-49 fiber.
(A) whole fiber view, (B) high magnification view of the interphase.
(A) bar = 1 μm (B) bar = 100 nm

adhesion but without detectable skin darkening. This observation is consistent with the XPS results which showed a surface composition close to the untreated fibers (**Figure 7.1**). **Figures 7.2** and **7.3** exhibit increased fiber-matrix adhesion compared to the untreated (**Figure 3.9**) fibers. Similar increased fiber-matrix adhesion is observed for all other ion implanted aramid fibers (discussed later).

Although, the aramid carbonization appears to take place at doses at or above 10^{14} ions/cm^2, the carbonization dose also depends on the implantation energy and the implanted ion mass. Generally, the polymer carbonizing dose increases for lighter and lower energy ions (Venkatesan *et al.* 1987). **Figure 7.4** shows the TEM micrographs of a 10^{14} N^+/cm^2 30 keV implanted fiber. The fiber does not show the near surface darkened region observed in the 10^{14} N^+/cm^2 400 keV implanted fiber (**Figure 7.2**). **Figure 7.4** also shows good overall aramid-epoxy adhesion, but on closer inspection of the interphase, extensive interfacial fibrillation is observed (**Figure 7.4B**). This interfacial fibrillation is within the fiber which suggests cohesive fiber failure.

Figure 7.5 shows TEM micrographs of the 10^{15} Ti^+/cm^2 100 keV implanted fiber. This combination of energy and dose is well above the carbonizing dose of the aramid fibers and the carbonized skin layer is clearly visible around the perimeter of the fiber-matrix interface ($\sim$ 150 nm thick). The carbonized fiber surface has adhered well to the matrix and the locus of failure is between the implanted skin and the its bulk interior. The presence of bubbles trapped at the fiber-matrix interface confirms that the fiber skin adheres to the matrix and the interfacial failure are within the fiber. Similarly, **Figure 7.6** shows the TEM micrograph of a 10^{14} N^+/cm^2 400 keV implanted fiber, made after

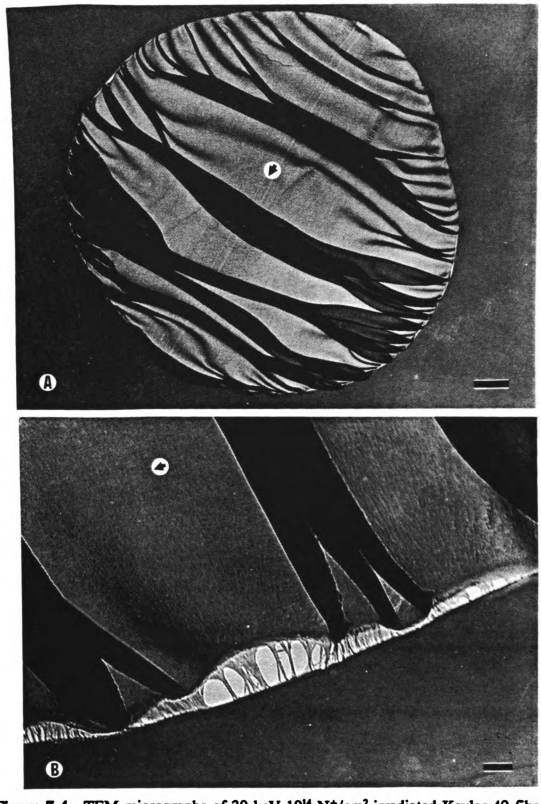

Figure 7.4 - TEM micrographs of 30 keV 10^{14} N^+/cm^2 irradiated Kevlar-49 fiber.
(A) whole fiber view, (B) detailed view of the interphase.
(A) bar = 1 μm (B) bar = 100 nm

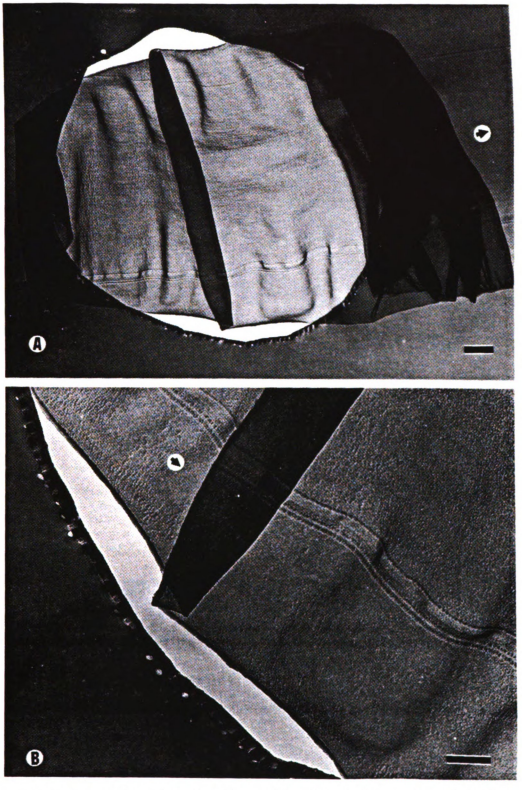

Figure 7.5 - TEM micrographs of 100 keV 10^{15} Ti^{+}/cm^{2} irradiated Kevlar-49 fiber.
(A) whole fiber view, (B) fiber-matrix interphase.
(A) bar = 1 μm (B) bar = 500 nm

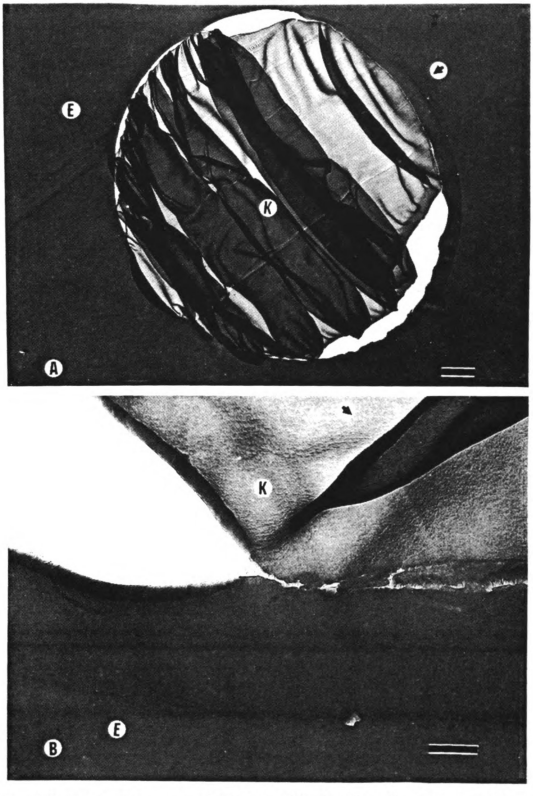

Figure 7.6 - TEM micrographs of 400 keV 10^{14} N^+/cm^2 irradiated Kevlar-49 fiber after failure in ISS test. (A) whole fiber view, (B) skin-bulk interphase.
(A) bar = 1 μm (B) bar = 200 nm

failure in the interfacial shear strength test. Again, the implanted fiber exterior adheres well to the matrix and the locus of failure has shifted toward the fiber interior.

In Chapter 3, it was demonstrated that for the untreated Kevlar-49 aramid fibers the fiber-matrix failure mode is interfacial with some fiber surface cohesive fibrillations (**Figure 3.9**). Similar failure modes are also observed for fibers implanted below the carbonizing dose as shown in **Figures 7.3** and **7.4**. However, for carbonized implantation ($\geq 10^{14}$ ions/cm^2) the fiber-matrix failure mode is more cohesive. **Figures 7.5, 7.6** and other micrographs of carbonized aramid fibers show the locus of failure to be between the carbonized implanted skin and the fiber bulk interior. The difference between the failure modes of the carbonized and the lower dose implantation may be due to mechanical weakening of the carbonized fiber region. Degradation of mechanical properties of the implanted aramids are more severe for the higher dose implantation (discussed later). The carbonized skin is a weak boundary layer that shifts the locus of failure into the fiber interior. The carbonized fiber skin may also have increased microscopic porosity that can promote its epoxy adhesion through mechanical interlocking mechanisms. Although, SEM observations of the carbonized aramid fibers actually showed somewhat smoother surface topography than untreated fibers (similar to **Figure 6.5**), the morphological changes may be at a scale smaller than that discernable at 20 k× magnification.

Adequate wetting of the fiber surface by liquid resin is a prerequisite for good adhesion. **Figure 7.7** compares the surface energy of several N^+ implanted aramid fibers with the epoxy resin. The irradiated Kevlar fibers show about half the polar energy

component of the untreated fiber along with marginal changes in their dispersive energy components. Gutowski (1990) has shown that in the absence of chemical bonding, maximum adhesion between the matrix and fiber occurs when the surface energy of the fiber (γ_f) and matrix (γ_m) are equal. Gutowski proposes theoretical relations that suggest for (γ_f/γ_m) > 1 complete wetting occurs but the strength of fiber-matrix adhesion decreases as the ratio increases. For the surface energy ratios (γ_f/γ_m) < 1 incomplete wetting occurs and fiber-matrix strength rapidly drops to zero as the ratio approaches 0.7, hence the ion implanted Kevlar-49 fibers are expected to have incomplete wetting with the epoxy resin. Therefore, the enhanced fiber-matrix adhesion of the ion implanted fibers must be due to physical mechanisms such as mechanical interlocking and/or

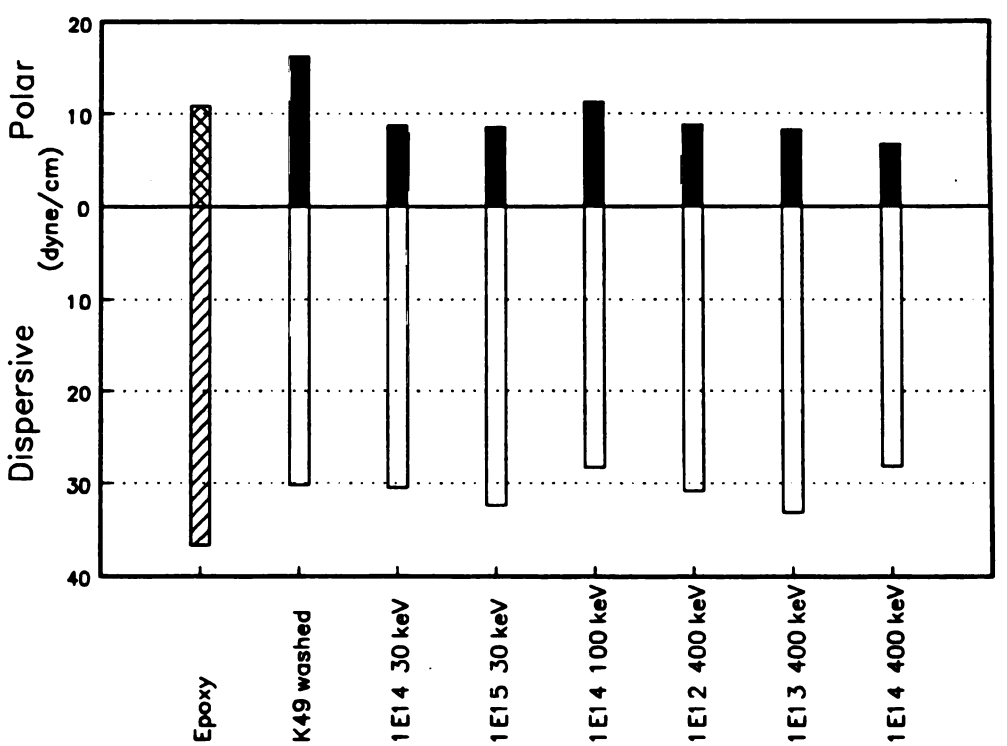

Figure 7.7 - Polar and dispersive components of surface free energy for N^+ implanted Kevlar-49 fibers and liquid epoxy.

mechanical interpentration, or introduction of active chemical sites that can form covalent bonds with the matrix molecules.

Figure 7.8 shows the interfacial shear strength of N^+ implanted aramid fibers for various doses. There are no significant increases in the aramid-epoxy interfacial shear strength despite the apparent improved interfacial adhesion observed for all ion implanted aramid fibers. There is about a 16% interfacial shear strength reduction for the carbonized aramid fibers, that, along with the previous TEM observations, suggest creation of a weak interphase between the carbonized fiber skin and the fiber interior.

The fibers examined in **Figure 7.8**, all were impregnated immediately after their removal from their sealed bags. For some samples, fibers were kept exposed for one month in the atmospheric condition. This environmental exposure caused no detectable ISS change.

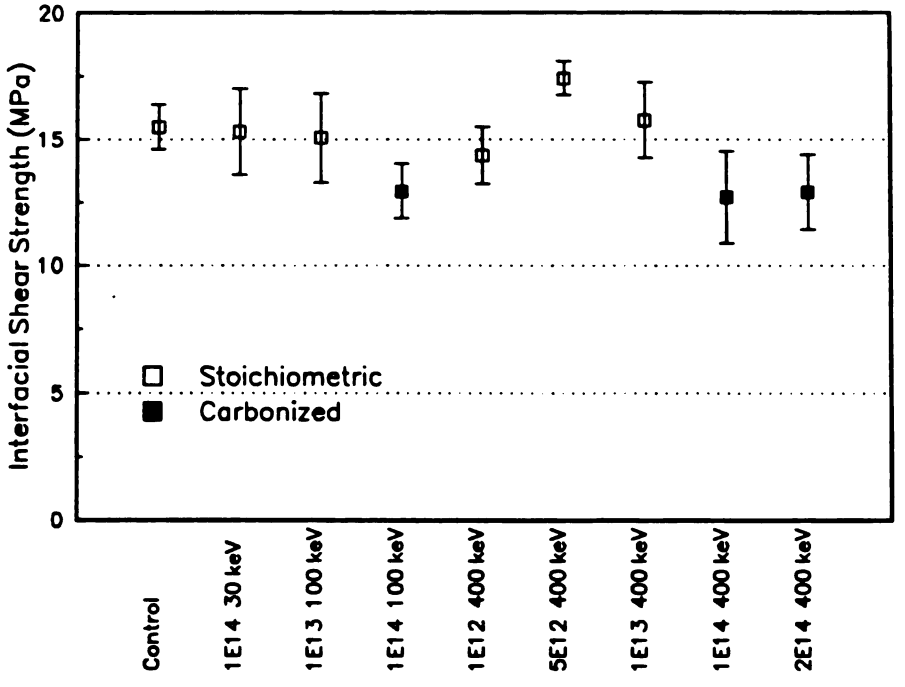

Figure 7.8 - Interfacial shear strength of N^+ implanted Kevlar-49 fibers.

Aramid degradation by ion implantation is also exhibited in the tensile properties of the fiber. **Figure 7.9** shows the tensile strength of the implanted aramid fiber along with their expected implantation depths (**Table 7.1**). The implanted aramid fibers that were carbonized, were distinguishable by their brownish coloration compared to the bright yellow color of untreated and the low dose implanted fibers. The qualitatively identified carbonized fibers are shown by the solid symbols. In general, ion implantation produces tensile strength losses that increase with the implantation depth (energy) and dose. All fibers implanted at 400 keV (~1 to 1.5 μm implantation depth) show a loss of tensile strength, however, the carbonized fibers exhibit the lowest tensile strengths. This suggest that the scission reactions dominate the chemistry of ion-target interactions in polyaramids, as they reportedly do in the case of ion irradiated polymethylmethacrylate

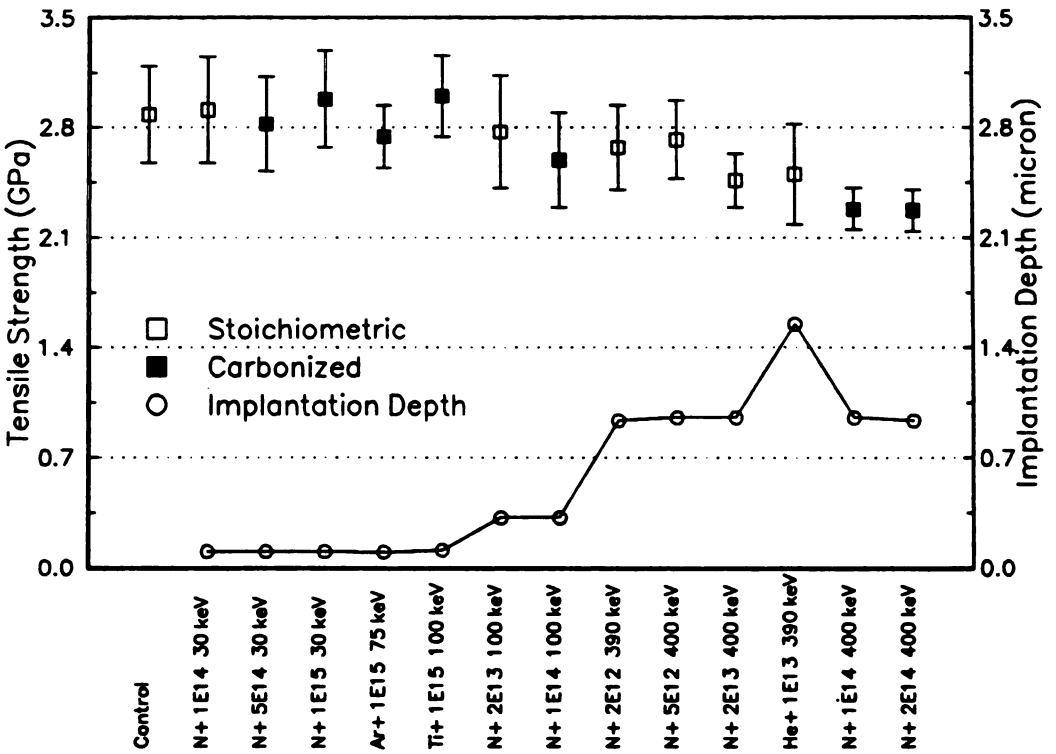

Figure 7.9 - Tensile strength and implantation depth of irradiated aramid fibers.

(Vankatesan *et al.* 1987). The tensile strength reductions in the low energy implantation are less evident because the low penetration implantation only modify a small volume of fiber structure.

The combination of enhanced fiber-matrix adhesion and reduced mechanical properties of the ion implanted aramid fibers is also exhibited in the fracturing process of their impregnated samples. **Figure 7.10** shows the optical micrographs of fracturing process of a 10^{14} N^+/cm^2 400 keV sample impregnated in an epoxy system. The ion implanted aramid fiber produces matrix fractures that do not occur in the untreated aramid fibers. This type of matrix fracture indicates the presence of a brittle fiber-matrix interphase (see **Figure 6.20**). For the carbonized implantation, the brittle skin layer probably fractures and causes cracks that propagate into the matrix, nonetheless, the fiber-matrix adhesion has to be strong because cracks are not deflected along the fiber-matrix interface.

7.3.2 Polyethylene Ion Implantation

Grummon *et al.* (1991 [a,b]) have reported on the effects of implantation dose on polyethylene composition. Their XPS results show that at doses below 10^{15} ions/cm^2, increases in oxygen and decreases in carbon content relative to the untreated fibers occurs. At doses above 10^{15} ions/cm^2, however, the fiber carbonization begins to predominate (O↓, C↑). Like the aramid fibers, the carbonization of the polyethylene fibers were accompanied by visible darkening of the fiber exterior. Implanted polyethylene also exhibited surface morphological changes such as melting of the fibrillar

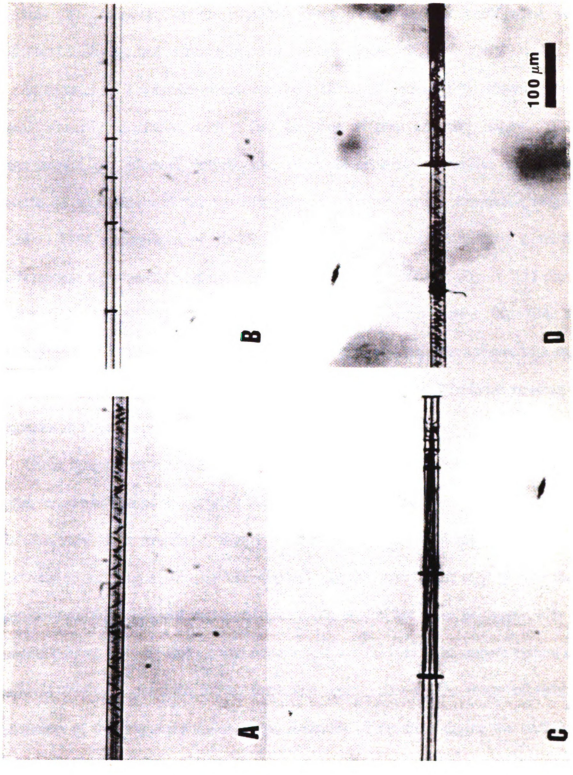

Figure 7.10 - Fracturing of 10^{14} N^+/cm^2 400 keV implanted aramid fiber. (A) 0% strain, initial curing kinks, (B) 2% strain, fiber fractures, (C) 5% strain, matrix fractures, (D) strain released, kinks reappear.

tendrils that are present on the untreated fibers. These surface modification were attributed to the thermal effects of the implantation process ($T_m = \sim 150°C$).

In Chapter 3, it was shown that the shear failure of untreated polyethylene fibers were primarily interfacial, with a few locations of fiber cohesive failure. TEM micrographs of untreated polyethylene fibers demonstrated extensive fiber-epoxy interfacial separation with the sporadic presence of fiber surface fibrillation (**Figure 3.14**). TEM micrographs of the ion implanted polyethylene fibers show a marked difference in their interfacial morphology and shear failure behavior. **Figure 7.11** shows a 10^{15} Ti^+/cm^2 100 keV polyethylene fiber imbedded in an epoxy system. This fiber has been implanted above the carbonizing dose and the carbonized skin appears as a dark band around fiber perimeter. A marked improvement in the interfacial bonding is apparent in the ion implanted fiber.

Other polyethylene implantation also exhibit improved fiber-matrix adhesion, however, the implanted skin appears to adhere to the epoxy and the locus of failure shifts to within the fiber structure. **Figure 7.12** shows the TEM micrographs of a 10^{14} Ar^+/cm^2 75 keV and a 10^{13} He^+/cm^2 400 keV polyethylene fibers. For both of these implantation the implanted region is discernable around the fiber perimeter with its smooth texture, reduced folding, and relatively dark coloration. The smooth texture and reduced folding appearance of the implanted region may be the result of reduced toughness of the implanted region. The stretching of the fiber during the sectioning process produces the fiber folding observed in the TEM micrographs. Ion implantation of polyethylene fibers below the carbonizing dose tends to cross-link the fiber which

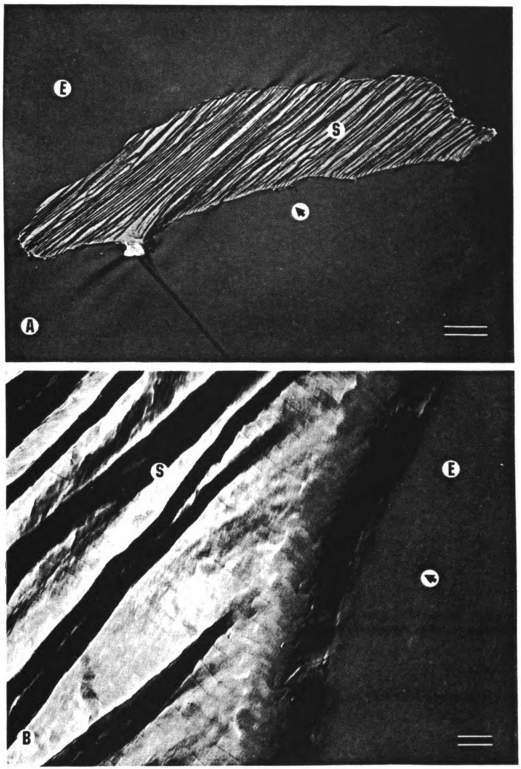

Figure 7.11 - TEM micrographs of 100 keV 10^{15} Ti^{+}/cm^{2} irradiated Spectra-1000 fiber.
(A) whole fiber view, (B) detailed view of the fiber-matrix interphase.
(A) bar = 5 μm (B) bar = 100 nm

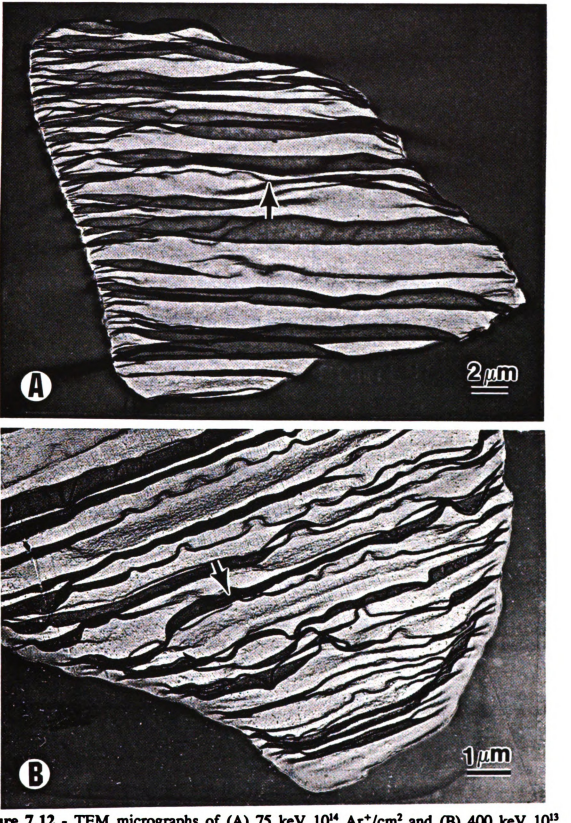

Figure 7.12 - TEM micrographs of (A) 75 keV 10^{14} Ar^+/cm^2 and (B) 400 keV 10^{13} He^+/cm^2 irradiated Spectra-1000 fibers.

reduces the fiber toughness, thus, producing a smoother texture and fewer folding.

The appearance of the implanted regions in the TEM micrographs was not observed for the aramid fibers that were irradiation below the carbonizing condition, which may be due to the greater thermal sensitivity of the polyethylene fibers (T_m = 150°C) than the aramid fibers (T_g = 350°C, $T_{decom.}$ = 500°C).

Figure 7.13 shows the TEM micrographs of a 10^{14} Ar^+/cm^2 75 keV and a 10^{15} Ti^+/cm^2 400 keV irradiated polyethylene fibers. These micrographs show that the fiber-matrix separation is taking place between the implanted skin and the fiber bulk interior. **Figure 7.13** and other micrographs of ion implanted polyethylene fibers show that the ion implantation treatment shifts the locus of polyethylene-epoxy separation from an adhesive separation for the untreated fibers to a cohesive separation between the implanted region and the fiber interior for the treated fibers.

Surface energy measurements by Grummon *et al.* (1991[a]) have suggested that the improved adhesion can be attributed to the enhanced wetting properties of the implanted fibers. The polar component of surface energy were increased sharply (200-300%) to values close to the epoxy component. The dispersive components, however, were not significantly altered but remained close to the epoxy component. Therefore, the ion implanted polyethylene fibers showed much improved surface energy compatibility with the epoxy which can significantly enhance their thermodynamic wetting properties.

The interfacial shear strength (ISS) of the ion implanted polyethylene fibers characterized by the droplet technique has been reported by Ozzello *et al.* (1989). Generally, fibers implanted near or above the carbonizing dose show about 250% to

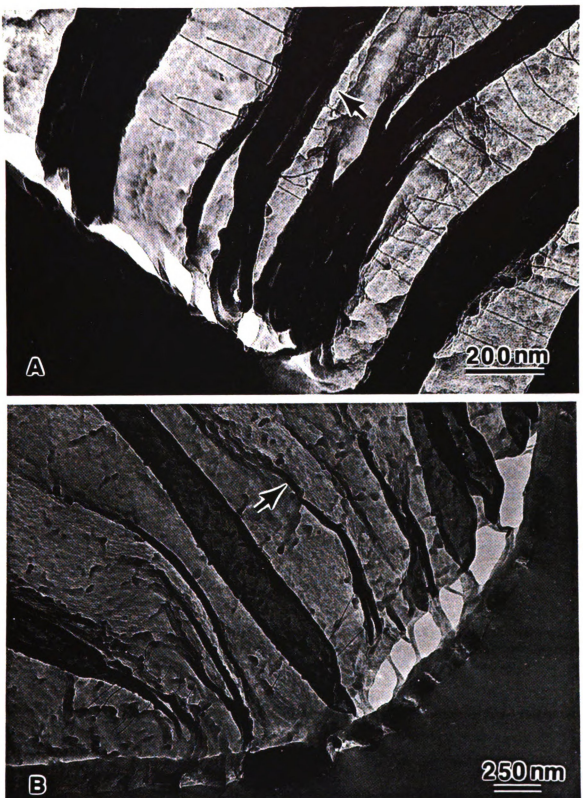

Figure 7.13 - TEM micrographs of (A) 75 keV 10^{14} Ar^+/cm^2 and (B) 100 keV 10^{15} Ti^+/cm^2 irradiated Spectra-1000 fiber.

300% ISS increases relative to the untreated fibers. These ISS results were not affected by the chemical nature of the implanted ions suggesting that only the density of irradiation energy controls the extent of adhesion modification. The improved ISS results along with the TEM observations suggest that polyethylene ion implantation can significantly increase the fiber-matrix adhesion, but then the locus of failure shifts to within the fiber structure and between the implanted and untreated regions.

Grummon *et al.* (1991[a]) have also identified several polar functional groups on the implanted polyethylene fibers using an ATR-FTIR technique. Covalent chemical bonding between these functional groups and the epoxy may be possible, however, their contribution to the overall adhesion level is not clear. Hook *et al.* (1990) have determined that the contribution of the covalent chemical bonding to shear bond strength between AS4 carbon fiber and an epoxy-amine polymer is less than 5%. The presence of the new polar groups on the implanted polyethylene fibers can explain the increase in the polar component of the surface energy and consequently enhanced thermodynamic wetting with the epoxy resin, but the contribution of covalent chemical bonding between epoxy polymer and these polar group to the improved fiber-matrix adhesion requires further evaluation.

Effects of ion implantation on the mechanical properties of the polyethylene fibers can be observed in the fiber tensile properties. Table 7.2 compares the mechanical properties of the untreated and 400 keV 10^{13} He^+/cm^2 implanted Spectra-1000 fiber. Data shows a reduction in the toughness of the implanted fiber (tensile strength and fracture strain) but the tensile modulus is increased. Similar tensile properties of

Table 7.2 - Mechanical Properties of untreated and 400 keV 10^{13} He^+/cm^2 implanted Spectra-1000 polyethylene fibers.

Property	Untreated	400 keV 10^{13} He^+/cm^2
Implantation Depth (μm $\pm$ 10% var.)	-	1.6
No. of Tests	12	12
Diameter (μm)	28.7 $\pm$ 2.7	28.7 $\pm$ 2.5
Tensile Modulus (GPa)	67.8 $\pm$ 9.2	82.5 $\pm$ 3.0
Tensile Strength (GPa)	2.65 $\pm$ 0.29	1.77 $\pm$ 0.26
Fracture Strain (%)	6.91 $\pm$ 1.30	3.42 $\pm$ 0.42
ISS droplet test (MPa)	2.95 $\pm$ 0.17	10.3 $\pm$ 0.5

implanted polyethylene fibers with implanted ranges less than 0.15 μm (Ozzello *et al.* 1989) did not show significant tensile property changes probably because only a marginal volume of the fiber structure was modified. For polyethylene, aggregation reactions are known to dominate the low dose implantation (Puglisi 1989) that can result in cross-linking of the polyethylene structure. The increased interactions among adjacent polymer chains in the cross-linked polymer tend to reduce their relative mobility which reduces toughness but increases modulus of the structure. The reduced toughness and increased modulus of the implanted polyethylene fiber shown in the Table 7.2, suggests that the implantation process produces a higher modulus but more brittle polyethylene structure for irradiations below the carbonization condition.

Other researchers have also reported modulus increases for the cross-linked polyethylene fibers. Chapiro (1988) has examined the radiation chemistry of polyethylene and has proposed a cross-linking chemical mechanism. He reports that cross-linking increases the modulus and hardness of the polyethylene and imparts a non-melting behavior to the material. Postema *et al.* (1988) have reported that chlorosulfonation of ultra-high strength polyethylene fibers decreases the fiber tensile strength but increases the fiber modulus by more than 50%.

The brittle nature of the ion implanted polyethylene is also evident in their fracturing process. **Figure 7.14** shows the optical micrographs of shear fractured ion implanted polyethylene fibers that were imbedded in an epoxy matrix. In **Figure 7.14A** the 100 keV 10^{15} Ti^{+}/cm^{2} implanted fiber shows thin surface fractures along the fiber radius which are less than half a fiber diameter apart. In **Figure 7.14B** the 400 keV 10^{13} He^{+}/cm^{2} implanted fiber shows thick fracture lines that are angled and about two fiber diameters apart. These angled fracture lines are along the compressive helical kink lines of the fiber that are produced during the fiber manufacturing process. The thermal stresses induced during the fiber imbedding process in the epoxy matrix results in greater displacements along these kink lines than the rest of the fiber, therefore, the implanted fiber skin is more apt to break along these kink lines. The closely packed fractures of the carbonized fiber (**Figure 7.14A**) are more frequent than the fiber kink lines, which suggests that carbonizing implantation are producing a brittle structure. The 400 keV 10^{13} He^{+}/cm^{2} implanted polyethylene fiber shows a moderately higher ISS increase (~360%, **Table 7.2**) than the increases reported by Ozzello *et al.* (1989) for the

carbonizing implantation conditions (250 to 300%). For the implanted fibers, mechanical coupling between polyethylene bulk and its implanted surface may be weaker for the brittle carbonized surfaces than the cross-linked non-carbonized surface.

The shear strength limitations of the implanted polyethylene fibers were clearly demonstrated during their droplet-pullout ISS test. **Figure 7.15** shows SEM micrographs of a separated droplet on a 400 keV 10^{13} He^+/cm^2 implanted Spectra-1000 fiber. In **Figure 7.15B** the blade side of the droplet shows a section of the fiber that has been fractured within the fiber, while, on the back side of the fiber the separated skin has folded (**Figure 7.15C**). In **Figure 7.15**, the fiber fractures are not symmetrical around the fiber probably because the implanted fiber was not uniformly irradiated. Non-uniformity of the fiber implantation is also evident in the fiber-droplet meniscus, where the fractured fiber side shows a epoxy wetted surface while other sides appear unwetted. These SEM micrographs demonstrate that the locus of shear failure has been shifted from the fiber-matrix interface to within the fiber structure and between the implanted and untreated regions.

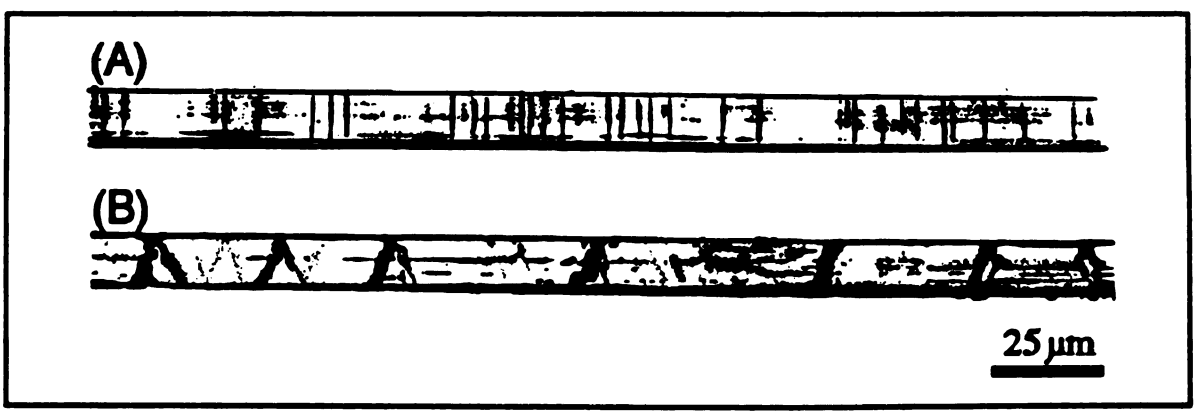

Figure 7.14 - Digitized optical micrograph of sheared ion implanted Spectra-1000 fibers. (A) 100 keV 10^{15} Ti^+/cm^2 implanted, and (B) 400 keV 10^{13} He^+/cm^2 implanted fibers.

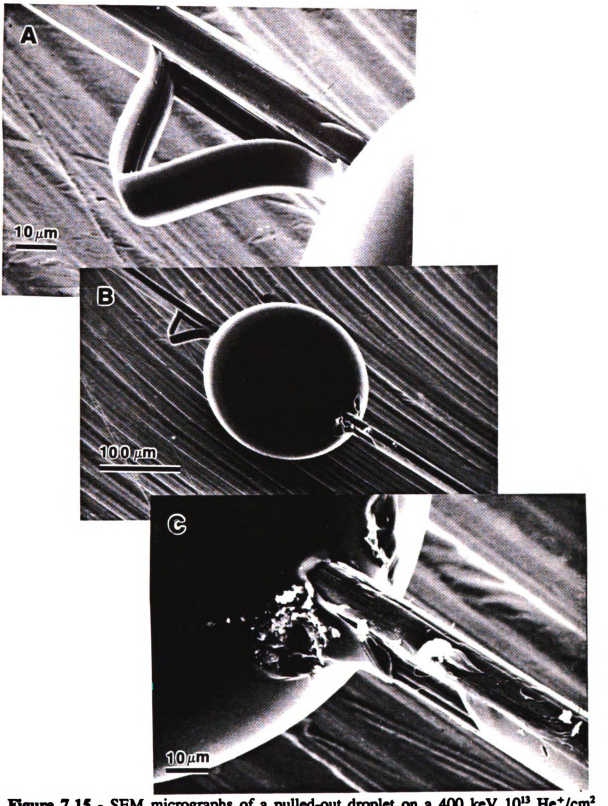

Figure 7.15 - SEM micrographs of a pulled-out droplet on a 400 keV 10^{13} He^+/cm^2 implanted Spectra-1000 fiber. (A) Back side, (B) overall view, and (C) blade side of the droplet.

7.4 CONCLUSIONS

- For both aramid and polyethylene fibers, surface carbonization takes place at ion doses near or above the 10^{14} ions/cm^2. Below the carbonizing dose, aggregation reactions tend to dominated chemical modification of polymers with aliphatic backbone chains such as polyethylene, resulting in a cross-linked fiber structure that has reduced toughness but higher modulus properties. For polymers with non-carbon elements in their backbone such as aramids, the scission reactions tend to dominate the chemical modification resulting in reduced mechanical properties of the implanted region.

- For the polyethylene fibers ion implantation produced more epoxy compatible surface energy components that could significantly enhance their thermodynamic wetting properties. Conversely, ion implantation reduced the epoxy wetting compatibility of the aramid fibers. Nonetheless, for both fibers improved fiber-matrix adhesion were observed.

- Ion implanted Spectra-1000 polyethylene fibers exhibit 250 to 360% increases in the fiber-matrix interfacial shear strengths (ISS), however, Kevlar-49 aramid fibers did not exhibit any significant (ISS) increases. For both fiber, improved interfacial adhesion changed the locus of shear failure from fiber-matrix interphase to within the fiber structure and between the implanted region and the untreated bulk.

Result of this study demonstrate that increasing the interactions between fiber polymer chains increases the fiber tensile modulus and interfacial shear strength, but decreases the fiber fracture strain and tensile strength. However, if the lateral chain interactions are not advanced throughout the fiber structure, then the locus of shear failure shifts to an untreated region of the fiber structure. Therefore, the key to improving the fiber-matrix interfacial load transfer of high performance polymer fibers is to introduce polymer chain interaction throughout the fiber structure.

CHAPTER 8

Structural Modification of High Performance Polymer Fibers

Polymer treatments discussed in the previous chapters have been able to increase the interfacial load transfer capacity of the high performance polymer fibers to the point where the fiber lateral cohesive strength becomes the limiting factor. Although, interfacial shear strength (ISS) increases obtained by some of these treatment techniques are significant relative to their untreated values, these ISS improvements are still far lower than their theoretically predicted values (Figure 3.3). For the high performance polymer fibers, previous results indicate that higher interfacial shear strengths may be obtainable if the fiber transverse cohesive properties could be enhanced throughout the fiber structure. In this chapter, approaches to structural modification of high performance polymer fibers are investigated.

8.1 INTRODUCTION

As discussed in the Chapters 3 and 7, the highly aligned structure of high performance polymer fibers results in their excellent tensile properties, however, since only weak secondary forces connect the chains radially, the fibers exhibit weak shear and compressive properties. Therefore, increasing cross-chain interactions is the key to increasing the shear properties of the high performance polymer fibers. In this study, approaches to structural modification of high performance polymer fibers are investigated.

Mechanical evaluation of structurally modified polymer fibers require special considerations. An experimental and theoretical study of axial compressive behavior of high performance polymer fibers by Deteresa (1985) has suggested that the longitudinal shear modulus of fibers are equal to their compressive strength when fibers fail by a cooperative chain buckling mode. This concept is important for the mechanical evaluation of the structurally modified polymer fibers. Using ISS tests to evaluate structurally modified fibers may produce erroneously low results because of the presence of a weak surface layers produced by the treatment. Observation of the compressive properties of the fibers is an indirect but more reliable approach to evaluation of shear property changes of the high performance polymer fibers. In Appendix A, it is shown that the single fiber compressive tests are insensitive to the extent of fiber-matrix bond strength as long as fiber and matrix undergo the same strain conditions, (*i.e.* no debonding occurs before the fiber compressive failure, see Equation A.3). Furthermore, Deteresa (1985) has shown that the longitudinal shear modulus of high performance

polymer fibers are equal their compressive strength, therefore, changes in shear moduli of treated fibers should be reflected directly in their compressive strength measurements. In this study, single fiber compressive test were adopted to evaluate the effects of fiber structural modification.

Two approaches to reinforce lateral chain interactions of polymer fibers were examined in this study: infusion of SiO_2 and epoxy into interfibrillar space of liquid crystalline polymers to provide lateral support and to mechanically couple the fibrils, and Friedel-Crafts acylation reactions to covalently bond adjacent polymer chains.

8.1.1 Infusion of a Second Phase

The use of a second phase rational to infiltrate and reinforce the fibrillar microstructure of PZT films have been patented by Kovar *et al.* (1989). However, the patent applies to films and does not claim application to polymer fibers. In this study, two types of infusion agents have been investigated: SiO_2 by sol-gel reactions and epoxy resins dissolved in a solvent.

Sol-gel reactions generally refer to chemical systems where a colloidal suspension of small particles (sol) link together forming a solid mass (gel). Metal alkoxides are a common type of sol reagents. Metal alkoxides have the general chemical formula $M(OR)_x$ where M is the metal, R is an alkyl group (CH_3, C_2H_5, etc.), and x is the valence state of the metal atom. These metal alkoxides can be hydrolyzed to form their corresponding hydroxide. One of the alkoxides used in this study is tetra-ethyl-orthosilicate (TEOS). The overall hydrolysis reaction of TEOS can be represented as

follows:

$$Si(OC_2H_5)_4 + nH_2O \rightarrow Si(OH)_n(OC_2H_5) + nC_2H_5OH$$

$$Si(OH)_n(OC_2H_5) \rightarrow SiO_2 + (n\text{-}1)H_2O + C_2H_5OH$$

This hydrolysis reaction can be acid or base catalyzed. The final morphological state of the silica gel is dependent on the pH of the sol solution (LaCourse 1988 and Jones 1989). A high pH (<9) tend to form non-interacting spherical particles. At pH 5-8 the particles coalesce into microgel regions. A low pH (>3) tends to form linear molecules that are occasionally cross-linked. The other silicon alkoxide examined is tetra-methyl-orthosilicate (TMOS) that undergoes similar hydrolysis as TEOS. The water solubility of TMOS is much greater than TEOS which is an important consideration (discussed later). Silica sol-gel reactions are easy to process and have a high tensile modulus plus high compressive mechanical properties. In this study, sol-gel reactions of silicon alkoxides to form silica gels (SiO_2) were considered to mechanically couple the fibrillar structure of liquid crystalline polymers.

Epoxy resins were the other infusion agent that was investigated. Unlike the brittle and high modulus SiO_2 gels, epoxy systems can provide a ductile and low modulus matrix around the fibrils. This ductility could be a critical factor since the high performance polymer fibers undergo a significant amount of processing stresses that may destroy the reinforcing network of a brittle infusion agent.

8.1.2 Friedel-Crafts Reactions

The other approach to increase the interaction between adjacent polymer chains is Friedel-Crafts acylation reactions to covalently bond the benzene rings in the PBO polymer chains. Friedel-Crafts reactions are types of chemical reactions in which an alkyl (RC-) or acyl (RCO-) group is substituted into a benzene ring by reaction of an alkyl or acyl halide (Streitwieser *et al.* 1981). In this study, Friedel-Crafts reactions of difunctional acid chlorides have been examined to bridge the benzene rings on adjacent PBO chains. **Figure 8.1** shows an overall scheme of the Friedel-Crafts acylations. Using a difunctional acid halide, it should be possible to cross-link adjacent PBO polymer chains at various sites. **Figure 8.1** also shows some possible sites for cross-linking the

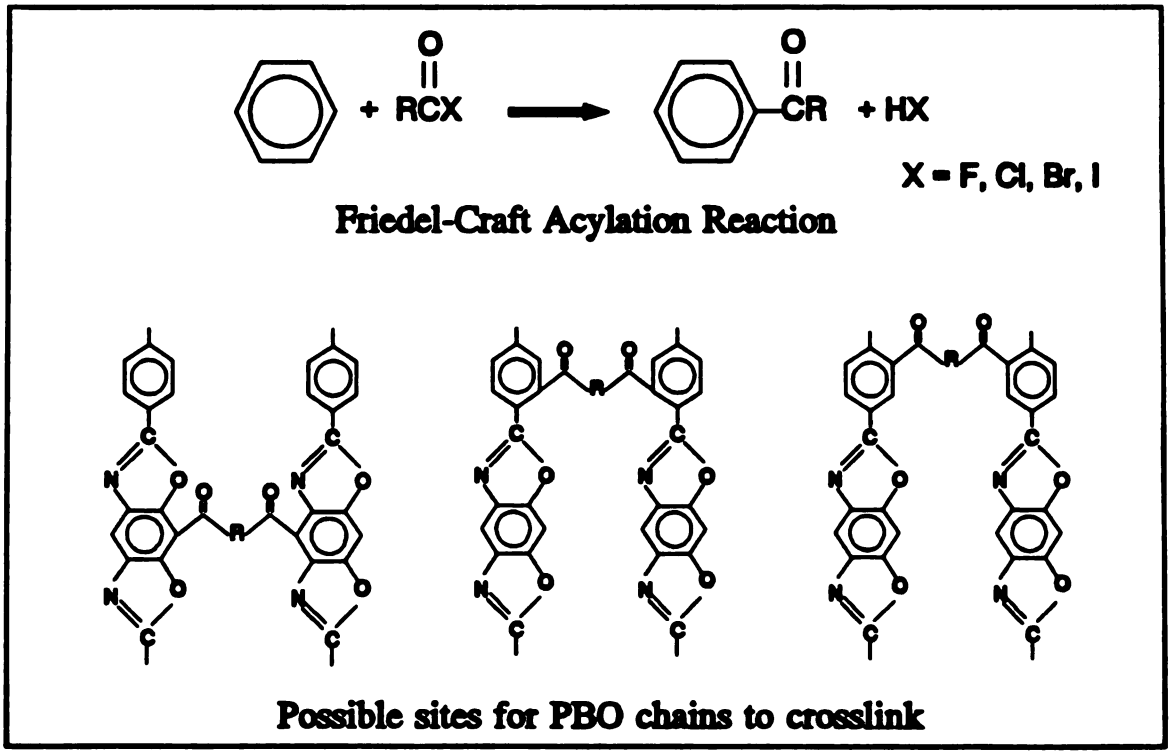

Figure 8.1 - An overall scheme of Friedel-Crafts acylation reaction. A difunctional acid halide can cross-link adjacent PBO chains at several site.

PBO chains, of course, other combinations of intramolecular and intermolecular cross-linking are also possible.

Applications of the Friedel-Crafts reactions to high performance polymer fibers have been reported by Mercx *et al.* (1990), where, oxalylchloride (Cl-OC-CO-Cl) was used to surface treat Twaron aramid fibers. Their proposed treatments assumed that only nitrogen acylation occurs rather than the benzene ring reactions. This work suggests that for the aramid polymers there are more sites for the chemical cross-linking by Friedel-Crafts reactions than there are for the PBO polymer.

8.1.3 Compressional Behavior of Liquid Crystalline Polymer Fibers

Liquid crystalline polymer fibers exhibit low compressive strength and limited compressive elasticity compared to inorganic reinforcing fibers such as carbon and glass fibers. Composites made from liquid crystalline reinforcing fibers have a tensile to compressive strength ratio of 5:1, whereas, carbon and glass fiber reinforced composites have about the same tensile and compressive strengths. **Figure 8.2** compares some compressive strength values determined from single fiber measurements (see Appendix A). The compressive strengths of polymer fibers were measured by observing the onset of kink band formations. **Figure 8.3** shows an optical micrograph of compressive kink bands for PBO fibers. The low compressional properties of the high performance polymer fibers result from their rigid-rod morphology (Deteresa 1985, Dobb *et al.* 1981). These fibers are composed of fibrillar crystallites with poor lateral interactions between adjacent fibrils. **Figure 8.4** shows SEM micrographs of a fractured PBO fiber that

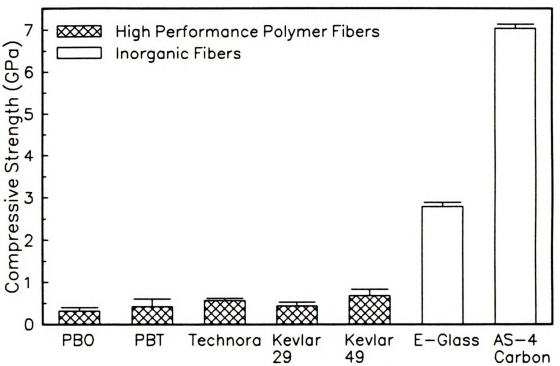

Figure 8.2 - Compressive strength of several high performance polymer and inorganic fibers determined by the single fiber compression test.

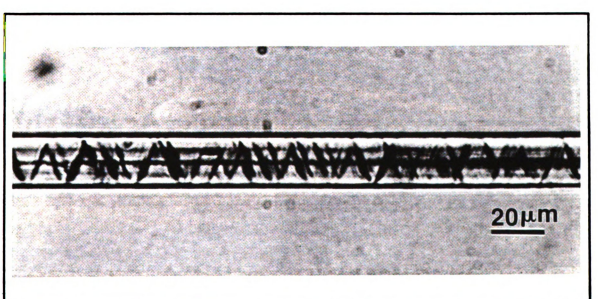

Figure 8.3 - An optical micrograph of compression kink bands in PBO fibers.

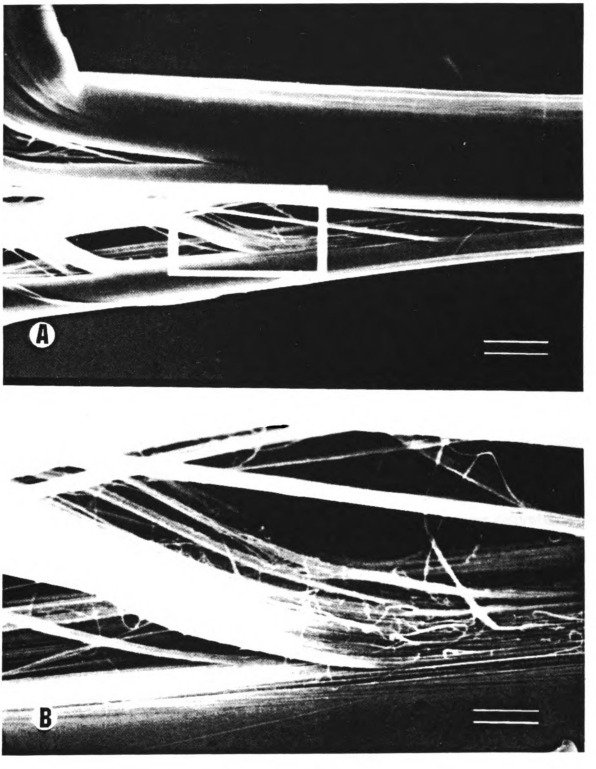

Figure 8.4 - SEM micrographs of a fibrillated PBO fiber.
(A) bar = 10 μm (B) bar = 2 μm

clearly demonstrates the fibrillar morphology of the fiber. On compression the absence of strong lateral interactions results in cooperative buckling of the fibrils that are exhibited as formation of kink bands at oblique angles to the fiber axis (Figure 8.3). Examining the local bending of the PBO fibers by high resolution electron microscopy, Martin *et al.* (1991) have determined that the formation of the kink bands involves bending and/or covalent bond breaking of the rigid-rod polymer. They also observe that kinks are initiated at the fiber surface and then grow towards the fiber interior. This observation suggests surface hardening techniques that can make the kinks harder to initiate may be useful for improving the compressive strength of polymer fibers. Previous investigations suggest that to increase compressive properties of the rigid-rod polymer fibers the lateral interactions between the fibrils must be increase. However, Martin *et al.* (1991) warn that such microstructural modifications will be successful only if they do not introduce additional sites for kink initiations.

For polyethylene fibers, Attenburrow *et al.* (1979) have demonstrated that the compression kink band formation of the fibers are the result of the shear deformation of their lamellar crystals. Kazuyo *et al.* (1975) have reported that during kink band formation of the polyethylene fibers, the fiber axis rotates from the original axis by 70-75° which explains the formation of the helical kink bands.

Deteresa (1985) has investigated the compressive behavior of the aramid fibers. On axial compression the aramid fiber forms regularly spaced helical kink bands at 50° to 60° with respect to the fiber long axis. The compression kinks occur at about 0.5% bending strain but they disappear on removal of the load without any apparent affect on

the fiber tensile properties. Only after approaching 3% compressive strains do the fibers show a 10% loss in tensile strength. Deteresa (1985) has proposed a model for compressive failure by elastic microbuckling of the extended-chain polymers. The model shows, and the experimental results confirm, that the stress required to buckle these fibers is equal to the minimum longitudinal shear modulus of the fiber (not the shear strength). Deteresa also concludes from his model that the compressive strength of extended-chin polymer fibers is about one-third of their torsion moduli.

Cohen (1986) has investigated the structural elements of PBT fibers and films. He proposes that the basic structural features responsible for the mechanical properties are set during the initial coagulation process rather than the later heat treatment and drying processes. Cohen reports that the PBT fibers consist of an interconnected network of oriented microfibrils with "Y-shaped" junctions between the microfibrils. TEM micrographs of the buckled fibers show that the compressive failure of the fiber is the result of the buckling of the individual microfibrils. Cohen suggests that the dimension of the microfibrils significantly influences the compressive strength of the fibers and the post-treatments may perfect the chain packing but do not alter the fibrillar morphology. The measured compressive strength of aramid fibers is about twice PBO or PBT fibers (Figure 8.2). PBO and PBT fibers lack the intramolecular hydrogen bonding interactions that are present in the aramid fibers (Figure 3.1). In addition, the presence of "Y-shaped" microfibril junctions has not been reported for the aramid fibers. Since the "Y-shape" junctions can be the locus of compressive failure, the presence of these junctions may be another limitation of the PBO and PBT morphology.

8.2 EXPERIMENTAL

The polymer fiber examined in this study was p-Phenylene BenzobisOxazole (PBO) aromatic heterocyclic supplied by Dow Chemical (Midland, MI). Through an special agreement with Dow Chemical, the PBO fibers were supplied in two conditions: fibers that were just coagulated in water and were still water swollen (referred to as Wet-PBO in this report), and fibers that had undergone a proprietary drying process after their coagulation (referred to as AR-PBO). The Wet-PBO fibers were examined because their swelled structure was considered more conducive to the infusion of the examined treatments than the high crystalline structure of the AR-PBO fibers.

The epoxy matrix was the DER331/MPDA 75°C/2hr/125°C/2hr system used for the measurements of single fiber compressive test (Appendix A) and interfacial shear strength by fragmentation test (described in details in the Chapter 2). Single fiber tensile strengths were measured by ASTM D3379 tensile test. Fiber diameters were characterized with the aid of a video caliper. Water content of the Wet-PBO after various treatments were measured by a DuPont 951 Thermogravimetric analyzer (TGA), ramped at 10°C/min. from ambient temperature to 400°C. Fiber-matrix internal morphology was characterized by TEM microscopy. Elemental characterizations of the treatments were conducted by AES and XPS techniques.

Solvent exchanges of the Wet-PBO fibers were done by attaching a ~5 inch long wet fiber tow on a stainless steel rod using an aluminum fine wire. The sample rod was then placed in a 6 inch long test tube with a twist-off cap and the tube was filled with the solvent of interest. For mutually immiscible solvents such as water and Freon, a third

transitory solvent such as acetone with mutual solubility in both water and Freon was used to exchange between the two immiscible solvents.

For the sol-gel reactions, two types of silicone alkoxides were examined:

TMOS (tetra-methyl-orthosilicate) $Si(OCH_3)_4$

TEOS (tetra-ethyl-orthosilicate) $Si(OC_2H_5)_4$

Because TEOS is immiscible in water and TMOS is only slowly miscible in water, for some treatments methyl or ethyl alcohols were used as a co-solvent. The various sol-gel reagents and treatment conditions are described in the results section.

For the epoxy treatments, the water in the Wet-PBO fibers were first exchanged with acetone, and then fiber tows were immersed in a dilute solution of DGEBA epoxy (DER331), DDS (DiaminoDiphenyl Sulfone), DETA (DiEtyleneTriAmine), or H31 (a proprietary Dow Curing Agent), dissolved in acetone. The various treatment conditions are also described in the results section.

For the Friedel-Crafts reactions, three difunctional acid chlorides were used:

oxalyl chloride (Cl-OC-CO-Cl)

succinyl chloride (Cl-OC-CH_2-CH_2-CO-Cl)

adipyl chloride (Cl-OC-CH_2-CH_2-CH_2-CH_2-CO-Cl)

The Friedel-Crafts reaction were carried out by exchanging water in the Wet-PBO fibers with dichloromethane (CH_2Cl_2) and then adding acid chlorides into the solvent. Initially, $SnCl_4$ was used as a catalyst, but the reactions were vigorous even without the catalyst as evidenced by a high rate of HCl gas bubbling from the fibers. The treatment reagents consisted of ~1.5 gram acid chloride mixed in ~40 grams of dichloromethane.

8.3 RESULTS AND DISCUSSION

Wet-PBO fibers were chosen for the study of structural modifications because their open and water swollen structure was considered more readily accessible by various infiltration processes. A series of fiber diameter measurements of PBO fibers were conducted to determine how much swelling is present in the wet fibers and how the swelling changes when water is exchanged with another solvent. Fiber diameters were measured while the fibers were being soaked in the same medium as their final solvent, to prevent fibers from drying during the examination.

Table 8.1 lists the PBO diameters for wet, dried, and various solvent exchanged fibers. In general, fibers that were not dried remained swollen even when water was exchanged with other solvents. However, once the fibers were dried, the fibers could not be reswollen by the solvents exchange. These fiber diameter measurements show that in swollen state PBO fibers are about 80% larger than the dried state. The ability to exchange water with other solvent without reducing the fiber volume is critical for conducting treatments that are water inhibited. Thermogravimetric (TGA) measurements of the Wet-PBO fibers also confirm the previous results. TGA weight loss measurements for various treatments of Wet-PBO are listed in the **Table 8.2**. These TGA results suggest that the wet or solvent exchanged Wet-PBO fiber have about 35 wt% of water content before they are dried. However, once the fibers are dried they can not be reswollen by soaking in water again. Both diameter and TGA measurements suggest that the higher temperature drying conditions (400°C) tend to reduce the fiber free-volume more than the ambient drying.

Table 8.1 - Fiber diameter for dried, wet, and solvent exchanged PBO fibers.

Condition	Test Medium	Diameter (μm)[1]
Water swollen	water	26.9 ± 4.1
2 weeks in Ethanol	Ethanol	26.0 ± 4.6
1 day Acetone, 1 day Freon, 1 day Acetone, 1 day water	water	26.3 ± 4.6
1 day Ethanol, 1 day Acetone, 5 days Freon	Freon	27.9 ± 4.7
1 day liquid N_2 Frozen, 1 day ambient dried	water	21.5 ± 4.3
1 day ambient dried, 1 day liquid N_2 Frozen, 1 day ambient dried	water	21.5 ± 4.3
1 day ambient dried, 2 day Acetone	Acetone	20.6 ± 3.6
2 weeks ambient dried, 24 hour water soaked	water	19.3 ± 3.6
1 day ambient dried	dry	18.8 ± 3.8
1 day Ethanol, 1 day Acetone, 1 day Freon, 5 hour ambient dried	dry	21.7 ± 2.9
5 days ambient dried, 400°C dried	water	19.2 ± 3.5
5 days ambient dried, 440°C dried	dry	18.4 ± 3.1

[1] Average of 30 measurements.

Table 8.2 - TGA weight loss measurements for various treatments of Wet-PBO fibers.

Condition	Weight loss (%)
Wet-PBO	36.6 ± 8.3
Wet-PBO → EtOH → Water	34.7 ± 4.6
Wet-PBO 10 min liquid N_2 frozen, 24 hrs in water	37.3 ± 2.3
Wet-PBO 24 hrs ambient dried, 48 hrs in water	9.7 ± 1.1
Wet-PBO 400°C dried, 1 week in water	3.64 ± 2.9

For the Wet-PBO fibers, exchanging water with other solvents appears to affect tensile properties of the final dried fiber. **Table 8.3** lists the tensile properties of the solvent exchanged Wet-PBO fibers. In general, drying fibers at high temperature increased fiber tensile modulus which suggest a higher degree of chain orientation. Exchanging water with acetone or alcohol tend to reduce modulus and tensile strength of the fibers which may be due to partial solubility of the fiber polymer in these solvents, decreasing molecular orientation. These observations suggest that the choice of solvents used in a treatment not only affects the chemistry of the treatment but it could also influence the morphology the fibers.

Table 8.4 lists XPS elemental composition of the AR-PBO, Wet-PBO, 12-hour water soxhlet extracted Wet-PBO, 12-hour methanol extracted Wet-PBO, and 12-hour water

Table 8.3 - Material property data for solvent exchanged Wet-PBO fibers.

Treatment	Tensile Strength (GPa)	Tensile Modulus (GPa)	Diameter (μm)	Fracture Strain (%)
Wet-PBO → RT dried	3.28 ± 0.51	110 ± 11	21.8 ± 2.6	3.3 ± 0.5
Wet-PBO → RT dried *RT→8hr→350°C→8hr→RT*	3.55 ± 0.87	146 ± 14	20.8 ± 2.6	2.8 ± 0.5
Wet-PBO → Acetone → RT dried	2.62 ± 0.31	83 ± 18	22.0 ± 3.0	3.5 ± 0.5
Wet-PBO → MeOH → RT dried	2.78 ± 0.26	77 ± 8	22.3 ± 2.4	4.2 ± 0.3
Wet-PBO → Acetone *RT→8hr→200°C→8hr→RT*	2.86 ± 0.46	115 ± 7	21.7 ± 1.3	2.7 ± 0.4
Wet-PBO → EtOH → CO_2 (*liq.* → *gas*) → RT dried	2.09 ± 0.60	78 ± 9	20.8 ± 2.5	2.4 ± 0.3

RT = Room Temperature

soxhlet extracted Wet-PBO that was dried at 400°C for 1 hour in a nitrogen environment. The AR-PBO appears to have a slightly oxidized surface, but all of the Wet-PBO fibers before heat treatment exhibit about twice the oxygen content of heat treated fibers. **Figure 8.5** shows superimposed narrow scans of carbon, oxygen, and nitrogen for the 12-hour water soxhlet extracted Wet-PBO fibers before and after the 400°C drying. Carbon and nitrogen signals show similar compositions, although, there are some resolution difference between signals of the two treatments. The oxygen signal for the Wet-PBO fibers, however, shows the presence of another type of oxygen in the 531-532 eV region. The lower binding energy oxygen signals typically correspond to more electronegative oxygens; in this case most likely those of carboxylic or ester oxygens in the ketone position. The non-stoichiometric amount of oxygen on the Wet-PBO fibers may be due to presence acidic functionalities that are left from the fiber spinning process and have not been neutralized by the coagulation process.

Table 8.4 - Atomic concentrations for Dow PBO fibers, measured by XPS (average of three runs for each treatment).

Treatment	C (%)	O (%)	N (%)
Stoichiometric	78	11	11
AR-PBO	79.0 ± 0.4	13.2 ± 0.5	7.78 ± 0.37
Wet-PBO	69.7 ± 0.4	23.0 ± 0.8	7.29 ± 0.37
Wet-PBO, 12 hrs soxhlet extracted in water	70.0 ± 0.9	23.3 ± 0.8	6.75 ± 0.13
Wet-PBO, 12 hrs soxhlet extracted in MeOH	68.2 ± 0.5	25.4 ± 1.0	6.38 ± 0.50
Wet-PBO, 12 hrs soxhlet extracted in water 1 hour @ 400°C in 70 cc/min. N_2	77.5 ± 0.4	13.8 ± 0.9	8.63 ± 0.47

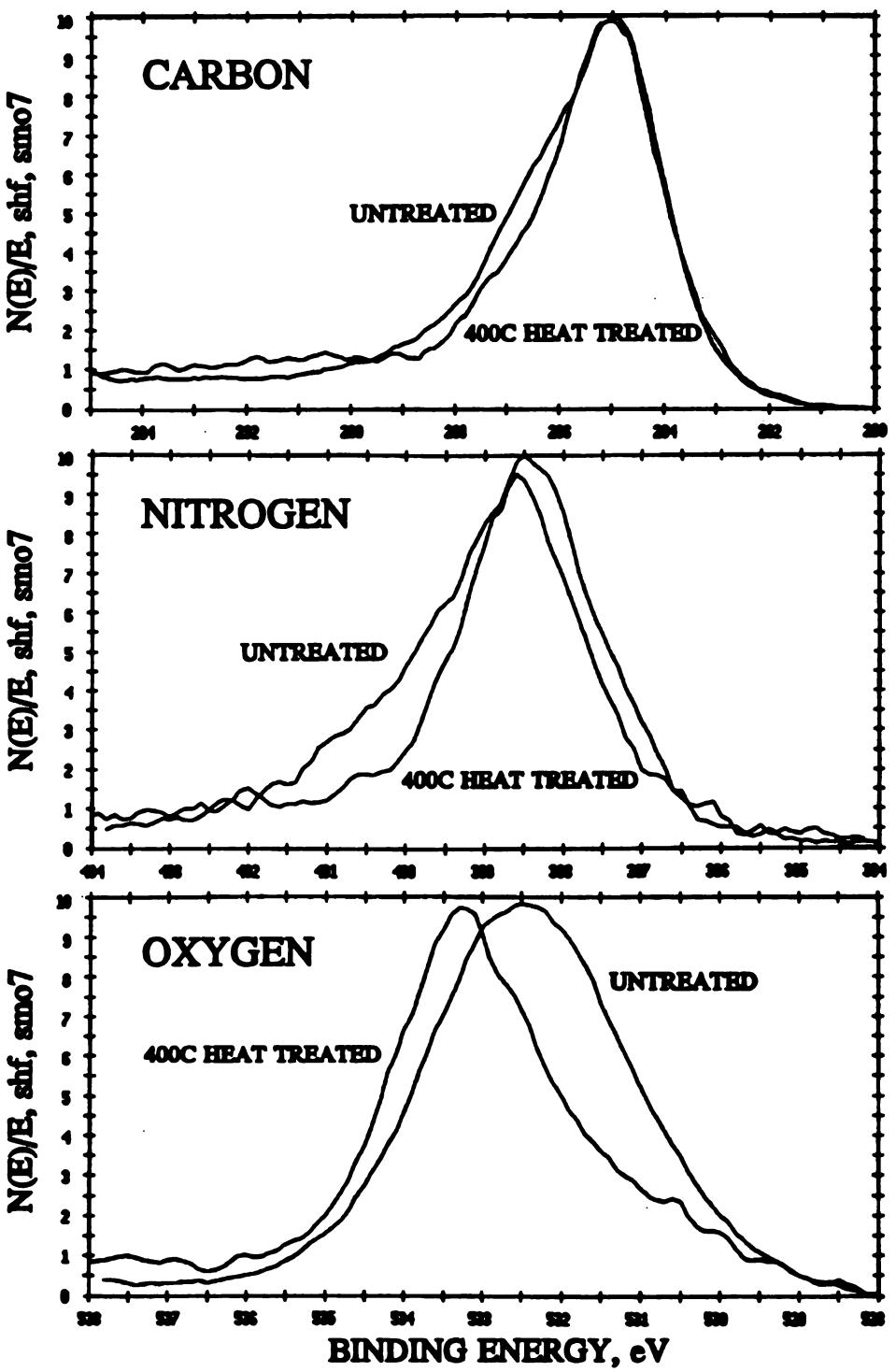

Figure 8.5 - Superimposed XPS signals of carbon, oxygen, and nitrogen regions for the 12 hour water soxhlet extracted Wet-PBO fibers before and after 400°C drying.

8.3.1 Sol-Gel Treatments

The sol-gel approach attempts to form a three-dimensional gel network inside the fiber structure that can reinforce the fibrillar morphology of the liquid crystalline polymer and improve its shear and compressive properties.

The first set of sol-gel treated PBO fibers were provided by Foster-Miller, Inc. (Waltham, MA). A Wet-PBO fiber tow was infiltrated with a silica sol-gel reagent while mounted on a spring-loaded C-shaped metal fixture, and then dried to 350°C. Another tow of untreated PBO fibers underwent the same drying procedure to provide the control material. The target sol-gel concentration was 5 wt% in the fiber.

Table 8.5 compares the tensile, compressive, and interfacial shear strength of the "as received" (DOW PBO XV-0383-C8700975-008) and Foster-Miller control and sol-gel treated PBO fibers. The compressive strength data are determined by Equation A.3

Table 8.5 - Material property data for Foster-Miller (F-M) sol-gel treated and untreated PBO fibers.

Property	Dow As Received	F-M control	F-M Sol-Gel
Tensile Strength (GPa)	3.42 ± 0.55	2.97 ± 0.55	2.51 ± 0.29
Tensile Modulus (GPa)	181 ± 17	197 ± 17	135 ± 15
Fracture Strain (%)	2.05 ± 0.45	1.63 ± 0.26	2.29 ± 0.39
Diameter (μm)	18.8 ± 2.1	16.9 ± 2.3	19.8 ± 2.4
Compressive Strength[1] (MPa)	368 ± 99	457 ± 107	294 ± 100
Interfacial Shear Strength[2] (MPa)	17.8 ± 1.4	15.0 ± 3.0	6.89 ± 0.57

[1] from single fiber compressive measurements using uniform cross-section specimen.
[2] for 175°C cured epoxy matrix.

using uniform-Cross-Section specimen. The sol-gel fibers do not show any compressive strength improvement over the control fibers, however, there is about 15% reduction in their tensile strength. Interfacial shear strength of the sol-gel treated fibers is also about half the untreated values.

The interfacial shear strength reduction of the sol-gel treated fibers can be attributed to the presence of SiO_2 weak boundary layer on the surface of the treated fibers. **Figure 8.6** shows SEM micrographs of the sol-gel treated fibers. The micrographs show two types of silica gel topography, gel is either in the form of large and thick islands or thin nonuniform coatings. With a nominal 5 wt% gel concentration and its accumulation on the fiber exterior, the internal gel concentration is expected to be low. EDX and AES examinations of the sol-gel treated fibers were unable to detect the presence of silicon more than a micron below the surface of the fiber. **Figure 8.7** shows the AES line-scan of Si atoms superimposed on a SEM image of a sol-gel treated PBO-epoxy interphase. Only about 1 μm of Si is present near the fiber-matrix interphase and there is no significant SiO_2 penetration into the fiber structure. TEM micrographs of a sol-gel treated PBO fibers also demonstrate SiO_2 accumulation on the fiber exterior. **Figure 8.8** shows an axially sectioned Sol-Gel treated PBO fiber, showing the gel coating (dark band) around the fiber perimeter. These observations suggest that SiO_2 gel did not penetrate into the bulk of the PBO structure. Furthermore, presence of the SiO_2 surface layer on the sol-gel treated fibers creates a new weak boundary layer between the fiber and matrix which reduces the fiber-matrix interfacial shear strength. Compressive strengths of the sol-gel treated fibers were unaffected by the sol-gel treatments since the

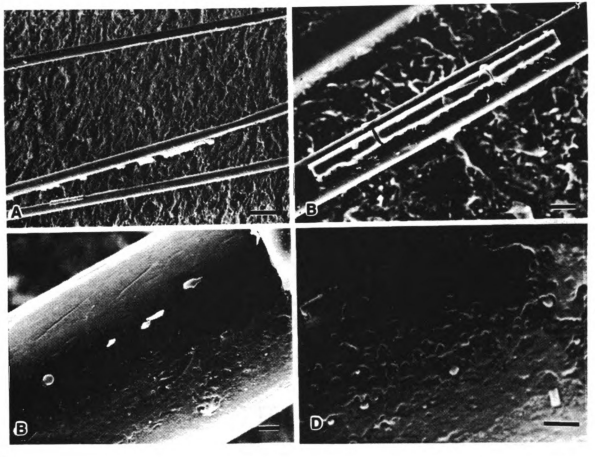

Figure 8.6 - SEM micrographs of Foster-Miller sol-gel treated PBO fibers.
(A) bar = 50 μm (B) bar = 10 μm (C) bar = 2 μm (D) bar = 1 μm

SiO_2 gel network did not penetrate into the fiber bulk.

The previous results demonstrate that evaluation of fiber structural modifications from interfacial shear strength measurements can lead to inaccurate conclusions because of the aberration that may be introduced by the fiber-matrix interphase. For example, a structurally modified polymer fiber with increased shear properties may exhibit reduced interfacial shear strength if a mechanically weak layer accumulates on its exterior. Conversely, compressive tests are insensitive to the extent of fiber-matrix bond strength as long as no debonding occurs before compressive failure (see **Appendix A**). Consequently, compression tests are emphasized for the remainder of this study.

Other sol-gel treatments of the Wet-PBO fibers with various silica sol reagents were

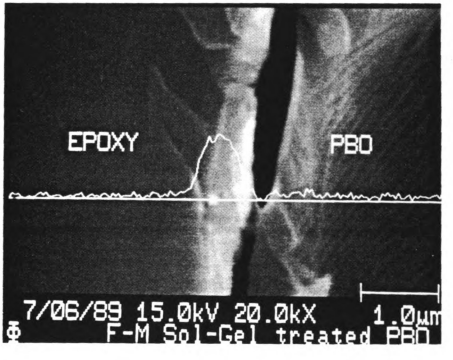

Figure 8.7 - AES line-scan of silicon superimposed on a SEM micrograph of a Foster-Miller sol-gel treated PBO fiber imbedded in an epoxy matrix. (O cross-sectional view).

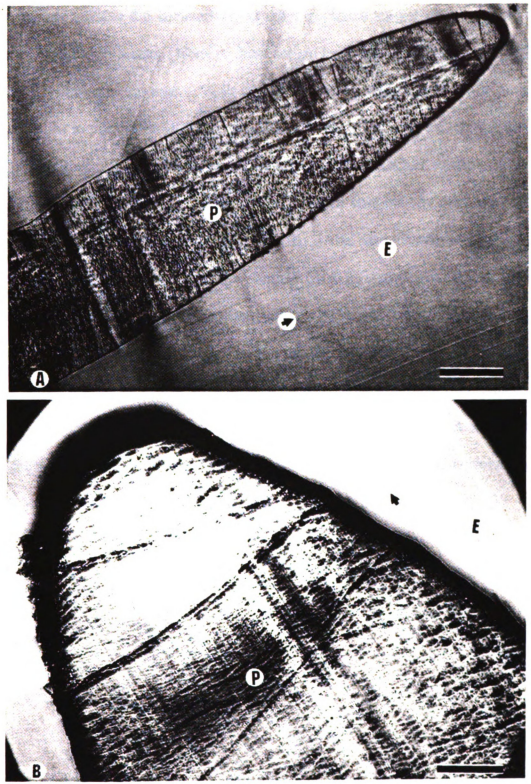

Figure 8.8 - TEM micrographs of an axially sectioned Foster-Miller sol-gel treated PBO fiber. Note the accumulation of kink bands near the fiber exterior.
(A) bar = 5 μm (B) bar = 1 μm

also examined. **Table 8.6** summarizes the other examined sol-gel treatments and their compressive strength results. None of these sol-gel treatments produced any significant compressive strength increase. Their SEM, TEM and AES observations produced similar results to the Foster-Miller sol-gel treated fibers, suggesting that the gel network is not penetrating into the fiber structure for any of these examined conditions.

The inability of the SiO_2 gel to infuse into the fiber core may be due to a diffusion limited mass-transfer phenomena. In Chapter 6, it was demonstrated that sulfonation penetration into a polycarbonate film is limited by a formation of a barrier layer of sulfonated materials. A similar phenomena could be occurring with the sol-gel treatments of the PBO fibers. A fast conversion of sol species into an immobile gel could form a barrier to further sol diffusion into the fiber interior. Furthermore, the acidic surface of the PBO fibers (**Figure 8.5**) may catalyze the sol-gel reactions and accelerate the formation of the gel barrier or form long and linear gel molecules which would have difficulty diffusing into the fiber structure.

Table 8.6 - Wet-PBO sol-gel treatments and corresponding compressive strengths.

Condition	E_T (GPa)	σ_{ef} (MPa)
As Received (heat treated)	181 ± 17	315 ± 78
Wet-PBO 24 hour RT dried	110 ± 11	144 ± 31
1 day RT dried, *RT→8hr→350°C→8hr→RT NT*	146 ± 14	507 ± 102
1 day RT dried, *RT→8hr→350°C→8hr→RT 50g T*	146*	443 ± 74
1 hr sonicated in TMOS, *RT→1hr→150°C→1hr→RT NT*	84*	186 ± 78
TMOS/H_2O/H_2SO_4 (25ml/25ml/0.3ml) for 6hr (removed before gelation) *RT→0.5hr→125°C→0.75hr→RT NT*	84*	133 ± 78
TMOS/H_2O/H_2SO_4 (30ml/30ml/0.3ml) for 6hr (removed before gelation) *RT→3hr→350°C→8hr→RT NT*	84*	324 ± 50
TMOS/H_2O/H_2SO_4 (35ml/35ml/0.3ml) for 6hr (removed before gelation) *RT→3hr→350°C→8hr→RT 50g T*	84*	281 ± 56
80hr in TMOS, 24hr tensioned in water, 24hr RT dried *RT→3hr→350°C→8hr→RT NT*	84*	174 ± 27
TMOS/H_2O/EtOH (30ml/30ml/15ml) for 3 day (removed after gelation), 1 day RT dried *RT→6hr→350°C→8hr→RT 50g T*	74 ± 4	187 ± 66
TMOS/H_2O/EtOH (30ml/30ml/30ml) for 2 day (removed after gelation), 1 day RT dried under tension *RT→6hr→350°C→8hr→RT 50g T*	84*	169 ± 42
TMOS/H_2O/EtOH (30ml/30ml/30ml) for 2 day (removed after gelation), 1 day RT dried under tension *RT→6hr→350°C→8hr→RT NT*	84*	207 ± 59
TMOS/H_2O/EtOH (30ml/30ml/30ml) for 2 day (removed after gelation), 1 day RT dried tension-free *RT→6hr→350°C→8hr→RT NT*	84*	190 ± 59
TMOS/EtOH (30ml/30ml) for 3 day, 24 hr in 100% humidity @ 80°C, 24hrs RT dried	84*	70 ± 10
TMOS/EtOH/Z6020 (20ml/20ml/20ml) for 2 day, 2 day in water, 1 day RT dried	84*	80 ± 15
TMOS/EtOH/Z6020 (20ml/20ml/20ml) for 2 day, 2 day in water, 1 day RT dried, *RT→8hr→400°C→6hr→RT NT*	124 ± 8	298 ± 98
TMOS/EtOH (equimolar) 3 day, 12hr water, 12hr RT dried *RT→8hr→350°C→12hr→RT NT*	146*	287 ± 74
TMOS/EtOH (equimolar + 1cc Acetic Acid) for 3 day, 12hr water, 12hr RT dried, *RT→8hr→350°C→12hr→RT NT*	146*	202 ± 156
TEOS/EtOH (equimolar) 2 day, 12hr water, 12hr RT dried *RT→8hr→350°C→12hr→RT NT*	146*	232 ± 93
TEOS/EtOH (equimolar + 1cc Formic Acid) for 2 day, 12hr water, 12hr RT dried, *RT→8hr→350°C→12hr→RT NT*	146*	343 ± 159

* **Assumed modulus** **RT = Room Temperature** **NT = No Tension** **T = Tensioned**

8.3.2 Epoxy Infusion

The objective of the epoxy treatments is to produce a cross-linked epoxy network within the fiber structure. Table 8.7 lists the various attempts to impregnate the Wet-PBO fibers with epoxy resin and the resulting compressive strengths. In this approach, first the water content of the wet-PBO fibers was exchanged with acetone since acetone is a solvent for both the epoxy and the curing agent. Curing agent molecules are smaller than the epoxy monomer molecules, hence, fibers were first soaked in the curing agent solution to enhance the possibility of their complete infiltration. The acetone exchanged fibers were inserted in a solution of curing agent (DETA, DDS, or H31) in acetone, and were allowed to equilibrate. Next, the fibers were inserted in an epoxy (DER331) and

Table 8.7 - Compressive strengths of epoxy impregnated Wet-PBO fibers.

Condition	E_f (GPa)	σ_{cf} (MPa)
As Received (heat treated)	181 ± 17	315 ± 78
Wet-PBO 24 hour RT dried	110 ± 11	144 ± 31
Wet-PBO 48 hour Acetone washed, RT dried	83 ± 18	99 ± 34
Wet-PBO 13 hour MeOH washed, RT dried	77 ± 8	109 ± 40
AR-PBO DETA/Acetone (1/1) 19 hour → DER331/Acetone (1/6) 5 day, Acetone washed, RT Dried	181*	289 ± 91
Wet-PBO DDS/Acetone (1/4) 12 hour → DER331/Acetone (1/3) 2.5 day, Acetone washed, RT Dried	77*	91 ± 35
RT→1hr→180°C→1hr→180°C→12hr→RT 425g T	122 ± 7	119 ± 31
RT→1hr→220°C→1hr→220°C→12hr→RT 150g T	122*	139 ± 63
RT→1hr→220°C→1hr→220°C→12hr→RT NT	122*	176 ± 71
RT→8hr→350°C→12hr→RT NT	146*	309 ± 97
Wet-PBO Acetone washed 100% H31 2.5 hour, RT Dried	77*	61 ± 38
100% H31 4 days, RT Dried	77*	78 ± 17

NT = No Tension T = Tensioned RT = Room Temperature * Assumed modulus
DETA = DiEtyleneTriAmine DDS = DiaminoDiphenyl Sulfone
H31 = Proprietary Dow Curing Agent DER331 = Proprietary Dow DGEBA epoxy

acetone solution to allow the infiltration and reaction of the epoxy with the curing agent inside the fiber. Finally, fibers were rinsed with acetone to remove excess epoxy or curing agent, and were thermally cured to complete the reaction of the infiltrated epoxy system. **Figure 8.9** shows an AES nitrogen line-scan of DETA/Acetone soaked wet-PBO fiber. In this line-scan, contribution of the nitrogen from the fiber and the matrix molecules has been subtracted from the AES background and the remaining signal is due to DETA distribution. This nitrogen line-scan confirms that DETA has completely infiltrated the fiber.

None of the attempts given in **Table 8.7** resulted in significant compressive strength increases or fiber modulus changes, which suggests that the epoxy network is not penetrating into the fiber interior. The lack of epoxy infiltration is probably due to its large monomer size. Apparently, even though swollen wet-PBO fibers have 80% larger volume than the dried fibers, their free-volume is not freely accessed by large molecules such as the epoxy.

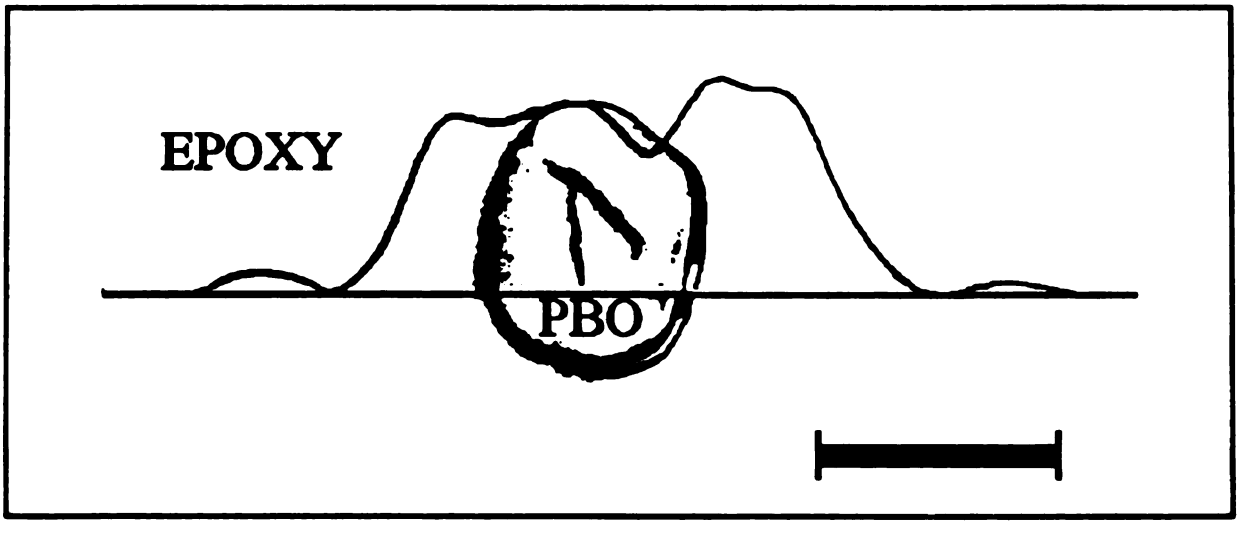

Figure 8.9 - AES nitrogen line-scan of a DETA infiltrated wet-PBO fiber, showing the digitized image of a fiber cross-section embedded in an epoxy matrix. bar = 25 μm

8.3.3 Chain Cross-linking by Friedel-Crafts Reactions

Table 8.8 compares the tensile properties of the PBO fibers treated with the three types of Friedel-Crafts treatment reagents. All of the treated fiber show reduced tensile strength and fracture strain, however, the fiber tensile moduli were unaffected. Since the tensile strength of the fibers are defect controlled, while, the fiber tensile modulus is bulk controlled, the data suggest that the treatments have not penetrated into the fiber structure and have only affected fiber surface morphology. **Figure 8.10** shows TEM micrographs of the oxalyl and succinyl treated PBO fibers. These TEM micrographs show the presence of a dark band around the fiber perimeter that is about 100 nm wide. This dark band is presumably the boundary layer of the reaction penetration. Therefore, TEM observations suggest that the Friedel-Crafts reactions have not proceeded into the fiber bulk and its penetration has been limited to the fiber exterior. The diffusion limitation of the Friedel-Crafts treatments is similar to the sulfonation diffusion limited mass-transfer problems that have was discussed previously; the treated surface forms a diffusion barrier that block the access of mobile reactive species into the fiber interior.

Table 8.8 - Material property data for Friedel-Crafts treated Wet-PBO fibers.

Treatment	Tensile Strength (GPa)	Tensile Modulus (GPa)	Diameter (μm)	Fracture Strain (%)
Wet-PBO → RT dried	3.28 ± 0.51	110 ± 11	21.8 ± 2.6	3.3 ± 0.5
Oxalyl Chloride reacted	1.78 ± 0.57	112 ± 9	19.8 ± 4.4	1.87 ± 0.57
Succinyl Chloride reacted	2.11 ± 0.40	108 ± 15	22.5 ± 3.7	2.44 ± 0.50
Adipyl Chloride reacted	1.24 ± 0.32	101 ± 16	20.8 ± 3.1	1.30 ± 0.28

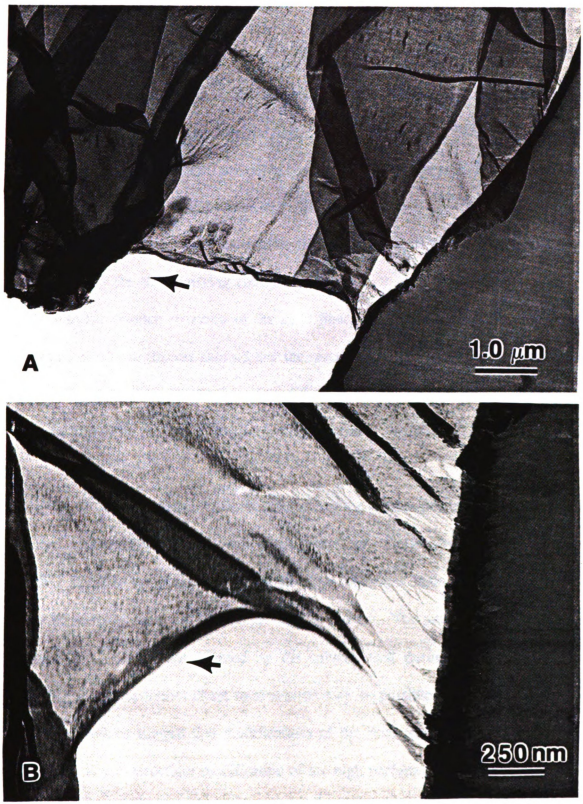

Figure 8.10 - TEM micrographs of (A) oxalyl and (B) succinyl treated PBO fibers showing only a ~100 nm of reaction penetration.

8.4 CONCLUSIONS

- Examination of water swollen PBO fibers show about 80% larger fiber volume for the swollen fibers compared to dried fibers. The swelling of the PBO fiber remained unchanged through different solvent exchanges, however, once the PBO fibers were dried their structures could not be reswollen.
- The Wet PBO fibers show an excess presence of carboxylic oxygen which was removed by the 400°C drying condition.
- Despite the swollen structure of the PBO fiber, the results of sol-gel, epoxy and Friedel-Crafts treatments showed that the reactive species were not penetrating into the fiber interior. Formation of a diffusion barrier by the reacted species is postulated to be the reason for the limited treatment penetration.

Results of this study suggest that the structure of the swollen polymer fiber has critical influence on the mechanical properties of the dried fiber. The free-volume of the swollen wet-PBO fibers is not easily accessible to large molecules making the infusion of a second reinforcing phase a difficult approach to execute. The mechanical properties of the dried PBO fiber were affected by the solvent used during the swollen phase, suggesting that the polymer chain reorientation may be possible in the swollen phase. These observations suggest that modifications of the fiber morphology in the swollen phase is the key to structural modification of the high performance polymer fibers.

CHAPTER 9

Conclusions & Recommendations

The goals of this dissertation were: to investigate structural properties of high performance polymer fibers that affect their adhesive behavior; to develop a fundamental understanding of the fiber structural limitations; to evaluate several novel techniques that can enhance the fiber adhesive performance properties; and to suggest ways to improve adhesive properties of the high performance polymer fibers.

During this study, several important polymer treatments were investigated and their particular results have been discussed in their corresponding chapters. This chapter presents the main conclusions of this dissertation on the structural properties of high performance polymer fibers and their effects on the fiber-matrix adhesion. Some recommendations for further studies on adhesive properties of high performance polymer fibers are presented.

9.1 CONCLUSIONS

Results of this study suggest that the adhesive properties of the high performance polymer fibers may be limited by the fiber surface morphology and/or wetting properties. Polymer treatment techniques examined in this study demonstrated their ability to overcome the surface limitations of the polymer fibers. **Table 9.1** lists the particular effectiveness of each polymer treatment on fiber-matrix adhesion enhancement mechanisms. In general, fiber-matrix wetting compatibility could be improved by all of the examine polymer treatments. Surface treatments which etch the polymer substrate to remove a weak surface layer on the fiber (*e.g.* PBO) and/or introduce sites for mechanical interlocking with the resin, were very effective for enhancing the fiber-matrix mechanical interactions. The polymer treatments also introducte new active sites for chemical bonding between fiber and matrix molecules.

Table 9.1 - Adhesion enhancement mechanisms introduced by various treatments of the high performance polymer fibers.

Treatment	Fiber-Matrix Adhesion Enhancement Mechanism			
	Wetting	Weak skin removal	Active surface functionalities	Mechanical interlocking
Coupling Agents & Polymer Coatings	+			
Plasma Treatments	+	+	+	+
Chemical Treatments	+		+	
Ion Implantations	+		+	+

The examined polymer treatments could increase the interfacial load transfer capacity of the high performance polymer fibers to the point where internal fiber fibrillations would occur, indicating that the fiber lateral cohesive strength has become the limiting factor. Although, interfacial shear strength (ISS) increases obtained by some of these treatment techniques are significant relative to the untreated values, these ISS improvements are still far lower than values measured for inorganic reinforcing fibers.

The results of polymer surface treatments suggest that surface morphology and/or wetting properties of high performance polymer fibers can limit their adhesive properties, however, once these limitations are overcome fiber lateral cohesive strength becomes the limiting factor. Therefore, the key to improving the fiber-matrix adhesion is to enhance both adhesive and cohesive properties of high performance polymer fibers.

Structural modifications of the high performance polymer fibers to reinforce lateral cohesive strength of the polymer fibers were attempted using approaches to infuse a secondary reinforcing phase (sol-gel, epoxy) or to chemically cross-link adjacent polymer fibrils (Friedel-Crafts reactions). These attempt were unsuccessful since the treatments were not penetrating into the fiber bulk structure. In these attempts, the penetration of the reacting phase was found to be hindered by formation of a barrier layer of reacted materials that blocked diffusion of the reaction front.

9.2 RECOMMENDATIONS

Several other workers (Deteresa 1985, Dobb *et al.* 1981, Cohen 1986) have investigated the morphology-property relations and compressional behavior of high performance polymer fibers, however, the process of the compressive failure is still not well understood. For example, it is not clear how a compressive failure initiates and propagates. An understanding of the compressive failure mechanism is important and should be pursued further.

The complication introduced by formation of a diffusion barrier during structural treatments of the polymer fibers suggests that post-treatment of these fibers is a difficult approach to the fiber structural modification. Manipulation of fiber internal and surface morphology during its manufacturing should be explored as the next step to modifying morphological properties of high performance polymer fibers. Infusion of a second phase into the polymer dope before spinning and coagulation may provide the desired mechanical reinforcement of the fiber fibrillar structure. Silicon alkoxides would be suitable candidates for the addition into the polymer dope because of their intrinsically high shear and compressive modulus as well as their ability to withstanding high processing temperatures. After the fiber spinning and its introduction into the water coagulation bath, the silicon alkoxides can quickly react with water to form the gel network. The presence of the solvent acid should catalyzed the sol-gel reaction and form long silica polymers chains that can tie between the adjacent fibrils.

Another area of interest that should be pursued is the modeling of various polymer surface treatments. Currently, there are numerous polymer surface treatment techniques

available; however, modeling of these treatment processes has been hindered by the lack of information on their treated interphase composition. The new sample preparation technique for electron beam analysis of polymers that was developed during this dissertation allows for data collection on interphase composition and distribution of the polymer treatments. Improved control of polymer treatments can be achieved by modeling and understanding their treatment processes.

Developing an analytical understanding of the diffusion-limited polymer surface treatments should provide valuable insights to approaches for controlling the penetration depths of these treatments. For the structural modification techniques examined in this dissertation, this knowledge is critical to achieve deep infiltration of treatments.

APPENDICES

APPENDIX A

Compressive Strength Measurements of High Performance Polymer Fibers

Compressive properties of reinforcing fibers are difficult properties to measure. Test method dependency and various failure criterion have produced large scatter in the reported values of the reinforcing fibers compressive properties. In this appendix, some of the techniques for measuring single fiber compressive strengths are reviewed and various fiber compressive failure criteria are discussed. Particular attention is given to the compressive properties of high performance polymer fibers. A new variation of an embedded single fiber compression test is also introduced.

A.1 Compression Measurement Techniques

There have been many techniques developed for the compression testing of fiber reinforced composites, however, presently there appears to be no universally accepted standard. The inconsistencies of compression testing are the result of matrix and interfacial dependencies of compressive properties and variabilities of compressive failure modes. Some aspects of these matrix and interfacial dependencies are briefly discussed and then single fiber techniques and their fiber failure criteria are reviewed.

Compressive failures of fiber reinforced composites are typically the result of the microbuckling of the fibers (Agrawal *et al.* 1980). Most inorganic fibers such as glass or carbon fibers have much higher compressive strength than polymer matrices. During the compression of an inorganic fiber and polymer matrix composite, the Poisson's ratio difference between fiber and matrix can introduce transverse stresses at the fiber-matrix interface that results in matrix yielding and/or fiber-matrix interfacial debonding before the fiber microbuckling occurs. For these composites, a strong interface and/or high matrix modulus can help to delay the onset of the fiber microbuckling. Therefore, matrix and interfacial conditions could critically affect the onset of fiber compressive failures.

Matrix and interfacial properties can also influence the ultimate tensile properties but to a lesser extend than the compressive properties. Typically, in the fiber reinforced composites with polymer matrices, the fiber is more brittle than the matrix and tensile failures are initiated by the fiber breakage at a defect or weak point. Once a crack is initiated it can then propagate through the matrix to produce another fiber failure or join

other cracks and eventually cause ultimate failure of the composite. Therefore, matrix and interfacial conditions that affect the crack prorogation can also affect the ultimate composite tensile properties. Madhukar *et al.* (in press) have investigated the effects of surface treatments on tensile and compressive properties of carbon fiber-epoxy composites. Using the same carbon fiber with different surface treatments, their work showed that the ultimate compressive properties are more matrix sensitive than the tensile properties for these composites.

Many workers have compared the various compression test methods for composite materials. Schoeppner *et al.* (1990) have published a comprehensive review of the compression test methods for polymer matrix composites, concluding, that no simple and reproducible compression test technique is yet available. Chou *et al.* (1980) have examined the test conditions that complicate compressional properties measurements. Working with glass-epoxy composites, they showed that the method of specimen gripping, fiber volume fraction, and fiber alignment all have a pronounced effect on the measured compressive properties. Using three test fixtures with different specimen loadings, Berg *et al.* (1989) have shown that direct end loading can result in premature failures because of end crushing and splitting of the test specimen and recommended shear loading such as those used in the IITRI or Celanese fixtures. Finally, because of the strong matrix dependency of the compressive properties the variation in the specimen fabrication technique can introduce significant scatter in the composite compressive values.

Problems encountered in compression testing of the fiber reinforced composites are

even more severe in the case of organic reinforcing fibers such as aramids and polyethylene fibers. Rueda *et al.* (1990) have shown that the standard compression tests are inadequate to measure the compressive properties of the Kevlar-Epoxy composites. The low level of the fiber-matrix adhesion aggravates the specimen loading problems (end crushing and splitting). Chou *et al.* (1980) also demonstrated that the critical Euler buckling load is significantly reduced if transverse failure occur during testing. Another difficulty is the lack of a clear failure criteria for organic fiber compression testing. As shown in the Chapter 8, the organic fiber have low inherent compressive properties and exhibit compressive failure by formation of the compressive kink bands (**Figures 3.11, 3.12, 5.4, and 8.2**). However, during composite compression testing, only gross failures of the test specimen is recorded, and the individual kink band formations of the fibers are not monitored. The aggravated problems with compression testing of the organic fiber composites suggests that the single fiber techniques may be better suited for the unambiguous compressional evaluation of these fibers.

Single fiber techniques eliminate or simplify the matrix dependency, and allow the in-situ fiber failure process to be closely monitored. The quantities of fiber needed in the single fiber techniques are far less than in the composite test techniques, making them attractive at the early stages of fiber development. Although, among various single fiber techniques, there is significant scatter in reported data on any particular fiber, the interpretation of this data is simpler than for composites.

A.2 Single Fiber Compression (SFC) Technique

In this test a single fiber is embedded along the center of a 0.75 inch long uniform cross-section or curved neck epoxy coupon. **Figure A.1** illustrates the three specimen geometries that can be used. The dogbone sample geometry is the new variation of the SFC tests that is introduced in this report. These SFC tests are conducted by loading a specimen at its ends and compressing it slowly until a fiber compressive failure is detected in the gauge section. The fiber compressive failure process is monitored with the aid of a transmitted light microscope at ~200× magnification. For the curve-neck specimen the first compressive failure occurs in the specimen neck region where stress

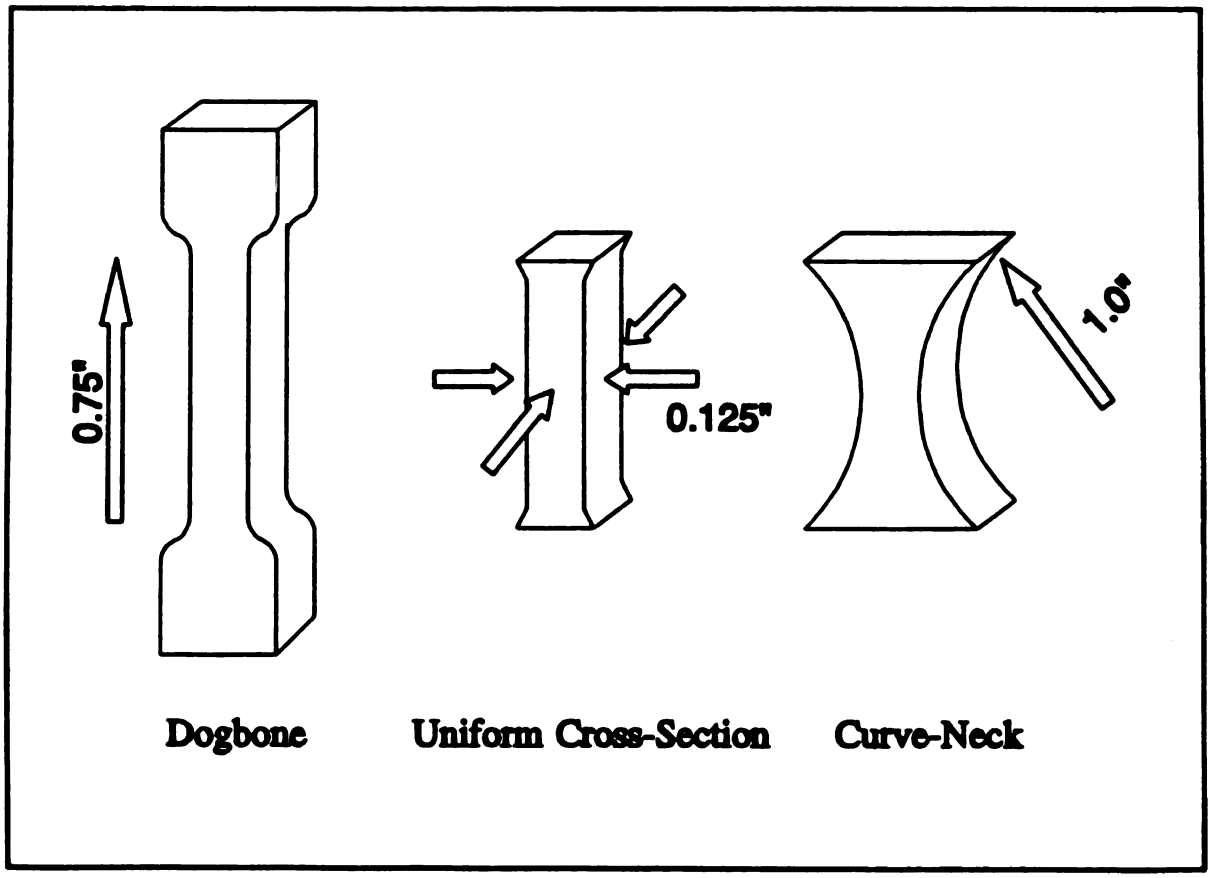

Figure A.1 - Test specimen geometries for the single fiber compression tests.

is concentrated, facilitating detection of the first failure. For the other two test geometries the first fiber failure could occur anywhere along their 0.75 inch long gauge length making the detection of the first failure somewhat more difficult. The dogbone geometry, however, has a major advantage over the other two sample geometries in ease of specimen alignment. Because a dogbone specimen could be gripped at its ends, with the grips loose the sample could be gently pulled to align the sample, then grips are fastened tightly and the sample is tested for compression. The ease of sample alignment and the rigid gripping of the dogbone samples is also a major safety advantage especially for the measurements of high compressive strength inorganic fibers.

The fiber compressive strength (σ_{cf}) can be related to the load (P) at the observation of the first compressive event:

$$P = \sigma_m A_m + \sigma_f A_f = \epsilon (E_m A_m + E_f A_f) \tag{A.1}$$

where σ_m = Matrix stress; ϵ = Fiber and Matrix strain; A_m = Matrix cross-sectional area; A_f = Fiber cross-sectional area; E_m = Matrix compressive moduli; E_f = Fiber compressive moduli

Equation A.1 assumes that fiber and matrix undergo the same strain deformation (ϵ). **Equation A.1** can be rearrange to obtain:

$$\sigma_{cf} = \frac{P}{A_f + \frac{E_m}{E_f} A_m} \tag{A.2}$$

In general, the fiber cross-sectional area (A_f) at most contributes by less than 0.2% to above equation and its contribution can be ignored:

$$\sigma_{cf} = \frac{P E_f}{E_m A_m} \tag{A.3}$$

Equation A.3 applies to any SFC specimen geometry as long as the fiber and matrix undergo the same strain deformations (*i.e.* no debonding occurs before the fiber compressive failure). The equation becomes invalid when debonding occurs (similarities of the organic fiber and matrix Poisson's ratio restrain such large gap formations). The curve-neck specimen is more sensitive to the effects of fiber-matrix debonding that the uniform cross-section test geometries. The load concentrations in the neck region of the curve-neck specimen causes the debonding to always occur in the neck region, whereas, with the uniform cross-section specimen even if the debonding occurs in some regions, there may be bonded regions that could be used to monitor the fiber compressive failure events.

An Study by Bazhenov *et al.* (1989) have shown that prior to the fiber failure the tensile and compressive modulus of organic fibers are similar, therefore, **Equation A.3** is evaluated using fiber and matrix tensile moduli. **Table A.1** compares the results of the SFC tests with other literature values for some high performance polymer fibers. The SFC test specimen were cast with the DER331/MPDA epoxy system cured 2 hours at 75°C followed by 2 hours at 125°C (see Chapter 2).

For the SFC tests the dogbone sample geometry tend to provide higher values than the curve-neck sample. For the high performance polymer fibers, detection of the first kink band is more laborious in the long gauge length of the dogbone samples than in the short neck region of the curve-neck samples. Therefore, the very first kink band formation could be missed when examining the dogbone samples leading to slightly higher results than those obtained by the curve-neck samples.

The SFC and Cantilever-Bending tests show similar compressive strength values for Kevlar-49, PBO, and PBT fibers. Recoil, Loop, and composite tests, however, only show trend similarities. Comparing aramid and copper wire compressive yield, Bazhenov *et al.* (1989) have suggested that the epoxy matrix constrain the kink formation of organic fiber failure, thus, the compressive strength of the embedded fibers should be greater than an isolated fiber. The higher matrix content the higher this constraining effect, therefore, single fiber composites (such as SFC and Cantilever Bending) should yield higher compressive strength values than multifilament composites or isolated fiber tests (Recoil and Loop).

Table A.1 - Fiber compressive strengths (MPa) from various test methods.

Fiber	E_f (GPa)	SFC tests		Cantilever Bending	Recoil[1]	Loop[1]	Compo-site
		Curve-Neck	Dogbone				
Kevlar-49	108	682 ± 152	648 ± 95	620 ± 63[2] 745[3]	365	740 790	400[1] 450[1,2]
Kevlar-29	94	545 ± 118	626 ± 76		350[1]		400[1] 414[3]
Technora	84	565 ± 57	614 ± 53				235[4]
PBO	181	315 ± 78	369 ± 154	276[3]	200	680	200[1]
PBT	258[5]	276 ± 117[5]		270 ± 75[2]	275	680	340[1] 310[2]

[1] Allen (1987) [2] Deteresa (1985) [3] Kumar (1989) [4] Takata (1987) [5] Drzal (1986)

APPENDIX B

Thermodynamics of Surface Tension

Newly formed liquid surfaces and interfaces can assume thermodynamic equilibrium quickly, however, the same is not true for solid surfaces. Therefore, the changes introduced by surface treatments on solids can result in thermodynamically metastable surface properties. There is evidence of changing adhesive properties on aging of treated polymer surfaces. For corona treated polyethylene films Carley *et al.* (1978) has shown the decay of the polar component of surface free energy with time that may be caused by reaction of surface oxidized species with airborne contaminates (Kinloch 1987). Corona treated poly(ethylene terephthalate) exhibits similar changing adhesive properties that are attributed to redistribution of the surface polar groups to form internal hydrogen bonding (Kinloch 1987). The dynamic surface properties of treated solid substrates are the result of the thermodynamic tendency of the surface to achieve its state of equilibrium.

Defay *et al.* (1966) have presented a discussion of non-equilibrium surface tension that provide insight into the thermodynamics of surface aging. When two phases ' and " are separated by an interface *b* a general change of Gibbs free energy of the system is given by:

$$dG = -SdT+V'dp'+V''dp''+\gamma dA+\sum_i \mu_i' dn_i'+\sum_i \mu_i'' dn_i''+\sum_i \mu_i^b dn_i^b \quad \text{(B.1)}$$

where G = Gibbs free energy; S = Entropy of the system; T = Temperature; V = Volume of the phase; p = Pressure of the phase; A = Interface area; n_i = Number of moles of component i; γ = Surface tension; μ_i = Chemical potential of component i

At constant temperature and pressure the contribution of the interface to the Gibbs free energy of the system (surface free energy) is:

$$dG^b = \gamma dA + \sum_i \gamma_i^b dn_i^b \quad \text{(B.2)}$$

The condition for spontaneous changes at constant temperature and pressure is the reduction of Gibbs free energy ($dG \geq 0$), therefore, equation (B.2) shows that the interface has a natural tendency to diminish its area, surface tension, or accumulate low free energy species.

Defay also derives a generalization of the classical Gibbs surface tension equation that is valid for non-equilibrium systems:

$$d\gamma = -S^b dT - \sum_i \Gamma_i d\mu_i^b + \sum_i \epsilon_i' dc_i' + \sum_i \epsilon_i'' dc_i'' \quad \text{(B.3)}$$

where Γ_i = Surface excess of component i = n_i/A

c_i = molar concentration of component i

ϵ_i = cross-chemical potential of component i = df/c_i

f = Helmholtz free energy per unit area

Function ϵ_i represents the influence of concentrations of species *i* on either side of the interface on the surface free energy. At equilibrium the cross-chemical potential terms become zero and equation (B.3) converges to the classical Gibbs surface tension equation, thus, at constant temperature and equilibrium:

$$d\gamma = -\sum_i \Gamma_i \, d\mu_i^b \qquad \text{(B.4)}$$

If only surfactant *D* accumulates at the interface, then equation (B.4) becomes:

$$d\gamma = -\Gamma_D d\mu_D \qquad \text{(B.5)}$$

Assuming dilute surfactant concentration *i.e.*

$$d\mu_D = RTd\ln c_D = RT\frac{dc_D}{c_D} \qquad \text{(B.6)}$$

where R = Gas constant. Then equation (B.5) becomes:

$$\frac{d\gamma}{dc_D} = -RT\frac{\Gamma_D}{c_D} \qquad \text{(B.7)}$$

Equation (B.7) shows the reduction of surface tension when the surfactant accumulates at the interface (Atkins 1978).

APPENDIX C

A Novel Sample Preparation Technique for Ion and Electron Beam Analysis of the Fiber-Matrix Interphase in Polymer Composites

Applications of ion and electron beam analysis to non-conductive and polymeric material surfaces can be hindered by sample charging problems. Interaction of the probe beam with the sample in surface sensitive techniques such as Auger Electron Spectroscopy (AES), Ion Scattering Spectroscopy (ISS), and Secondary Ion Mass Spectroscopy (SIMS) can produce charged surfaces that interfere with the analysis process (Werner *et al.* 1976). A novel sample preparation technique for ion and electron beam analysis of the fiber-matrix interphase in polymeric composite materials has been

developed. The proposed technique can also be adapted for analysis of other nonconductive materials.

Sample preparation by fracture and polishing techniques (Gabriel 1985) have several significant limitations in composite material applications. Use of typical fracture approaches for preparation of fibrous composite material samples can result in fiber pullout and rough surface topographies that promote surface charging. Polymers are also sensitive to surface polishing techniques and different constituents within the composite may be left with various topographies because of differences in abrasion rates. The sample preparation technique described in this report employs a diamond knife to prepare a smooth surface that assists in preventing surface charging, with the further advantage of producing highly clean surfaces and fine control for positioning of the interested area.

Our sample preparation technique is a modification of the standard Transmission Electron Microscopy (TEM) microtoming technique (Klomparens *et al.* 1986, Dawes 1971, Sawyer *et al.* 1987). To examine the fiber-matrix interphase, the fiber must be embedded in a polymer matrix. Low fiber volume fraction composites or a single fiber embedded in a matrix coupon are the appropriate samples. In general, there must be enough matrix around the fiber to allow razor blade trimming of a sample block. With high fiber volume fraction composites (*i.e.* many fibers per given cross section) preparation of the sample block is difficult.

The sample block must be trimmed first to fit the instrument sample holder. The dimensions of a block depends on the specific sample holder used; a rectangular block of 2×2×8 mm is typical. **Figure C.1** shows an unmounted sample block and PERKIN

ELMER sample holders (fracture type) with a sample block mounted in their center. To prepare the sample for the holder, the sample can be scored with a razor blade and then tapped to fracture the matrix. All the razor blades used in the cutting processes are new blades and their edges are cleaned with methanol soaked cotton swabs to remove contaminants. Once the sample block is formed it is cleaned in methanol and then handled with tweezers only.

Figure C.2 shows the major sectioning orientations possible for a fiber. Radial cuts provide circular cross-sections of the fiber-matrix interphase but the analysis area is relatively small. Axial and lateral cuts provide a greater analysis area but are more difficult to prepare. The axial cuts are generally preferred over the lateral cuts because the axial cuts are made parallel to the fiber-matrix interface that minimizes any smearing of phase boundaries.

Sectioning orientation of the fiber must be decided on before preparing the sample block because it can affect the trimming procedure. In radial cuts the block face always contains the fiber end and trimming can start around the fiber end (**Figure C.3A**). In axial and lateral cuts the fiber may be initially covered by polymer matrix so the matrix must be removed before reaching the fiber (**Figure C.4A**). Radial sectioning is described first. Axial and lateral cuts require additional steps that are described later.

For all sectioning orientations, the top of the sample block must be hand trimmed into a trapezoid of dimensions of about 0.25 mm (**Figure C.3C**) to avoid damaging the knife edge during diamond knife sectioning. To trim the trapezoidal block the sample is placed in a specimen grip under a sectioning microscope and the top face of the sample is

viewed at 10× to 50× magnification.

Figure C.3 shows the process of trapezoidal block preparation for the radial cuts. First, the location of the fiber is isolated by four large razor blade marks about 1 mm apart (**Figure C.3A**). With the fiber at the center of the blade marks the epoxy outside the marks is trimmed at 45(de angles (**Figure C.3B**). Next, the matrix around the fiber is gradually trimmed to a shallow depth (~0.5 mm) until two parallel edges and two angled edges about 0.25 mm apart around the fiber form the trapezoidal block (**Figure C.3C**). Razor blade cuts are always made at 45° and away from the trapezoidal block since otherwise a crack can initiate that fractures the small trapezoidal block at its base.

Figure C.4 shows the process of trapezoidal block formation for the lateral cuts. The fiber is initially covered by the matrix (**Figure C.4A**). The matrix over the fiber is removed at a shallow angle (~10°) until a fiber portion is exposed (**Figure C.4B**). The region of thin matrix coverage adjacent to the exposed fiber end is the region for trimming the trapezoidal block. This trapezoidal block is prepared in a similar procedure as the radial cuts. The thin matrix over the fiber can be removed during the diamond sectioning or partially left for sputter depth profiling through the fiber-matrix interphase. The same procedure is applied for the axial cuts.

Before the final trimming of the trapezoidal block face with a diamond knife, the sample block is removed from the specimen grip and is placed (face up) in a gold plasma coater. The block is covered with a thick gold coating (~100 nm). This coating is important in alleviating charge buildup on the analysis surface. The gold coated sample block is now ready for the final surface trimming by a diamond knife and is placed back

in the microtoming setup.

Sectioning of high performance fibers requires a diamond knife. A solution of de-ionized water with a low concentration of acetone (~ 1 droplet of acetone per 20 ml of water) is used to fill the diamond knife boat. Acetone reduces the contact angle of the water to produce better wetting of the knife edge. The trapezoidal shape of the sample block is selected to specify the diamond knife cutting direction which is from the wide base edge to the opposing parallel edge. The trapezoidal block is oriented so its wide base edge contacts the knife edge first. The knife is advanced manually toward the trapezoidal block face until reflection of the block face off the water meniscus is observed. The knife is then slowly advanced toward the block at 1 μm steps until cutting begins. Several 1 μm sections are cut to remove artifacts from the razor blade trimming. The thickness setting is adjusted to cut several ultra-thin sections (50 to 100 nm) to prepare a smooth and clean final surface.

At the completion of this stage a small, flat, and clean surface for analysis having gold coated boundaries is obtained. Every analysis area is at most 0.12 mm away from the conductive boundaries. For most materials this is enough to eliminate the charging problems, however, if the charging is still present, a fine gold coating (< 1 nm) can be applied onto the surface.

Two examples of sample preparations are illustrated. All sample preparations were carried out on a Reichert-Jung ULTRACUT E microtome and setup for analysis on a PERKIN ELMER PHI 660 Scanning Auger Multiprobe. **Figure C.5** shows SEM micrographs of an axially cut nickel coated carbon fiber embedded in an epoxy matrix.

The cut was made at 6° angle from the fiber long axis producing an oblong fiber cross-section. **Figure C.5A** shows the trapezoidal block face. The block face still has some of its initial gold coating covering its right half because of the angled cutting direction. **Figure C.5B** shows the oblong fiber cross-section. For this sample, line-scan or mapping analysis can be carried out at the fiber-matrix interphase, or, the adjacent matrix over the fiber on the advancing side of the sectioning direction (right side) could be the site for sputter depth profile analysis. **Figure C.6** shows a SEM micrograph of a copper coated carbon fiber radial cross-section.

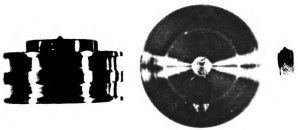

Figure C.1 - PERKIN-ELMER fracture stage sample holders. A sample block is shown placed at the center of the holders and another sample block is shown from its side view.

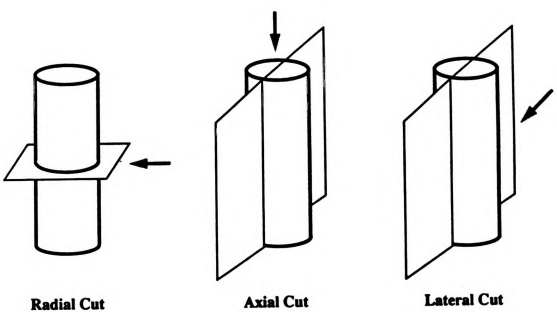

Figure C.2 - Major sectioning orientations of a fiber.

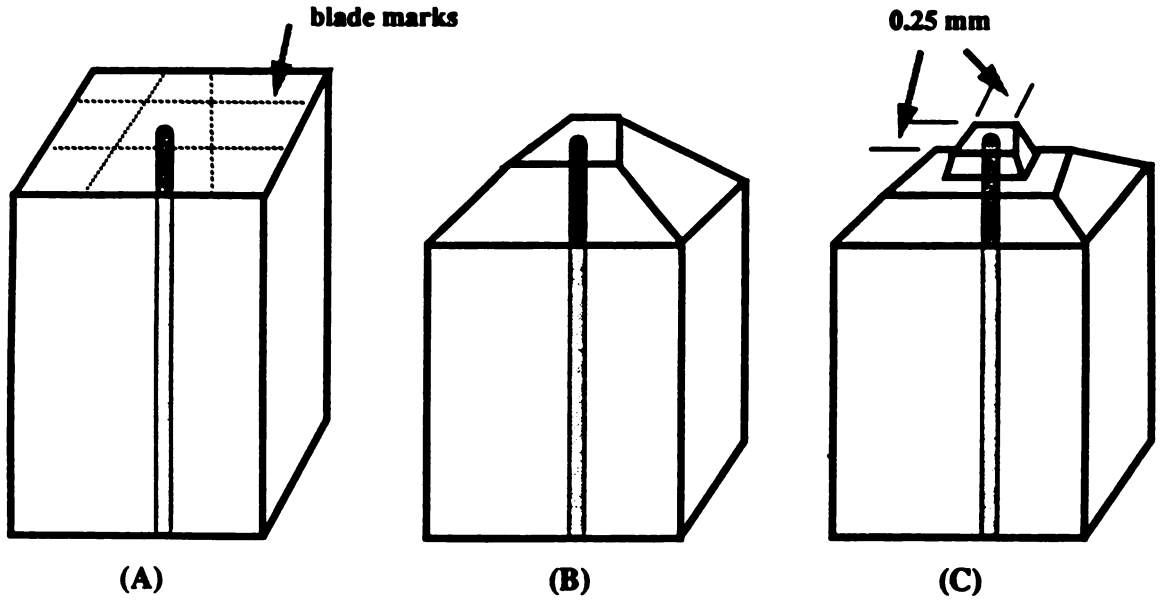

Figure C.3 - Trapezoidal block preparation for radial cuts. (A) Blade markings on the face isolate the fiber location. (B) Matrix around the fiber perimeter is trimmed off. (C) A shallow trapezoidal block is trimmed around the fiber.

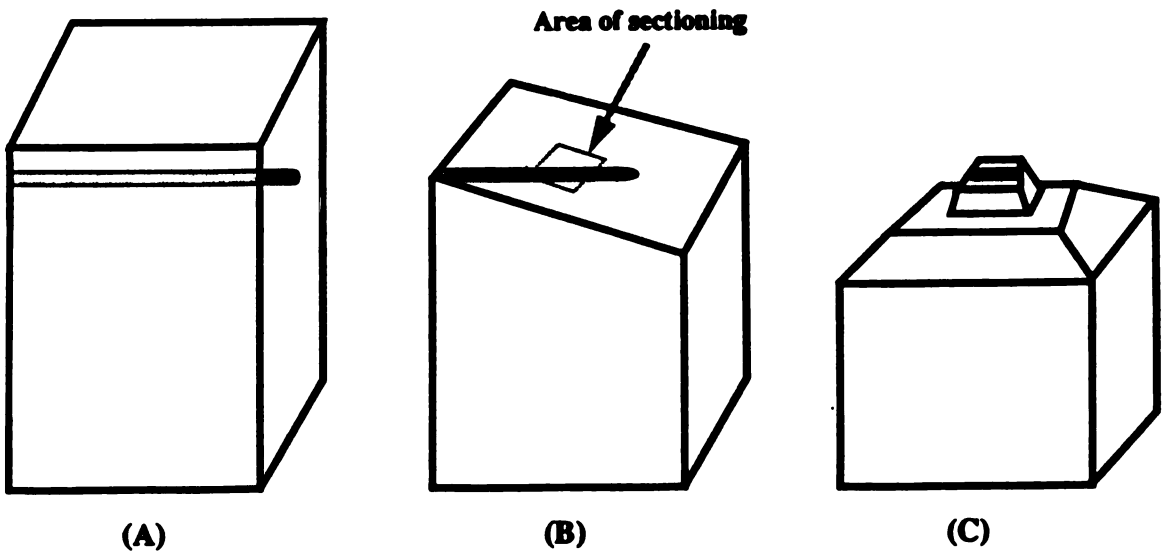

Figure C.4 - Trapezoidal block preparation for lateral cuts. (A) The fiber is initially covered. (B) The matrix is trimmed until a fiber portion is exposed. (C) The block is formed in the region adjacent to the exposed fiber end.

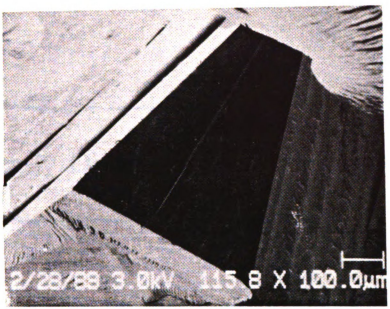

Figure C.5 - SEM micrographs of an axially cut nickel coated carbon fiber-epoxy composite. Cut was made at 6° angle from the fiber long axis. (A) Trapezoidal block face. (B) Oblong fiber cross section.

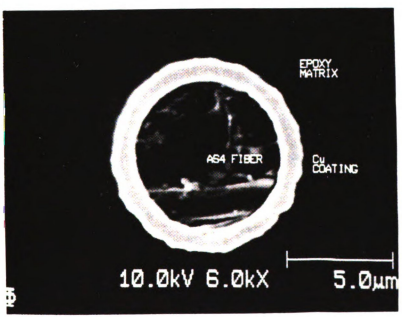

Figure C.6 - SEM micrograph of a radially cut copper coated carbon fiber.

APPENDIX D

Unsteady Diffusion in a Semi-Infinite Slab

To help to understand the mass-transfer phenomena affecting the penetration depth of sulfur into polycarbonate, the general concept of unsteady diffusion in a semi-infinite slab is reviewed here. This discussion is a modification and expansion of the topic as presented by Cussler (1984).

For species (1), concentration (C_1) and flux (j_1) as a function of position (z) and time (t) can be related by a mass balance on a thin layer of area A and thickness Δz,

(accumulation in volume $A\Delta z$) = (rate of diffusion into the layer at z)
− (rate of diffusion into the layer at $z+\Delta z$)
+ (amount produced by reaction in $A\Delta z$)

in mathematical terms, this is,

$$\frac{\delta}{\delta t}(A\Delta z C_1) = Aj_1|_z - Aj_1|_{z+\Delta z} + r_1 A\Delta z \qquad (D.1)$$

where r_1 is the rate of production per volume of species (1). By rearranging and using

the definition of a derivative equation D.1 becomes,

$$\frac{\delta C_1}{\delta t} = -\frac{\delta j_1}{\delta z} + r_1 \qquad (D.2)$$

The Fick's law of diffusion states,

$$-j_1 = D\frac{dC_1}{dz} \qquad (D.3)$$

where D is the diffusion coefficient. Combining equation D.3 with equation D.2,

$$\frac{\delta C_1}{\delta t} = D\frac{\delta^2 C_1}{\delta z^2} + \frac{\delta D}{\delta z}\frac{\delta C_1}{\delta z} + r_1 \qquad (D.4)$$

For the case where diffusion coefficient is independent of position, we get,

$$\frac{\delta C_1}{\delta t} = D\frac{\delta^2 C_1}{\delta z^2} + r_1 \qquad (D.5)$$

When the reacting solute is present in two forms, the mobile form (1) and the immobile reacted form (2), and the reaction is faster than diffusion, then, a first order reaction can be represented as,

$$C_2 = KC_1 \qquad (D.6)$$

where C_2 is the concentration of the reacted and immobile solute, and K is the equilibrium constant of reaction. A similar mass balance on species (2) gives,

$$\frac{\delta C_2}{\delta t} = -r_1 \qquad (D.7)$$

Adding equations D.5 and D.7 in combination with equation D.6 results,

$$\frac{\delta C_1}{\delta t} = \frac{D}{1 + K}\frac{\delta^2 C_1}{\delta z^2} \qquad (D.8)$$

The boundary conditions of this equation are,

$$\begin{array}{lll} t = 0, & C_1 = 0 & \text{for all } z \\ t > 0, & C_1 = C_{1i} & \text{at } z = 0 \\ & C_1 = 0 & \text{at } z = \infty \end{array} \qquad \text{(D.9)}$$

where C_{1i} is the solute concentration outside the slab. The differential equation D.8 has been solved using the method of "combination of variables." A new variable ζ is defined,

$$\zeta = \frac{z}{\sqrt{4\frac{D}{1+K}t}} \qquad \text{(D.10)}$$

The differential equation D.8 is then rewritten as,

$$\frac{d^2C_1}{d\zeta^2} + 2\zeta\frac{dC_1}{d\zeta} = 0 \qquad \text{(D.11)}$$

The boundary conditions D.9 become,

$$\begin{array}{lll} z = 0, & \zeta = 0 & C_1 = C_{1i} \\ z = \infty, \text{ or } t = 0 & \zeta = \infty & C_1 = 0 \end{array} \qquad \text{(D.12)}$$

Integration of equation D.11 results,

$$\frac{dC_1}{d\zeta} = \alpha e^{-\zeta^2} \qquad \text{(D.13)}$$

where α is an integration constant. A second integration with the use of boundary conditions D.13 gives,

$$\frac{C_{1i} - C_1}{C_{1i}} = erf\ \zeta = erf\ \frac{z}{\sqrt{4\frac{D}{1+K}\ t}} \qquad \text{(D.14)}$$

where,

$$erf\ \zeta = \frac{2}{\sqrt{\pi}} \int_0^{\zeta} e^{-t^2} dt \qquad (D.15)$$

equation **D.15** shows that for any fixed concentration of solute the position of that concentration is proportional to the square root of time. For example, for the position inside the slab where C_1 is only 1% of the C_{1i} (*i.e.* erf $\zeta = 0.01$), the value of ζ can be read from an "error function" table, thus,

$$\zeta = -2.33 = \frac{z}{\sqrt{4\frac{D}{1+K}\,t}} \qquad (D.16)$$

$$\Rightarrow\ z = [-2.33\sqrt{4\frac{D}{1+K}}]\sqrt{t} \qquad (D.17)$$

Equation **D.17** shows that when the diffusion coefficient is concentration independent then the penetration depth of the diffusing phase is linearly proportional to the square root of time.

For the case where diffusion coefficient is concentration dependent, equation **D.4** can be rewritten as,

$$\frac{\delta C_1}{\delta t} = D\frac{\delta^2 C_1}{\delta z^2} + \frac{\delta D}{\delta C_1}\frac{\delta C_1}{\delta z}\frac{\delta C_1}{\delta z} + r_1 \qquad (D.18)$$

$$\Rightarrow\ \frac{\delta C_1}{\delta t} = D\frac{\delta^2 C_1}{\delta z^2} + \frac{\delta D}{\delta C_1}\left(\frac{\delta C_1}{\delta z}\right)^2 + r_1 \qquad (D.19)$$

a model for concentration dependency of diffusion coefficient can be assumed (*e.g.* WLF model) and equation **D.19** can then be solved numerically by fitting experimental data such those presented in **Figure 6.8**.

APPENDIX E

Sulfonation Treatments of High Density Polyethylene Gas Tanks

Three samples of blow molded high-density polyethylene gas tanks that contained activated carbon, were sulfonated with ~12 vol% SO_3/N_2 gas phase treatments for 10 to 15 minutes. The samples were subsequently neutralization with three different cations, chromium (sample #2), calcium (sample #33), and copper (sample #46). Sample titration showed 1200 μg of SO_3 per square inch for all samples. **Table E.1** lists the results of XPS atomic concentration and AES elemental depth penetrations for the three examined samples. **Figure E.1** shows the elemental line scans superimposed on the SEM micrographs of the treated samples.

Table E.1 - XPS atomic% composition and AES elemental line-scans penetration depths for the sulfonated high-density polyethylene gas tanks samples.

	Chromium	Calcium	Copper
XPS Atomic% *			
C	38.4 ± 4.0	50.0 ± 0.4	28.4 ± 1.2
O	48.8 ± 3.1	38.5 ± 0.4	11.1 ± 1.4
S	1.69 ± 0.07	7.42 ± 0.02	25.8 ± 0.4
N	-	1.14 ± 0.05	-
Cr	9.94 ± 1.22	-	-
Ca	1.20 ± 0.23	2.89 ± 0.03	-
Cu	-	-	34.7 ± 0.7
AES line-scan			
S	15.5 ± 3.9 (4)	15.2 ± 3.0 (6)	15.3 ± 0.9 (5)
Cr	3.9 ± 0.9 (6)		
Ca		7.0 ± 0.6 (6)	
Cu			2.5 ± 0.2 (4)

* average of two runs.

Number in parenthesis represents the number of runs averaged.

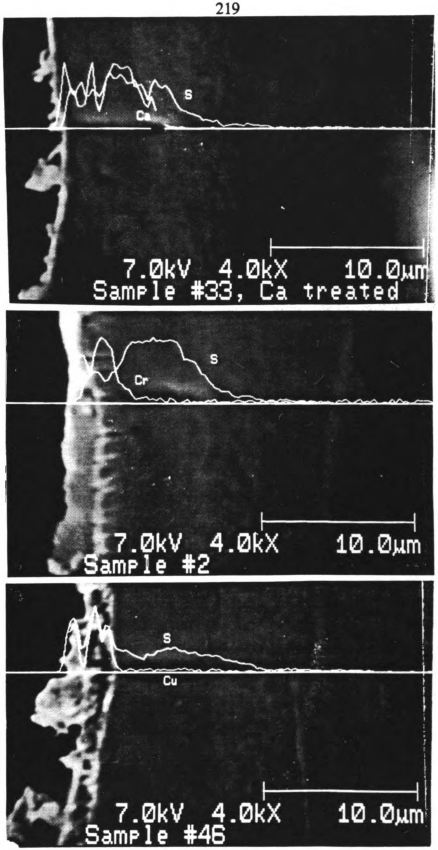

Figure E.1 - SEM micrographs of sulfonated samples and their elemental line-scans.

APPENDIX F

Procedures for Ultra-Thin Microtomy of Fiber Reinforced Composites

F.1 INTRODUCTION

An essential part of transmission electron microscopy (TEM) is the ultra-thin microtoming of samples. The TEM samples must be thin enough to transmit sufficient electrons to form an image. The samples must also be stable under the electron beam and in a high vacuum. TEM images are formed by combination of elastic, inelastic, and absorption interactions of the electron beam with the sample. Increasing the sample thickness increases the beam absorption and reduces the image resolution and sample stability. For a 100 kV electron beam the practical specimen thickness is limited to 100 nm.

Klomparens *et al.* (1986) have described the microtomy techniques for the biological materials and Malis *et al.* (1990) have reviewed the ultramicrotomy techniques for

metallic and ceramic materials. However, sectioning of high performance reinforcing fibers requires additional considerations than other materials. The epoxy resins used in composite are more brittle than those used in biological applications but more ductile than ceramic materials. In this report a procedure for ultra-thin microtomy of fiber-matrix interface is described.

F.2 PROCEDURE

To produce ultra-thin sections of reinforcing fibers, they must be first embedded in a polymer matrix. Low fiber volume fraction composites or single fibers embedded in a matrix coupon are the appropriate samples. In general, there must be enough matrix around the fiber to allow formation of a sectioning block. With high fiber volume fraction composites trimming the sectioning block is difficult.

To prepare the sectioning block, the sample is placed in a sample holder. The dimensions of a sample depends on the specific sample holder used; a rectangular block of 3×10 mm is typical. To prepare the sample for its holder, the sample can be cut by a razor blade, normally positioned and then tapped to fracture the parts. All the razor blades used in the cutting processes are new blades and their edges are cleaned with ethanol soaked cotton swabs to remove contaminant.

Orientation of the sectioning must be decided on before preparing the sample block because it can affect the trimming procedure. **Figure C.1** shows various sectioning orientations of a fiber. In radial cuts the block face always contains the fiber end and trimming can start around the fiber end. In axial and lateral cuts the fiber may be

initially covered by polymer matrix and the matrix must be trimmed before reaching the fiber. Radial sectioning is described first. Axial and lateral cuts require additional steps that will be described later.

The sectioning block must be hand trimmed into a trapezoid of dimensions no longer than 0.25 mm before diamond knife is used. The dimensions and quality of the trapezoid block determines the quality of the final sections. To trim the trapezoid block, the sample holder is placed under a sectioning microscope and the top face of the sample is viewed at 10× to 50× magnification. The top sample face may have to be removed before trimming the trapezoid block. This is to remove the artifacts of the blade cuts or to approach the fiber for the lateral and axial cuts.

Figure C.2 shows the process of sectioning block preparation for the radial cuts. First, the location of the fiber is isolated by four large blade marks about 1 mm apart (**Figure C.2A**). With the fiber at the center of the blade marks, the epoxy outside the marks are trimmed at 45° angles (**Figure C.2B**). Next, the matrix around the fiber is gradually trimmed with a shallow depth until two parallel edges and two angled edges about 0.25 mm apart around the fiber are obtained (**Figure C.2C**). It is important to have the two parallel edges as parallel as possible to obtain good ribbon formation during the microtoming. Cuts are always made at 45° and away from the trapezoid block face since otherwise a crack can initiate that fractures off the small trapezoid block. The final trapezoid block should be less than 0.25 mm thick since thicker blocks are more susceptible to vibration than the shallower blocks.

For axial and lateral cuts the fiber is initially covered by the matrix (**Figure C.3A**).

The matrix over the fiber is removed at a shallow angle (< 10°) till a fiber portion is exposed (Figure C.3B). The region of thin matrix coverage over the fiber is the region for trimming the trapezoid sectioning block. The trapezoid sectioning block is prepared in a similar procedure as the radial cuts. The thin matrix over the fiber is removed during the diamond sectioning.

Ultra-thin microtoming of high performance fibers requires a diamond knife. Sectioning of the trapezoid block face should start from a dull knife edge and once the trapezoid block face is ready for ultra-thin sectioning the face is sectioned with a sharp knife edge. The mounting angle of the knife varies depending on the knife edge angle set by manufacturer (~55°) and type of sample being sectioned. A solution of de-ionized water with low concentration of acetone ~1 droplet of acetone per 20 cc of water) is used to fill the diamond knife boat. Acetone reduces the contact angle of the water to produce better wetting of the knife edge. The knife boat is filled using a syringe. Initially, the boat in filled to brink of overflow and then excess water is drawn off to form a concave fluid surface behind the diamond edge. This procedure insures good wetting of the knife edge. The knife is advanced manually toward the block face until reflection of the block face off the water meniscus is observed. The knife is then slowly advanced toward the block at 1 μm steps until cutting begins. Several 1 μm sections are cut to remove the trimming artifacts and prepare a clean smooth face for the ultra-thin sectioning. The knife is then withdrawn and shifted to a sharp knife edge. Again the knife is slowly advanced until thin sections of gold or purple color are cut (0.2 to 1 μm). Motorized sample advancing is turned on and a cutting speed of 0.40 mm/sec

is selected. The thickness setting is adjusted to obtain silver-gold colored sections (50 to 100 nm).

In a successful ultra-thin sectioning, the sections remain attached and form ribbons that float on the water. To manipulate ribbons, an eyelash applicator is prepared. An eyelash applicator is simply an eyelash mounted on a wooden applicator using a drop of nail-polish. With the eyelash applicator, the ribbons are assembled for the pick up by a TEM grid.

To collect TEM sections, first the knife is receded and water is added to the boat. The ribbons are then arranged away from the diamond edge. The grids used are 200 or 300 mesh fine wire copper grids that have small end tabs for easy pick up. A grid is picked up by a tweezer and passed over a flame to burn off its hydrocarbon contaminates and increase its wetting. Under the microscope of the microtome a grid is submerged in water and approaches the assembled ribbons from underneath the surface. The ribbons are picked up and the grid is drained on a filter paper. The grids are stored in a dessicator for later sample staining and carbon coating.

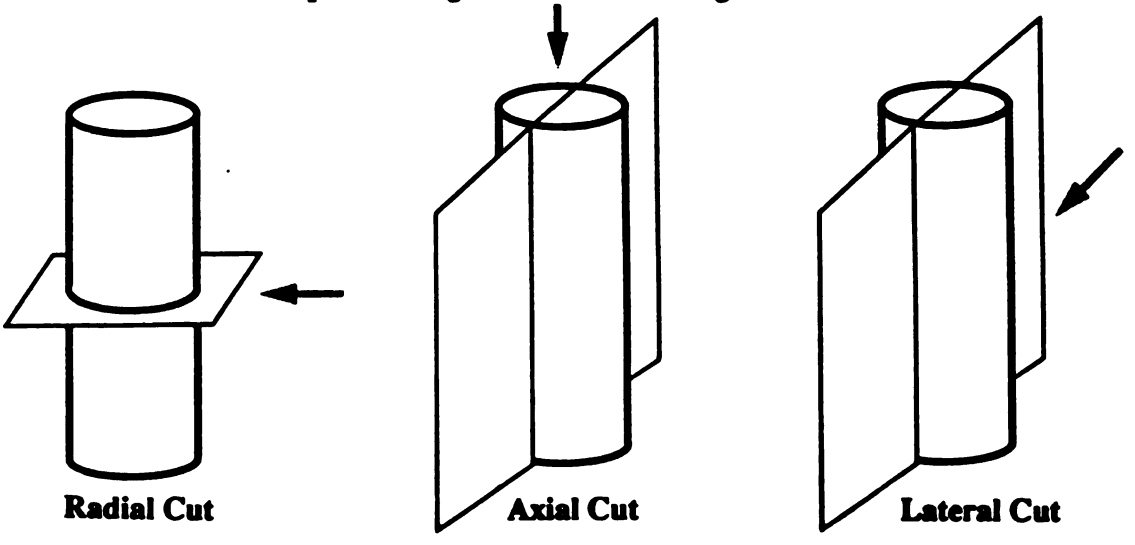

Figure F.1 - Major sectioning orientations of a fiber.

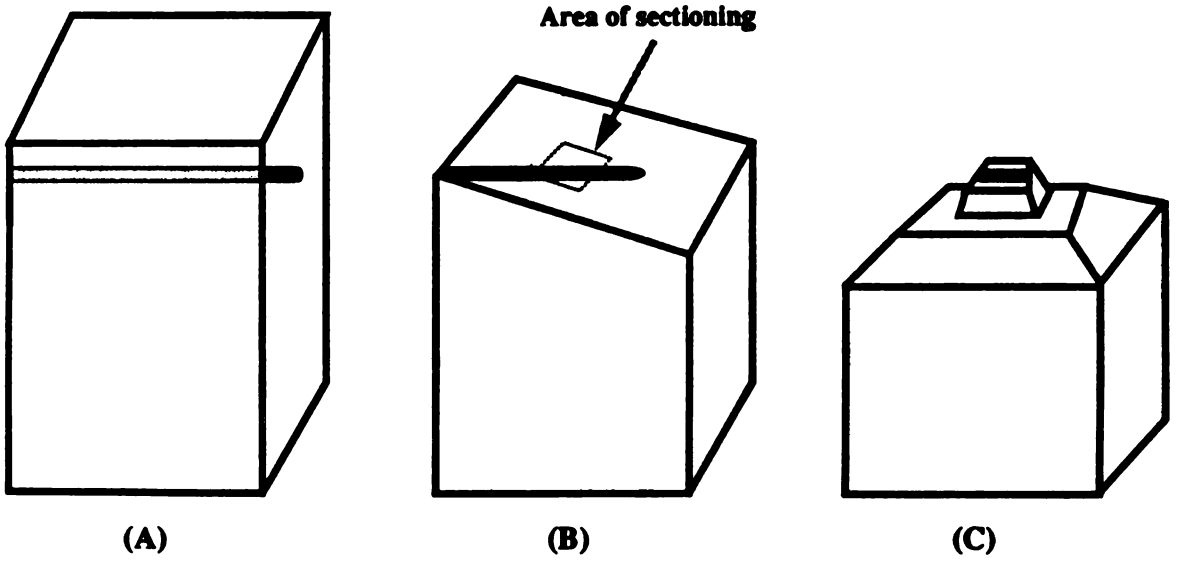

Figure F.2 - Trapezoidal block preparation for radial cuts. (A) Blade markings on the face isolate the fiber location. (B) Matrix around the fiber perimeter is trimmed off. (C) A shallow trapezoidal block is trimmed around the fiber.

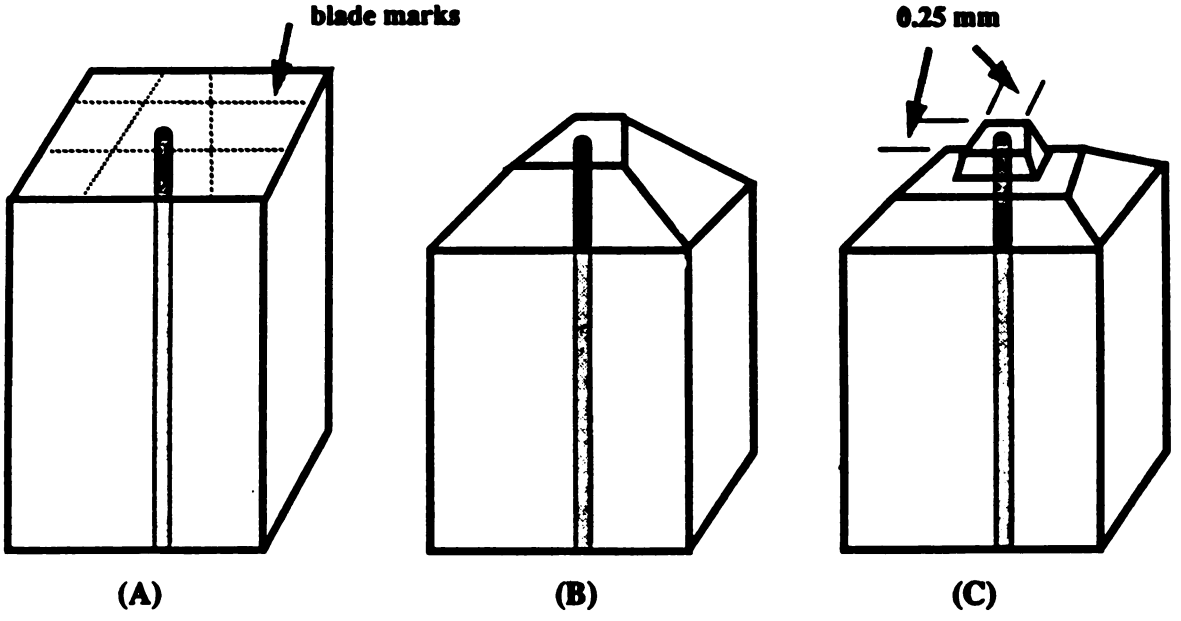

Figure F.3 - Trapezoidal block preparation for lateral cuts. (A) The fiber is initially covered. (B) The matrix is trimmed until a fiber portion is exposed. (C) The block is formed in the region adjacent to the exposed fiber end.

APPENDIX G

Wilhelmy Program

```
C*     Linear regression program to determine surface energy components
C*     from contact angle measurements
C*
C*     Mat. Stat., Mendenhall pp. 425-441

       integer I,J,K,N,DONE,NUM(10)
       real SLOP,YINT,SP,SD,A,B,C,TSE,STDTSE,STDSL,STDYI
       real SUMX,SUMY,SUMXX,SUMYY,SUMXY,SUMXM
       real MEANX,XXI11,XXI2,XXI22,S2,ANG(200),Y(200),X(200)
       real MEAN(10),STD(10)
       character*99 DATAIN(10),NAME(10),DATAOUT
       character*1 QUE
       DONE = 0
       print *, ' ENTER THE OUTPUT FILE NAME : '
       read (*,'(A)') DATAOUT
       OPEN (unit=1,file=DATAOUT,status='unknown')
       rewind 1
       DONE = 0
       do WHILE (DONE .lt. 1)
       K = 0
       print *, 'How many liquids?    '
       read *, N
       do 100 J=1, N
 1           print *, 'W - Water'
             print *, 'E - Ethylene Glycol'
             print *, 'F - Formamide'
             print *, 'M - Methylene Iodide'
             print *, 'H - Hexadecane'
             print *
             print *, 'Chose liquid (W,E,F,M,H): '
             read (*,'(A)') QUE
             IF (QUE .eq. 'w') then
                   A= 72.8
                   B= 21.8
                   C= 51.0
                   NAME(J) = 'Water'
             ELSEIF (QUE .eq. 'e') then
                   A= 48.3
                   B= 29.3
                   C= 19.0
                   NAME(J) = 'Ethylene Glycol'
             ELSEIF (QUE .eq. 'f') then
                   A= 58.3
                   B= 32.3
                   C= 26.0
```

```
            NAME(J) = 'Formamide'
          ELSEIF (QUE .eq. 'h') then
            A= 27.6
            B= 27.6
            C= 0
            NAME(J) = 'Hexadecane'
          ELSEIF (QUE .eq. 'm') then
            A= 50.8
            B= 48.4
            C= 2.4
            NAME(J) = 'Methylene Iodide'
          ELSE
            GOTO 1
          endif
          write (*,50) NAME(J)
50        format ('Enter ',a17,' data file: ')
          read (*,'(A)') DATAIN(J)
          print *
          OPEN(unit=2,file=DATAIN(J),status='unknown')
          rewind 2
          DO 200 i=1, 1000
            READ (2,*,end=250) ANG(i)
            K = K+1
            Y(K) = (A*(1+COS(ANG(i)*0.0174533)))/(2*((B)**0.5))
200         X(K) = (C/B)**0.5
250       NUM(J) = i-1
100       CALL STAT (ANG,NUM(J),MEAN(J),STD(J))

          SUMX = 0
          SUMXX = 0
          SUMY = 0
          SUMYY = 0
          SUMXY = 0
          SUMXM = 0
          do 300 j=1, K
            SUMX = SUMX + X(J)
            SUMXX = SUMXX + (X(J)*X(J))
            SUMY = SUMY + Y(J)
            SUMYY = SUMYY + (Y(J)*Y(J))
300         SUMXY = SUMXY + (X(J)*Y(J))
          MEANX = SUMX/K
          do 350 j=1, K
350         SUMXM = SUMXM + (X(J) - MEANX)**2
          XXI11 = SUMXX / (K*SUMXM)
          XXI2 = -SUMX / (K*SUMXM)
          XXI22 = 1/SUMXM
          YINT = (XXI11*SUMY) + (XXI2*SUMXY)
          SLOP = (XXI2*SUMY) + (XXI22*SUMXY)
          S2 = (SUMYY - ((YINT*SUMY) + (SLOP*SUMXY)))/(K-2)
          STDYI = (XXI11*S2)**0.5
          STDSL = (XXI22*S2)**0.5
          SP = 2*SLOP*STDSL
          SD = 2*YINT*STDYI
          TSE = (YINT**2) + (SLOP**2)
          STDTSE = SD + SP

      DO 400 j=1, N
        write (*,410) DATAIN(J),NAME(J),MEAN(J),STD(J),NUM(J)
400     write (1,410) DATAIN(J),NAME(J),MEAN(J),STD(J),NUM(J)
410     format (a10,a16,' contact angle: ',f6.2,' +- ',f4.2,' (',i2,')')
        print *
        write (1,*)
```

```
      write (*,420) YINT,STDYI
      write (1,420) YINT,STDYI
420   format ('Sqrt Disp. Comp. = ',f6.3,' +- ',f5.3)
      write (*,430) SLOP,STDSL
      write (1,430) SLOP,STDSL
430   format ('Sqrt Polar Comp. = ',f6.3,' +- ',f5.3)
      print *
      write (1,*)
      write (*,440) (YINT)**2,SD
      write (1,440) (YINT)**2,SD
440   format ('Disp. Comp. mN/m = ',f6.2,' +- ',f5.2)
      write (*,450) (SLOP)**2,SP
      write (1,450) (SLOP)**2,SP
450   format ('Polar Comp. mN/m = ',f6.2,' +- ',f5.2)
      print *
      write (1,*)
      write (*,460) TSE,STDTSE
      write (1,460) TSE,STDTSE
460   format ('Total surface energy mN/m = ',f6.2,' +- ',f4.2)
      print *
      write (1,*)
    print *, 'DONE ? Y/N :  '
    read (*,'(A)') QUE
    IF (QUE .eq. 'Y'.or. que .eq. 'y') then
      done = 1
    ENDIF
    END DO
    END

    SUBROUTINE STAT (AVE,K,MEAN,STD)
    REAL VAR,AVE(200),MEAN,STD
    INTEGER J,K

    SUM = 0
    DO 10 J=1,K
10    SUM = SUM + AVE(J)
      MEAN = SUM/K
      VAR = 0
    DO 20 J=1,K
20    VAR = VAR + (AVE(J)-MEAN)**2
    STD = (VAR/(K-1))**0.5
    END
```

APPENDIX H

Experimental Data

Fluorinted Kevlar-49 (t-test)

 # Of Breaks

Untreated-175	25	18.8000	±	1.0801		
ap-a	12	18.5833	±	1.6765	d.f.= 35	t = 0.476
ap-b	14	21.7143	±	1.7728	d.f.= 37	t = 6.400
ap-c	12	18.8333	±	2.5166	d.f.= 35	t = 0.057
ap-d	12	19.6667	±	1.3707	d.f.= 35	t = 2.093

Diameter

Untreated.dia	30	12.6853	±	0.5970		
a.dia	16	12.0938	±	0.5599	d.f.= 44	t = 3.269
b.dia	16	12.7963	±	0.4273	d.f.= 44	t = 0.657
c.dia	15	12.3787	±	0.6442	d.f.= 43	t = 1.583
d.dia	16	12.2425	±	0.6239	d.f.= 44	t = 2.359

Tensile Strength

k49-javid.dia	30	2.8770	±	0.3167		
a.gpa	16	2.9935	±	0.2637	d.f.= 44	t = 1.255
b.gpa	14	2.6078	±	0.3765	d.f.= 42	t = 2.473
c.gpa	14	3.0221	±	0.3538	d.f.= 42	t = 1.364
d.gpa	16	3.1175	±	0.3531	d.f.= 44	t = 2.357

ISS

FILE NAME	# OF BREAKS	L_o (mm)	L_o/d	τ (MPa)
KU175MD.DAT	18.8 ± 1.1 (25)	1.17	97.5	15.62 ± 0.90
AP-A	18.6 ± 1.7 (12)	1.18	98.7	15.27 ± 1.38
AP-B	21.7 ± 1.8 (14)	1.01	84.4	16.49 ± 1.35
AP-C	18.8 ± 2.5 (12)	1.17	97.3	16.00 ± 2.14
AP-D	19.7 ± 1.4 (12)	1.12	93.2	17.07 ± 1.19

Compressive Strength

UNTREATED	107	752 ± 168		
AP-A	10	742 ± 132		
AP-B	10	713 ± 167		
AP-C	10	767 ± 104		
AP-D	15	862 ± 162	d.f.= 120	t = 2.386

Coupling agents

AS4	L_c (um)	L_c/d	τ (MPa)
175as4md	266.3 ± 74.8 (572)	34.6 ± 9.7	84.73 ± 23.81
KR-AS4-H.LC	275.7 ± 86.0 (201)	35.8 ± 11.2	81.82 ± 25.53
KR-AS4-L.LC	266.1 ± 79.8 (202)	34.6 ± 10.4	84.79 ± 25.43
lz-as4-h	304.9 ± 96.7 (189)	39.6 ± 12.6	73.99 ± 23.47
lz-as4-l	302.7 ± 96.6 (200)	39.3 ± 12.5	74.53 ± 23.77

Kevlar-49	# OF BREAKS	L_c (mm)	L_c/d	τ (MPa)
ku175md	18.8 ± 1.1 (25)	1.17	97.5	16.97 ± 0.98
kr55l	17.7 ± 0.8 (7)	1.24	103.5	15.99 ± 0.68
kr55h	19.0 ± 1.1 (8)	1.16	96.5	17.15 ± 0.97
lz37l	19.0 ± 1.3 (8)	1.16	96.5	17.15 ± 1.18
lz37h	17.9 ± 1.4 (8)	1.23	102.6	16.14 ± 1.22

F = 10.509

IF F > F (table) then there is enough data for a diferernce

Untreated Fibers

	# OF BREAKS	L_c (mm)	L_c/d	τ (MPa)
TECHNORA-AR	36.3 ± 2.2 (15)	0.607	47.7	32.28 ± 1.95
TECHNORA-Washed	28.3 ± 2.5 (15)	0.776	60.7	25.22 ± 2.25
K29-175MD-AR	24.0 ± 3.3 (8)	0.917	72.2	19.95 ± 2.74
K29-175MD-Washed	24.4 ± 3.7 (7)	0.901	70.9	20.31 ± 3.11
K49-175MD-AR	18.8 ± 1.1 (25)	1.170	92.1	15.63 ± 0.90
PBO-AR	10.7 ± 0.8 (14)	2.053	102.7	16.56 ± 1.28
PBO-Washed	10.8 ± 1.6 (9)	2.041	102.1	16.66 ± 2.42

Dogbone SFC tests

Kevlar-49 ar	648.200 ± 95.058 (10)
Kevlar-29 ar	502.000 ± 61.059 (10)
PBO-ar	401.000 ± 81.646 (9)
Technora-ar	610.625 ± 51.264 (8)
Technora-washed	618.125 ± 57.275 (8)

Tensile Properties

	As Rec. Kevlar-149	Washed Kevlar-149
Diameter (μm)	13.01 ± 0.524 (11)	12.94 ± 0.400 (10)
Tensile Strength (GPa)	2.318 ± 0.322 (10)	2.434 ± 0.150 (10)
Modulus (GPa)	145.6 ± 5.428 (10)	150.3 ± 4.963 (10)
Second Modulus (GPa)	108.5 ± 5.187 (9)	108.7 ± 7.279 (10)
Fracture Strain (%)	1.678 ± 0.307 (10)	1.762 ± 0.110 (10)

	As Rec. Technora	Washed Technora
Diameter (μm)	13.23 ± 0.912 (11)	12.92 ± 0.734 (11)
Tensile Strength (GPa)	3.201 ± 0.246 (11)	3.195 ± 0.211 (11)
Modulus (GPa)	66.87 ± 3.090 (11)	70.00 ± 2.455 (11)
Fracture Strain (%)	4.880 ± 0.260 (11)	4.990 ± 0.320 (10)

	Combined Kevlar-149	Combined Technora
Diameter (μm)	12.97 ± 0.459 (21)	13.08 ± 0.823 (22)
Tensile Strength (GPa)	2.376 ± 0.252 (20)	3.198 ± 0.224 (22)
Modulus (GPa)	147.9 ± 5.607 (20)	68.44 ± 3.159 (22)
Second Modulus (GPa)	108.6 ± 6.203 (19)	
Fracture Strain (%)	1.720 ± 0.229 (20)	4.932 ± 0.288 (21)

	As Rec. PBO	Wet-PBO RT dried
Diameter (μm)	19.40 ± 1.822 (15)	20.05 ± 3.458 (10)
Tensile Strength (GPa)	2.847 ± 0.461 (15)	2.949 ± 0.809 (8)
Modulus (GPa)	165.9 ± 11.729 (15)	105.6 ± 5.459 (10)
Fracture Strain (%)	1.787 ± 0.294 (15)	3.245 ± 0.791 (8)

	PBO crit. point dried	W-PBO Sulfonated (PS1)
Diameter (μm)	20.75 ± 2.491 (10)	25.17 ± 3.265 (10)
Tensile Strength (GPa)	2.088 ± 0.599 (10)	1.492 ± 0.357 (10)
Modulus (GPa)	78.16 ± 9.252 (10)	64.38 ± 5.479 (10)
Fracture Strain (%)	2.439 ± 0.292 (10)	2.327 ± 0.433 (10)

	W-PBO Adipoyl (FCA3.1)
Diameter (μm)	20.77 ± 3.09 (10)
Tensile Strength (GPa)	1.24 ± 0.32 (8)
Modulus (GPa)	100.8 ± 16.2 (8)
Fracture Strain (%)	1.30 ± 0.28 (8)

Spectra-1000 untreated

	Full set	Corrected
Diameter (μm)	29.5 ± 3.8 (12)	28.7 ± 2.7 (11)
Tensile Strength (GPa)	2.56 ± 0.43 (11)	2.65 ± 0.29 (10)
Modulus (GPa)	64.5 ± 11.9 (14)	67.8 ± 9.22 (12)
Fracture Strain (%)	7.62 ± 2.00 (11)	6.91 ± 1.30 (9)

Spectra-1000, 400 keV 10^{13} He^+/cm^2 ion implanted

	Full set	Corrected
Diameter (μm)	28.7 ± 2.5 (14)	27.8 ± 1.3 (12)
Tensile Strength (GPa)	1.66 ± 0.30 (12)	1.77 ± 0.26 (9)
Modulus (GPa)	77.0 ± 12.5 (11)	82.5 ± 3.0 (9)
Fracture Strain (%)	3.94 ± 0.73 (13)	3.42 ± 0.42 (6)

Ion Implanted Fibers

Kevlar-49	Diameter (μm)	Ten. Str. (GPa)	Comp. Str. (MPa)
Untreated	12.59 ± 0.61 (37)	2.88 ± 0.31 (37)	752 ± 168 (107)
30 N^+ 10^{14}		2.91 ± 0.34	746 ± 164
30 N^+ 4×10^{14}		2.82 ± 0.30	743 ± 140
30 N^+ 10^{15}		2.98 ± 0.31	706 ± 128
75 Ar^+ 10^{15}		2.74 ± 0.20	690 ± 96
100 Ti^+ 10^{15}		2.77 ± 0.36	745 ± 161
100 N^+ 2×10^{13}	12.22 ± 0.31 (10)	2.77 ± 0.36 (10)	820 ± 84 (10)
100 N^+ 10^{14}	12.75 ± 0.66 (11)	2.59 ± 0.30 (10)	777 ± 107 (10)
390 N^+ 2×10^{12}	12.33 ± 0.39 (12)	2.67 ± 0.27 (10)	728 ± 61 (9)
400 N^+ 5×10^{12}	12.45 ± 0.26 (12)	2.72 ± 0.25 (11)	750 ± 70 (10)
400 N^+ 2×10^{13}	12.52 ± 0.32 (14)	2.46 ± 0.17 (11)	785 ± 104 (10)
400 N^+ 10^{14}	12.78 ± 0.73 (10)	2.28 ± 0.13 (10)	748 ± 83 (9)
390 N^+ 2×10^{14}	12.46 ± 0.29 (19)	2.27 ± 0.13 (20)	876 +- 66 (8)
390 He^+ 10^{13}	12.41 ± 0.46 (11)	2.50 ± 0.32 (11)	713 +- 133 (8)

Fiber	# OF BREAKS	L_c (mm)	L_c/d	τ (MPa)	
Untreated	18.8 ± 1.1 (25)	1.170	92.9	15.49 ± 0.89	
30 N^+ 10^{14}	18.6 ± 2.1 (7)	1.185	94.1	15.30 ± 1.71	
30 N^+ 10^{14} old	17.9 ± 1.1 (13)	1.227	97.5	14.7 7± 0.92	
100 N^+ 10^{13}	19.0 ± 2.2 (11)	1.158	92.0	15.06 ± 1.77	
100 N^+ 10^{13} old	17.2 ± 0.9 (10)	1.279	101.6	13.63 ± 0.73	
100 N^+ 10^{14}	17.5 ± 1.4 (11)	1.260	100.1	12.94 ± 1.07	
100 N^+ 10^{14} old	17.0 ± 0.9 (10)	1.294	102.8	12.60 ± 0.70	
100 N^+ 10^{14} old	16.0 ± 1.2 (10)	1.375	109.2	11.86 ± 0.92	MPDA
400 N^+ 10^{12}	18.8 ± 1.5 (10)	1.170	92.9	14.36 ± 1.13	
400 N^+ 5×10^{12}	22.4 ± 0.8 (10)	0.982	78.0	17.43 ± 0.66	
390 He^+ 10^{13}	21.4 ± 1.1 (11)	1.030	81.8	15.28 ± 0.80	
400 N^+ 10^{13}	22.4 ± 2.1 (20)	0.982	78.0	15.77 ± 1.49	
400 N^+ 10^{14}	19.5 ± 2.8 (13)	1.130	89.8	12.70 ± 1.82	
400 N^+ 10^{14}	19.9 ± 2.3 (23)	1.107	87.9	12.91 ± 1.50	[illegible]
400 N^+ 10^{14} old	21.0 ± 1.9 (10)	1.048	83.2	13.70 ± 1.23	
400 N^+ 10^{14} old	21.0 ± 1.4 (8)	1.048	83.2	13.70 ± 0.92	MPDA

Ion Implanted Kevlar-49 XPS DATA (t-test)

ion/kco	19.810 ± .414 (13)		
ion/k12o	19.083 ± .370 (3)	d.f.= 14	t = 2.783
ion/kcn	7.397 ± .257 (13)		
ion/k12n	7.573 ± .145 (3)	d.f.= 14	t = 1.126
ion/kcc	72.785 ± .440 (12)		
ion/k12c	73.343 ± .515 (3)	d.f.= 13	t = 1.912
ion/kco	19.810 ± .414 (13)		
ion/k512o	20.290 ± .529 (4)	d.f.= 15	t = 1.911
ion/kcn	7.397 ± .257 (13)		
ion/k512n	7.320 ± .156 (4)	d.f.= 15	t = .559
ion/kcc	72.785 ± .440 (12)		
ion/k512c	72.390 ± .589 (4)	d.f.= 14	t = 1.437
ion/kco	19.810 ± .414 (13)		
ion/k13o	18.515 ± .114 (4)	d.f.= 15	t = 6.064
ion/kcn	7.397 ± .257 (13)		
ion/k13n	7.610 ± .181 (4)	d.f.= 15	t = 1.526
ion/kcc	72.785 ± .440 (12)		
ion/k13c	73.872 ± .259 (4)	d.f.= 14	t = 4.615
ion/kco	19.810 ± .414 (13)		
ion/k14o	16.207 ± .080 (3)	d.f.= 14	t =14.644
ion/kcn	7.397 ± .257 (13)		
ion/k14n	6.423 ± .156 (3)	d.f.= 14	t = 6.189
ion/kcc	72.785 ± .440 (12)		
ion/k14c	77.370 ± .079 (3)	d.f.= 13	t = 17.491

If t > t(table) then there is enough data for a diferernce

Wet-PBO Diameters (Video Calipers)

File	Condition	test medium	(μm)
pbo-1	wet	water	26.9 ± 4.1 (30)
pbo-2	one day RT dried	dry	18.8 ± 3.8 (30)
pbo-3	2 weeks in EtOH	EtOH	26.0 ± 4.6 (30)
pbo-4	1d EtOH, 1d Act, 1d Fre, 5hr RT dry	dry	21.7 ± 2.9 (30)
pbo-5	2 wks RT dried, 24hrs water soak	water	19.3 ± 3.6 (30)
pbo-6	1d Acet, 1d Fre, 1d Acet, 1d water	water	26.3 ± 4.6 (30)
pbo-7	LN2 frozen, 1d RT dried	water	21.5 ± 4.3 (30)
pbo-8	1d RT dry, LN2 frozen, 1d RT dry	water	20.3 ± 3.6 (30)
pbo-9	1d RT dried, 2d Acetone	Acetone	20.6 ± 3.6 (30)
pbo-10	1d EtOH, 1d Acetone, 5d Freon	Freon	27.9 ± 4.7 (30)
pbo-11	5d RT dried, 400C dried	water	19.2 ± 3.5 (30)
pbo-12	5d RT dried,440C dreid	dry	18.4 ± 3.1 (30)

t-tests

pbo-2	18.8 ± 3.8 (30)		
pbo-4	21.7 ± 2.9 (30)	d.f.= 58	t = 3.330
pbo-4	21.7 ± 2.9 (30)		
pbo-7	21.5 ± 4.3 (30)	d.f.= 58	t = 0.195
pbo-2	18.8 ± 3.8 (30)		
pbo-9	20.6 ± 3.6 (30)	d.f.= 58	t = 1.932
pbo-11	19.2 ± 3.5 (30)		
pbo-12	18.4 ± 3.1 (30)	d.f.= 58	t = 0.927
pbo-1	26.9 ± 4.1 (30)		
pbo-10	27.9 ± 4.7 (30)	d.f.= 58	t = 0.823

Plasma Treated PBO (Set One)

Fiber	date	# of breaks	τ (MPa)
pbo-ar	10-22-88	10.6 ± 0.5 (7)	15.8 ± 0.8
pbo-wash	10-19-88	12.6 ± 1.3 (5)	18.8 ± 2.0
pbo1	10-17-88	10.8 ± 0.4 (5)	16.1 ± 0.7
pbo2	10-17-88	16.2 ± 1.5 (6)	15.9 ± 1.4
pbo3	10-24-89	14.2 ± 1.5 (5)	19.6 ± 2.0
pbo4	10-17-89	12.0 ± 1.4 (6)	

FIBER	Diameter (Microns)	Tensile Strength (GPa)
PBO- as rec.	19.46 ± 2.52 (15)	3.37 ± 0.50 (13)
PBO-1	20.87 ± 1.93 (17)	3.37 ± 0.51 (13)
PBO-2	17.18 ± 2.43 (14)	2.44 ± 0.41 (14)
PBO-3	18.88 ± 1.91 (13)	3.22 ± 0.49 (13)
PBO-4	20.78 ± 2.83 (13)	3.34 ± 0.49 (13)
PBO-5	20.18 ± 2.29 (14)	3.38 ± 0.47 (12)
PBO-6	19.36 ± 1.83 (15)	3.41 ± 0.58 (14)
PBO-7	20.16 ± 2.00 (14)	3.41 ± 0.46 (11)
PBO-8	19.85 ± 2.08 (15)	3.15 ± 0.30 (13)
PBO-9	20.31 ± 1.77 (14)	3.34 ± 0.29 (14)
PBO-10	19.54 ± 1.85 (15)	3.53 ± 0.45 (15)
PBO-11	20.07 ± 2.02 (15)	3.38 ± 0.58 (15)
PBO-12	19.38 ± 1.79 (15)	3.30 ± 0.35 (14)
PBO-13	19.45 ± 1.78 (15)	3.35 ± 0.43 (14)

Fiber	Compressive Str. (MPa)	Treatment
PBO-As Rec.	397 ± 98 (27)	none
PBO-1	392 ± 121 (10)	O2 50%
PBO-2	359 ± 114 (11)	O2 25 CF4 25%
PBO-3	366 ± 115 (12)	He 50%
PBO-4	344 ± 80 (12)	CO2 50%
PBO-5	321 ± 78 (12)	NH3 50%
PBO-6	379 ± 95 (14)	NH3 50%
PBO-7	409 ± 127 (15)	N2O 50%
PBO-8	397 ± 107 (30)	N2O 50%
PBO-9	347 ± 76 (14)	Ar 50%
PBO-10	374 ± 100 (16)	H2/N2 50%
PBO-11	341 ± 105 (14)	Ar 50%, CO2 100%
PBO-12	374 ± 123 (15)	Ar 50%, O2 100%
PBO-13	331 ± 99 (15)	H2O 100%

Plasma Treated PBO (Set Two, 1-30-89)

Fiber	# of Breaks	Treatment
PBO-as rec.	10.7 ± 0.8 (14)	CONTROL
PBO-1	15.3 ± 1.0 (9)	CO_2 50 1.00 MIN 301 WATTS
PBO-2	12.9 ± 1.6 (10)	CO_2 50 0.75 MIN 301 WATTS
PBO-3	13.0 ± 1.6 (10)	CO_2 50 0.50 MIN 301 WATTS
PBO-4	12.1 ± 0.9 (9)	CO_2 50 1.00 MIN 479 WATTS
PBO-5	12.4 ± 1.9 (9)	CO_2 50 0.75 MIN 479 WATTS
PBO-6	12.4 ± 2.0 (8)	CO_2 50 0.50 MIN 478 WATTS
PBO-7	14.8 ± 1.8 (8)	O_2 25 CF_4 25 1.00 MIN 301 WATTS
PBO-8	15.3 ± 1.3 (8)	O_2 25 CF_4 25 0.75 MIN 301 WATTS
PBO-9	12.8 ± 1.4 (8)	O_2 25 CF_4 25 0.50 MIN 301 WATTS
PBO-11	13.8 ± 2.1 (10)	O_2 25 CF_4 25 0.75 MIN 397 WATTS
PBO-12	16.8 ± 2.2 (14)	O_2 25 CF_4 25 0.50 MIN 395 WATTS
PBO-13	19.3 ± 2.2 (10)	O_2 25 CF_4 25 1.00 MIN 395 WATTS

Fiber	diameter (μm)	Ten. Str. (GPa)	Comp. Str. (MPa)
PBO-as rec.	19.95 ± 1.95 (39)	3.19 ± 0.48 (29)	397 ± 98 (27)
PBO-1	20.50 ± 1.83 (7)	3.44 ± 0.58 (7)	358 ± 107 (7)
PBO-2	21.68 ± 1.45 (7)	3.41 ± 0.47 (7)	367 ± 98 (5)
PBO-3	22.15 ± 2.59 (6)	3.29 ± 0.43 (6)	382 ± 108 (5)
PBO-4	19.49 ± 1.27 (7)	3.45 ± 0.51 (7)	392 ± 112 (8)
PBO-5	20.67 ± 1.47 (7)	3.56 ± 0.41 (7)	405 ± 74 (5)
PBO-6	20.35 ± 1.12 (10)	3.25 ± 0.60 (9)	451 ± 57 (5)
PBO-7	18.80 ± 1.04 (6)	3.46 ± 0.49 (7)	501 ± 106 (5)
PBO-8	19.90 ± 0.73 (8)	3.22 ± 0.39 (7)	391 ± 80 (5)
PBO-9	19.57 ± 0.97 (8)	3.69 ± 0.49 (8)	359 ± 75 (5)
PBO-11	20.20 ± 2.16 (6)	3.31 ± 0.46 (7)	404 ± 106 (9)
PBO-12	18.10 ± 2.24 (8)	3.49 ± 0.52 (8)	387 ± 62 (5)
PBO-13	18.34 ± 1.54 (10)	2.02 ± 0.55 (9)	645 ± 159 (12)

FILE NAME	# OF BREAKS	L_e	L_e/D	τ (MPa)
pbo-ar	10.7 ± 0.8 (14)	2.05	114.1	16.558 ± 1.276
pbo1	15.3 ± 1.0 (9)	1.43	79.7	23.697 ± 1.545
pbo2	12.9 ± 1.6 (10)	1.71	94.7	19.936 ± 2.465
pbo3	13.0 ± 1.6 (10)	1.69	94.0	20.091 ± 2.416
pbo4	12.1 ± 0.9 (9)	1.82	100.9	18.717 ± 1.434
pbo5	12.4 ± 1.9 (9)	1.77	98.2	19.232 ± 3.004
pbo6	12.4 ± 2.0 (8)	1.78	98.8	19.125 ± 3.084
pbo7	14.8 ± 1.8 (8)	1.49	82.9	22.795 ± 2.832
pbo8	15.3 ± 1.3 (8)	1.44	80.1	23.568 ± 1.981
pbo9	12.8 ± 1.4 (8)	1.73	95.9	19.705 ± 2.146
pbo11	13.8 ± 2.1 (10)	1.59	88.6	21.327 ± 3.323
pbo12	16.7 ± 2.1 (14)	1.32	73.1	25.831 ± 3.232
pbo13	19.3 ± 2.2 (10)	1.14	63.3	17.721 ± 2.032

Wilhelmy Data

Kevlar-29 As Received
k29are Ethylene Glycol contact angle: 27.22 ± 6.30 (30)
k29arm Methylene Iodide contact angle: 42.32 ± 12.7 (25)
k29arw Water contact angle: 60.52 ± 3.57 (25)
Sqrt Disp. Comp. = 5.264 ± .089
Sqrt Polar Comp. = 4.102 ± .090
Disp. Comp. (dyne/cm) = 27.71 ± .94
Polar Comp. (dyne/cm) = 16.83 ± .74
Total surface energy (dyne/cm) = 44.54 ± 1.67

Kevlar-29 Washed
k29we Ethylene Glycol contact angle: 27.70 ± 5.52 (25)
k29wm Methylene Iodide contact angle: 40.49 ± 5.77 (44)
k29ww Water contact angle: 59.94 ± 3.47 (25)
Sqrt Disp. Comp. = 5.434 ± .056
Sqrt Polar Comp. = 4.014 ± .062
Disp. Comp. (dyne/cm) = 29.53 ± .61
Polar Comp. (dyne/cm) = 16.11 ± .50
Total surface energy (dyne/cm) = 45.64 ± 1.11

Kevlar-49 As Received
k49-ar-e Ethylene Glycol contact angle: 57.24 ± 6.86 (25)
k49-ar-m Methylene Iodide contact angle: 31.89 ± 6.45 (26)
k49-ar-w Water contact angle: 62.70 ± 3.24 (25)
Sqrt Disp. Comp. = 5.231 ± .212
Sqrt Polar Comp. = 3.632 ± .212
Disp. Comp. (dyne/cm) = 27.37 ± 2.21
Polar Comp. (dyne/cm) = 13.19 ± 1.54
Total surface energy (dyne/cm) = 40.56 ± 3.75

Kevlar-49 Washed
k49-w-e Ethylene Glycol contact angle: 30.13 ± 5.18 (8)
k49-w-f Formamide contact angle: 24.97 ± 4.62 (3)
k49-w-m Methylene Iodide contact angle: 36.32 ± 5.44 (5)
k49-w-w Water contact angle: 59.93 ± 4.48 (12)
Sqrt Disp. Comp. = 5.498 ± .219
Sqrt Polar Comp. = 4.022 ± .194
Disp. Comp. (dyne/cm) = 30.23 ± 2.41
Polar Comp. (dyne/cm) = 16.18 ± 1.56
Total surface energy (dyne/cm) = 46.40 ± 3.97

PBO As Received
pbo-ar-e Ethylene Glycol contact angle: 45.43 ± 4.78 (20)
pbo-ar-m Methylene Iodide contact angle: 40.05 ± 7.43 (20)
pbo-ar-w Water contact angle: 76.73 ± 3.59 (35)
Sqrt Disp. Comp. = 5.779 ± .094
Sqrt Polar Comp. = 2.458 ± .083
Disp. Comp. (dyne/cm) = 33.39 ± 1.09
Polar Comp. (dyne/cm) = 6.04 ± .41
Total surface energy (dyne/cm) = 39.43 ± 1.50

PBO Washed
pbo-w-e Ethylene Glycol contact angle: 45.18 ± 6.15 (5)
pbo-w-w. Water contact angle: 75.54 ± 3.88 (7)
Sqrt Disp. Comp. = 5.206 ± .470
Sqrt Polar Comp. = 2.964 ± .368
Disp. Comp. (dyne/cm) = 27.10 ± 4.89
Polar Comp. (dyne/cm) = 8.78 ± 2.18
Total surface energy (dyne/cm) = 35.88 ± 7.07

Technora As Received
tech-ar-e Ethylene Glycol contact angle: 38.38 ± 3.78 (25)
tech-ar-m Methylene Iodide contact angle: 32.18 ± 5.46 (30)
tech-ar-w Water contact angle: 65.76 ± 2.43 (25)
Sqrt Disp. Comp. = 5.784 ± .079
Sqrt Polar Comp. = 3.271 ± .081
Disp. Comp. (dyne/cm) = 33.45 ± .91
Polar Comp. (dyne/cm) = 10.70 ± .53
Total surface energy (dyne/cm) = 44.15 ± 1.44

Technora Washed
tech-w-e Ethylene Glycol contact angle: 24.48 ± 3.74 (25)
tech-w-m Methylene Iodide contact angle: 26.60 ± 5.81 (25)
tech-w-w Water contact angle: 45.56 ± 6.21 (25)
Sqrt Disp. Comp. = 5.364 ± .147
Sqrt Polar Comp. = 4.905 ± .146
Disp. Comp. (dyne/cm) = 28.77 ± 1.58
Polar Comp. (dyne/cm) = 24.06 ± 1.43
Total surface energy (dyne/cm) = 52.83 ± 3.01

Kevlar-49 100keV N^+ 10^{14}
kn10014e Ethylene Glycol contact angle: 49.01 ± 5.60 (40)
kn10014m Methylene Iodide contact angle: 34.70 ± 5.79 (25)
kn10014w Water contact angle: 67.41 ± 8.58 (37)
Sqrt Disp. Comp. = 5.321 ± .177
Sqrt Polar Comp. = 3.351 ± .168
Disp. Comp. mN/m = 28.31 ± 1.89
Polar Comp. mN/m = 11.23 ± 1.12
Total surface energy mN/m = 39.54 ± 3.01

Kevlar-49 30keV N^+ 10^{14}
kn3014e Ethylene Glycol contact angle: 41.76 ± 2.53 (25)
kn3014m Methylene Iodide contact angle: 43.62 ± 10.4 (20)
kn3014w Water contact angle: 73.02 ± 4.31 (45)
Sqrt Disp. Comp. = 5.519 ± .107
Sqrt Polar Comp. = 2.955 ± .092
Disp. Comp. (dyne/cm) = 30.46 ± 1.18
Polar Comp. (dyne/cm) = 8.73 ± .54
Total surface energy (dyne/cm) = 39.19 ± 1.73

Kevlar-49 30keV N^+ 10^{15}
kn3015e Ethylene Glycol contact angle: 42.19 ± 3.36 (25)
kn3015m Methylene Iodide contact angle: 38.88 ± 7.96 (30)
kn3015w Water contact angle: 71.48 ± 2.27 (25)
Sqrt Disp. Comp. = 5.692 ± .068
Sqrt Polar Comp. = 2.913 ± .070
Disp. Comp. (dyne/cm) = 32.39 ± .77
Polar Comp. (dyne/cm) = 8.49 ± .41
Total surface energy (dyne/cm) = 40.88 ± 1.18

Kevlar-49 400keV N^+ 10^{12}
kn40012e Ethylene Glycol contact angle: 36.44 ± 6.06 (23)
kn40012m Methylene Iodide contact angle: 45.50 ± 8.41 (50)
kn40012w Water contact angle: 73.20 ± 2.87 (24)
Sqrt Disp. Comp. = 5.548 ± .061
Sqrt Polar Comp. = 2.968 ± .070
Disp. Comp. (dyne/cm) = 30.77 ± .68
Polar Comp. (dyne/cm) = 8.81 ± .42
Total surface energy (dyne/cm) = 39.58 ± 1.10

Kevlar-49 400keV N^+ 10^{13}
kn40013e Ethylene Glycol contact angle: 45.77 ± 5.95 (15)
kn40013m Methylene Iodide contact angle: 37.26 ± 7.06 (30)
kn40013w Water contact angle: 70.78 ± 3.78 (15)
Sqrt Disp. Comp. = 5.759 ± .096
Sqrt Polar Comp. = 2.860 ± .109
Disp. Comp. (dyne/cm) = 33.17 ± 1.11
Polar Comp. (dyne/cm) = 8.18 ± .63
Total surface energy (dyne/cm) = 41.34 ± 1.73

Kevlar-49 400keV N^+ 10^{14}
kn40014e Ethylene Glycol contact angle: 53.29 ± 6.38 (39)
kn40014m Methylene Iodide contact angle: 47.35 ± 15.5 (35)
kn40014w Water contact angle: 78.52 ± 5.89 (40)
Sqrt Disp. Comp. = 5.306 ± .121
Sqrt Polar Comp. = 2.563 ± .118
Disp. Comp. (dyne/cm) = 28.16 ± 1.29
Polar Comp. (dyne/cm) = 6.57 ± .60
Total surface energy (dyne/cm) = 34.72 ± 1.89

Kevlar-49 100keV Ti^+ 10^{15}
kti-e Ethylene Glycol contact angle: 54.01 ± 7.56 (40)
kti-m Methylene Iodide contact angle: 49.84 ± 3.40 (25)
kti-w Water contact angle: 71.41 ± 5.77 (40)
Sqrt Disp. Comp. = 4.794 ± .138
Sqrt Polar Comp. = 3.434 ± .129
Disp. Comp. (dyne/cm) = 22.99 ± 1.32
Polar Comp. (dyne/cm) = 11.79 ± .88
Total surface energy (dyne/cm) = 34.78 ± 2.21

Kevlar-49 390keV He^+ 10^{13}
khe39013-1 Ethylene Glycol contact angle: 38.94 ± 6.78 (5)
khe39013-1 Water contact angle: 62.95 ± 2.54 (4)
sqrt Disp. Comp. = 4.103 ± .355
Sqrt Polar Comp. = 4.731 ± .300
Disp. Comp. (dyne/cm) = 16.83 ± 2.91
Polar Comp. (dyne/cm) = 22.38 ± 2.84
Total surface energy (dyne/cm) = 39.21 ± 5.74

Kevlar-49 75keV Ar^+ 10^{15}
kar-e Ethylene Glycol contact angle: 40.32 ± 5.53 (5)
kar-m Methylene Iodide contact angle: 47.74 ± 1.44 (4)
kar-w Water contact angle: 68.20 ± 3.14 (5)
Sqrt Disp. Comp. = 5.187 ± .171
Sqrt Polar Comp. = 3.542 ± .165
Disp. Comp. (dyne/cm) = 26.90 ± 1.78
Polar Comp. (dyne/cm) = 12.54 ± 1.17
Total surface energy (dyne/cm) = 39.45 ± 2.95

Regression Plots for Wilhelmy Data

Kevlar-49 AR

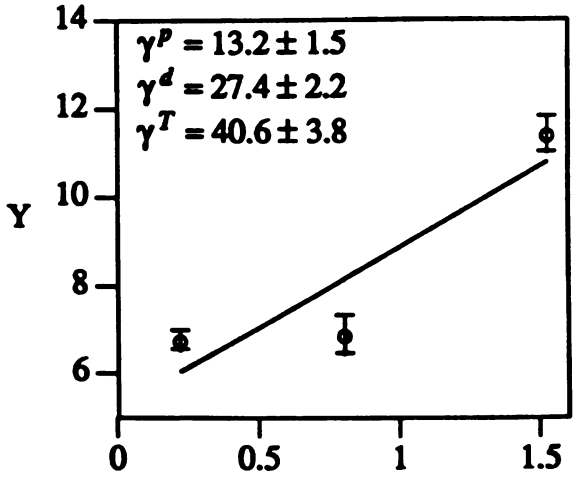

Kevlar-49 Washed

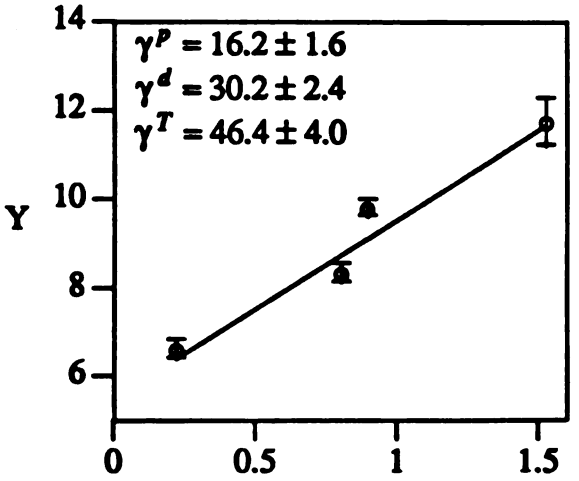

Kevlar Ar+ 75keV 1E15 old

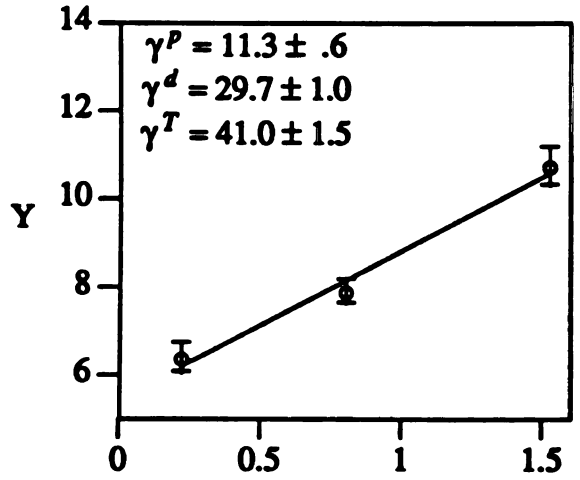

Kevlar Ti+ 100keV 1E15

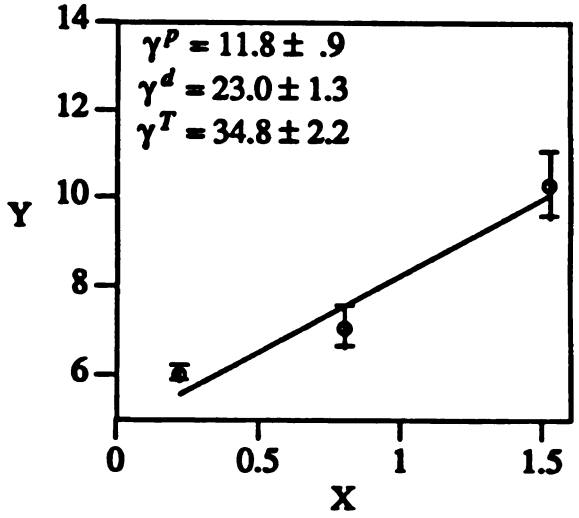

Kevlar N+ 400keV 1E14

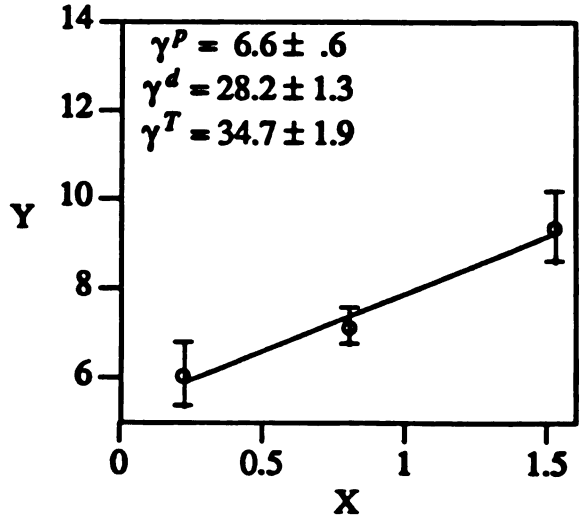

$$X = \sqrt{\frac{\gamma^p}{\gamma^d}}$$

$$Y = \frac{\gamma^T (1 + \cos \Theta)}{2\sqrt{\gamma^d}}$$

Kevlar N+ 100keV 1E14

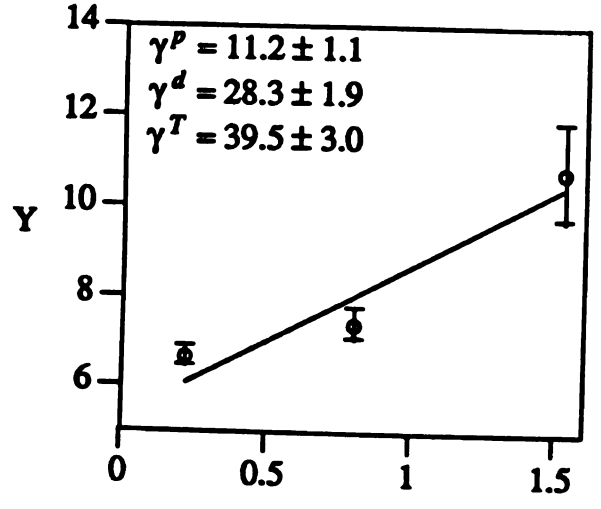

Kevlar N+ 400keV 1E12 old

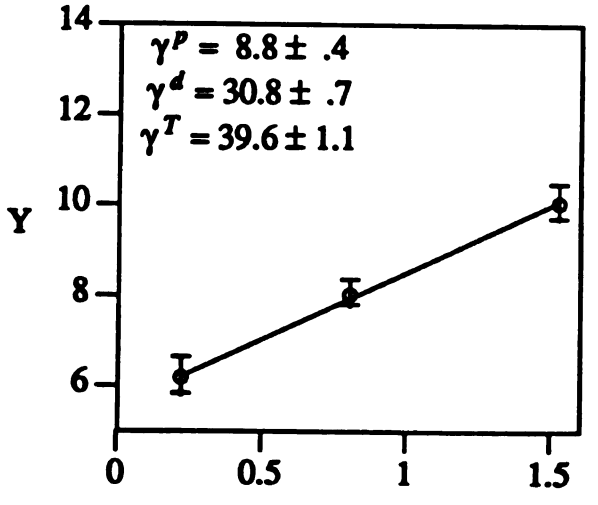

Kevlar N+ 400keV 1E13 old

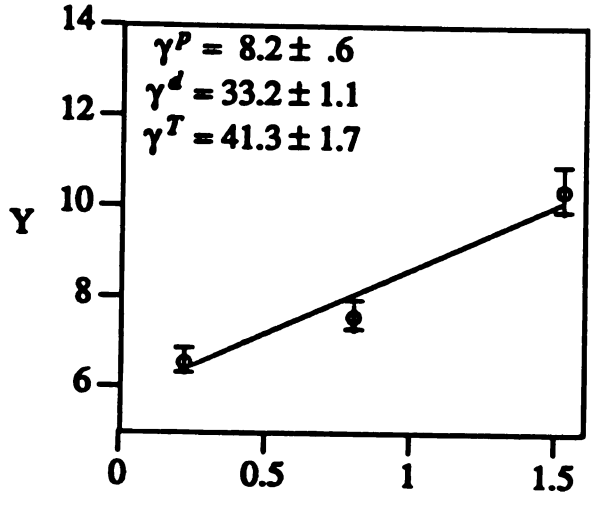

Kevlar N+ 30keV 1E14 old

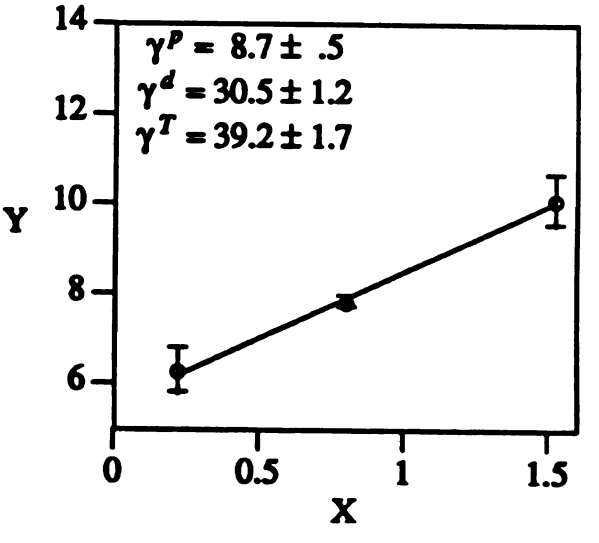

Kevlar N+ 30keV 1E15 old

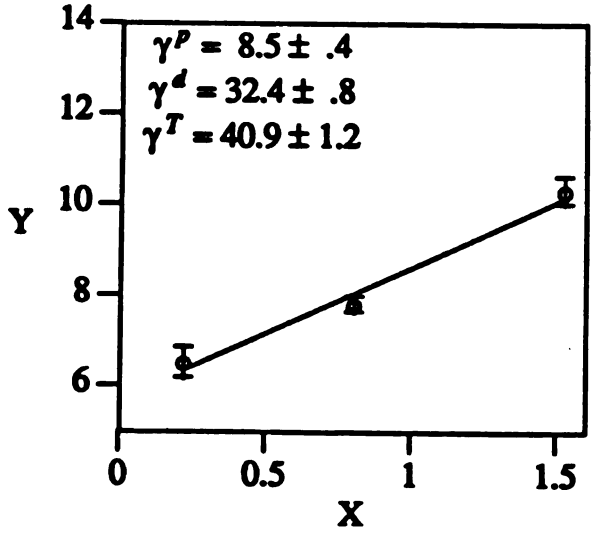

$$X = \sqrt{\frac{\gamma^p}{\gamma^d}}$$

$$Y = \frac{\gamma^T (1 + \cos \Theta)}{2\sqrt{\gamma^d}}$$

Kevlar-29 AR

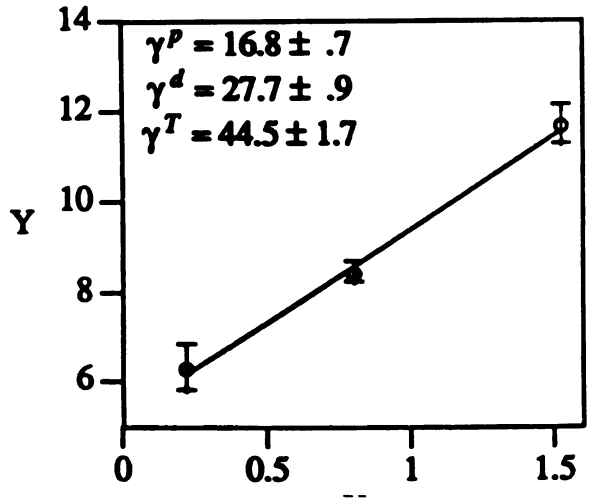

Kevlar-29 Washed

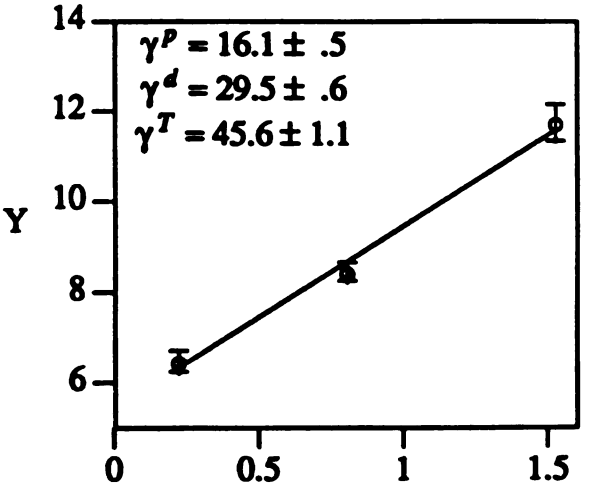

Technora AR

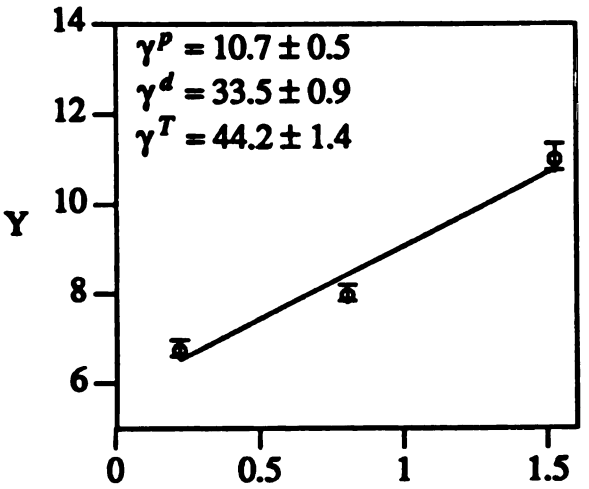

Technora Washed

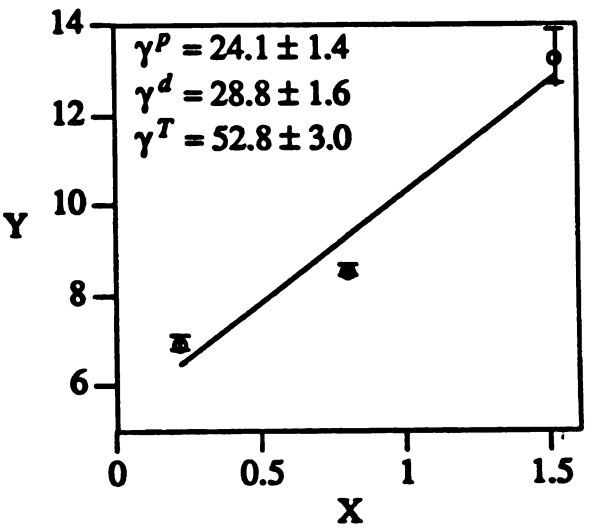

PBO AR

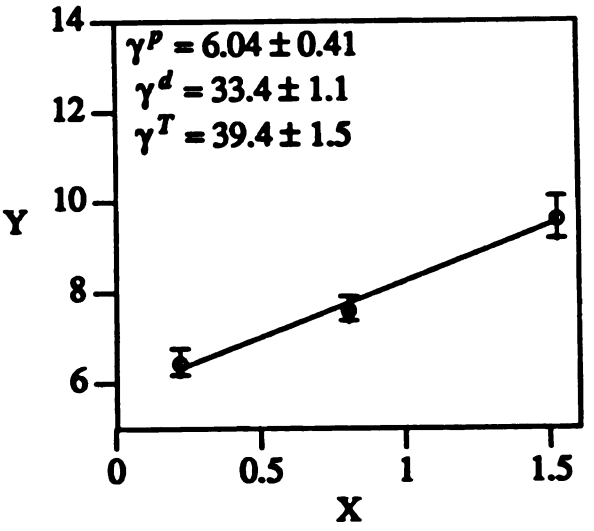

$$Y = \frac{\gamma^T (1 + \cos\Theta)}{2\sqrt{\gamma^d}}$$

$$X = \sqrt{\frac{\gamma^p}{\gamma^d}}$$

Two Points Wilhelmy Data

Fiber	Water Cont. Ang. (°)	Et. Gly. Cont. Ang. (°)	γ_s^D dyne/cm	γ_s^P dyne/cm	γ_s^T dyne/cm
DER331 Epoxy			36.7	10.8	47.5
K29 As Rec.	60.5 ± 3.6 (25)	27.2 ± 6.3 (30)	23.3 ± 1.4	19.8 ± 1.1	43.1 ± 2.5
K29 Washed	59.9 ± 3.5 (25)	27.7 ± 5.5 (25)	22.3 ± 1.4	20.8 ± 1.1	43.1 ± 2.5
K49 As Rec.	62.7 ± 3.2 (25)	57.2 ± 6.9 (25)	3.41 ± 0.73	38.7 ± 2.0	42.2 ± 2.7
K49 Washed	60.7 ± 4.4 (60)	30.2 ± 5.8 (38)	21.4 ± 1.5	20.7 ± 1.1	42.2 ± 2.7
Ti^+ *100KeV 1E15*	74.1 ± 5.7 (25)	55.1 ± 4.5 (30)	16.2 ± 1.6	14.2 ± 1.8	30.4 ± 3.4
Ar^+ *75KeV 1E15*	68.0 ± 3.4 (25)	40.0 ± 5.3 (25)	22.1 ± 1.6	15.4 ± 1.1	37.6 ± 2.7
N^+ *30KeV 1E15*	71.5 ± 2.3 (25)	42.2 ± 3.4 (25)	24.7 ± 1.1	12.0 ± 0.6	36.7 ± 1.8
N^+ *30KeV 1E14*	73.0 ± 4.3 (45)	41.8 ± 2.5 (25)	27.6 ± 2.1	9.91 ± 0.98	37.5 ± 3.1
N^+ *100KeV 1E14*	75.1 ± 6.8 (30)	47.4 ± 3.6 (30)	24.1 ± 2.8	10.2 ± 1.5	34.3 ± 4.2
N^+ *400KeV 1E14*	76.5 ± 6.3 (42)	46.8 ± 4.4 (22)	26.9 ± 3.5	8.34 ± 1.5	35.2 ± 4.9
1E13 1 day old	62.8 ± 4.3 (25)	48.1 ± 7.2 (24)	9.29 ± 1.4	29.5 ± 2.0	38.8 ± 3.3
1E13 2 days old	68.3 ± 3.3 (15)	49.0 ± 3.7 (15)	13.9 ± 1.5	20.6 ± 1.5	34.5 ± 3.1
1E13 3 days old	65.8 ± 5.5 (15)	44.3 ± 5.0 (10)	15.4 ± 3.2	21.3 ± 2.9	36.7 ± 6.1
5E12 1 day old	63.3 ± 4.1 (24)	36.2 ± 5.3 (20)	19.7 ± 1.8	20.1 ± 1.5	39.8 ± 3.3
5E12 2 days old	67.9 ± 6.4 (13)	37.0 ± 5.6 (15)	25.1 ± 3.6	13.9 ± 2.2	39.0 ± 5.8
5E12 3 days old	79.5 ± 4.7 (15)	44.3 ± 5.5 (15)	34.7 ± 3.6	4.74 ± 1.08	39.4 ± 4.6
2E12 day 1	61.3 ± 7.2 (25)	31.1 ± 6.9 (29)	21.5 ± 2.5	20.3 ± 2.1	41.7 ± 4.6
2E12 day 2	52.9 ± 6.7 (19)	29.5 ± 5.6 (21)	13.8 ± 2.1	32.7 ± 2.7	46.6 ± 4.8
2E12 1 month	73.2 ± 2.9 (24)	36.4 ± 6.1 (23)	33.5 ± 1.9	7.74 ± 0.74	42.3 ± 2.6
1E13 day 1	62.9 ± 1.8 (17)	37.6 ± 4.8 (22)	18.1 ± 1.0	21.5 ± 0.9	39.6 ± 1.9
1E13 day 2	64.6 ± 4.2 (20)	37.5 ± 6.4 (25)	20.0 ± 1.8	19.0 ± 1.5	39.0 ± 3.3
2E14 day 1	71.3 ± 3.2 (25)	39.2 ± 4.8 (23)	27.6 ± 1.8	10.9 ± 0.9	38.5 ± 2.6
2E14 day 2	70.7 ± 2.4 (25)	49.1 ± 5.0 (21)	16.3 ± 1.2	17.1 ± 1.0	33.4 ± 2.2
2E14 1 month	82.8 ± 1.4 (25)	57.3 ± 4.4 (24)	22.5 ± 1.1	6.92 ± 0.49	29.5 ± 1.6
2E14 1m wash	76.0 ± 4.1 (29)	51.9 ± 7.6 (30)	19.6 ± 1.9	11.8 ± 1.2	31.4 ± 3.1
Air Prod. B	60.1 ± 6.6 (54)	32.6 ± 5.8 (25)	19.0 ± 2.6	22.8 ± 2.1	41.8 ± 4.8
Par-N 100nm	86.5 ± 4.3 (34)	52.8 ± 6.2 (25)	34.7 ± 2.8	2.41 ± 0.57	37.1 ± 3.3
Technora as rec.	65.8 ± 2.4 (25)	38.4 ± 3.8 (25)	20.9 ± 1.1	17.7 ± 0.8	38.5 ± 1.8
Technora washed	45.6 ± 6.2 (25)	24.5 ± 3.7 (25)	10.8 ± 1.3	42.3 ± 2.1	53.0 ± 3.5
PBO as rec.	76.7 ± 3.6 (35)	45.4 ± 4.8 (20)	28.7 ± 2.2	7.63 ± 0.88	36.3 ± 3.1
PBO washed	76.0 ± 4.1 (35)	45.3 ± 5.5 (24)	27.6 ± 2.3	8.40 ± 0.98	36.0 ± 3.3
PBO#1 (set two)	68.3 ± 3.7 (45)	29.6 ± 3.0 (20)	33.0 ± 2.3	10.4 ± 0.9	43.3 ± 3.2
PBO#4 (set two)	53.5 ± 6.2 (30)	31.9 ± 5.8 (24)	12.9 ± 1.8	33.2 ± 2.3	46.1 ± 4.1
PBO#7 (set two)	51.8 ± 4.0 (25)	26.7 ± 6.6 (22)	14.2 ± 1.3	33.4 ± 1.7	47.6 ± 3.0
PBO#8 (set two)	53.9 ± 9.1 (28)	29.9 ± 3.6 (30)	14.9 ± 2.4	30.7 ± 2.8	45.6 ± 5.2
PBO#12 (set two)	58.8 ± 5.3 (25)	35.7 ± 5.4 (24)	15.2 ± 1.7	26.9 ± 1.9	42.0 ± 3.6

Droplet Results Regression Plots

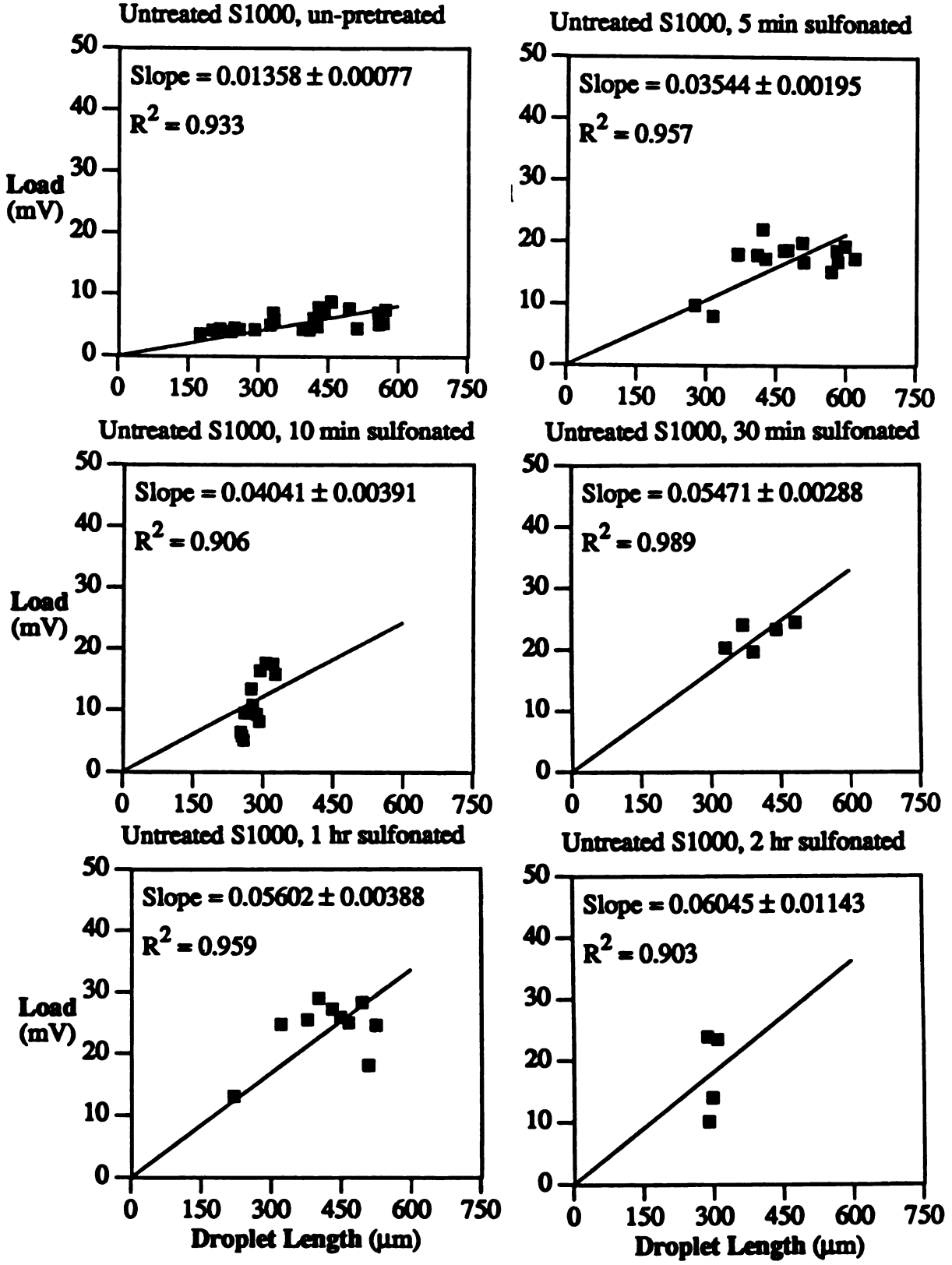

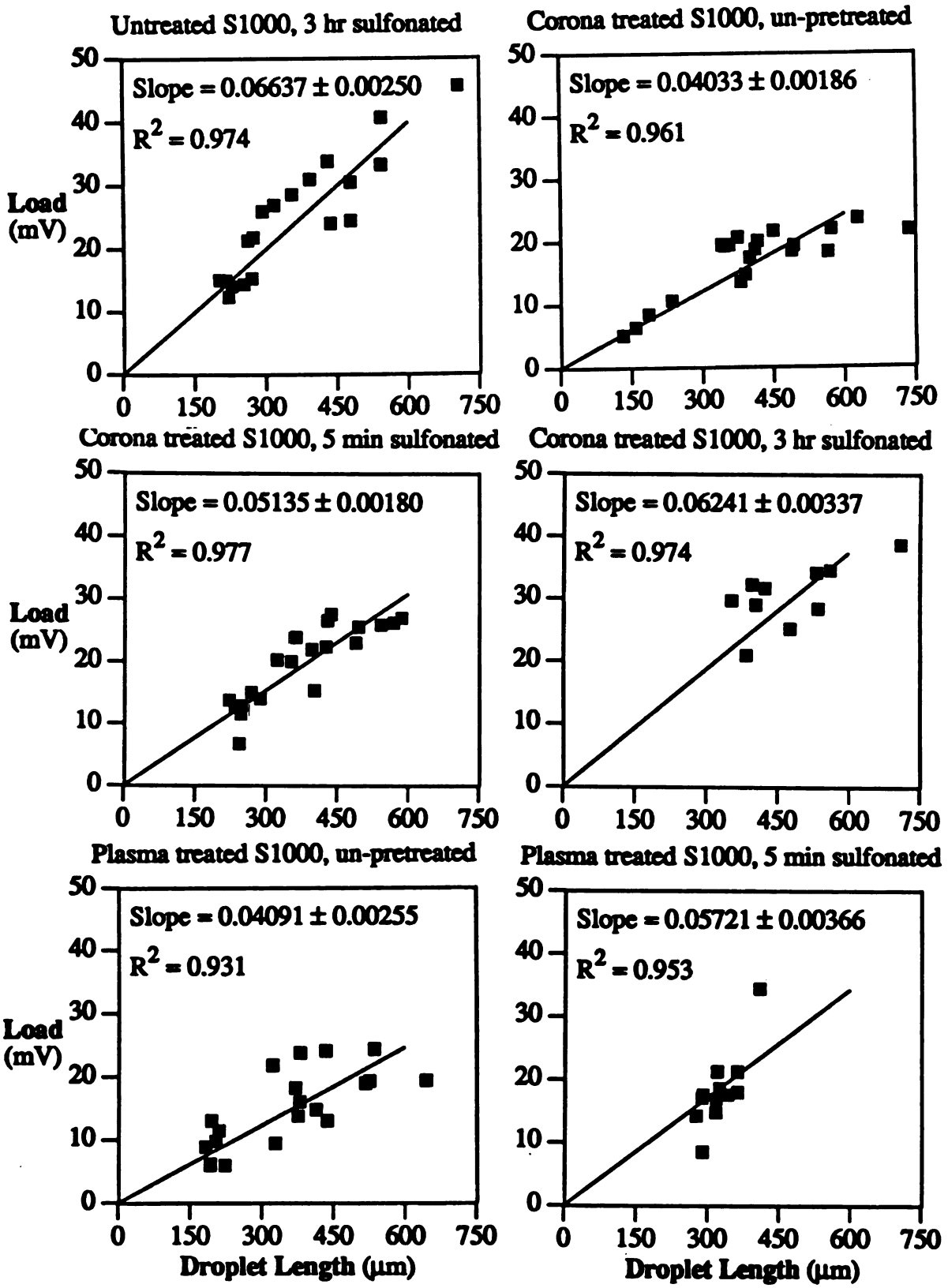
Untreated S1000, 3 hr sulfonated
Slope = 0.06637 ± 0.00250
R^2 = 0.974
Corona treated S1000, un-pretreated
Slope = 0.04033 ± 0.00186
R^2 = 0.961
Corona treated S1000, 5 min sulfonated
Slope = 0.05135 ± 0.00180
R^2 = 0.977
Corona treated S1000, 3 hr sulfonated
Slope = 0.06241 ± 0.00337
R^2 = 0.974
Plasma treated S1000, un-pretreated
Slope = 0.04091 ± 0.00255
R^2 = 0.931
Plasma treated S1000, 5 min sulfonated
Slope = 0.05721 ± 0.00366
R^2 = 0.953
Load (mV)
Droplet Length (μm)
0
10
20
30
40
50
0
150
300
450
600
750

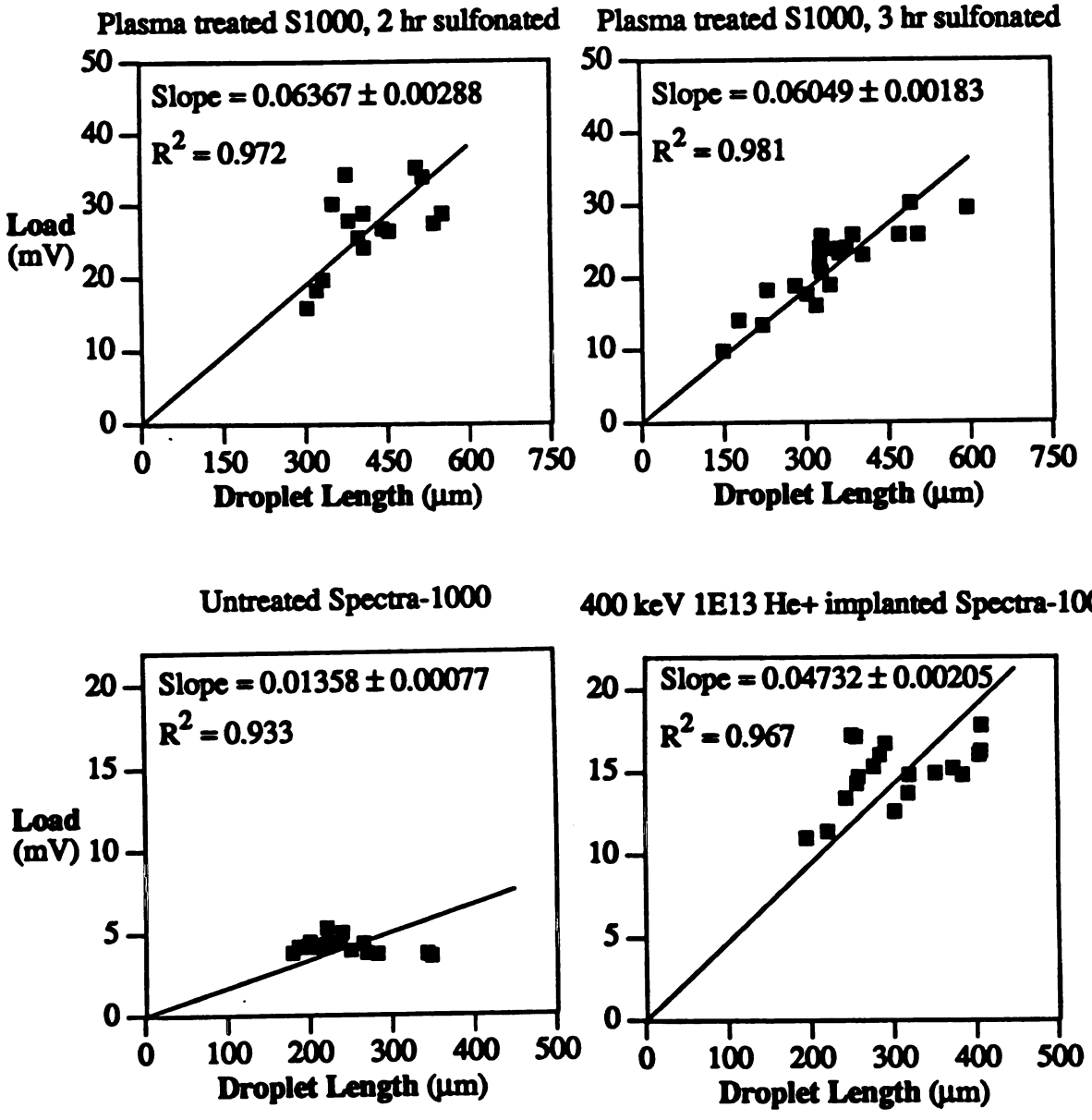
Plasma treated S1000, 2 hr sulfonated
Slope = 0.06367 ± 0.00288
R^2 = 0.972
Load (mV)
Droplet Length (μm)
Plasma treated S1000, 3 hr sulfonated
Slope = 0.06049 ± 0.00183
R^2 = 0.981
Droplet Length (μm)
Untreated Spectra-1000
Slope = 0.01358 ± 0.00077
R^2 = 0.933
Load (mV)
Droplet Length (μm)
400 keV 1E13 He+ implanted Spectra-1000
Slope = 0.04732 ± 0.00205
R^2 = 0.967
Droplet Length (μm)

Sulfonated PC Sulfur Penetration Depths (AES Results)

Time (hr)	Chilled (μm)	Ambient (μm)	Warm (μm)
0.167	-	0.7 ± 0.2 [6]	1.4 ± 0.3 [6]
0.50	-	1.1 ± 0.2 [6]	-
0.75	-	-	4.3 ± 0.3 [6]
1.0	-	1.5 ± 0.2 [5]	-
2.0	-	2.2 ± 0.1 [6]	-
3.0	-	2.8 ± 0.2 [6]	-
7.0	-	3.6 ± 0.4 [6]	-
10.0	0.9 ± 0.2 [6]	-	-
12.0	-	4.0 ± 0.4 [6]	-
20.0	-	4.3 ± 0.2 [5]	-
24.0	1.4 ± 0.2 [6]	-	6.2 ± 0.6 [4]
45.0	-	4.7 ± 0.4 [7]	-
60.0	2.2 ± 0.2 [5]	-	7.4 ± 0.5 [6]
72.0	-	5.1 ± 0.3 [5]	-
168.0	3.7 ± 0.3 [5]	5.6 ± 0.2 [6]	7.6 ± 0.9 [6]
672.0	-	6.2 ± 0.3 [6]	-

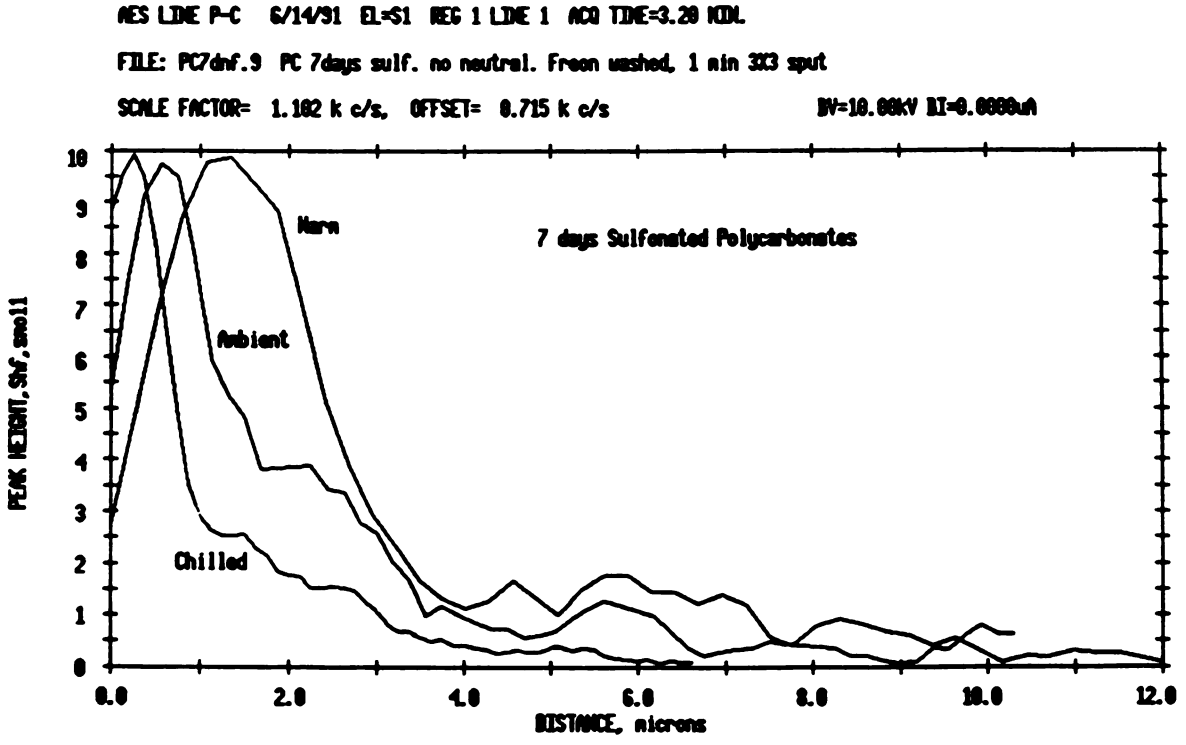

BIBLIOGRAPHY

BIBLIOGRAPHY

Adem, E.H., S.J. Bean, C.M. Demanet, A. LeMoel, and J.P. Duraud, "XPS as a Tool for Investigation of Polymers Irradiated by Energetic Ions," *Nuclear Instruments and Methods in Physics Research*, B32, 182 (1988).

Agrawal, B.D. and L.J. Broutman, *Analysis and Performance of Fiber Reinforced Polymers*, John Wiley and Sons, In. N.Y., 48 (1980).

Allen, S.R., "Tensile Recoil Measurement of Compressive Strength for Polymeric High Performance Fibers," *J. Mater. Sci.*, 22, 853 (1987).

Allred, R.E., *Surface Chemical Modification of Polyaramid Filaments with Amine Plasmas*, Ph.D. dissertation, Massachusetts Institute of Technology, (1983).

Allred, R.E., E.W. Merrill and D.K. Roylance, *Molecular Characterization of Composite Interfaces*, H. Ishida and G. Kumar, Eds, Plenum Press, New York, 333 (1985).

Armistead, J.P., A.W. Snow, W.D. Bascom, "Butadiyne Vapor Deposition Polymerization on Carbon Fibers," *19th International SAMPE Technical Conference*, October, 644 (1987).

Atkins, P.W., *Physical Chemistry*, W.H.Freeman & Company, San Francisco, 850 (1978).

Attenburrow, G.E. and D.C. Bassett, "Compliance and Failure Modes of Oriented Chain Extended Polyethylene" *J. Material Science*, 14, 2679 (1979).

Baszkin, A. and L. Ter-Minassin-Saraga, "Effect of Surface Polarity on Self-Adhesion of Polymers," *Polymer*, 19, 10833 (1978).

Baun, W.L., *Appl. Surface Sci.*, 4, 291 (1980).

Bazhenov, L., V.V. Kozey, and A.A. Berlin, "Compressive Fracture of Organic Fiber Reinforced Plastics," *J. Mater. Sci.*, 24, 4509 (1989).

Beach, W.F., "A Model for the Vapor Deposition Polymerization of p-Xylylene," *Macromolecules*, 11, 72 (987).

Bell, A.T., "The First Annual International Conference of Plasma Chemistry and Technology, Ed. H.V. Boenig, Technomic Publishing Co. Inc., Lancaster, PA, 29 (1983).

Bellamy, L.T., *The Infrared Spectra of Complex Molecules*, John Wiley & Sons, New York (1958).

Berg, J.S. and D.F. Adams, "An Evaluation of Composite Materials Compression Test Methods," *J. of Composites Technology & Research*, 41 (1989).

Bertrand, P., Y. DePuydt, J.M. Beuken, P. Lutgen, and G. Feyder, "Modification of Polymer (PET) surface Reactivity by Low Energy Ion Bombardment," *Nuclear Instruments and Methods in Physics Research*, **B19/20**, 887 (1987).

Biersack, J.P. and L. G. Haggmark, *Nucl. Instr. Meth.*, **174**, 257 (1980).

Billmeyer, F.W., *Textbook of Polymer Science*, John Wiley & Sons, New York, 289 (1984).

Bjorksten, J. and L.L. Yaeger, "Vinyl Silane Size for Glass Fabrics", *Mod. Plast.*, **29**, 124 (1952).

Blades, H., "Dry-Jet Wet Spinning Process," U.S. Patent 3,767,756 (1973).

Blythe, A.R., D. Briggs, C.R. Kendall, D.G. Rance and V.J.I. Zichy, "Surface Modification of Polyethylene by Electrical Discharge Treatment and the Mechanism of Autoadhesion," *Polymer*, **19**, 1273 (1978).

Bodo, P. and J.E. Sundgren, *J. Appl Phys.*, **60**, 1161 (1986).

Bowden, P.B. and R.J. Young, "Deformation Mechanisms in Crystalline Polymers," *J. Material Science*, **9**, 2034 (1974).

Brady, J.M. and E.L. Thomas, "The Deformation of Oriented High Density Polyethylene, Part 2: The Formation of Long Crystalline Fibrils at Elevated Temperatures," *J. Material Science*, **24**, 3319 (1989).

Brady, J.M. and R.S. Porter, "Composites Reinforced with Fibers of a Thermotropic Liquid Crystal Copolyester," *J. Thermoplastic Composite Materials*, **3**, 252 (1990).

Brice, D.K., "Ion Implantation Range and Energy Deposition Distributions," Plenum Data Company, New York, (1975).

Briggs, D., C.R. Kendall, A.R. Blythe and A.B. Wootton, "Electrical Discharge Treatment of Polypropylene Film," *Polymer*, **24**, 27 (1983).

Cameron, G. and B.R. Main, *Polym. Degrad. Stab.*, **11**, 9 (1985).

Carley, J.F. and P.T. Kitze, "Corona-Discharge Treatment of Polyethylene Films. I. Experimental Work and Physical Effects," *Polymer Eng. Sci.*, **18**, 326 (1978).

Carter, G. and J.S. Colligon, *Ion Bombardment of Solids*, Ch. 5, American Elsvier Publishing Company Inc., New York, (1968).

Cazeneuve, C., J.E. Castle and J.F. Watts, *J. Mater. Sci.*, **25**, 1902 (1990).

Chand, N., R.K. Tiwary, and P.K. Rohatgi, "Resource Structure Properties of Natural Cellulosic Fibers - an Annotated Bibliography," *J. Material Science*, **23**, 381 (1988).

Chamis, C.C., "Mechanics of Load Transfer at the Interface," *Interfaces in Polymer Matrix Composites*, E. P. Pluddemann, ed. Academic Press, New York, 31 (1974).

Chapiro, A., "Chemical Modifications in Irradiated Polymers," *Nuclear Instruments and Methods in Physics Research*, **B32**, 111 (1988).

Chou, T. and A. Kelly, "The Effects of Transverse Shear on the Longitudinal Compressive Strength of Fiber Composites," *J. of Material Science*, **15**, 327 (1980).

Choe, C.R. and J. Jang, "Adhesion Promotion of Ultra High Modulus Polyethylene Fiber/Epoxy Composite Interface," in *Controlled Interphase in Composite Materials*, H. Ishida, Ed., Proceedings of the Third International Conference on Composite Interfaces, Elsevier, NY, 97 (1990).

Cohen, Y., "Structure Formation in Solutions of Rigid Polymers Undergoing a Phase Transition," Ph.D. dissertation, University of Massachusetts, (1986).

Cooke, T.F., "High Performance Fiber Composites with Special Emphasis on the Interface", *J. Poly. Eng.*, **7**, 197 (1987).

Cox, H.L., "The Elasticity and Strength of Paper and Other Fiberious Materials," *J. Appl. Phys. B.*, **3**, 72 (1952).

Cussler, E.L., *Diffusion*, Cambridge University Press, New York, NY (1984).

Dawes, C.J., *Biological Techniques in Electron Microscopy*, Barnes and Noble Inc., New York, (1971).

Defay, R., I. Prigogine, A. Bellemans and D.H. Everett, "Surface Tension and Adsorption," Ch. XIX, John Wiley and Sons Inc., New York, (1966).

DeLong, J.D., K.J. Hook, M.J. Rich, J. Kalantar and L.T. Drzal, "Spectroscopic Characterization of Fiber-Matrix Interphase," in Controlled Interphase in Composite Materials, H. Ishida, Ed., *Proceedings of the Third International Conference on Composite Interfaces*, Elsevier, NY, 87 (1990).

Dersselhaus, M.S., B. Wasserman, and G.E. Wnek, "Ion Implantation of Polymers," 28." A.J. Kinloch, *Adhesion and Adhesives*, Chapman And Hall, New York, 129 (1987).

Deteresa, S.J., S.R. Allen, R.J. Farris and R.S. Porter, "Compressive and Torsional Behavior of Kevlar-49 Fibres," *J. Mater Sci.*, **19**, 57 (1984).

Deteresa, S.J., "The Axial Compressive Strength of High Performance Polymer Fibers," Ph.D. dissertation, University of Massachusetts, (1985).

Dixon, D.D., L.J. Hayes, *Sulfo-Fluorination of Synthetic Resins*, U.S. Patent 3940520, (1976).

Dixon, D.D., L.J. Hayes, *Fluorination of Polyesters and Polyamide Fibers*, U.S. Patent 3988491, (1976).

Dixon, D.D., W.M. Smith, *Fluorinated Polyester Tire Reinforcement Materials*, U.S. Patent 4009304, (1977).

Dixon, D.D., L.J. Hayes, *Fluorination of Polyolfin and Polyacrylonitrile Fibers*, U.S. Patent 4020223, (1977).

Dobb, M.G., D.J. Johnson and B.P. Saville, "Supramolecular Structure of a High-Modulus Polyaromatic Fiber (Kevlar 49)," *J. Polymer Science, Polymer Physics Ed.*, **15**, 2201 (1977).

Dobb, M.G., D.J. Johnson and B.P. Saville, "Compressional Behavior of Kevlar 49 Fibers," *Polymer*, **22**(7), 960 (1981).

Drzal, L.T., "Interfacial Behavior of Aramid and Graphite Fibers in an Epoxy Matrix", *15th National SAMPE Tech. Conf.*, Cincinnati OH, (1983).

Drzal, L.T., "The Interfacial and Compressive Properties of Polybenzothiazole Fibers," *AFWAL-TR-86-4003* (1986).

Drzal, L.T., M.J. Rich, and S. Subramoney, "Fiber-Matrix Interface and Its Effects On Composite Properties," *Proceedings of the Third Annual Conference on Advanced Composites*, Detroit, MI, 305 (1987).

Drzal, L.T. and P.J. Herrera-Franco, "Composite Fiber-Matrix Bond Tests," *Engineered Materials Handbook*, 3, 391 (1991).

Gabayson, S.M., G. Sugerman, and S.J. Monte, "Role of Coupling Agents in Aerospace Composite Failure," in Proceedings of the SPE Annual Technical meeting, New York (1989).

Gabriel, B.L., *SEM: A User's Manual For Materials Science*, American Society for Metals, Metals Park, (1985).

Gaur, U and T. Dividson, "Interfacial Effects of Plasma Treatment of Fiber Pull-out," *Materials Research Society Symposium Proceedings 170*, Pittsburgh, PA, 315 (1990).

Gilbert, A.H., B. Goldstein and G. Marom, "A Liquid Droplet Measurement Technique as a Means of Assessing the Interlaminar Shear Strength of Fiber-Reinforced Composites," *Composites*, 21, 408 (1990).

Gillberg, G., "Polymer Surface Characterization: An Overview," *J. Adhesion*, 21, 129 (1987).

Greszczuk, L.B., "Theoretical Studies of the Mechanism of the Fiber-Matrix Interface in Composites," Interface in Composites, ASTM, STP 452, Am. Soc. Testing and Materials, Phil. PA, 42 (1969).

Grummon, D.S., R. Schalek, A. Ozzello, and L.T. Drzal, "Modification of Fiber-Matrix Adhesion in Polyethylene Reinforced Composites by Energetic Ion Irradiation," in *Proceedings of the Sixth Annual ASM/ESD Advanced Composites Conference*, Detroit, MI, 155 (1990).

Grummon, D.S., R. Schalek, A. Ozzello, J. Kalantar and L.T. Drzal, "High Energy Ion Implantation of Polymeric Fibers for Modification of Reinforcement-Matrix Adhesion," *Nuclear Instruments and Methods in Physics Research* (1991 in press).

Guimaraes, R.B., L. Amaral, M. Behar, and F.C. Zawislak, "Anomalous Depth Profiles of Light Ions and Nobel Gases Implanted Into Polymers," *Nuclear Instruments and Methods in Physics Research*, B39, 800 (1989).

Gutowski, W., "Effect of Fiber-Matrix Adhesion on Mechanical Properties of Composites", *Controlled Interphase in Composite Materials*, H. Ishida Ed., Elsevier Science Publishing Co., New York, NY, 505 (1990).

Hammer, G.E. and L.T. Drzal, "Graphite Fiber Surface Analysis by X-ray Photoelectron Spectroscopy and Polar/Dispersive Free Energy Analysis," *Applications of Surface Science 4*, North-Holland Publishing Company, 340, (1980).

Hansen, R.H., J.V. Pascale, T.D. Benedictis, and P.M. Rentzepis, "Effects of Atomic Oxygen on Polymers," *J. Polymer Science: A*, **3**, 2205 (1965).

Holden, P.S., G.A.J. Orchard, and I.M. Ward, "A Study of the Gas Barrier Properties of Highly Oriented Polyethylene," *J. Polymer Science: Polymer Physics Edition*, **23**, 709 (1985).

Holmes, S. and P. Schwatrz, "Ammination of Ultra-high Strength Polyethylene using Ammonia Plasma," *Composite Science and Technology*, **38**, 1 (1990).

Hook, K.J., R.K. Agrawal and L.T. Drzal, "Effects of Microwave Processing on Fiber-Matrix Adhesion. II. Enhanced Chemical Bonding of Epoxy to Carbon Fibers," *J. Adhesion*, **32**, 157 (1990).

Ihata, J., *J. Polym. Sci., Part A, Polym. Chem.*, **26**, 167 (1988).

Inagaki, N., A. Kishi and K. Katsuura, *Int. J. Adhesion Adhesives*, **2**, 233 (1982).

Ishitani, A., K. Shoda, H. Ishida, T. Watanabe, and K. Yoshida, "Characterization of Oxygen-Implanted Polyethylene by Various Analytical Techniques," *Nuclear Instruments and Methods in Physics Research*, **B39**, 783 (1989).

Jones, R.W., *Fundamental Principles of Sol-Gel Technology*, The Institute of Metals, Brookfield, VT (1989)

Kaelble, D.H., *Physical Chemistry of Adhesion*, Wiley-Interscience, New York, (1971).

Kalantar, J., D.S. Grummon and L.T. Drzal, "Effects of Ti^+, Ar^+ and N^+ Ion Implantation on Aramid Fiber Adhesive Properties," in Interfaces in Composites, C.G. Pantano and E.J.H. Chen, Eds., *Materials Research Society Symposium Proceedings 170*, Pittsburgh, PA, 315 (1989).

Kalantar, J. and L.T. Drzal, "The Bonding Mechanism of Aramid Fibers to Epoxy Matrices, Part I: A Review of the Literature," *J. Mater. Sci.*, **25**, 4186 (1990).

Kalantar, J. and L.T. Drzal, "The Bonding Mechanism of Aramid Fibers to Epoxy Matrices, Part II: An Experimental Investigation," *J. Mater. Sci.*, **25**, 4194 (1990[b]).

Kalantar, J., L.T. Drzal and K.J. Hook, "A Novel Sample Preparation Technique for Ion and Electron Beam Analysis of the Fiber-Matrix Interphase in Polymeric Composites," *J. Vac. Sci. Technol. A.*, **8**, 3878 (1990[c]).

Kalantar, J., L.T. Drzal and D.S. Grummon, "Structural Properties of Aramid Fibers and Their Influence on Fiber Adhesion," in *Controlled Interphase in Composite Materials*, H. Ishida, Ed., Proceedings of the Third International Conference on Composite Interfaces, Elsevier, NY, 685 (1990[d]).

Kalantar, Y. Muraoka, and L.T. Drzal, "Effects of Temperature on Atomic Distribution of Sulfonated Species in Polymers," (manuscript in preparation, 1991[a]).

Kalb, B. and A.J. Pennings, "Maximum Strength and Drawing Mechanism of Hot Drawn High Modulus Molecular Weight Polyethylene," *J. Material Science*, **15**, 2584 (1980).

Kazuyo, S., K. Imada, and M. Takayanagi, "Formation of Kink Bands by Compression of the Extruded of Solid Linear Polyethylene," *J. Polymer Science*, **13**, 73 (1975).

Kelly, A. and W.R. Tyson, "Tensile Properties of Fiber-Reinforced Metals: Copper/Tungsten and Copper/Molybdenum," *J. Mech. Phys. Solids*, **13**, 329 (1965).

Kim, C.Y., J. Evans, and D.A.I. Goring, "Corona-Induced Autohesion of Polyethylene," *J. Appl. Polymer Sci.*, **15**, 1365 (1971).

Klomparens, K.L., S.L. Flegler, and G.R. Hooper, *Procedures for Transmission and Scanning Electron Microscopy for Biological and Medical Science*, LADD Research Industries, Burlington, VT, (1986).

Kovar, R. and R.R. Wallis, "Interpenetrated Polymer Films," *U.S. Patent 4,845,150* (1989).

Krause, S.J., T.B. Haddock, D.L. Vezie, P.G. Lenhert, W.F. Hwang, G.E. Price, T.E. Helminiak, J.F. O'Brien, and W.W. Adams, "Morphology and Properties of Rigid-Rod Poly(p-Phenylene Benzobisoxazole) (PBO) and stiff-chain poly(2,5(6)-Benzoxazole) (ABPBO) Fibers," *Polymer*, **29**, 1354 (1988).

Krause, S.J., D.L. Vezie, and W.W. Adams, "Straightening of Pleated Sheet Structure in Fibers of Poly(p-Phenylene Terephthalamide)-Kevlar 149," *Polymer Communications*, **30**, 10 (1989).

Kumakhov, M.A. and F.F. Komarov, "Energy Loss and Ion Ranges in Solids," Gordon and Breach, Science Publishers Inc., New York, (1981).

Kumar, S., "Compressive Strength of High Performance Fibers," *SAMPE Journal*, **26**, 51 (1990).

Kupper, K. and P. Schwartz, "Modification of the Fiber-Matrix Interface of p-Aramid Fibers Using Gas Plasma," *J. Adhesion Sci. Technol.*, **5**, 165 (1991).

LaCourse, W.C., "Continuous Filament Fibers by the Sol-Gel Process," in *Sol-Gel Technology for Thin Films, Fibers, Preforms, Electronics and Specialty Shapes*, L.C. Kelin Edt., Noyes Publications, Park Ridge, NJ, 184 (988).

Ladizesky, N.H. and I.M. Ward, "A Study of the Adhesion of Drawn Polyethylene Fiber/Polymeric Resin Systems," *J. Material Science*, **18**, 533 (1983).

Ladizesky, N.H. and I.M. Ward, "The Adhesion Behavior of High Modulus Polyethylene Fibers Following Plasma and Chemical Treatments," *J. Material Science*, **24**, 3763 (1989).

Lanauze, J.A. and D.L. Myers, "Ink Adhesion on Corona-Treated Polyethylene Studied by Chemical Derivatization of Surface Functional Groups," *J. Applied Polymer Science*, **40**, 595 (1990).

Licciardello, A., O. Puglusi, L. Calcagno, and G. Foti, "XPS Study of Polystyrene Gel Induced by Ion and Electron Bombardment," *Nuclear Instruments and Methods in Physics Research*, **B19/20**, 903 (1987).

Liston, E.M., "Plasma Treatment for Improved Bonding: A review," *J. Adhesion*, **30**, 199 (1989).

Madhukar, M.S. and L.T. Drzal, "Fiber-Matrix Adhesion and its Effects on Composite Mechanical Properties. III. Longitudinal (0°) Compressive Properties of Graphite/Epoxy Composites," (in press)

Malis, T.F. and D. Steele, "Ultramicrotomy for Materials Science," in Workshop on Specimen Preparation for TEM of Materials II, R. Anderson, Ed., *Materials Research Society Symposium Proceedings 199*, Pittsburgh, PA, 315 (1990).

Mark, V., Ger. Offen. 2,458,968 (1975).

Martin, D.C. and E.L. Thomas, "Micromechanisms of Kinking in Rigid-Rod Polymer Fibers," *J. Material Science*, (in press, 1991).

Mayer, W.J., L. Eriksson and J.A. Davies, "Ion Implantation in Semiconductors," Ch. 2., Academic Press, New York, (1970).

Mcalea, K. and G. Besio, "Adhesion Between Polybutylene Terephthalate and E-Glass Measured with a Microdebond Technique," *Polymer Composites*, **9**, 285 (1988).

Mercx, F.P.M. and P.J. Lemstra, "Surface Modification of Aramid Fibres," *Polymer Communications*, **31**, 252 (1990).

Michalske, T.A. and B.C. Bunker, "The Fracturing of Glass," *Scientific American*, **257**, 122 (1987).

Miller, B., P. Muri and L. Rebenfeld, "A Microbond Method for Determination of the Shear Strength of a Fiber/Resin Interface," *Comp. Sci. Tech.*, **28**, 17 (1987).

Mittelman, H., I. Roman, and G. Marom, "The Morphology of Shear Fracture of Kevlar Fiber-Reinforced Epoxy Composites," *J. Material Science Letters*, **4**, 845 (1985).

Mittlefehldt, E.R. and J.A. Gardella, Jr., *Appl. Spectrosc.*, **48**, 1172 (1989).

Montoneri, E., *J. Polym. Sci., Part A, Polym. Chem.*, **27**, 3043 (1989).

Montoneri, E., M. Gleria, G. Ricca and G.C. Pappalardo, *J. Macromol. Sci., Chem.*, **A26**, 645 (1989).

Morgan, R.J., C.O. Pruneda, and W.J.Steele, "The Relationship Between the Physical Structure and the Microscopic Deformation and Failure Processes of Poly(p-Phenylene Terephthalamide) Fibers," *J. Polym. Sci. Part B*, **21**, 1757, (1983).

Morgan, R.J. and R.E. Allred, *Reference Book for Composite Tech.*, S.M. Lee Edt., Technomic, Lancaster, PA, 143 (1989[a]).

Morgan, R.J., *Private Communication*, (1989[b]).

Morra, M., E. Occhiello, L. Gila and F. Garbassi, "Surface Dynamics vs. Adhesion in Oxygen Plasma Treated Polyolefins," *J. Adhesion*, **33**, 77 (1990).

Muraoka, Y., J. Kalantar, L.T. Drzal and K.J. Hook, "Analytical Techniques Used to Quantify Chemistry and Atomic Distribution of Sulfonated Species in Polymers," (manuscript in preparation, 1991[a]).

Muraoka, Y., J. Kalantar, and L.T. Drzal, "Sulfonation of Ultra High Molecular Weight Polyethylene Fibers, Part I: Chemical Investigation," (manuscript in preparation, 1991[b]).

Muraoka, Y., J. Kalantar, and L.T. Drzal, "Sulfonation of Ultra High Molecular Weight Polyethylene Fibers, Part II: Mechanical Investigation," (manuscript in preparation, 1991).

Nakayama, Y., F. Soeda, and A. Ishitani, "Surface Analysis of Plasma Treated Poly (ethylene terephthalate) Films," *Polymer Engineering and Science*, **31**, 812 (1991).

Nguyen, H.X., G. Riahi, G. Wood and A. Poursartip, "Optimization of Polyethylene Fiber Reinforced Composites Using A Plasma Surface Treatment," *Allied Signal Technical Publication*, (1988).

Occhiello, E., F. Garbassi, M. Morra and L. Nicolais, "Spectroscopic Characterization of Interfaces in Polymer Composites," *Compos. Sci. and Technol.*, **36**, 133 (1989).

Occhiello, E., M. Morra, G. Morini, F. Garbassi and D. Johnson, "On Oxygen Plasma-Treated Polypropylene Interface with Air, Water, and Epoxy Resins. II. Epoxy Resins," *J. Applied Polymer Science*, **42**, 2045 (1991).

Owens, D.K., "Mechanism of Corona-Induced Self-Adhesion of Polyethylene Film," *J. Appl. Polymer Sci.*, **19**, 265 (1975).

Ozzello, A., D.S. Grummon, J. Kalantar, L.T. Drzal, I.H. Loh and R.A. Moody, "Interfacial Shear Strength of Ion Beam Modified UHMW-PE Fibers in Epoxy Matrix Composites," in Interfaces Between Polymers, Metals and Ceramics, B.M. Dekoven, A.J. Gellman and R. Rosenberg, Eds., *Materials Research Society Symposium Proceedings 153*, Pittsburgh, PA, 217 (1989).

Panar, M., P. Avakian, R.C. Blume, K.H. Gardner, T.D. Gierke, and H.H. Yang, "Morphology of Poly(p-Phenylene Terephthalamide) Fibers," *J. Polymer Science: Polymer Physics Ed.*, **21**, 1955 (1983).

Penn, L.S., F.A. Bystery and H. Marchionni, "Relation of Interfacial Adhesion in Kevlar/Epoxy Systems to Surface Characterization and Performance", *Poly. Composites*, **4**(1), 27 (1983).

Penn, L.S., F. Bystry, W. Krap and S. Lee, "Aramid/Epoxy vs. Graphite/Epoxy: Origin of the Difference in Strength at the Interface," *Polym. Sci. Technol.*, **27**, 93 (1985).

Perry, R.H. and D. Green, *Perry's Chemical Engineers' Handbook*, sixth ed., McGRAW-HILL, New York, 3-49 (1984).

Postema, A.R. and A.J. Pennings, "Chlorosulfonation of Ultra-High Strength Polyethylene Fibers," in Ultra High Modulus Polymers: Approaches to Design and Development, Marcel Dekker Inc., New Yourk, 431 (1988).

Postema, A.R., W. Hoogsteen, and A.J. Pennings, "Crazing in Ultra-high Molecular Weight Polyethylene Gel-Fibers," *Polymer Communications*, **28**, 148 (1987).

Puglisi, O., *Materials Science and Engineering*, **B2**, 167 (1989).

Rao, V. and L.T. Drzal, "The Dependence of Interfacial Shear Strength on Matrix and Interphase Properties," *Polymer Composites*, **12**, 48 (1991[a]).

Rao, V., P. Herrera-Franco, A.D. Ozzello and L.T. Drzal, "A Direct Comparison of the Fragmentation Test and the Microbond Pull-out Test for Determining the Interfacial Shear Strength," *J. Adhesion*, **34**, 65 (1991[b]).

Riggs, D.M., R.J. Shuford and R.W. Lewis, "Graphite Fibers and composites", *Handbook of Composites*, G. Lubin, ed., Van Nostrand Reinhold Co., New York, 196 (1982).

Rose, P.W. and S.L. Kaplan, *Plastic Finishing and Decoration*, Ch 4, Ed. Don Sata, Van Nostrand Reinhold Company, (1986).

Rosenberg, R., *Materials Research Society Proceedings 153*, Pittsburgh, PA, 217 (1989).

Rueda, G., F.L. Matthews and E.W. Godwin, "An Experimental Comparison of Standard Test Methods for the Determination of Tensile, Compressive and Flexural Properties of Kevlar Fibre/Epoxy Laminates," *J. Reinforced Plastics and Composites*, **9**, 182 (1990).

Sawyer, L.C. and M. Jaffe, "The Structure of Thermotropic Copolyesters," *J. Materials Science*, **21**, 1897 (1986).

Sawyer, L.C. and D.T. Grubb, in *Polymer Microscopy*, Chap. 4, Chapman and Hall, New York, (1987).

Schellekens, R. and H. Ketels, "Preparation and Characterization of Solution(gel)-Spun Ethylene-Vinyl Alcohol Fibers," *Polymer Communications*, **31**, 212 (1990).

Schoepnner, G.A. and R.L. Sierakowski, "A review of Compression Test Methods for Organic Matrix Composites," *J. Comp. Tech. & Res.*, **12**, 3 (1990).

Smith, K.J., "The Breaking Strength of Perfect Polymer Fibers," *Polymer Engineering and Science*, **30**, 437 (1990).

Smith, P.A., D,G, Gilbert and A. Poursartip, "Matrix Cracking of Composites Inside a Scanning Electron Microscope," *J. Materials Science Letters*, **4**, 1361 (1985).

Snow, A.W., *Nature*, **292**, 40 (1981[a]).

Snow, A.W., *Carbon*, **19**, 467 (1981[b]).

Snow, A.W., *New Monomers and Polymers*, B.M. Culbertson and C.U. Pittman J., eds., Plenum, New York, 399 (1984).

Snow, A.W., "Thermal Characterization of Polybutadiyne," *J. Macromol. Sci. Chem.*, **A22(10)**, 1429 (1985).

Streitwieser, A. and C.H. Heathcock, *Introduction to Organic Chemistry*, Macmillan Publishing Co., New York, NY (1981).

Sugerman, G., S.J. Monte, S.M. Gabayson, and W.E. Chitwood, "Enhanced Bonding of Fiber Reinforcements to Thermoset Resins," in *Proceedings of the SAMPE Annual Technical Conference*, Paper 2C, Minneapolis (1988).

Suzuki, Y. and M. Kusakabe, "Surface Modification of Silicone Rubber by Ion Implantation," *Nuclear Instruments and Methods in Physics Research*, **B33**, 120 (1988).

Takata, T., "Interface Problems Between Aramid Fibers and Matrix Regions in Fiber-Reinforced Plastics (ArFRP)," translation from Japanese, *Sen-I-Gakkasishi*, **44(2)**, 67 (987).

Tamikawa, M., H. Kaji and K. Ueda, *Kobunshi Kagaku*, **24**, 385 (1967).

Tirpak, G., J. Silibia, *J. Appl. Polym. Sci.*, **17**, 643 (1973).

Tsai, S.W. and H.T. Hahn, "Role of the Interface on the Strength of Composite Materials," *Adhesion and Absorption of Polymers*, L.H. Lee, ed., Plenum Press, New York, 217 (1974).

Torrisi, L., L. Calcagno, and A.M. Foti, "MeV Helium Ion Beam Etching of Poly-TetraFluoroEthylene," *Nuclear Instruments and Methods in Physics Research*, **B32**, 142 (1988).

Ueno, J., M. Watanabe and Y. Tanaka, Jpn. Patent 24,998 (1965).

Venkatesan, T., L. Calcagno, B.S. Elman and G. Foti, *Ion Beam Modification of Insulators*, Elsevier, New York, 301 (1987)

Walles, W.E., U.S. Patent 3,779,840 (1973).

Walles, W.E., *Amer. Chem. Soc. Meeting*, Dallas, TX (1989).

Waterbury, M.C., "The Influence of Processing, Chemistry, and Interphase Microstructure on the Adhesion of Carbon Fibers to Thermoset and Thermoplastic Matrices," Ph.D. dissertation, Michigan State University, (1991).

Werner, H.W. and A.E. Morgan, *J. Appl. Phys.*, **47**, 1232 (1976).

Wertheimer, M.R. and H.P. Schreiber, "Surface Property Modification of Aromatic Polyamides by Microwave Plasmas", *J. Appl. Poly. Sci.*, **26**, 2087 (1981).

White, J.L., "Historical Survey of Polymer Liquid Crystals," *J. Appl. Polym. Sci., Appl. Polym. Symp. 41*, 3 (1985).

Whitney, J.M. and L.T. Drzal, "Three Dimensional Stress Distribution ArounD an Isolated Fiber Fragment," in *Toughened Composites*, ASTM STP **937**, 179 (1980).

Wilson, R.G. and G.R. Brewer, *Ion Beams*, John Wiley & Sons, New York, (1973).

Woodward, E., *Atlas of Polymer Morphology*, Hanser Publishers, NY, 266 (1988).

Wu, S., *Polymer Interface and adhesion*, Marcel Dekker, Inc. New York (1982).

Wu, Y. and G.C. Tesoro, "Chemical Modification of Kevlar Fibers Surface and of Model Diamides," *J. Appl. Poly. Sci.*, **31**, 1041 (1986).

Yasuda, H., *Plasma Polymerization*, Academic Press Inc., Orlando, (1985).

Yates, J.B., D.J. Smith and J.R. Campbell, Eur. Patent 213,466 (1987).

Yoshida, K. and M. Iwaki, "Structure and Morphology of Ion-Implanted Polyimide Films," *Nuclear Instruments and Methods in Physics Research*, **B19/20**, 878 (1987).

Yue, J., A.J. Epstein and A.G. MacDiarmid, *Amer. Chem. Soc. Meeting*, Atlanta, GA (1991).

Zahr, G.E. and P.G. Riewald, "Composite Systems Containing Aramid Fibers: An Overview," *44th Annual Conference, Composite Institute, The Society of the Plastics Industry*, 2E-1 (1989).

Ziegler, J.F., J.P. Biersack, U. Littmark, *The Stopping and Range of Ions in Solids*, Pergamon Press, New York, (1985).